

METAMORPHIC-MAGMATIC EVOLUTION OF THE ULUDAĞ MASSIF

A THESIS SUBMITTED TO
THE GRADUATE SCHOOL OF NATURAL AND APPLIED SCIENCES
OF
MIDDLE EAST TECHNICAL UNIVERSITY

BY

GÜLEN ŞAHİN

IN PARTIAL FULFILLMENT OF THE REQUIREMENTS
FOR
THE DEGREE OF DOCTOR OF PHILOSOPHY
IN
GEOLOGICAL ENGINEERING

JULY 2024

Approval of the thesis:

METAMORPHIC-MAGMATIC EVOLUTION OF THE ULUDAĞ MASSIF
submitted by **GÜLEN ŞAHİN** in partial fulfillment of the requirements for the
degree of **Doctor of Philosophy in Geological Engineering, Middle East**
Technical University by,

Prof. Dr. Naci Emre Altun
Dean, **Graduate School of Natural and Applied Sciences**

Prof. Dr. Erdin Bozkurt
Head of the Department, **Geological Engineering**

Assoc. Prof. Fatma Toksoy Köksal
Supervisor, **Geological Engineering, METU**

Prof. Dr. Erdin Bozkurt
Co-Supervisor, **Geological Engineering, METU**

Examining Committee Members:

Prof. Dr. Erdinç Yiğitbaş
Geological Engineering, Çanakkale Onsekiz Mart University

Assoc. Prof. Dr. Fatma Toksoy Köksal
Geological Engineering, METU

Prof. Dr. Kaan Sayıt
Geological Engineering, METU

Assoc. Prof. Dr. Erman Özsayın
Geological Engineering, Hacettepe University

Assoc. Prof. Dr. Ulaş Avşar
Geological Engineering, METU

Date: 25.07.2024

I hereby declare that all information in this document has been obtained and presented in accordance with academic rules and ethical conduct. I also declare that, as required by these rules and conduct, I have fully cited and referenced all material and results that are not original to this work.

Name Last name : Glen Őahin

Signature :

ABSTRACT

METAMORPHIC-MAGMATIC EVOLUTION OF THE ULUDAĞ MASSIF

Şahin, Gülen

Doctor of Philosophy, Geological Engineering
Supervisor: Assoc. Prof. Dr. Fatma Toksoy Köksal
Co-Supervisor: Prof. Dr. Erdin Bozkurt

July 2024, 230 pages

The objective of this study is to investigate the geological processes of metamorphic, and magmatic evolution of the Uludağ Massif units. The Uludağ Massif is located in the northwestern Anatolia and represents the basement of the Sakarya Zone. The Uludağ Massif is a metamorphic core complex bounded by the Bursa Fault in the north and the Soğukpınar Fault in the south.

This research includes a comprehensive survey of the vicinity of the Bursa Fault, and the metamorphic and magmatic rocks crop out in four different regions, of the Uludağ Massif. The findings indicate that the magmatic and metamorphic rocks of the massif were occurred in either an island arc or active continental margin environment. The metabasalt samples of the Kalabak Unit, the cover unit of the Uludağ Massif, were derived from the mid-ocean ridge basalt.

The directional samples taken from the gneisses and metagranites, were examined for microstructural analyses and it was determined that the dominant deformation stress in the gneisses are in the N-S direction and in the metagranites in the NNE-SSW direction in the study area.

U-Pb zircon studies provide evidence for tectono-thermal impact ages of 53 Ma, suggest that the massif was significantly uplifted in the region during this period.

Metamorphism ages ranging from 32.03 to 35.53 Ma were detected in metagranites, whereas crystallisation ages ranging from 29.53 to 47.87 Ma were reported in granitic rocks. The Uludağ Granites show geochemistry characteristic of A-type granite, while the Kapıdağ Granites display geochemistry characteristic of I-S type granite.

Keywords: Geochemistry, Sakarya Zone, Tectonics, Uludağ Massif, U-Pb zircon

ÖZ

ULUDAĞ MASİFİNİN METAMORFİK-MAGMATİK EVRİMİ

Şahin, Gülen
Doktora, Jeoloji Mühendisliği
Tez Yöneticisi: Doç. Dr. Fatma Toksoy Köksal
Ortak Tez Yöneticisi: Prof. Dr. Erdin Bozkurt

Temmuz 2024, 230 sayfa

Bu çalışmanın amacı, Uludağ Masifi birimlerindeki metamorfik ve magmatik gelişimin jeolojik süreçlerini incelemektir. Uludağ Masifi kuzeybatı Anadolu'da yer almakta ve Sakarya Zonunun temelini oluşturmaktadır. Uludağ Masifi kuzeyde Bursa Fayı güneyde ise Soğukpınar Fayı tarafından sınırlandırılan metamorfik bir çekirdek komplekstir.

Araştırma, Bursa Fayı ve çevresinin kapsamlı bir incelemesini ve Uludağ Masifinde dört farklı bölgede açığa çıkan metamorfik ve magmatik kayaçların kapsamlı bir incelemesini içermektedir. Bulgular, masifin magmatik ve metamorfik kayaçlarının ya ada yayı volkanizması ya da iki kıtanın çarpışması sırasında aktif kıta kenarı magmatizması tarafından oluşturulduğunu göstermektedir. Metabazalt örnekleri okyanus ortası sırtı bazaltının mantosundan türediği gözlenmiştir.

Çalışma alanında yüzlek veren gnayslar ve metagranitlerden mikroyapısal analizler yapılabilmesi için alınan yönlü örnekler incelenmiş ve gnayslardaki baskın deformasyon stresinin K-G yönlü, metagranitlerde ise KKD-GGB yönlü olduğu tespit edilmiştir.

U-Pb zirkon alıřmaları, 53 Ma tektono-termal etki yařlarına dair kanıtlar sunmakta ve bu dnemde blgede masifin nemli lde ykseldiđini gstermektedir. Metagranitlerde 32.03 ila 35.53 Ma arasında deđiřen metamorfizma yařları tespit edilirken, granitik kayalarda 29.53 ila 47.87 Ma arasında deđiřen kristalleřme yařları elde edilmiřtir. Uludađ Granitleri A tipi granit jeokimyası zelliđi gsterirken, Kapıdađ Granitleri I-S tipi granit jeokimyası zelliđi gstermektedir.

Anahtar Kelimeler: Jeokimya, Sakarya Zonu, Tektonik, Uludađ Masifi, U-Pb zirkon

This thesis is dedicated to the memory of our Eternal Leader Atatürk and all his comrades-in-arms. Liberty is not earned, it is taken.

ACKNOWLEDGMENTS

The author wishes to express his deepest gratitude to his supervisor, Assoc. Prof. Dr. Fatma TOKSOY KÖKSAL and co-supervisor Prof. Dr. Erdin BOZKURT, thank you for your guidance, advice, criticism, encouragement, and insight throughout the research.

I should especially open a parenthesis for my supervisor, Assoc. Prof. Dr. Fatma TOKSOY KÖKSAL. Fatma TOKSOY KÖKSAL's belief in this study and mine has enabled this study and the project resulting from this study to take its final form. Fatma TOKSOY KÖKSAL, this study would not have become this if you had not given me so much strength and believed in me. Fortunately, you were always there whenever I needed you, scientifically and mentally.

The author would also like to thank Prof. Dr. Erdinç YİĞİTBAŞ, Prof. Dr. Kaan SAYIT, Assoc. Prof. Dr. Erman ÖZSAYIN, and Assoc. Prof. Dr. Dr. Ulaş AVŞAR, for their suggestions and comments.

I thank my husband, Dr. İsmail Onur TUNÇ, for his moral support and technical assistance. I would also like to thank my family for their moral support during my thesis studies. I would also like to thank my dear friends Kübra ÇEVİRİM, Cihan ERSALI, M. Sungur DEMİR, M. Vedat GÜN, and İbrahim Özgür DEDEOĞLU, Nuray ALPASLAN who always helped me during my studies and gave me moral support. Finally, I would like to thank my three department heads, Salih DİNÇ, Abdullah MURATOĞLU, and H. Alim BARAN, who never caused any difficulties for me to commute between Batman and Ankara for years during my entire doctoral study and always supported me.

This work is partially funded by the Scientific and Technological Research Council of Turkey under grant number TÜBİTAK 122Y258.

TABLE OF CONTENTS

ABSTRACT.....	v
ÖZ	vii
ACKNOWLEDGMENTS	x
TABLE OF CONTENTS.....	xi
LIST OF TABLES	xvi
LIST OF FIGURES	xvii
LIST OF ABBREVIATIONS	xxxi
1 INTRODUCTION	1
1.1 Study Area	1
1.2 General Overview	2
1.3 Current Problems	4
1.4 Research Objectives	6
1.5 Research Contributions	7
1.6 Methodology	7
1.7 Methods of the Study	8
1.7.1 Field Study	8
1.7.2 Laboratory Study	9
1.7.3 Office Study	14
2 REVIEW OF PREVIOUS STUDIES	15
2.1 Introduction.....	15
2.2 Regional Geology and Tectonics	17
2.2.1 Tectonic and stratigraphic terranes	18
2.2.2 Tectonics	20

2.3	The Relationship Between Sutures and Evolution	21
2.4	The Uludağ Massif	23
2.4.1	Geological Features of the Uludağ Massif	27
2.4.2	Ductile Shear Zone Exhumation	32
2.5	Metamorphism and Shear Zone Activity	36
2.6	Exhumation.....	37
2.7	Present day activity of Bursa Fault and Eskişehir Fault.....	39
3	GEOLOGICAL FINDINGS.....	41
3.1	Introduction	41
3.2	Macro-scale Deformations in the Field	42
3.3	South Uludağ Metagranite and Timing of the Shear Zone.....	47
3.4	Tectonostratigraphic units	49
3.4.1	North of the Bursa Fault	49
3.4.2	The Uludağ Massif	51
3.4.3	South of Eskişehir Fault	56
3.5	Structural Elements of the Massif	58
3.5.1	North of the Bursa Fault	58
3.5.2	The Bursa Fault	58
3.5.3	The Uludağ Massif	59
3.5.4	The Eskişehir Fault.....	59
3.5.5	South of Eskişehir Fault	60
4	PETROGRAPHIC STUDIES AND MICRO-SCALE OBSERVATIONS	61
4.1	Introduction	61
4.2	Petrographic Interpretation	63

4.2.1	The South Uludağ Metagranites	64
4.2.2	Uludağ Massif Gneisses.....	72
4.2.3	Uludağ Granites	83
4.2.4	The Sazak Formation Metabasalt.....	88
4.3	Implications by Petrographic Interpretation	89
5	GEOCHEMISTRY	103
5.1	Introduction of Geochemistry	103
5.2	Trace Element Modelling.....	106
5.3	Radiogenic Isotope Data	107
5.3.1	Petrogenetic Utilization of Radiogenic Isotopes.....	107
5.3.2	Characterization of Isotope Reservoirs	109
5.3.3	Formation of the Continental Crust	110
5.4	Geochemistry of the Uludağ Massif	112
5.4.1	Major and Trace Element Geochemistry of the Uludağ Massif ...	112
5.4.2	Tectono-magmatic differentiation of the study area.....	123
5.4.3	Radiogenic Isotopes of the Rocks.....	138
6	GEOCHRONOLOGY	153
6.1	Sample Preparation	153
6.2	LA-ICP-MS U-Pb Analysis	154
6.3	LA-ICP-MS U-Pb Zircon Analysis Results.....	155
6.3.1	South Uludağ Metagranites.....	156
6.3.2	Uludağ Massif Gneisses.....	162
6.3.3	Uludağ Granites	169
7	DISCUSSIONS AND CONCLUSIONS	173

7.1	Discussions	173
7.2	Tectono-metamorphic Evolution of the Uludağ Massif	178
7.3	Magmatic and Geochemical Evolution of the Uludağ Massif	183
7.4	Interpretation of Geochronology and Isotope Geochemistry Together.	184
7.5	Geological Evolution	187
7.6	Conclusions and Final Thoughts	190
7.6.1	Relationship between Uludağ and Kazdağ Massifs	190
7.6.2	Relationship between granitic intrusions	191
7.6.3	Role of major faults in the evolution of the Uludağ Massif	191
7.6.4	Tectono-metamorphic and magmatic evolution	192
7.7	Recommendations	193
	REFERENCES	195
8	APPENDICES	215
A.	LA-ICP-MS U-Pb zircon analysis results for sample 1802	215
B.	LA-ICP-MS U-Pb zircon analysis results for sample 1803	216
C.	LA-ICP-MS U-Pb zircon analysis results for sample 1809	217
D.	LA-ICP-MS U-Pb zircon analysis results for sample 1810	218
E.	LA-ICP-MS U-Pb zircon analysis results for sample 1811	219
F.	LA-ICP-MS U-Pb zircon analysis results for sample 1812	220
G.	LA-ICP-MS U-Pb zircon analysis results for sample 1813	221
H.	A-ICP-MS U-Pb zircon analysis results for sample 1814	222
İ.	LA-ICP-MS U-Pb zircon analysis results for sample 1817	223
J.	LA-ICP-MS U-Pb zircon analysis results for sample 1819	224
K.	LA-ICP-MS U-Pb zircon analysis results for sample 1820	225

L. LA-ICP-MS U-Pb zircon analysis results for sample 1821	226
M. LA-ICP-MS U-Pb zircon analysis results for sample 1903	227
N. LA-ICP-MS U-Pb zircon analysis results for sample 1904.....	228
CURRICULUM VITAE	229

LIST OF TABLES

TABLES

Table 4.1. Coordinates, lithologies and sampling purposes of the taken samples. .63	
Table 5.1. Major, trace, and radiogenic isotope elements used in geochemical studies. 105	105
Table 5.2. Current isotopic composition of mantle and crustal reservoirs. 108	108
Table 5.3 Sr, Nd and Pb isotope ratios for some common rock types. 110	110
Table 5.4. The table shows oxide, main and trace elements for gneisses and metabasalts. 113	113
Table 5.5. The table shows oxide, main and trace elements for metagranites and granites. 116	116
Table 5.6. Samples names and radiogenic isotope data results. Table 6.5. Samples names and radiogenic isotope data results..... 139	139
Table 6.1 Units analysed for U-Pb zircon, their formations and cathodoluminescence (CL) mount numbers. 156	156
Table 6.2. U-Pb zircon analysis results of samples taken from the field according to coordinates, formation, and lithology..... 172	172

LIST OF FIGURES

FIGURES

Figure 1.1. The jaw crusher is the first step in preparing samples for geochemical analysis. a) The jaw crusher is cleaned with alcohol to prevent contamination and made ready for use; b) Samples are placed in the hopper on the jaw crusher.	10
Figure 1.2. The first step of sample preparation is completed by removing the samples placed in the jaw crusher from the hopper at the bottom.	10
Figure 1.3. Operations with the grinder a) shows the grinder device, and b) samples from the jaw crusher are placed in the upper chamber of the grinder.	11
Figure 1.4. Some of the pictures taken during sieve analysis are a) the preparation of the sieve system before sieve analysis and b) the approximate amount of sample to be put on the sieve.	12
Figure 2.1. Sample locations for this study and geological map of the Uludağ massif modified after Okay et al. (2008).	16
Figure 2.2. Tectonic plates, faults, and their relative motions in and around Türkiye, location of the Uludağ Massif showed with a red square.....	17
Figure 2.3. Tectonic regions of Anatolia were determined by today's tectonic activity, as taken from Selçuk and Gökten (2012).....	18
Figure 2.4. The diagram illustrates sutures exhibited in Türkiye. The study area is shown with a yellow box (taken from Okay and Tüysüz, 1999; Okay, 2008).	19
Figure 2.5. The GPS velocities concerning Eurasia indicate Anatolia's anticlockwise rotation (adapted from Reilinger et al. 2006).....	21
Figure 2.6. Geological map of the Uludağ Massif and its surroundings taken from Okay et al. (2008). The Eskişehir Fault mentioned relates to the Soğukpınar Fault seen on this map. According to Okay et al. (2008), the rocks north of this fault are part of the Sakarya Zone of the Pontides, whereas the rocks to the south are part of the Anatolide-Tauride Block.....	25
Figure 2.7. Geological map of the study area created in this study.	26

Figure 2.8. Simplified tectonostratigraphic columns of Uludağ Massif as basement of Sakarya Zone and the Tavşanlı Zone within the Anatolide-Tauride Block.....	27
Figure 2.9. The stratigraphic column reveals several terranes on both sides of the İzmir-Ankara suture and Eskişehir Fault (modified from Okay and Satır, 2006; Okay et al. 2008).	31
Figure 2.10. İnönü-Eskişehir Fault Zone is reaching the Bursa-Uludağ (modified from Özsayın and Dirik, 2007).....	34
Figure 2.11. Google Earth image of the Bursa Fault.....	35
Figure 2.12. The study conducted by Okay et al. (2008) presents data that illustrates the transformation of the Uludağ Massif, starting with its highest pressure and temperature conditions and progressing towards its exposure over the Oligocene and Miocene periods.	37
Figure 2.13. Evolutionary changes of the Uludağ Massif have been exposed from the Early Oligocene (a) to the Early Miocene (c). (Okay et al. 2008).	38
Figure 2.14. Seismicity of Bursa - Eskişehir and surroundings [AFEAD (Active Faults of Eurasia Database), GEM (Global Earthquake Model Foundation), and USGS (U.S. Geological Survey) data set merged with field study].....	40
Figure 3.1. Shear sense markers are present in the ductile zone. Figure a and b exhibit winged mantled clasts with σ -type characteristics inside an amphibole gneiss. Samples exhibit dextral lineation illustrated at an angle of approximately 120°	43
Figure 3.2. Shear sense markers are present in the ductile zone. Figura a and b exhibit winged mantled clasts with σ -type characteristics inside an amphibole gneiss. Samples exhibit dextral lineation illustrated at an angle of approximately 116°	43
Figure 3.3. Shear sense markers are present in the ductile zone. a) and b) show mylonitic quartz-feldspar veins sheared into folds, revealing C-type shear bands. All samples exhibit dextral displacement along the fault, as illustrated at an angle of approximately 118°	44
Figure 3.4. Amphibole bands in the gneiss.	45

Figure 3.5. Amphibole-gneiss migmatization from the northern side of the study area.	46
Figure 3.6. Marble layers of the Zirve marble unit from Uludağ Massif, southern peak of the Mount Uludağ. Amphibolite intrusions are seen as a result of right lateral shear sense.....	46
Figure 3.7. Marble layers of the Zirve marble in the Kar Çukuru area, marble bedding measured as N7W-23NE and amphibole boudinaged between layers measured as N5W-23 NE.....	47
Figure 3.8. Mica-schist from the north of the study field.	49
Figure 3.9. The contact zone between the gneisses of the Gökdere formation and Uludağ granites.	50
Figure 3.10. Figure shows the folding in gneisses of the Gökdere formation due to tectonic forces.	50
Figure 3.11. Outcrops of the Bursa marble on the road from Saitabat to Alaçam..	51
Figure 3.12. The red line shows the contact between the Zirve marble and the Kilimligöl formation.	53
Figure 3.13. Contact between the Zirve marble and gneiss-amphibolite alternation of the Kilimligöl formation around the Aynalı Lake.	53
Figure 3.14. Quartzo-feldspathic gneisses of the Gökdere formation showing well-foliation, banded structures with red dashed lines (UTM coordinate: 0698279E – 4438364N).	54
Figure 3.15. Local granite intrusions cut the South Uludağ Metagranite in the NE of Soğukpınar Village (UTM coordinate: 0680628E - 4437989N).....	55
Figure 3.16. Outcrop views of the Kapıdağ Granite in the south of the study area.	57
Figure 4.1. Sample locations from the study field.	62
Figure 4.2. The South Uludağ Metagranite (sample 1819). a) and c) PPL images, b) and d) XPL images. (Kfs: alkali feldspar, plag: plagioclase, qrtz: quartz).	65
Figure 4.3. The South Uludağ Metagranite (sample 1902-P(A)). a) and c) PPL images, b) and d) XPL images. (GBM: grain boundary migration, Kfs: alkali feldspar, mica: mica, plag: plagioclase, SGR: sub-grain rotation, qrtz: quartz.)...	65

Figure 4.4. The South Uludağ metagranite (sample 1903). a) and c) PPL images, b) and d) XPL images. (GBM: grain boundary migration, Kfs: alkali feldspar, mica: mica, plag: plagioclase, qrtz: quartz.).....	66
Figure 4.5. The South Uludağ Metagranite (sample 1904). a) and c) PPL images, b) and d) XPL images. (K-fs: alkali feldspar, bio: biotite, plag: plagioclase, qrtz: quartz, epd: epidote)	66
Figure 4.6. The South Uludağ Metagranite (sample 1801). a) and c) PPL images, b) and d) XPL images (red arrow: north direction, yellow arrow: shear direction, bio:biotite, K-fs: alkali feldspar, plag: plagioclase, qrtz: quartz, myrm: myrmekite).	67
Figure 4.7. The South Uludağ Metagranite (sample 1802) a) and c) PPL images, b) and d) XPL images (red arrow: north direction, yellow arrow: shear direction, bio:biotite, K-fs: alkali feldspar, mica: mica, plag: plagioclase, fsp: feldspar, qrtz: quartz, myrm: myrmekite).....	69
Figure 4.8. The South Uludağ Metagranite (sample 1814) a) and c) PPL images, b) and d) XPL images (red arrow: north direction, yellow arrow: shear direction, bio:biotite, K-fs: alkali feldspar, mica: mica, plag: plagioclase, qrtz: quartz, myrm: myrmekite).	69
Figure 4.9. The South Uludağ Metagranite (sample 1817) a) and c) PPL images, b) and d) XPL images. (GBM: grain boundary migration, Kfs: alkali feldspar, mica: mica, plag: plagioclase, qrtz: quartz, srct: sericitisation).	71
Figure 4.10. The South Uludağ Metagranite (sample 1818) a) and c) PPL images, b) and d) XPL images. (Kfs: alkali feldspar, mica: mica, plag: plagioclase, SGR: sub-grain rotation, qrtz: quartz.).....	72
Figure 4.11. The Uludağ Massif Gneiss (sample 1803) a) and c) PPL images, b) and d) XPL images. (Kfs: alkali feldspar, mica: mica, qrtz: quartz).....	73
Figure 4.12. The Uludağ Massif Gneiss (sample 1804) a) and c) PPL images, b) and d) XPL images. (BLG: dynamic recrystallisation by bulging, GBM: grain boundary migration, mica: mica, plag: plagioclase, qrtz: quartz).	74

Figure 4.13. The Uludağ Massif Gneiss (sample 1805) a) and c) PPL images, b) and d) XPL images. (epd: epidote, hbl: hornblende, mica: mica, plag: plagioclase, qrtz: quartz).....	75
Figure 4.14. The Uludağ Massif Gneiss (sample 1806) a) and c) PPL images, b) and d) XPL images. (red arrow: north direction, bio: biotite, Kfs: alkali feldspar, msct: muscovite, qrtz: quartz, SGR: sub-grain rotation).	76
Figure 4.15. The Uludağ Massif Gneiss (sample1809) a) PPL images, b), c) and d) XPL images. (red arrow: north direction, BLG: dynamic recrystallisation by bulging, GBM: grain boundary migration, plag: plagioclase, qrtz: quartz, SGR: sub-grain rotation.).....	77
Figure 4.16. The Uludağ Massif Gneiss(sample1810) a) and c) PPL images, b) and d) XPL images. (red arrow: north direction, bio: biotite, fsp: feldspar, kfs: alkali feldspar, plag: plagioclase, qrtz: quartz).	78
Figure 4.17. The Uludağ Massif Gneiss (sample 1811) a) and c) PPL images, b) and d) XPL images (red arrow: north direction, mica: mica, plag: plagioclase, qrtz: quartz).	79
Figure 4.18. The Uludağ Massif Gneiss sample (1812) a) and c) PPL images, b) and d) XPL images. (bio: biotite, hbl: hornblende, kfs: alkali feldspar, plag: plagioclase, qrtz: quartz, opq: opaque).	80
Figure 4.19. The Uludağ Massif Gneiss (sample 1820) a) and c) PPL images, b) and d) XPL images. (Kfs: alkali feldspar, plag: plagioclase, qrtz: quartz).....	81
Figure 4.20. The Uludağ Massif Gneiss (sample 1902 P(B)). a) and c) PPL images, b) and d) XPL images. (Kfs: alkali feldspar, mica: mica, plag: plagioclase, qrtz: quartz).	82
Figure 4.21. The Central Uludağ Granite (sample 1815). a) PPL images, b), c) and d) XPL images. (Kfs: alkali feldspar, srct: sericitisation, plag: plagioclase, qrtz: quartz).	84
Figure 4.22. The Central Uludağ Granite (sample 1808) a) and c) PPL images, b) and d) XPL images (hbl: hornblende, Kfs: alkali feldspar, plag: plagioclase, qrtz: quartz).	84

Figure 4.23. The Central Uludağ Granite (sample 1816)a) and c) PPL images, b) and d) XPL images (Kfs: alkali feldspar, plag: plagioclase).....	85
Figure 4.24. The Central Uludağ Granite (sample 1821)a) and c) PPL images, b) and d) XPL images. (Kfs: alkali feldspar, mica: mica, plag: plagioclase, qrtz: quartz).....	85
Figure 4.25. The Central Uludağ Granite (sample 1822) a) and c) PPL images, b) and d) XPL images. (Kfs: alkali feldspar, mica: mica, plag: plagioclase).	86
Figure 4.26. The Kapıdağ Granite (sample 1813-(P1)) a) and c) PPL images, b) and d) XPL images (hbl: hornblende, Kfs: alkali feldspar, bio: biotite, plag: plagioclase, qrtz: quartz).	87
Figure 4.27. The Kapıdağ Granite (sample 1813-(P2)) a) and c) PPL images, b) and d) XPL images. (hbl: hornblende, kfs: alkali feldspar, mica: mica, plag: plagioclase, qrtz: quartz).	88
Figure 4.28. The Sazak Formation Metabasalt (sample 1905) a) and c) PPL images, b) and d) XPL images (plag: plagioclase, hbl: hornblende, ep: edpidote).	89
Figure 4.29. Thin section images of the South Uludağ Metagranite (sample 1801-P) (a): PPL, b): XPL; red arrow: north direction; qrtz: quartz, plag: plagioclase, bio: biotite).....	91
Figure 4.30. Thin section images of the South Uludağ Metagranite (sample 1801-P) (a): PPL, b): XPL; red arrow: north direction; qrtz: quartz, bio: biotite, Kfs: alkali feldspar, myrm: myrmekite).....	91
Figure 4.31. Thin section images of the South Uludağ Metagranite (sample 1801-P) (a): XPL, b): XPL; red arrow: north direction; qrtz: quartz, plag: plagioclase, Kfs: alkali feldspar).....	92
Figure 4.32. Thin section images of the South Uludağ Metagranite (sample 1801-P) (XPL image; red arrow: north direction; qrtz: quartz, plag: plagioclase).	92
Figure 4.33. Thin section images of the Kilimligöl Formation Gneiss (sample 1805-P) (a): XPL, b): PPL; red arrow: north direction; ep: epidote, qrtz: quartz, amp: amphibole, plag: plagioclase).....	93

Figure 4.34. Thin section images of the Kilimligöl Formation Gneiss (sample 1805-P) (a): XPL, b): PPL; red arrow: north direction; ep: epidote, qrtz: quartz, amp: amphibole, plag: plagioclase).	93
Figure 4.35. Thin section images of the Kilimligöl Formation Gneiss (sample 1805-P) (a): XPL, b): PPL; red arrow: north direction; ep: epidote, qrtz: quartz, amp: amphibole, fspar: feldspar, plag: plagioclase).	94
Figure 4.36. Thin section images of the Central Uludağ Granite (sample 1809-P) (left: PPL, right: XPL; red arrow: north direction; qrtz: quartz, plag: plagioclase, bio: biotite).	95
Figure 4.37. Thin section images of the Gökdere Formation Gneiss (sample 1811-P) (a): PPL, b): XPL; red arrow: north direction; qrtz: quartz, plag: plagioclase, bio: biotite, zn: zircon).	95
Figure 4.38. Thin section images of the Gökdere Formation Gneiss (sample 1811-P) (a): PPL, b): XPL; red arrow: north direction; plag: plagioclase, bio: biotite). ..	96
Figure 4.39. Thin section images of the Kapıdağ Granite (sample 1813-P1) (a): PPL, b): XPL; red arrow: north direction; plag: plagioclase, hb: hornblende).	96
Figure 4.40. Thin section images of the Kapıdağ Granite (sample 1813-P1) (a): PPL, b): XPL; red arrow: north direction; plag: plagioclase, mica: mica).	97
Figure 4.41. Thin section images of the Kapıdağ Granite (sample 1813-P1) (a): XPL, b): PPL; red arrow: north direction; hb: hornblende, zn: zircon).	97
Figure 4.42. Thin section images of the Kapıdağ Granite (sample 1813-P1 , zn: zircon (a): XPL, b): PPL; red arrow: north direction; plag: plagioclase, hb: hornblende).	98
Figure 4.43. Microstructures of all three recrystallisation methods of Stipp et al. (2002). a) Dynamic recrystallisation by bulging (BLG) occurring at grain boundaries and microcracks. b) Sub-grain rotation (SGR) refers to forming core-mantle systems where recrystallised grains replace ribbon grains. c) Grain boundary migration (GBM) leads to inconsistent grain shapes and sizes, as well as the formation of interfingering sutures.	99

Figure 4.44. Depth-temperature-time path for the exhumation of the Uludag massif, which was created by combining the data obtained in this study with previous studies.	101
Figure 5.1. Origins of the mantle. Mantle sources are illustrated in $^{87}\text{Sr}/^{86}\text{Sr}(\text{T})$ vs. $^{143}\text{Nd}/^{144}\text{Nd}(\text{T})$ (Zindler and Hart, 1986).	111
Figure 5.2. Alteration in the samples according to the K_2O and Na_2O loss.	119
Figure 5.3. Bivariate plots against TiO_2	120
Figure 5.4. Bivariate plots against Zr/Ti	123
Figure 5.5. $\text{Rb}/100\text{-Y}/44\text{-Nb}/16$ diagram (Thieblemont and Cabanis, 1990).	124
Figure 5.6. Bivariate plots of VICE/MICE ratios against $^{143}\text{Nd}/^{144}\text{Nd}$ and Nb/Y	126
Figure 5.7. Tectonic classification of the samples according to Rb versus $\text{Y}+\text{Nb}$, Nb versus Y , Rb versus $\text{Ta}+\text{Yb}$ and Ta versus Yb (Perce et al. 1984).	127
Figure 5.8. Sample plots on the $\text{Rb}/30\text{-Hf-}3\text{xTa}$ diagram by Harris et al. (1986).	128
Figure 5.9. The revised $\text{Th}/\text{Yb} - \text{Ta}/\text{Yb}$ diagram is divided into three tectonic zones: oceanic arcs, active continental margins (ACM), and intraplate volcanic zones (WPVZ). The intraplate basalts (WPB) and MORB (mid-ocean ridge basalts) represent the zones previously defined by Pearce (1982, 1983), Schandl and Gorton (2002).	129
Figure 5.10. The $\text{Ta}/\text{Yb}\text{-Th}/\text{Yb}$ diagram (Pearce, 1982) shows that all samples have geochemistry related to volcanic arcs except for the 1901 and 1905 Sazak Formation metabasalts. Metabasalts appear to be in the transition zone.	130
Figure 5.11. Plots of the samples on the granite classification diagrams by Whalen et al. (1987): $10000\text{Ga}/\text{Al}$ versus $\text{K}_2\text{O}/\text{MgO}$, Nb , Ce , Y , Zn binary plots are meaningful for differentiation into A, I and S-type granites.	131
Figure 5.12. Spider diagrams of all samples normalized to primitive mantle (normalizing values are taken from Sun and McDonough, 1989), showing negative K , P and Ti anomalies and relatively negative Zr and Hf anomalies. The figure also shows positive U , Pb and Li anomalies.	132

Figure 5.13. Spider plots of the primitive mantle separated by units show negative K, P and Ti anomalies and relatively negative Zr anomalies. U and Pb anomalies are positive.	133
Figure 5.14. Spider diagram of all samples normalized to chondrite (normalizing values are taken from McDonough and Sun, 1995).	134
Figure 5.15. Unit-specific REE spider plots normalized to chondrite (normalizing values are taken from McDonough and Sun, 1995).	135
Figure 5.16. Spider diagram of all samples normalized to ORG (Ocean Ridge Granite) shows negative Zr and Hf anomalies (Pearce et al. 1984).....	136
Figure 5.17. Unit-specific spider diagrams of all samples normalized to ORG (Ocean Ridge Granite) show negative Zr and Hf anomalies in each rock unit sample.	136
Figure 5.18. REE spider plot for all the samples normalized to the upper crust shows negative K, P and Ti anomalies (normalization values are from Taylor and McLennan, 1985).....	137
Figure 5.19. Unit-specific REE spider plots for the samples normalized to the upper crust shows negative K, P and Ti anomalies.....	138
Figure 5.20. $^{87}\text{Sr}/^{86}\text{Sr}$ and ϵNd values when age data is calculated as 33 Ma for metagranites.	142
Figure 5.21. $\epsilon\text{Nd}(\text{T}) - ^{87}\text{Sr}/^{86}\text{Sr}(\text{T})$ Metagranites data.....	142
Figure 5.22. $^{87}\text{Sr}/^{86}\text{Sr}$ and ϵNd values when age data is calculated as 220 Ma for gneisses.	144
Figure 5.23. $\epsilon\text{Nd}(\text{T}) - ^{87}\text{Sr}/^{86}\text{Sr}(\text{T})$ gneisses data.	145
Figure 5.24. $^{87}\text{Sr}/^{86}\text{Sr}$ and ϵNd values when age data is calculated as 29.53 Ma for the Central Uludağ Granite and 47.87 Ma for the Kapıdağ Granite (1813-P1) in granites.....	147
Figure 5.25. $\epsilon\text{Nd} - ^{87}\text{Sr}/^{86}\text{Sr}$ granite data for 29.53 Ma ago for the Central Uludağ Granite and 47.87 Ma ago for the Kapıdağ Granite (1813-P1)	148

Figure 5.26. $^{87}\text{Sr}/^{86}\text{Sr}$ and ϵNd values when age data is calculated as 455 Ma for metabasalts.	150
Figure 5.27. $\epsilon\text{Nd}(\text{T})$ - $^{87}\text{Sr}/^{86}\text{Sr}(\text{T})$ data belongs to metabasalts.	150
Figure 5.28. a) Zindler and Hart (1986), b) All samples $\epsilon\text{Nd}(\text{T})$ - $^{87}\text{Sr}/^{86}\text{Sr}(\text{T})$ values.	151
Figure 6.1. Cathodoluminescence (CL) images of typical zircon grains from South Uludağ Metagranite (Sample No. 1802) showing the internal structure and laser analysis location.	157
Figure 6.2. U-Pb zircon ages of South Uludağ Metagranite (Sample No. 1802) a) Concordia diagram, b) Mean age diagram and c) Combined binned frequency and probability density distribution plots of zircon grains in the range of 0–100 Ma, show that the metamorphism age of the metagranite sample is $33.47\pm 0.21\text{Ma}$	157
Figure 6.3. Cathodoluminescence (CL) images of typical zircon grains from South Uludağ Metagranite (Sample No. 1814) showing the internal structure and laser analysis location.	158
Figure 6.4. U-Pb zircon ages of South Uludağ Metagranite (Sample No. 1814) a) Concordia diagram, b) Mean age diagram and c) Combined binned frequency and probability density distribution plots of zircon grains in the range of 0–100 Ma, show that the metamorphism age of the metagranite for this sample is $34.44\pm 0.20\text{Ma}$	158
Figure 6.5. Cathodoluminescence (CL) images of typical zircon grains from South Uludağ Metagranite (Sample No. 1817) showing the internal structure and laser analysis location.	159
Figure 6.6. U-Pb zircon ages of South Uludağ Metagranite (Sample No. 1817) a) Concordia diagram, b) Mean age diagram and c) Combined binned frequency and probability density distribution plots of zircon grains in the range of 0–100 Ma, show that the metamorphism age of the metagranite sample is $35.43\pm 1.5\text{Ma}$	159

Figure 6.7. Cathodoluminescence (CL) images of typical zircon grains from South Uludağ Metagranite (Sample No. 1819) showing the internal structure and laser analysis location.	160
Figure 6.8. U-Pb zircon ages of South Uludağ Metagranite (Sample No. 1819). a) Concordia diagram, b) Mean age diagram and c) Combined binned frequency and probability density distribution plots of zircon grains in the range of 0–100 Ma, show that the age of metamorphism of the metagranite sample is 34.36 ± 0.35 Ma.	160
Figure 6.9. Cathodoluminescence (CL) images of typical zircon grains from metagranite sample of the Gökdere formation (Sample No. 1903) showing the internal structure and laser analysis location.	161
Figure 6.10. U-Pb zircon ages of metagranite of the Gökdere formation (Sample No. 1903). a) Concordia diagram, b) Mean age diagram and c) Combined binned frequency and probability density distribution plots of zircon grains in the range of 0–100 Ma, show that the metamorphism age of the metagranite sample is 32.03 ± 0.74 Ma.	161
Figure 6.11. Cathodoluminescence (CL) images of typical zircon grains from gneiss sample of the Gökdere formation (Sample No. 1803) showing the internal structure and laser analysis location.	162
Figure 6.12. U-Pb zircon ages of gneiss sample of the Gökdere formation (Sample No. 1803). a) Concordia diagram, b) Mean age diagram and c) Combined binned frequency and probability density distribution plots of zircon grains in the range of 0–400 Ma, show that the protolith crystallisation age of the gneiss sample is 236.8 ± 1.1 Ma.	162
Figure 6.13. Cathodoluminescence (CL) images of typical zircon grains from gneiss sample of the Gökdere formation (Sample No. 1809) showing the internal structure and laser analysis location.	163
Figure 6.14. U-Pb zircon ages of gneiss sample of the Gökdere formation (Sample No. 1809). a) Concordia diagram, showing the major events. The discordia line intersects the concordia curve at two points. The upper intercept is interpreted as	

the protolith crystallisation age, whereas the lower intercept defines the final episodic lead loss., b) Mean age diagram and c) Combined binned frequency and probability density distribution plots of zircon grains in the range of 0–400 Ma, show that the protolith crystallisation age is 236 Ma. 163

Figure 6.15. Cathodoluminescence (CL) images of typical zircon grains from gneiss sample of the Gökdere formation (Sample No. 1810) showing the internal structure and laser analysis location. 164

Figure 6.16. U-Pb zircon ages of gneiss sample of the Gökdere formation (Sample No. 1810). a) Concordia diagram, showing the major events. The discordia line intersects the concordia curve at two points. The upper intercept is interpreted as the protolith crystallisation age, whereas the lower intercept defines the final episodic lead loss., b) Mean age diagram and c) Combined binned frequency and probability density distribution plots of zircon grains in the range of 0–400 Ma, show that the protolith crystallisation age is 225 Ma. 164

Figure 6.17. Cathodoluminescence (CL) images of typical zircon grains from gneiss sample of the Gökdere formation (Sample No. 1811) showing the internal structure and laser analysis location. 165

Figure 6.18. U-Pb zircon ages of gneiss sample of the Gökdere formation (Sample No. 1811). a) Concordia diagram, showing the major events. The discordia line intersects the concordia curve at two points. The upper intercept is interpreted as the protolith crystallisation age, whereas the lower intercept defines the final episodic lead loss., b) Mean age diagram and c) Combined binned frequency and probability density distribution plots of zircon grains in the range of 0–300 Ma, show that the protolith crystallisation age is 104 Ma. 165

Figure 6.19. Cathodoluminescence (CL) images of typical zircon grains from gneiss sample of the Gökdere formation (Sample No. 1820) showing the internal structure and laser analysis location. 166

Figure 6.20. U-Pb zircon ages of gneiss sample of the Gökdere formation (Sample No. 1820). a) Concordia diagram, showing the major events. The discordia line intersects the concordia curve at two points. The upper intercept is interpreted as

the protolith crystallisation age, whereas the lower intercept defines the final episodic lead loss., b) Mean age diagram and c) Combined binned frequency and probability density distribution plots of zircon grains in the range of 0–400 Ma, show that the protolith crystallisation age is 192 Ma.....	166
Figure 6.21. Cathodoluminescence (CL) images of typical zircon grains from gneiss sample of the Gökdere formation (Sample No. 1904) showing the internal structure and laser analysis location.	167
Figure 6.22. U-Pb zircon ages of gneiss sample of the Gökdere formation (Sample No. 1904). a) Concordia diagram, showing the major events. The discordia line intersects the concordia curve at two points. The upper intercept is interpreted as the protolith crystallisation age, whereas the lower intercept defines the final episodic lead loss., b) Mean age diagram and c) Combined binned frequency and probability density distribution plots of zircon grains in the range of 0–400 Ma, show that the protolith crystallisation age is 252 Ma.....	167
Figure 6.23. Cathodoluminescence (CL) images of typical zircon grains from gneiss sample of the Kilimligöl formation (Sample No. 1812) showing the internal structure and laser analysis location.	168
Figure 6.24. U-Pb zircon ages of gneiss sample of the Kilimligöl formation (Sample No. 1812). a) Concordia diagram, b) Mean age diagram and c) Combined binned frequency and probability density distribution plots of zircon grains in the range of 0–100 Ma, show that the age of tectonothermal event for this sample is 53.98 ± 0.28 Ma.	168
Figure 6.25. Cathodoluminescence (CL) images of typical zircon grains from granite sample of the Central Uludağ Granite (Sample No. 1821) showing the internal structure and laser analysis location.	169
Figure 6.26. U-Pb zircon ages of gneiss sample of the Kilimligöl formation (Sample No. 1821). a) Concordia diagram, b) Mean age diagram and c) Combined binned frequency and probability density distribution plots of zircon grains in the range of 0–40 Ma, show that the crystallisation age of the granite sample is 29.53 Ma.	169

Figure 6.27. Cathodoluminescence (CL) images of typical zircon grains from granite sample of the Kapıdağ granite (Sample No. 1813) showing the internal structure and laser analysis location. 170

Figure 6.28. U-Pb zircon ages of granite sample of the Kapıdağ granite (Sample No. 1813). a) Concordia diagram, b) Mean age diagram and c) Combined binned frequency and probability density distribution plots of zircon grains in the range of 0–100 Ma, show that the crystallisation age of the granite sample is 47.87 ± 0.27 Ma. 171

Figure 7.1. A ductile shear zone is overprinted on the figure during the exhumation process. a) In the middle of the crust, a ductile shear zone is actively deforming, with comparatively undisturbed zones surrounding it. The mid-crustal ductile shear zone is exhumed along the faults illustrated in b). The faults engaged in exhumation show a sub-vertical lineation that overprints the initial sub-horizontal ductile lineation. 179

Figure 7.2. Geological map of the study area reconstructed as a result of field observations. 181

Figure 7.3. a) Geological map of the study area reconstructed from field observations and b) X'-X cross-section taken from this geological map. 182

Figure 7.4. a) Mantle sources from Zindler and Hart (1986) and Rollinson and Pease (2021), b) mantle source results of this study. 185

Figure 7.5. Simplified geological evolution model of the Uludağ Massif and its environment. 188

Figure 7.6. The general geological history of the Uludağ Massif and its surroundings. 189

LIST OF ABBREVIATIONS

ABBREVIATIONS

ACM: Active continental margin

Amp: Amphibole

BE: The composition of the Bulk Earth

BLG: Dynamic recrystallisation by bulging

BSE: Bulk silicate Earth (the composition of the bulk Earth without the core)

CC: Continental Crust

Cpx: Clinopyroxene

DM: Depleted mantle

EM1: Enriched mantle source 1

EM2: Enriched mantle source 2

EMORB: Enriched-MORB

Ep: Epidote

Fspar: Feldspar

GBM: Grain boundary migration

Gdt: Granodiorite

Grt: Garnet

Hb: Hornblend

HIMU: High μ mantle source region

HREE: Heavy REE

HSE: Highly siderophile element

ICP: Inductively coupled plasma

ICP-MS: ICP mass spectrometry

ICP-OES: ICP optical emission spectrometry

K: Kelvin

K-fsp: Alkalifeldspar

LA-ICP-MS: Laser ablation multi-collector ICP-MS

LOI: Loss of ignition

LREE: Light REE

MC-ICP-MS: Multi-collector ICP-MS

MORB: Mid-ocean ridge basalt

MREE: Middle REE

Mscvt: Muscovite

NE: North East

NMORB: Normal-MORB

NW: North West

OIB: Ocean island basalt

Olv: Olivine

Opx: Orthopyroxene

ORG: Ocean ridge granite

PGE: Platinum group element

Plag: Plagioclase

PM: Primitive mantle

PPL: Plain Polarized Light

ppm: Part per million (1 in 10⁶)

PREMA: Prevalent mantle reservoir (for oceanic basalts)

PUM: Primary uniform mantle reservoir

Qtz: Quartz

REE: Rare earth element

SGR: Sub-grain rotation

SynCOLG: Syn-collisional granite

TIMS: Thermal ionisation mass spectrometry

VA: Volcanic arc

VAG: Volcanic arc granite

WP: Within plate

WPB: Within plate basalt

WPG: Within plate granite

WPVZ: Within plate volcanic zone

wt. %: Weight percent

XPL: Crossed Polarized Light

Zn: Zircon

μ (μ): The isotopic ratio $^{238}\text{U}/^{204}\text{Pb}$

CHAPTER 1

INTRODUCTION

1.1 Study Area

Uludağ Massif located in the Mount Uludağ (Bursa - NW Anatolia), which reaches 2543 meters in height, is probably one of the most important mountains of Anatolia. The study area, covering the Uludağ Mountain is located between 39° 59' 07"N-40°04'14"N latitudes and 29°01'18"E-29°24'05"E longitudes to the southeast side of Bursa (Figure 1.1).

The study area is located in H22: c1-c2-c3-c4; d1,-d2-d3-d4 (Bursa) on Türkiye 1:25.000 scaled topographic maps (MTA).

The study area is generally covered with dense pine forests. This dense vegetation often makes finding outcrops in the area very difficult. While the slope is more than 45 degrees in the northern parts of the land, a more gentle slope prevails in the southern parts. There are 17 villages in the study area. Ski resorts and hotels generally surround the mountain summit for tourists and have been covered with snow for about 12 months. The study area is approximately 390 km from the capital city of Ankara and 5 hours by car.

The Uludağ Massif has variety of geotectonic structures (Figure 1.1). It is crucial to recognise the relevance of these structures to have a deeper comprehension of the magmatic and tectono-metamorphic evolution of the area. The development of the Uludağ massif is deeply connected to geological and tectonic formations such as the Bursa normal fault and the Soğukpınar right-lateral fault. The research primarily focuses on the Uludağ Massif and its adjacent region.

The Uludağ Massif has a gneiss and marble formation that reaches around 20 kilometers in length and 15 kilometers in width, extends northwest-southeast direction. The area is confined to the northeast and west by the brittle Bursa and Kirazlı faults (Okay et al. 2008) and is bounded in the south and southeast by the Soğukpınar right-lateral fault.

1.2 General Overview

The Northwestern Anatolia (Türkiye) shows a complex geology characterized by distinct but coexisting tectonic units such as İstanbul, Sakarya, and Armutlu zones. Although these tectonic units are located together, their geological relationships are not revealed clearly. Moreover, Northwest Anatolia contains remnants of Neotethys, Karakaya, Paleotethys Oceans, and other crustal fragments, which complicated the geodynamic setting.

Tectonic units in the study area, were first described by Ketin (1947). The geological and geodynamic character of NW Anatolia, especially the Paleozoic basement of the Uludağ Massif, has not been fully described. Therefore, there have been some gaps in the understanding of regional geology, which is the main scope of this thesis. This study focuses on the origin of the basement metamorphic rocks that form the Uludağ Massif, the magmatic rocks that cut these metamorphic rocks, and the geological relationships between these rocks. The metamorphic rocks that form the basement of this massif are overlain by older units (*i.e.* the Kalabak Unit; Yiğitbaş et al. 2018). Additionally, the role of the Bursa Normal Fault bordering the Uludağ Massif from the north, and the Soğukpınar Fault, which limits the massif from the south and has strike-slip components, in the evolution of the Uludağ Massif and its tectono-metamorphic and magmatic significance will be examined.

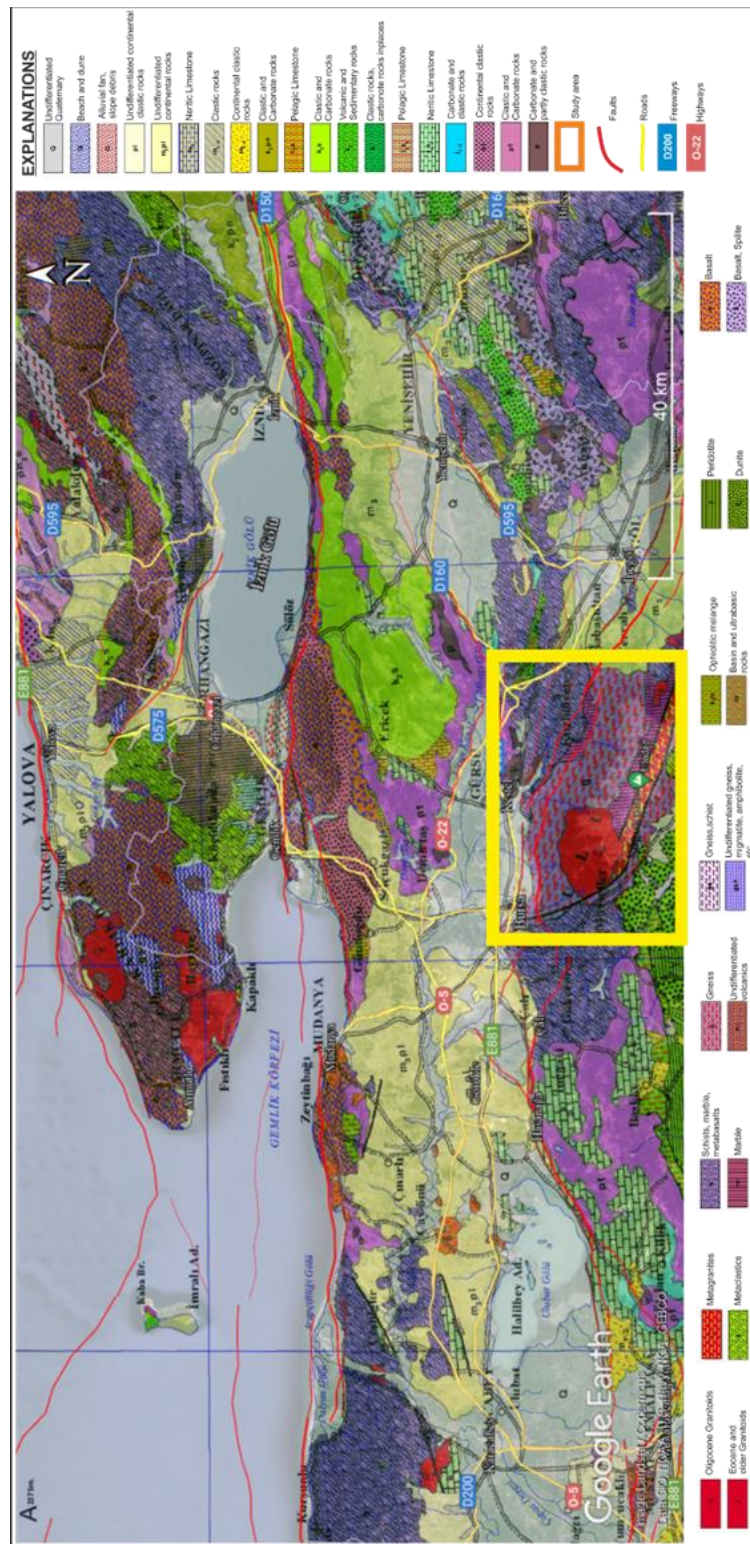


Figure 1.1. The geological map showing the location of the study area (Türkecan, and Yurtsever 2022).

1.3 Current Problems

There are two massifs in the basement of the Sakarya Zone in Northwestern Anatolia. These are the Kazdağ Massif and the Uludağ Massif. The following questions will help explore the origins and relationships of the Uludağ Massif units and their regional correlations.

- In which time interval and in which tectonic environments were the rocks of Uludağ Massif formed? What are the recent contact relationships of these rocks?
- Does the Soğukpınar fault, located at the northwest end of the Eskişehir fault and bounding the southern extension of the Uludağ Massif, have a significant impact on the development of the Uludağ Massif?
- Does the Uludağ Massif's development process and the following geological changes affect by the Bursa fault that forms the northern boundary of the Uludağ Massif? Is there a relationship between the historical evolution of the Uludağ Massif and the Bursa Normal fault? What effect does this fault have on the exhumation of the Uludağ Massif?
- The basement of the Sakarya Zone crops out in two massifs in NW Anatolia; the Kazdağ Massif and the Uludağ Massif. Can the metamorphic rocks, forming these massifs and their cover units, be correlated to each other?
- Except for some structural differences, the units in the Uludağ and Kazdağ massifs can be correlated lithologically and stratigraphically. From this point of view, Can the amphibolites and gneisses of the Kilimligöl Formation in the Uludağ Massif be correlated with the amphibolites and gneisses of the Fındıklı Formation in the Kazdağ Massif?
- Is the Zirve Marble in the Uludağ Massif equivalent to the Sarıkız Marble in the Kazdağ Massif?

- Can the quartzofeldspathic gneisses of the Gökdere Formation in the Uludağ Massif be correlated with the quartzofeldspathic gneisses of the Sütüven Formation in the Kazdağ Massif?
- Can the Bursa Marble of the Uludağ Massif be correlated with the Altınoluk Marble of the Kazdağ Massif. If so, that will help to determine the tectonostratigraphic position of these marble members of the Uludağ Massif.
- The Torasan and Sazak Formations of the Kalabak Unit (Yiğitbaş et al. 2018) are overlying the basement units in the Kazdağ Massif. The same situation is also observed in the Uludağ Massif. The basement units of the Uludağ Massif are covered by metabasalts of the Sazak Formation. Does this mean that, the Uludağ and the Kazdağ massifs have a similar tectonostratigraphic history? Is the Central Uludağ Granite similar in origin to the Tertiary Evciler and Eybek granites of the Kazdağ Massif? The suspicions are as follows;
- Is the South Uludağ Metagranite equivalent to the Devonian-aged Çamlık Metagranite? Eybek Granite and Çamlık Metagranite of the Kazdağ Massif show a spatial relationship with the Central Uludağ Granite and South Uludağ Metagranite in the Uludağ Massif.
- Is the South Uludağ Metagranite a Carboniferous migmatitic granite? Is the Carboniferous granite in the South Uludağ Zone similar to the Sakarya Zone basement?
- Based on the map pattern and spatial relationship of the South Uludağ Metagranite, can this granite be considered a magmatic complex?

To find answers to the above questions, besides the findings of the detailed field study, geochemical and Sr-Nd isotopic data are presented in this study. Furthermore, the crystallisation age of the protoliths of the metamorphic basement rock and their origin are determined by using the U-Pb zircon age determination method. The interpretation of all these data is expected to provide information on

the exhumation and uplift age of the massif in addition to the U-Pb zircon age determination approach.

1.4 Research Objectives

This study aims to provide a new perspective on the petrogenesis and geodynamic characteristics of the Uludağ Massif to clarify and demonstrate its relationship with regional geological elements such as tectonic-metamorphic and/or magmatic evolution. This study has the following main objectives:

- To reveal the internal order of the rocks forming the Uludag Massif and their contact relationships.
- To determine the stress fields, analyse the Soğukpınar right-lateral strike-slip and Bursa normal faults.
- To determine the origin of metamorphic or sedimentary sequences to explore their tectonic relationships in the Uludağ Massif and to define their formation, metamorphism, or tectono-thermal ages using a geochronological approach.
- To analyse tectonic units geochemically and petrographically. Thus; if the rocks forming the Uludağ Massif are of magmatic origin, determine what kind of magma source(s) (mantle and/or crustal) origin these rocks derive from.
- To reconstruct the tectonic-metamorphic and magmatic evolution of the Uludağ Massif.
- If possible, to compare the Uludağ Massif and Kazdağ Massif units according to the results of this study.

1.5 Research Contributions

A perspective on the spatial evolution and temporal development of the Uludağ Massif has been developed to achieve the purposes stated above. This perspective is accomplished by the following:

- clarification of the evolutionary history of the Uludağ Massif and its exhumation,
- reveal the tectonic-metamorphic, magmatic and tectonostratigraphic evolution of the Uludağ Massif and the interpretation of its tectonics and geological aspects,
- better explanations for the effects of strike-slip and normal faults on the evolution of massif and,
- detailed petrographic, geochronological, and geochemical analysis of the Uludağ Massif.

1.6 Methodology

The main basis of the study consists of fieldwork, which is crucial for understanding the geological and structural features of the studied rocks. Field studies were initiated at the Mount Uludağ's southwestern flank and continued through the central, eastern, northern, and southern sides.

Well-preserved outcrops from 28 different localities were selected for sampling. Detailed geological mapping was performed and relative ages of the metamorphic and magmatic units and their relations are examined in the field.

Mineralogical and petrographic analyses were performed on the samples from these 28 localities to identify microstructural and microtectonic deformations. All these samples were examined under a Leica DM2500P polarising microscope. Thin-section images were also obtained using the Leica Application Suite Version 4.0.0.

Further, petrographic and mineralogical data were compiled and interpreted according to the geological findings derived from the field studies to reveal the evolution phases of the Uludağ Massif from the point of tectonic-metamorphic-magmatic formational history.

1.7 Methods of the Study

In general, this study consists of three different phases of work. The first one is the field study. After the field studies, laboratory studies were carried out, and in the last stage, it was finalised by compiling and writing all the data obtained in the office. How all these studies were carried out in general is briefly mentioned below.

1.7.1 Field Study

To solve the problems observed in the study area, literature reviews on the geology of the region were carried out before the field study. The geological maps of Bursa, first made by Ketin (1947), then revised and reprinted by Okay et al. (2008), and finally by Kanar et al. (2013), were obtained. The basic units forming the Uludağ Massif were identified in the field, and the positions of these units in the field were studied. Subsequently, it was tried to reveal the relationships of these units observed in the field. The magmatic units observed in the field were identified. N-oriented directional samples were taken from the metamorphic units that form the basement of the Uludağ Massif. Taking directional samples enabled the development directions of the deformations in these units to be determined.

Approximately 50 samples were collected for petrographic, microstructural, geochemical and geochronological purposes. Topographic maps, satellite images, and Google Earth images were also used to make a 1/25.000 geological map of the Uludağ Massif and to overlay the units observed in the field.

1.7.2 Laboratory Study

Laboratory studies were carried out for petrographic studies, elemental and radiogenic isotope geochemical analyses, and geochronological analyses.

28 samples collected during the field study were prepared for geochemical analyses. In the laboratory, the rock samples were ground into a fine powder following a series of stages before geochemical analysis for fusion or dissolution.

These include:

- 1) crushing the rock and removing the remaining weathered material.
- 2) crushing the sample, usually in a hardened steel jaw crusher (see Figure 1.1 and Figure 1.2).
- 3) the sample is ground to a fine powder in a ball mill or disc mill (see Figure 1.3).

Two basic principles were taken into consideration when preparing the samples. Firstly, the entire sample was pulverized before sieving directly without the above processes. Secondly, the chemical composition of the machines used to pulverize the rock sample was chosen considering the sample geochemistry. For example, if tungsten (W) is the element of interest, it would be unwise to use a tungsten-carbide mill that contaminates sample.



Figure 1.1. The jaw crusher is the first step in preparing samples for geochemical analysis. a) The jaw crusher is cleaned with alcohol to prevent contamination and made ready for use; b) Samples are placed in the hopper on the jaw crusher.



Figure 1.2. The first step of sample preparation is completed by removing the samples placed in the jaw crusher from the hopper at the bottom.

According to the requirements of the geochemical analysis, the samples coming out of the jaw crusher are put into the grinder, and the grinder grain size is ensured to reach the final grain size before the screening process.



Figure 1.3. Operations with the grinder a) shows the grinder device, and b) samples from the jaw crusher are placed in the upper chamber of the grinder.

The samples from the grinder are separated for sieving to bring them to sizes suitable for the planned geochemical analyses. This study used sieve analysis to prepare the samples for geochemical analysis. Therefore, in sieving,

- 1) The sieves are arranged from bottom to top according to the sieve opening size, from small to large, with the pan at the bottom.
2. The weight of the powder sample to be sieved and analysed is approximately 300 grams.
3. The prepared sieve set is placed in the sieve shaker.

4. Pour the powder sample into the sieve at the top of the sieve set.
5. The cover of the sieve set is closed, and the screws are tightened.
6. The sieve shaker is operated for 15 minutes at the appropriate vibration.

After the sieve shaking process, the samples obtained are labelled and packaged according to size. The 500 μm and 63 μm sieves played an important role in the preparation of the samples used in this study, and the samples between 500 μm and 63 μm are used for U-Pb zircon separations and below these sieves 63 μm were used for geochemical analysis (Figure 1.4).

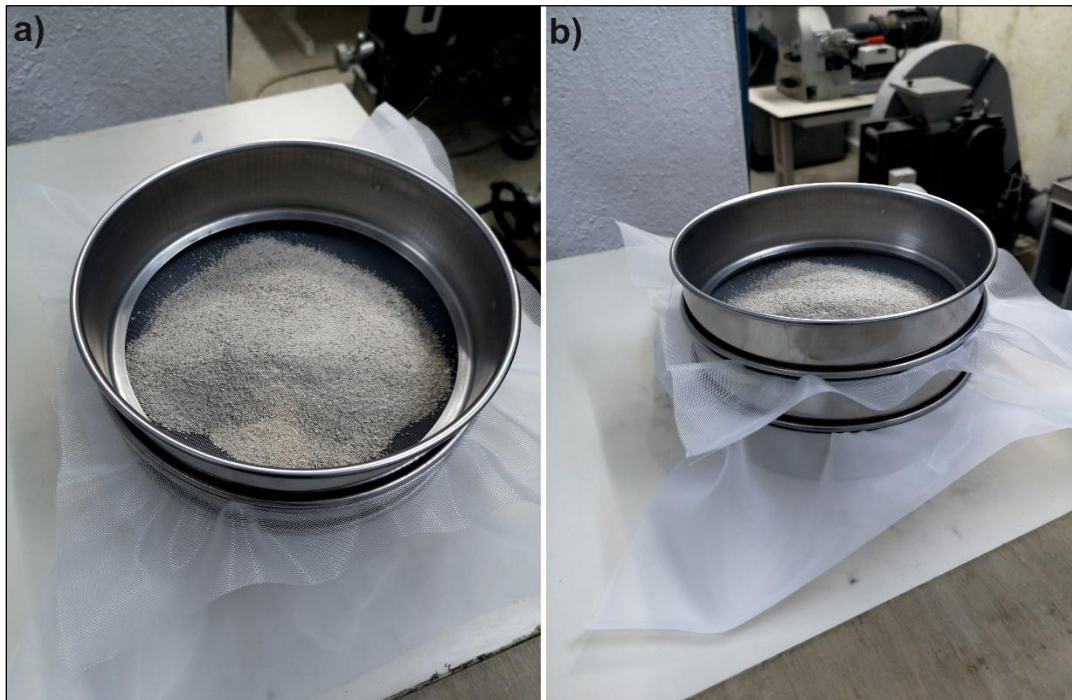


Figure 1.4. Some of the pictures taken during sieve analysis are a) the preparation of the sieve system before sieve analysis and b) the approximate amount of sample to be put on the sieve.

Firstly, 28 samples were selected for petrographic analyses. These samples were selected from the metamorphic units that form the basement of the Uludağ Massif,

mostly N-oriented samples. Apart from the basement units, it also includes magmatic units that cut these basement units.

According to the results of the petrographic analysis on the thin sections of the samples, 23 samples were selected for whole-rock geochemical analyses. Geochemical analyses of these 23 samples were performed using ICP-MS (Inductively coupled Plasma-mass Spectrometry) analysis to obtain major element and trace element concentration data. Acme Analytical Laboratories performed this analysis. Two processes mainly follow the analysing processes of the ACME laboratories. The PRP-70-250 coded procedure first includes crushing, splitting, and pulverizing 250-gram rock to 200 mesh, and then, the 4A-250 coded procedure applies, including four (4) acid digestion and ICP-MS analysis. Some samples were analysed twice as a quality control practice to confirm the accuracy of these results.

Regarding the field, petrography, and geochemical data, 20 samples were processed for mineral separation for U-Pb zircon dating. Mineral enrichment and separation procedures were performed in the sample preparation and mineral separation laboratory of the Geological Engineering Department of Middle East Technical University (METU) (Ankara/Türkiye). For these processes, the samples were first crushed in a jaw crusher. Then, they were passed through a grinder and finally sieved to the desired grain size (between 63-500 μm). The heavy mineral fraction of these samples was first enriched by Wilfley table. The samples were dried in an oven and passed through a magnetic separator to remove magnetic minerals. The heavy mineral fraction was further separated by using a heavy liquid (bromoform). The zircons were manually selected from this fraction using a stereomicroscope, and sample mounts were prepared for U-Pb zircon dating.

The 14 samples selected for U-Pb zircon dating were analyzed by Laser Ablation-Inductively Coupled Plasma-Mass Spectrometer (LA-ICP-MS) in the Geochronology Laboratory of the Central Laboratory at Çukurova University (Adana/Türkiye).

Strontium and Neodymium radiogenic isotope analyses were carried out in the Radiogenic Isotope Laboratory within the Central Laboratory of Middle East Technical University (METU) on selected 20 samples.

1.7.3 Office Study

The office work continued during all the fieldwork and laboratory work but gained momentum, especially at the end of the laboratory work. The office work aims not only at the writing process of this thesis but also at ensuring that the figures of the thesis are more appealing to the eye by using the many software programs used during this thesis. The main softwares used in the writing of this thesis are Corel Draw, Global Mapper, Leica Vision, GCDkit, Iolite, Google Earth, Surfer, and different versions of these programs were used to create most of the figures in the thesis. MS Office programs were also used during the thesis writing process.

CHAPTER 2

REVIEW OF PREVIOUS STUDIES

2.1 Introduction

The study was conducted in the Uludağ Massif, a region characterised by ductile shear zones (Okay et al. 2008) and adjacent locations. The Uludağ Massif is located in the south of Bursa on the northwestern part of the Anatolian Plate. Representative rocks were sampled in different parts of the Uludağ Massif during this study (Figure 2.1). One of the initial findings in the field was that the Uludağ Massif included syn-tectonic intrusions as South Uludağ Metagranite (SUM) and post-tectonic intrusions as Central Uludağ Granite (CUG), together with extensively deformed marbles and gneisses as mentioned by Okay et al. (2008).

The Anatolian plate, a subordinate tectonic plate inside the larger Eurasian Plate, presents a complex tectonic system located between the northern convergence of the Arabian and African Plates, as well as the southern transform boundary is known as the North Anatolian Fault Zone (NAFZ), which belongs to the Eurasian Plate (McKenzie, 1972). To the north, it displays strike-slip tectonics similar to an escape mechanism, whereas to the west and southwest, it shows extensions, graben, and horst structures (Bozkurt, 2001; Reilinger, 2006). Anatolian plate tectonics is even more complicated due to its long history of accumulation from numerous seaways that have opened and closed since its formation (Stampfli, 2000).

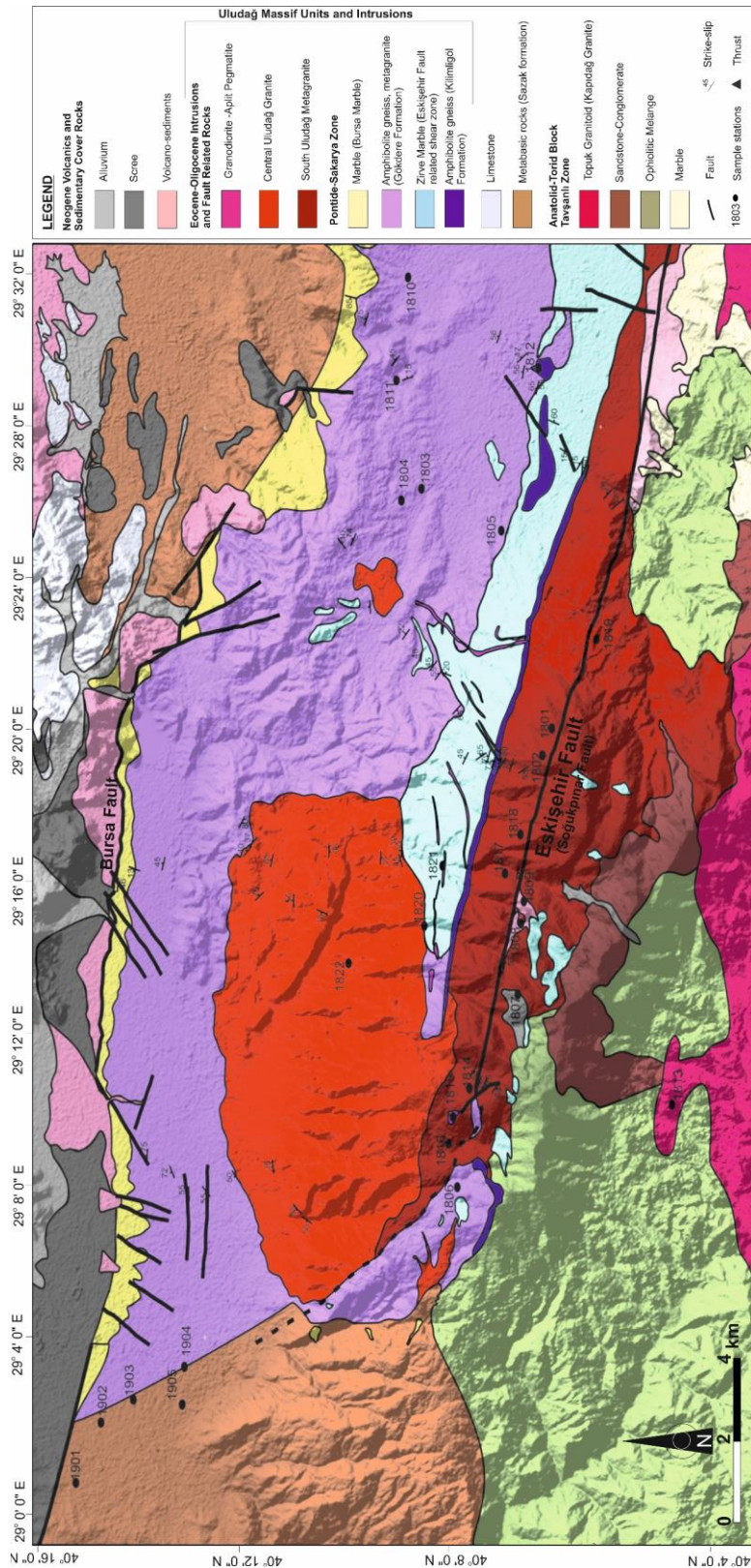


Figure 2.1. Sample locations for this study and geological map of the Uludağ massif modified after Okay et al. (2008).

2.2 Regional Geology and Tectonics

A complex geology characterizes the Anatolian Plate due to the interaction between the Arabian, African, and Eurasian tectonic plates (Figure 2.2) (McKenzie, 1972). The geodynamic history of the Anatolian plate is mainly classified into four distinct tectonic regimes (Selçuk and Gökten, 2012). The provinces shown in Figure 2.3 are located in Northern, Central, and Eastern Anatolia, as Selçuk and Gökten (2012) identified. Anatolia's complex tectono-stratigraphy can be further divided according to its geological evolution into Pontides and the Antatolide–Tauride Block or Arabian Platform, depending on their origin and dominant units (Figure 2.4).

In Figure 2.2, the arrows indicate the movement of plates. Extensional tectonics are observed in the southwest, and strike-slip and contractional regimes connected to "escape" tectonics are located in the north, which includes the North Anatolian Fault. The Uludağ Massif field is at the boundary between these two tectonic regimes (Figure 2.3).

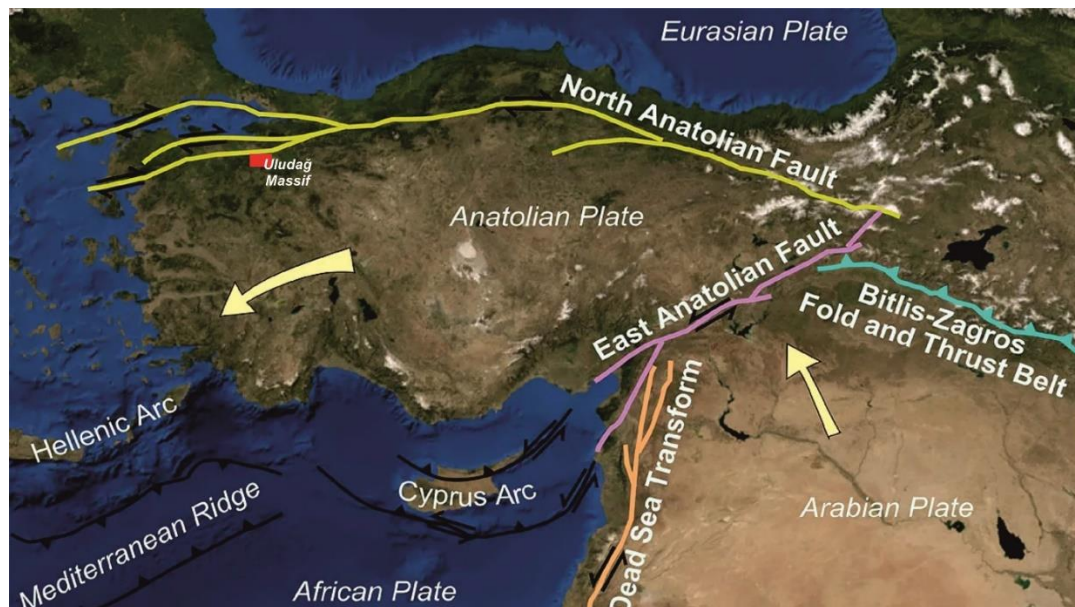


Figure 2.2. Tectonic plates, faults, and their relative motions in and around Türkiye, location of the Uludağ Massif showed with a red square.

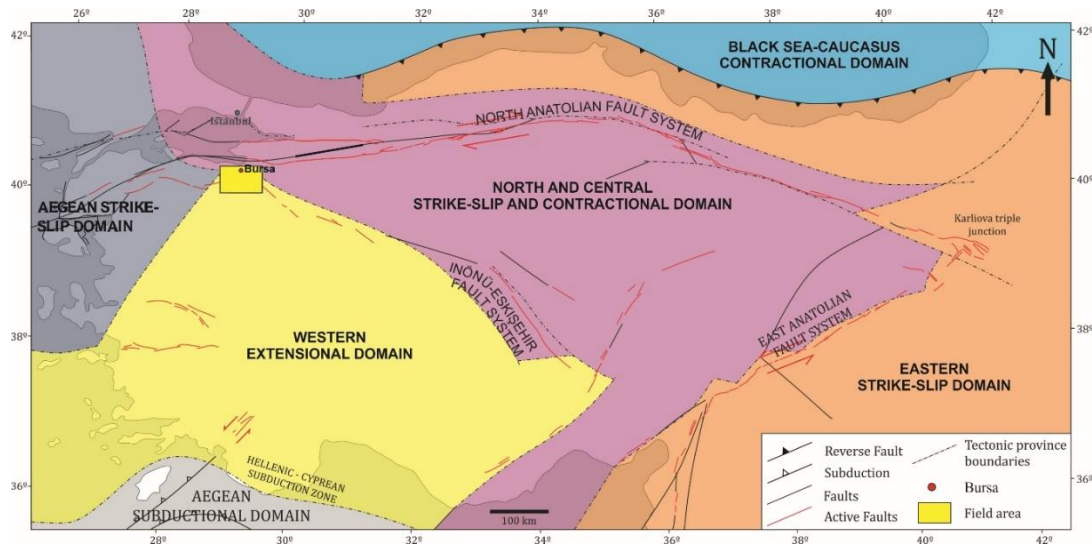


Figure 2.3. Tectonic regions of Anatolia were determined by today's tectonic activity, as taken from Selçuk and Gökten (2012).

The East Anatolian Fault is the defining feature of the eastern strike-slip domain and is mainly shaped by strike-slip tectonics like the Aegean strike-slip region. The subduction zone that includes the Hellenic and Cyprus regions is known as the Aegean subduction area.

2.2.1 Tectonic and stratigraphic terranes

Figure 2.4 illustrates the interconnections among various tectonic units. Some characteristics are unique to the Laurasia continent, located north of the Tethys Ocean. The Pontides are divided into three sub-units: Strandja, Istanbul, and Sakarya. Pontides have undergone significant deformation, which is seen as evidence of Variscan (350-300 Ma), Cimmeride (200-150 Ma), and Alpine (65-2 Ma) orogenic episodes (Okay, 2008). This study mainly focuses on the Sakarya Zone, which constitutes the basic crystalline bedrock of the Uludağ Massif.

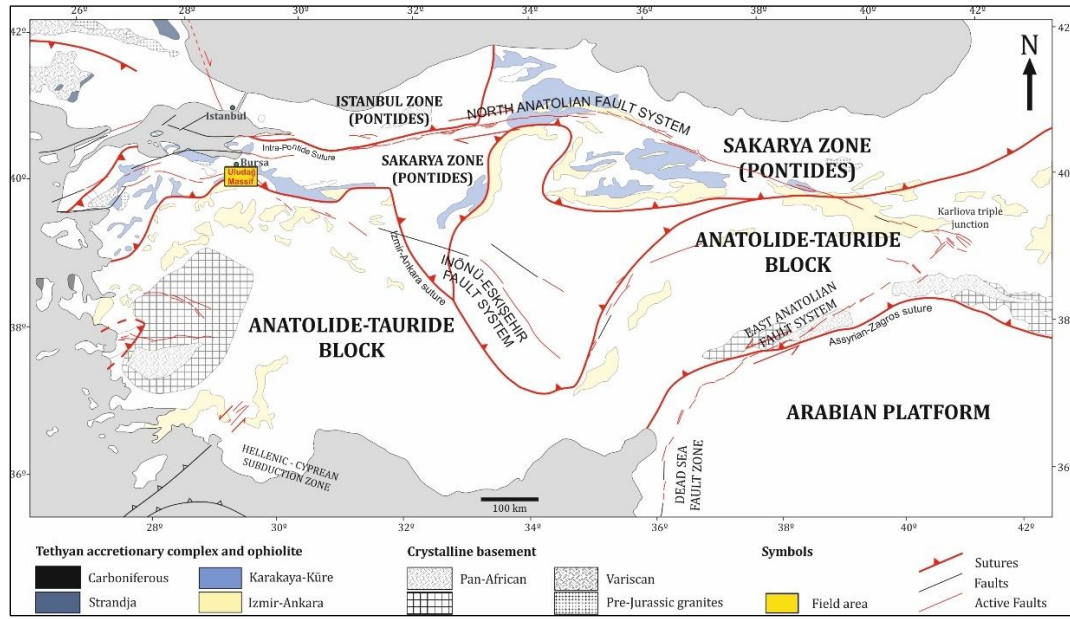


Figure 2.4. The diagram illustrates sutures exhibited in Türkiye. The study area is shown with a yellow box (taken from Okay and Tüysüz, 1999; Okay, 2008).

The Anatolide-Tauride Block was formed through Alpine orogenesis (Okay, 2008). It has undergone strong deformation and metamorphism during Cretaceous. Due to the varying levels of Alpine deformation in the thrust zone, the Anatolide-Tauride Block are divided into three distinct zones in the south of the study area. From north to south;

- Tavşanlı Zone, which is composed of Cretaceous blueschists
- Afyon Zone shows Paleocene Barrovian-type metamorphism and
- Menderes Massif is renowned for its Eocene Barrovian-type Eocene Metamorphism (Okay and Tüysüz, 1999).

The Tavşanlı Zone within the Anatolide-Tauride Block Tavşanlı covers the southern edge of the study field (Figure 2.4). Throughout the Paleozoic and Tertiary periods, several sedimentary sequences, related to the Anatolide-Tauride Block were created due to the continental collision during the Miocene epoch, covered a Pan-African basement (Okay, 2008; Moix et al. 2008).

2.2.2 Tectonics

The Anatolian plate can be sectioned into four neotectonic regions: Northern, Central, Eastern, and Western Anatolia (Selçuk and Gökten, 2012) (Figure 2.3). The Eastern Anatolian region can be divided into different neotectonic zones located both to the east and west of the Karlıova triple junction. The area east of the Karlıova Triple Junction is marked by compression in the north-south direction. This compression is caused by unidirectional and rightward strike-slip faults (Bozkurt, 2001). The North Anatolian Province is on the northern side of the North Anatolian Fault Zone (NAFZ) (Reilinger et al. 1997). The structure consists of robust east-west thrust components and strike-slip faults (Bozkurt, 2001). Because of the tectonic interaction between the Anatolian and African plates, Central Anatolia is expanding northwest to southeast and contracting northeast to southwest (Şengör, 1985). The Western Anatolia region moves at a rate ranging from 30 to 40 mm per year and is characterised by high seismic activity (Bozkurt, 2001). The extensional regime observed on the Anatolian Plate is caused by the westward escape mechanism, resulting from the NAFZ's northward compression and dextral thrust (Bozkurt, 2001). Figure 2.2 and Figure 2.3 show shifting of the Anatolian Plate towards the Hellenic Trench due to the northward motion of the African Plate, as documented by Reilinger et al. (2006). Taponnier et al. (1982) proposed that the collision between the Indian and Asian continents can be explained by tectonic escape or thrust tectonics, as previously hypothesised by Molnar and Taponnier in 1975 and 1978. Based on the GPS data, the Anatolian Plate exhibits an increasing rate of motion from the eastern to the southern direction (Reilinger et al. 2006). Reilinger et al. (2006) reported that Anatolia's westward movement is closely linked to the Arabian Plate's anticlockwise rotation (Figure 2.5).

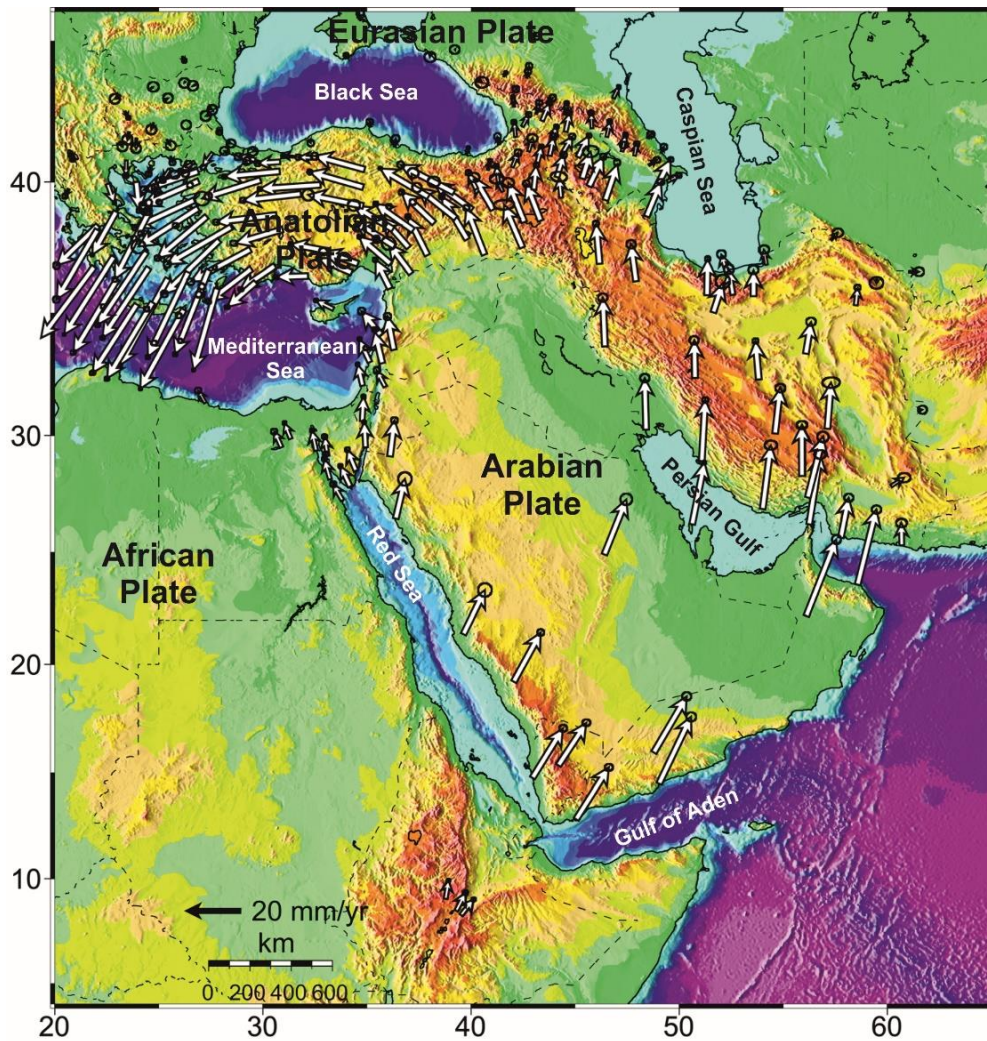


Figure 2.5. The GPS velocities concerning Eurasia indicate Anatolia's anticlockwise rotation (adapted from Reilinger et al. 2006).

2.3 The Relationship Between Sutures and Evolution

The Anatolian Plate terranes are connected by sutures, documenting the ancient oceans and waterways (Stampfli, 2000). These records illustrate the continuous patterns of divergence and convergence events over Anatolia's history, as seen in Figure 2.4. Since the Early Palaeozoic era, multiple oceans and seas have undergone opening and closing processes, forming sutures across Anatolia (Stampfli, 2000).

On the other hand, the Intra-Pontide suture that is located within the Pontides (Figure 2.4) significantly influences the neotectonics and morphology of the

Anatolian Plate and is evident in the NAFZ (North Anatolian Fault Zone), The Eskişehir Fault Zone, and several other regions.

The boundaries of Laurasia, Gondwana, and the Phanerozoic were constantly rifted during this period, creating continental areas separated by different seaways (Stampfli, 2000). Prototethys is the oldest ocean, a topic still up for debate, and the exact age is still unknown. Although much is known about its evolution, little is known about its origin. Stampfli (2000) suggests the Prototethys Ocean was active in the early Paleozoic. It opened and closed during this time. This closure resulted in the formation of back-arc faults that created larger oceanic realms like the Paleotethys and the Rheic Oceans (Stampfli and Kozur, 2006).

Figure 2.4 illustrates the distinction between the Istanbul Zone and the Sakarya Zone by the presence of the Intra-Pontide suture. It runs a distance of roughly 400 km between the two endpoints. The geological formation known as Paleocene-ophiolitic melanges occurred from the Upper Cretaceous to the Paleocene period (Okay, 2008). This information is supported by the studies conducted by Şengör and Yılmaz (1981), Görür et al. (1984), and Wong et al. (1995). Okay and Tüysüz (1999) stated that NAFZ had defined the Intra-Pontide Suture across its maximum extent. As the eastern part of the Rheic Ocean, the Intra-Pontide Ocean presumably formed during the Carboniferous. Okay et al. (2006) mentioned that the closure of the Intra-Pontide Suture occurred during the Mid-Carboniferous period, resulting in the preservation of its footprints.

The Paleo-Tethys Ocean had a very complex evolutionary process due to the rifting of continental pieces on both sides, forming several seaways and oceans. The primary Paleotethys Ocean formed due to the collapse of the tectonic plate from the southern movement of the mid-ocean ridge in the Rheic Ocean (Okay and Tüysüz, 1999; Stampfli, 2000). Stampfli (2000) described the closure of Palaeotethys as a progressive process occurring along an oblique convergence zone from the Moscovian period to the early Triassic period. The Palaeotethys subduction process facilitated the creation of the Neotethys ocean by the progressive building of a series of back-arc basins.

The current situation of the Eastern Mediterranean can be linked to the Neotethys Ocean. That provides a depiction of the first geological formations of many waterways, along with small sections of land that have separated from the Gondwana supercontinent (Floyd et al. 2000). Şengör (1987) suggested that the Neotethys could have a relation to the opening of the connection between the Alpine Tethys and the Atlantic Ocean. According to the Şengör (1987), The Neotethys Ocean first appeared in the early Jurassic(?) or Late Triassic(?) epochs. Evidence indicates that the Neotethys has existed since the Late Palaeozoic period, as indicated by studies conducted by Malpas et al. (1993), Stampfli (2000), and Stampfli et al. (2001). During the Late Triassic and Liassic periods, the Neotethys underwent northward subduction, as Berberian and Berberian (1981) mentioned. The closure occurred during the Late Cretaceous due to the convergence between the African and Eurasian plates (Stampfli and Kozur, 2006).

In the scope of this study, the İzmir - Ankara - Erzincan Suture (IAES), which is located between the Anatolide - Tauride Block and the Pontides, has a crucial importance (Okay, 2008).

IAES, extends from the eastern border of Türkiye with Georgia to the western Aegean Sea, where it meets with the Vardar suture (Okay and Tüysüz, 1999) (Figure 2.4). The Eskişehir Fault mostly aligns with IAES, as stated by Okay et al. (2008). Okay and Tüysüz (1999) proposed that the IAES is the northern segment of the Neotethys. It is situated between the Sakarya continent and the Anatolide-Tauride Block (Floyd et al. 2000). Stampfli (2000) argues that the IAES is not accurately related to the Neotethys. IAES is a geological formation suggested to have originated during the Jurassic period (Okay, 2008). It is considered a back-arc basin created when the Neotethys, a tectonic plate, subducted northward (Okay, 2008).

2.4 The Uludağ Massif

This section will specifically address the background information of the Uludağ Massif that targeted research location. The Uludağ Massif is located in the

northwestern region of Türkiye, situated on the south of Bursa (Figure 2.6). It is situated at the most northern point of the Soğukpınar Fault, a component of the İnönü-Eskişehir Fault Systems (IEFS). The fault recently exhibits oblique dip-slip motion (Seyitoğlu and Esat, 2022), although, in the past, it was as active as the strike-slip. (Okay et al. 2008). In 1947, Ketin produced the preliminary map of the study area. Subsequently, Okay et al. released a revised edition of the map in 2008, as seen in Figure 2.6. In this study, a new geology map was formed, as seen in Figure 2.7.

Figure 2.8 and Figure 2.9 display the lowest section of the Sakarya terrane, known as the Uludağ group, located in the Mount Uludağ. The group comprises a superior quality, transformed basement, and a sedimentary layer from the Permo-Triassic period (Ketin, 1947). The metamorphic basement consists of marbles, amphibolites, and gneisses that underwent metamorphism and deformation during the Hercynian orogeny in the Carboniferous period (Okay and Tüysüz, 1999; Okay and Satır, 2006; Okay et al. 2008). According to the Uludağ Group's highest recorded temperatures of 670°C and the cooling rate of 12°C per million years for muscovite or biotite, an approximation of the date when metamorphism reached its highest point is estimated to be in the Cretaceous period, around 64 million years ago (Okay et al. 2008) (Figure 2.9 and Figure 2.12). The exact age of the original rock from which the Uludağ Group formed is uncertain. The presence of poorly preserved corals in marble suggests that the Uludağ Group comes from a period after the Ordovician era (Okay et al. 2008).

The granites of the Uludağ Group are of Oligocene age. The syn-kinematic intrusion of the South Uludağ Granite is evidenced by the widespread presence of fault parallel foliation, a solid-state microstructure, and continued crystallisation dates ranging from 30 to 39 Ma (Okay et al. 2008).

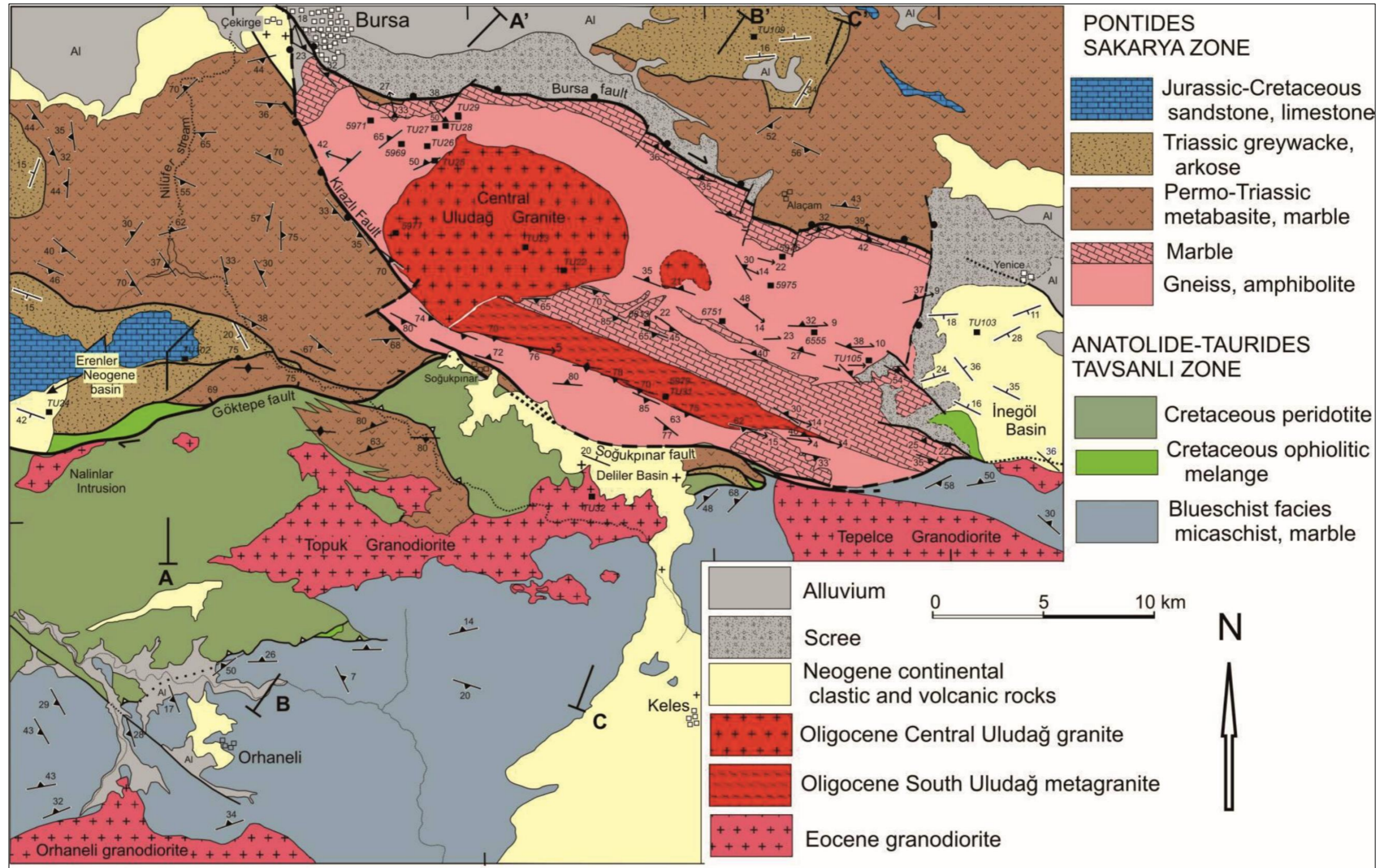


Figure 2.6. Geological map of the Uludağ Massif and its surroundings taken from Okay et al. (2008). The Eskişehir Fault mentioned relates to the Soğukpınar Fault seen on this map. According to Okay et al. (2008), the rocks north of this fault are part of the Sakarya Zone of the Pontides, whereas the rocks to the south are part of the Anatolide-Tauride Block.

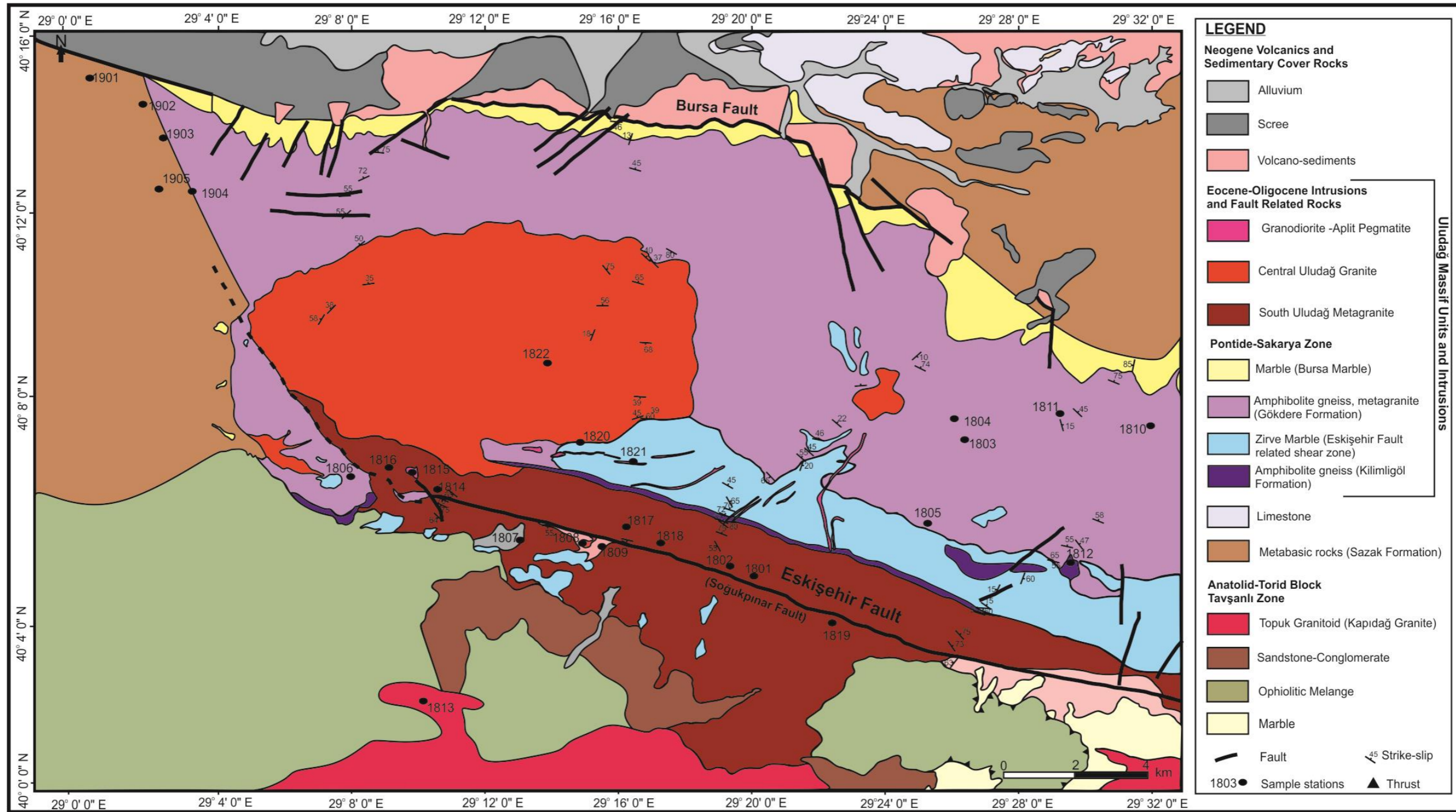


Figure 2.7. Geological map of the study area created in this study.

2.4.1 Geological Features of the Uludağ Massif

Metamorphic rocks of the Uludağ Massif, were defined as the Hercynian basement of the Sakarya Zone by Şengör and Yılmaz (1981). These high-grade metamorphic rocks of the Uludağ Massif crop out in the Mount Uludağ, south of Bursa and subdivided into four units. These units from bottom to top are; the Kilimli formation, the Zirve marble, the Gökdere formation and the Bursa marble.

The Kilimli formation, which consists of amphibolites and gneisses with amphibolite intercalations, lies at the bottom of these metamorphics (Figure 2.8). The Zirve marble unconformably overlies the Kilimli formation, and is tectonically overlain by the quartzo-feldspathic gneisses of the Gökdere formation (Figure 2.8). The Bursa marble overlies the quartzo-feldspathic gneisses conformably, the Oligocene aged granites and metagranites cut all these metamorphic units, were identified and named as the Central Uludağ Granite and South Uludağ Metagranite, respectively (Figure 2.8).

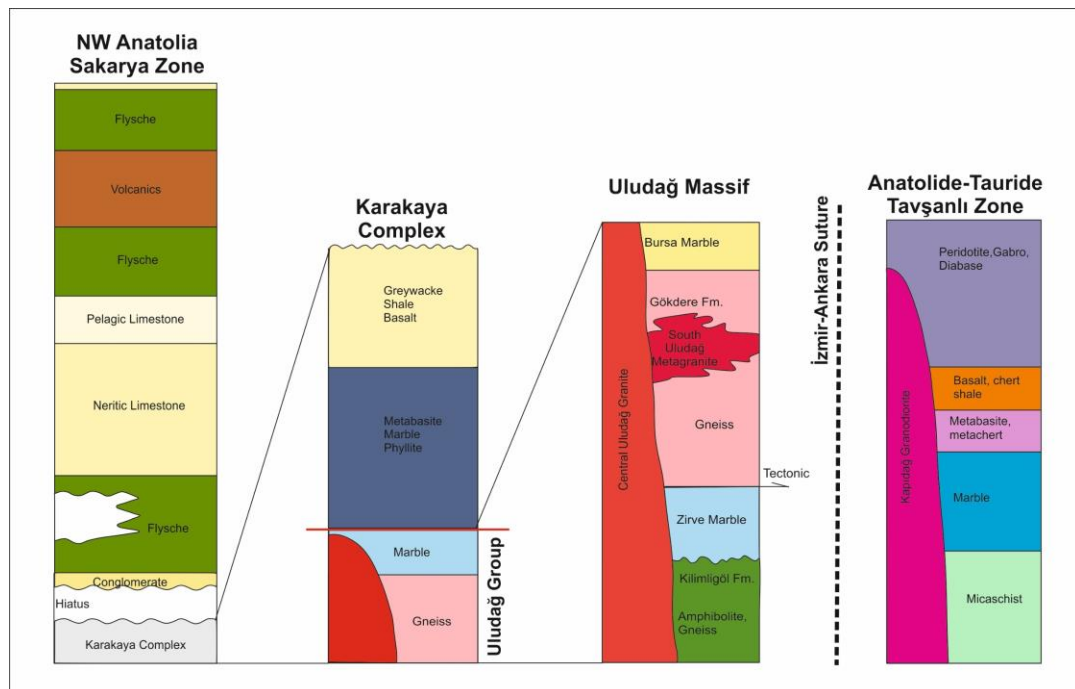


Figure 2.8. Simplified tectonostratigraphic columns of Uludağ Massif as basement of Sakarya Zone and the Tavşanlı Zone within the Anatolide-Tauride Block.

2.4.1.1 Kilimligöl Formation

The Kilimligöl formation was first named by Pehlivan et al. (2014), contains amphibolites and gneisses with amphibolite intercalations. Ronner (1954) stated that this unit is underlying marble and gneisses. Kilimligöl formation is located at the lowest level of Uludağ metamorphics. It crops out as a thin level with a thickness of approximately 40-50 metres and a length of 13-15 km, extending NW-SE between the Zirve marble and metagranites in the vicinity of Kilimli Lake and Aynalı Lake in the lakes region in the summit region of Uludağ. In addition, in the south of Uludağ, along the Soğukpınar Fault, in the valley interiors, there are some outcrops under fault debris.

According to the MTA, H-22 (2013) report, the researchers could not obtain any age data within this formation. According to the zircon dating made by Okay et al. (2008), values between 300-200 Ma. were described as the age of metamorphism.

MTA H-22 report stated that the Kilimligöl formation could be compared with the Basic Series (Bingöl, 1969) and the Tozlu Formation (Bingöl et al. 1973; Duru et al. 2007), which have similar lithological characteristics and are composed of ophiolites within the Kazdağ Massif.

2.4.1.2 Gökdere Formation

The Gökdere formation was first named in the report of Pehlivan et al. (2014). Its outcrops are observed along Süleymaniye in the south of Bursa, Bursa in the west, Cumalıkızık, Saitabat and Kıran Villages towards the east. The unit is predominantly composed of quartzofeldspathic gneisses with well-foliated, banded structures. Amphibolite lenses and occasional migmatite levels are observed in the gneisses, which constitute the main lithology of the formation. The formation is cut by aplite and granitic rocks. It overlies the underlying Zirve marble with a tectonic contact.

The Bursa marble is conformably overlying this unit. In the central and western parts of the Uludağ Massif, gneisses are cut by Oligo-Miocene-aged Central

Uludağ Granite and dykes. MTA H-22 report (2013) states that the age of the Gökdere formation is considered pre-Carboniferous.

2.4.1.3 Central Uludağ Granite and South Uludağ Metagranite

Oligocene-aged granites and metagranites cutting the metamorphic rocks of the Uludağ Massif were identified as Central Uludağ Granite and South Uludağ Metagranite by Okay et al. (2008). In this study, the units are analysed under the same name. The Uludağ Granite is located within the borders of Uludağ National Park from the Süleymaniye village in the west of the study area.

When going east and south from the Central Uludağ Granite, the part extending in the NW-SE direction forms the South Uludağ Metagranite (Figure 2.6 and Figure 2.7).

The reason for the metamorphism of the South Uludağ Metagranite is that this granite is located within the right-lateral shear zone formed by the Eskişehir (Soğukpınar) Fault in the latest Eocene-Oligocene (38-27 My.) interval, extending in the NW-SE direction and undergoing ductile deformation (Okay et al. 2008).

The Central Uludağ Granite consists mainly of quartz, K-feldspar, plagioclase, biotite and muscovite. Okay et al. (2008) suggests that the Central Uludağ Granite was emplaced about 25 My. ago according to isotopic age determinations. In addition, along the eastern margin of the Uludağ Granite, marbles belonging to the Uludağ Metamorphics were cut, and wolfram mineralisation occurred along this cutting margin.

2.4.1.4 Kapıdağ Granodiorite

The unit was first named as Kapıdağ Granite by Ketin (1946) and its typical outcrops are observed in the Kapıdağ Peninsula in the northwest of Anatolia. Since the unit is located in the granodiorite area in Streickesen's (1976) triangle diagram, the name Kapıdağ Granodiorite was adopted by Ercan and Türkecan (1984). These Eocene-aged plutons cut the units of the Tavşanlı zone, and are also crop out in the

south and southeast of the Mount Uludağ, in the study area. This unit, known as Topuk granodiorite in the literature (Okay et al. 1998), is analysed as Kapıdağ granodiorite/granite in this study.

The mineral composition of the unit is; quartz, plagioclase, K-feldspar, hornblende, biotite, and opaque ferrous minerals. Magma intrusions belonging to relatively different phases that cut each other are frequently observed in the unit. This pluton, a granodioritic and granitic type of intrusion, is highly weathered on the outer surfaces and quite clean and intact on the inner parts .

Regarding the age of Kapıdağ granodiorite, Delaloye and Bingöl (2000) determined ages between 38-42 My for biotite, while Okay et al. (1998) determined the age of the pluton as 48 My by the Ar-Ar method. In other words, the age of the unit was determined as Eocene in previous studies.

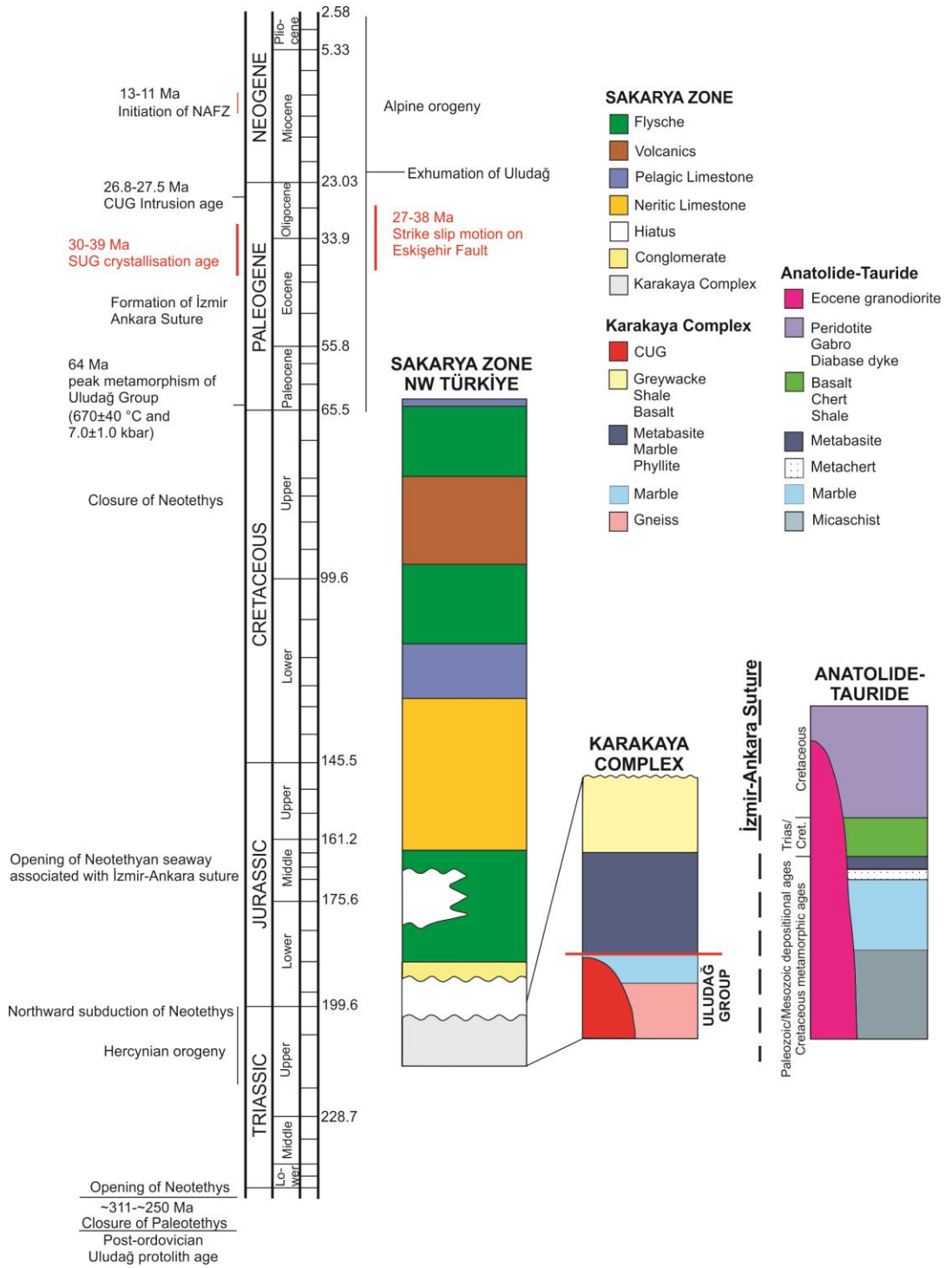


Figure 2.9. The stratigraphic column reveals several terranes on both sides of the İzmir-Ankara suture and Eskişehir Fault (modified from Okay and Satır, 2006; Okay et al. 2008).

2.4.2 Ductile Shear Zone Exhumation

As an exhumed mid-crustal strike-slip zone, the Uludağ Massif consists of a ductile segment. Figure 2.10 illustrates that the overall orientation of structures and foliation in the massif is in the ESE-WNW direction (Özsayın and Dirik, 2007). Okay et al. (2008) proposed that the Eskişehir fault originated during the Oligocene period due to a right-lateral strike-slip fault. The fault near the town of Eskişehir in the south-eastern section of the field area is now active (Figure 2.10 and Figure 2.14).

The existence of a dominant fabric within the Uludağ group serves as proof of ductile shear. This fabric aligns the mountain ranges and the Eskişehir fault in the same direction (Figure 2.6 and Figure 2.7). The fabric exhibits many shear-sense markers, suggesting a right-lateral movement (Okay et al. 2008). There are further pieces of evidence besides the foliation. The massif has a sub-horizontal mineral stretching lineation that decreases gradually towards the edges (Okay et al. 2008). Different mineral compositions in gneiss and amphibolite rock samples provide evidence of a long-lasting re-equilibration process during shear zone deformation (Okay et al. 2008). The prevailing WNW/ESE orientation of the South Uludağ Metagranite is aligned with that of the massif. That indicates it was probably moved in during lateral migration along the fault line.

2.4.2.1 Eskişehir Fault

Okay et al. (2008) and Seyitoğlu and Esat (2022) present different interpretations of the geological history of the Uludağ Massif in northwest Türkiye, particularly regarding the Soğukpınar and Eskişehir Faults.

Okay et al. (2008) propose that the Uludağ Massif represents an Oligocene ductile strike-slip shear zone, indicating a tectonic history involving ductile deformation and significant right-lateral strike-slip displacement. This interpretation suggests a complex tectonic regime involving strike-slip movements that may have influenced the formation and evolution of the Uludağ Massif and the associated faults.

On the other hand, Seyitođlu and Esat (2022) suggest that the Uludađ Massif is an extensional metamorphic core complex based on their field observations. This classification implies that the massif underwent large-scale extensional tectonics, leading to the exhumation of deep-seated rocks. The presence of extensional structures and metamorphic features in the Uludađ Massif supports the interpretation of it being an extensional metamorphic core complex.

The differences in the interpretations of the formation of the Uludađ Massif and its relationship to the Sođukpınar and Eskişehir Faults may come up from variations in the methodologies employed, the focus of the studies, and the interpretation of field observations. Okay et al. (2008) have emphasised the structural characteristics indicative of a ductile strike-slip shear zone, while Seyitođlu and Esat (2022) have focused on features supporting the classification of the massif as an extensional metamorphic core complex.

According to Figure 2.10, the Eskişehir Fault is a component of a broader fault known as the İnönü-Eskişehir Fault System (IEFS). The IEFS extends from Uludađ in the western region to Tuz Gölü (Tuz Lake) in the eastern region. The system is often thought to extend south-eastern beyond Tuz Lake, reaching as far as Sultanhanı in the east. According to Özsayın and Dirik (2007), this length is around 470 kilometres. This fault system consists of numerous fault zones and is partially interconnected. According to Özsayın and Dirik (2007), it is a notable structure in Western Anatolian tectonics.

Ocakođlu (2007) states that the fault developed during the Oligocene period as a strike-slip fault in reaction to subduction in the Aegean region. That facilitated the westward translation of Anatolia.

In addition, Okay et al. (2008) have conducted mapping and measurements of the Eskişehir Fault Zone (EFZ), determining its length to be around 225 km. They have calculated a right-lateral offset of 100 ± 20 km.

The Eskişehir fault defines the interface between several tectonic systems. The Eskişehir Fault Zone (EFZ), located to the south, experienced extension following an orogenic collapse during the middle Miocene to mid-Pliocene periods. Initially,

the direction of movement was from the northwest to the southeast. However, it shifted significantly from the north-northeast to the south-southwest (Koçyiğit, 2005). The northern half of the EFZ (Eskişehir Fault Zone) is dominated by strike-slip tectonics, as documented by Okay and Tüysüz (1999) and Barka et al. (1995). The fault has a parallel alignment with the İzmir-Ankara suture over most of its extent (Okay and Tüysüz, 1999; Barka et al. 1995; Koçyiğit, 2005). Barka et al. (1995) determined distinct rates of displacement for Central Anatolia (northern) (15-20 mm/yr) and Western Anatolia (southern) (30-40 mm/yr) using GPS readings. The measurements acquired from the EFZ scarps indicate horizontal and vertical movement. The fault scarp has a dip of 150° and a strike of 90° , while the slickensides have a dip of 81° and a strike of 323° , with another set of slickensides having a dip of 03° and a strike of 038° (Ocakoglu, 2007).

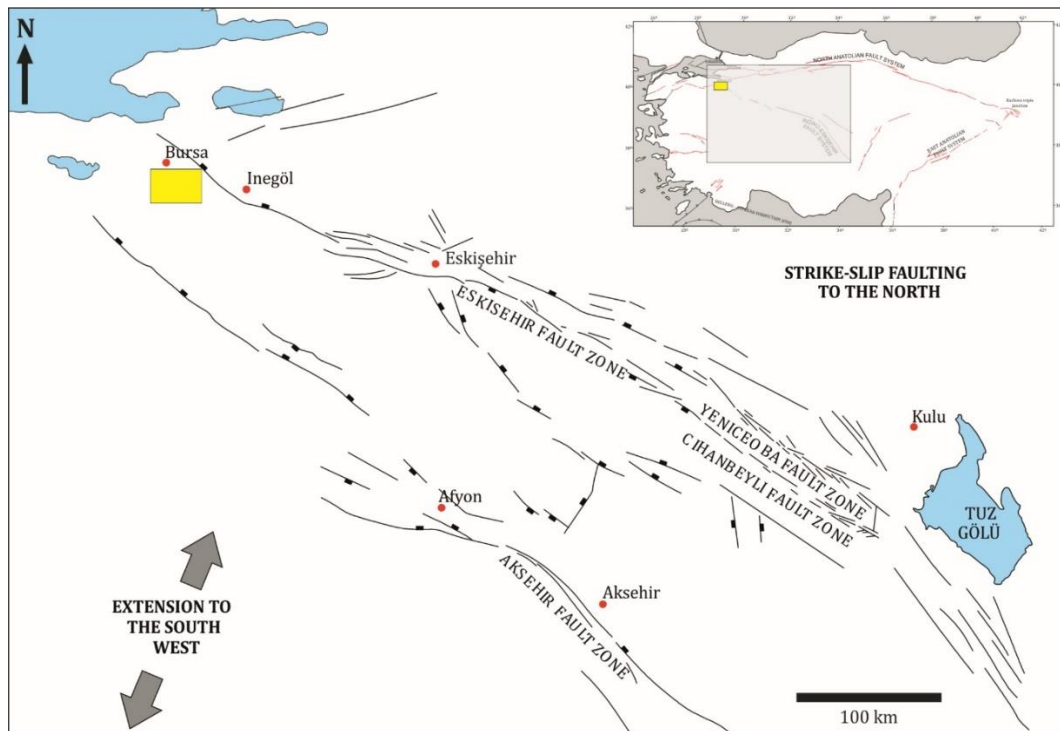


Figure 2.10. İnönü-Eskişehir Fault Zone is reaching the Bursa-Uludağ (modified from Özsayın and Dirik, 2007).

2.4.2.2 The Bursa Fault

The Bursa Fault, located on the northern part of the Uludağ Masif, creates an impressive and steep geographical characteristic as it descends the Bursa Plain (Figure 2.11). The Bursa Fault, located to the north, forms the northern boundary of the massif. This fault is classified as normal with a little right-lateral oblique component (Okay et al. 2008). Okay et al. (2008) conducted measurements of the fault at many places. They observed that the fault has a shallow dip and is oriented towards the northeast, specifically at an azimuth of 140° and a dip angle of 25° . Selim and Tüysüz (2013) divided the fault into four distinct segments: Kayapa-Çalı and Misiköy, Çekirge-Hamamlıkızık, Saitabat, and Çekirge-Hamamlıkızık.

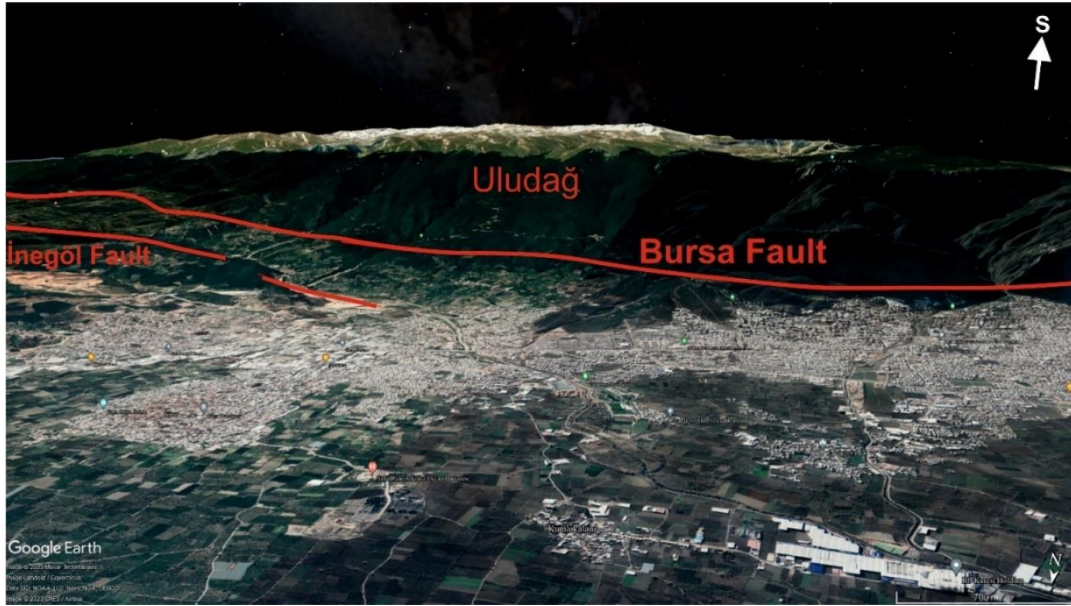


Figure 2.11. Google Earth image of the Bursa Fault.

The segments constitute the northern boundary of the field area. Their striking characteristics differ significantly from the parts next to the northeastern mountain. In their study, Selim and Tüysüz (2013) observed that the fault planes inside Çekirge and Hamamlıkızık had a dip angle of 50° to the north and 35° to the east, particularly in the Saitabat area.

2.5 Metamorphism and Shear Zone Activity

Before the strike-slip event, the Uludağ Group underwent metamorphism in the amphibolite facies (Yıldırım et al. 2005; Okay et al. 2008). Most of the gneiss comprises biotite, with a mineral combination that includes quartz, plagioclase, biotite, and muscovite. The localisation process leads to the formation of amphibolite-gneisses, consisting of quartz, plagioclase, biotite, and muscovite (Okay et al. 2008). The Uludağ Group gneisses reached their highest level of metamorphism at temperatures of $670 \pm 40^\circ\text{C}$ and pressures of 7.0 ± 1.0 kilobars.

The precise timing of the highest level of metamorphism is uncertain. It is estimated to have occurred throughout the Cretaceous until the early Paleocene. This event occurred simultaneously with the Anatolide–Tauride Block and Pontide collision, as Okay et al. (2008) documented.

Granites of the Oligocene age penetrate the Uludağ Group. Bingöl et al. (1982) and Delaloye and Bingöl (2000) determined the K-Ar biotite dates of 26.8 and 24.7 Ma, respectively. According to Okay et al. (2008), the ages determined for Rb/Sr biotite and muscovite were somewhat higher, measuring 27.5 ± 0.5 Ma and 27.2 ± 0.3 Ma, respectively (Figure 2.9). Rb/Sr geochronology provided dates for the gneisses from the most recent Eocene-Oligocene period (36-24 million years ago).

Furthermore, the age of the South Uludağ Granite has been determined by Okay et al. (2008). The syn-kinematic intrusion is characterised by the prominent fault parallel foliation that has developed inside the unit (Okay et al. 2008). This unit experienced significant deformation due to high temperatures. The crystallisation age, ranging from 30 to 39 Ma, was determined by U/Pb zircon dating (Figure 2.9). This age is suitable for undergoing shearing and subsequent deformation caused by movement along the Eskişehir Fault, hence limiting the activity of shear zones (Okay et al. 2008). According to Okay et al. (2008), the deformation temperature of 400°C is indicated by the quartz and feldspar shown in Figure 2.12.

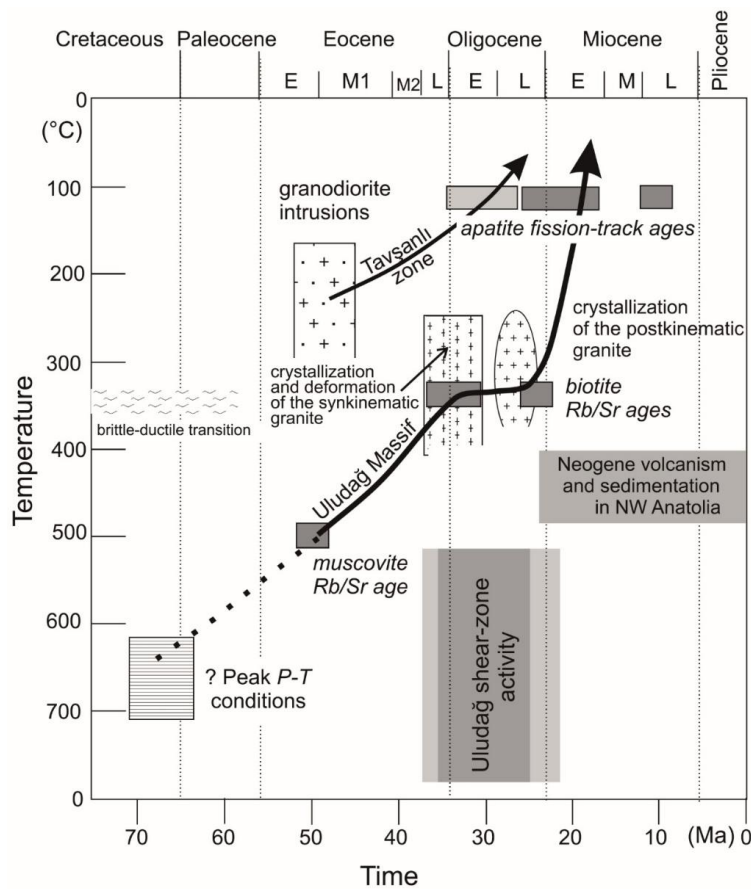


Figure 2.12. The study conducted by Okay et al. (2008) presents data that illustrates the transformation of the Uludağ Massif, starting with its highest pressure and temperature conditions and progressing towards its exposure over the Oligocene and Miocene periods.

2.6 Exhumation

The Uludağ Massif was exhumed during the Oligocene-Miocene period. The primary exhumation event occurred in the Early Miocene, as shown in Figure 2.13 (Okay et al. 2008). According to Okay et al. (2008) the hanging wall of the massif, located towards the south, has remained geologically stable relative to the Earth's surface since the Eocene period. The exhumation rate from the depths of Topuk granodiorite emplacement is estimated to be between 0.2 and 0.3 km per million year. The age range for the Tavşanlı Zone is from 48 Ma to 30 Ma (Harris and Satır, 2006; Okay et al. 2008). The northeastern side was expected to be deeply

buried at a 4-5 km depth. In addition, the AFT ages from the mid-Eocene period (39.4 ± 4.8 Ma) suggest that the exhumation process is not connected to any strike-slip activity during the Oligocene period. This information is supported by Ketin (1947) and Okay et al. (2008). The Uludağ Shear Zone is home to several Neogene basins containing terrigenous deposits (Okay et al. 2008). Based on the AFT data provided by Okay et al. (2008), Deliler and Erenler basins located south of the massif are determined to be of Oligocene age, around 26.3 ± 3 Ma. That suggests a substantial increase in the displacement of normal faults throughout this period (Figure 2.13). The İnegöl Basin, located northeast of the massif, stretches in a WNW–ESE direction, following the path of the shear zone. The ages of the AFT samples are determined based on the gneiss fragments originating from the Uludağ Massif. The fossils assigned a certain date show that the middle Miocene period occurred around 14.3 ± 2 Ma. That suggests the Uludağ Massif was undergoing deposition during this period (Genç, 1987; Okay et al. 2008).

The Uludağ Masif remained undisturbed throughout shear zone activity (38-27 Ma) since there was no vertical displacement seen in the mineral stretching lineations and no evidence of transpression or tension structures in the basins located to the south of it (Okay et al. 2008). According to Okay et al. (2008), the different types of rocks in the massif have AFT dates ranging from 22 to 20 Ma. This suggests that a large amount of erosion occurred during the early Miocene period (Işık and Tekeli, 2001; Okay and Satır, 2006). The exhumation of the Uludağ Massif, and the Lower Karakaya Complex may have been influenced by their density and viscosity (Okay et al. 2008).

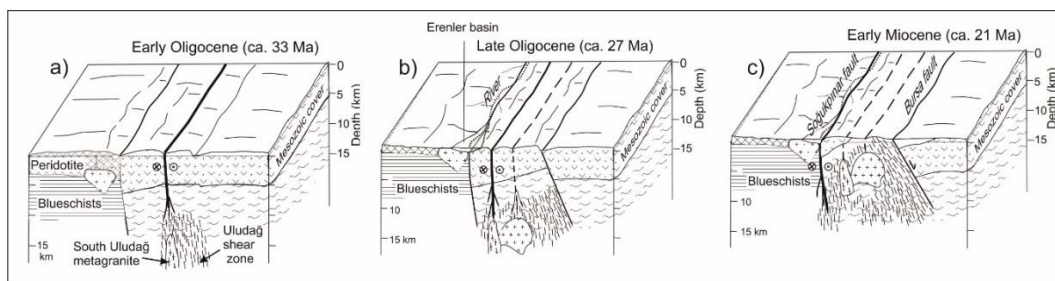


Figure 2.13. Evolutionary changes of the Uludağ Massif have been exposed from the Early Oligocene (a) to the Early Miocene (c). (Okay et al. 2008).

2.7 Present day activity of Bursa Fault and Eskişehir Fault

Bursa and Eskişehir cities are seismically active areas influenced by various faults (Figure 2.14). The seismicity in these regions is primarily controlled by active faults such as the Bursa Fault, İnönü-Eskişehir Fault Zone (IEFZ). These faults play a significant role in shaping the seismic activity in the area (Aslan et al. 2019; Seyitoğlu et al. 2022).

Historically, Bursa has experienced devastating earthquakes (Selim and Tüysüz, 2013). Historical records indicate a long history of seismic activity in the Bursa region, with destructive earthquakes reported as far back as 358 BC. The seismicity in the Bursa region has been a recurring phenomenon over centuries (Ambraseys and Jackson, 2000; Bıçakcı, 2023). Sandison (1855) mentioned a seismic event on February 28, 1855. The most common theory is that the Bursa fault caused it. Another seismic event was also documented on April 11, 1855. The length of the shock this time was around 30 seconds, resulting in the overturning of nearly all stone buildings. The number of fatalities in this town is believed to range from 300 to 400, according to Sandison's report in 1855. Ambraseys (2002) conducted research and determined the magnitude of this earthquake to be 7.1. Notable earthquakes around Bursa include the following: a magnitude=4.6 earthquake on September 5, 1992, a magnitude=4.9 earthquake on October 21, 1983, and a magnitude=3.5 earthquake on February 21, 1994 (Sellami et al. 1997).

According to Meade et al. (2002), the Bursa Fault's rates of movement are determined to be 8.0 ± 4.3 mm/yr in normal offset and 3.6 ± 2.0 mm/yr in strike-slip motions. Additional field observations, such as the presence of hot springs in Bursa and deposits of alluvial fan and slope wastes, provide evidence that the Bursa Fault is now active (Selim and Tüysüz, 2013).

On the other hand, Eskişehir has also been prone to seismic events, with a destructive earthquake recorded in 1956. The city has faced several seismic challenges, including co-seismic surface ruptures and mass movements during past earthquakes. The geological and topographical conditions of Eskişehir have

influenced the seismic risk profile of the region (Orhan et al. 2007; Ocakoğlu and Açıkalm, 2010).

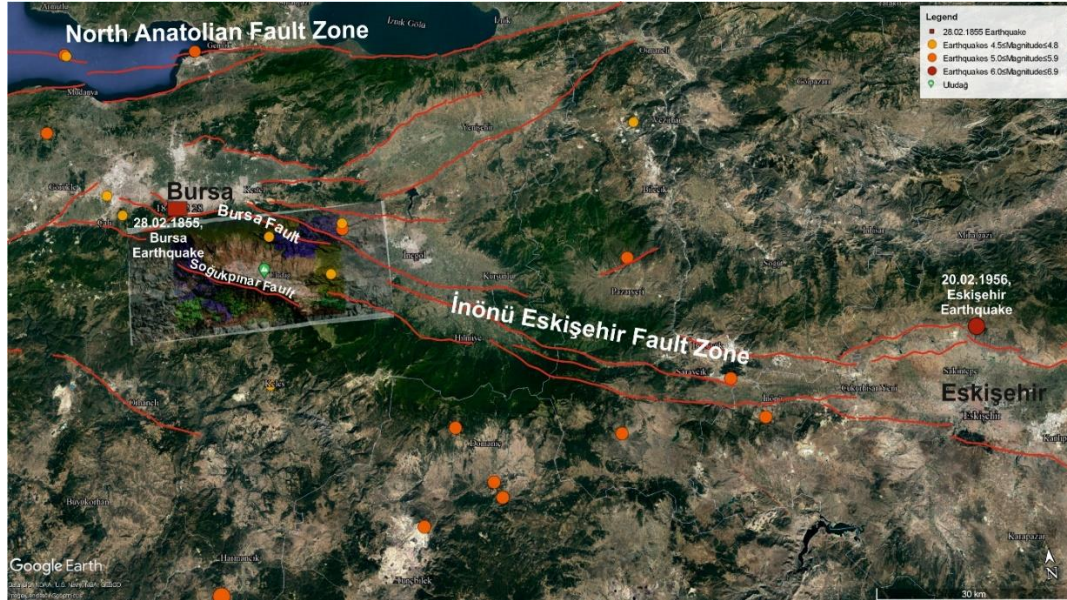


Figure 2.14. Seismicity of Bursa - Eskişehir and surroundings [AFEAD (Active Faults of Eurasia Database), GEM (Global Earthquake Model Foundation), and USGS (U.S. Geological Survey) data set merged with field study].

The epicentre of the catastrophic earthquake near Eskişehir on February 20, 1956 (Mw=6.5) can be seen in Figure 2.14. (Ocakoğlu, 2007; Ocakoğlu and Açıkalm, 2010). According to McKenzie (1972), the earthquake was triggered by the migration of a normal fault, which had a little right-lateral component. The EFZ exhibits a dextral strike-slip motion, accompanied by a notable normal component (Selçuk and Gökten, 2012). According to GPS measurements and geological observations, the deformation rate along the İnönü-Eskişehir Fault Zone was calculated to be 0.15 mm per year (Kahle et al. 1998). According to Ocakoğlu (2007), recent data from the dating terrace deposits indicates a pace of 1mm each year.

CHAPTER 3

GEOLOGICAL FINDINGS

3.1 Introduction

In this chapter, geological observations in the study area are presented. Figure 2.7 displays a geological map of the study area and its surrounding region. This part includes field observations on the massif's lithologies and structure in combination with relevant data from the previous studies. In general, the Uludağ Massif consists of gneiss-marble successions, granites and metagranites. Two faults bound the Uludağ Massif, the Bursa Fault in the north and the Eskişehir Fault in the south. The study area is analysed according to the geographical position of these two faults. Tectonostratigraphic units is divided into three sections: the basin north of the Bursa Fault, the Uludağ Massif and the basin south of the Eskişehir Fault. Although the main study area is the Uludağ Massif between these two faults, brief information about the basins outside the faults are given in this section.

Mapping and sampling were conducted throughout two periods of field studies. This chapter presents information about type of rock, linear features, layering patterns, and faults association with units to find answers to the following questions and problems. The sample data is given in Table 4.1.

- a. How many deformation phases and (perhaps) related/contemporaneous metamorphic phases are there?
- b. What is the spatial and temporal relationship of the possible phases?
- c. What are the kinematics of each stage and the geometry of the shear zone/fault zone?
- d. Are there igneous processes representing and/or preceding/after the phases?
- e. What is the tectonic setting(s) of these phases?

- f. What is their relationship with known regional geological processes?
- g. What kind of evolution model is there?
- h. Which existing question(s) are answered by this study?
- i. Are there any new questions (s)?

3.2 Macro-scale Deformations in the Field

Based on field investigations, the Uludağ Massif consists of marble, amphibolite, gneiss successions, granitic intrusions, metagranites, and other metamorphic rocks. The Bursa Fault situated on the northern edge of the Mount Uludağ, between the Uludağ Massif and the Bursa city marks its northern boundary (Figure 2.7). It exhibits typical features of a normal fault. However, the southern boundary of the massif is delineated by the Soğukpınar segment of the Eskişehir Fault. The Soğukpınar Fault is characterised by a well-defined zone, approximately 20-30 meters wide, that exhibits strong foliation and consists of phyllites and marbles. The units have a prevailing foliation oriented about 120° parallel to the Soğukpınar Fault, located at the northern end of the Eskişehir Fault (Figure 2.7). The foliation of the South Uludağ Metagranite (SUM) and the Soğukpınar Fault is characterised by mylonitic deformation. The Uludağ Massif is determined to be a right-lateral ductile shear zone based on identifying sub-parallel shear sense indicators in the field (Figure 3.1, Figure 3.2, Figure 3.3) and in thin sections (from Figure 4.2). Additionally, deformed microstructures, including mineral lineaments and quartz recrystallisation, can be seen (from Figure 4.2 to Figure 4.42).

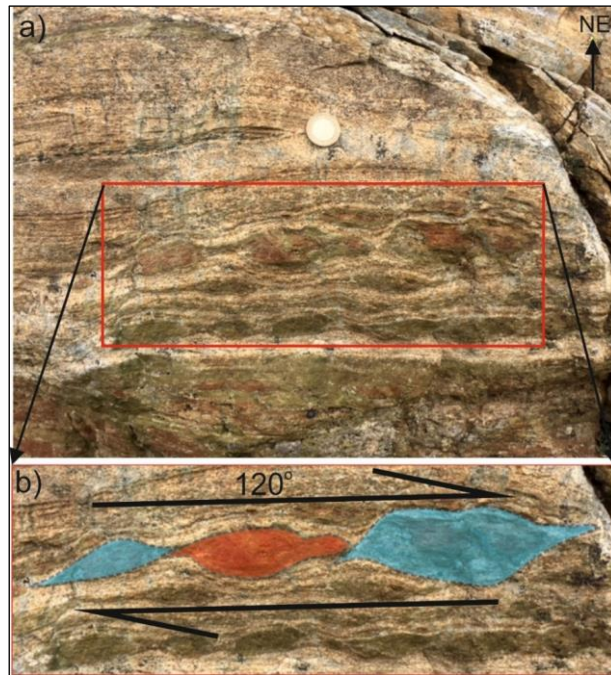


Figure 3.1. Shear sense markers are present in the ductile zone. Figure a and b exhibit winged mantled clasts with σ -type characteristics inside an amphibole gneiss. Samples exhibit dextral lineation illustrated at an angle of approximately 120° .

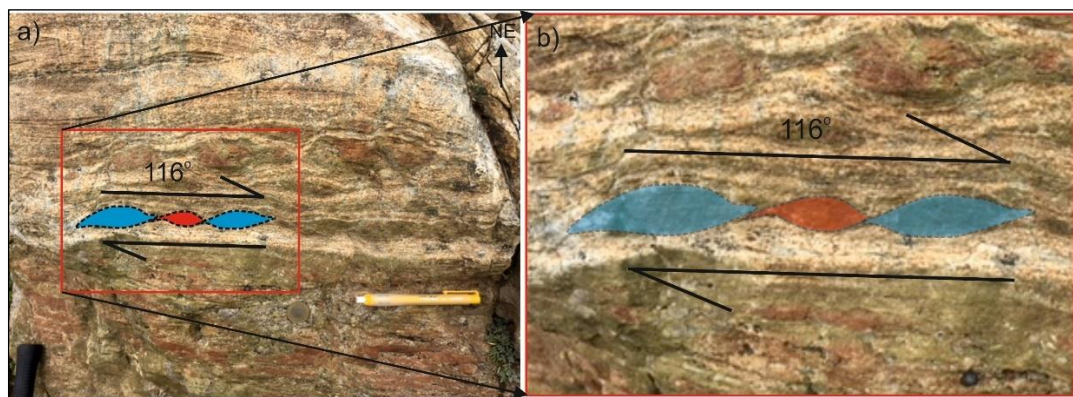


Figure 3.2. Shear sense markers are present in the ductile zone. Figure a and b exhibit winged mantled clasts with σ -type characteristics inside an amphibole gneiss. Samples exhibit dextral lineation illustrated at an angle of approximately 116° .

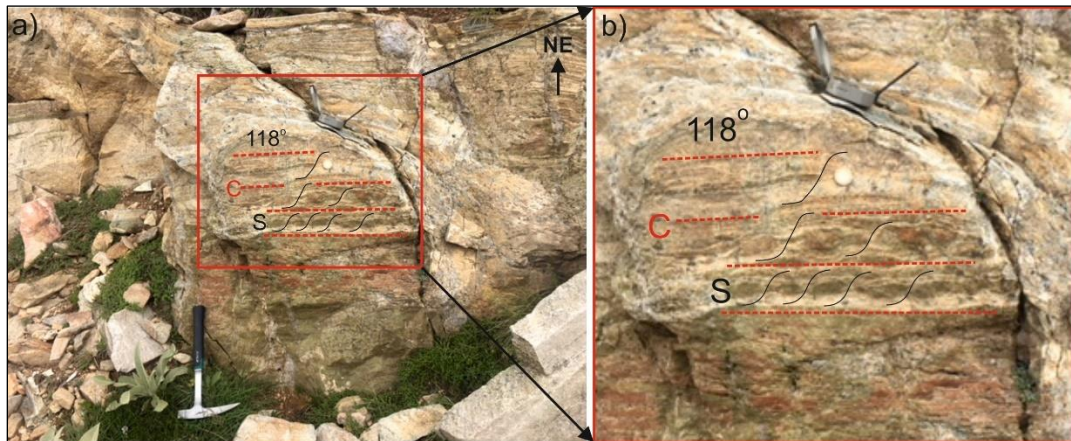


Figure 3.3. Shear sense markers are present in the ductile zone. a) and b) show mylonitic quartz-feldspar veins sheared into folds, revealing C-type shear bands. All samples exhibit dextral displacement along the fault, as illustrated at an angle of approximately 118° .

Amphiboles form under specific temperature and pressure conditions, usually associated with medium to high-grade metamorphism (Currin et al. 2018) (Figure 3.4). Their presence suggests that the gneiss has undergone metamorphism at these conditions (Lepland and Whitehouse, 2010; Currin et al. 2018). Also, the orientation and distribution of the amphibole bands can provide insights into the stress regimes that affected the rock (Lepland and Whitehouse, 2010; Brückner, 2023). Another situation about the presence of amphibole bands may indicate metasomatic processes, where the chemical composition of the gneiss has been altered by the introduction of new elements through fluid interaction (Lepland and Whitehouse, 2010).

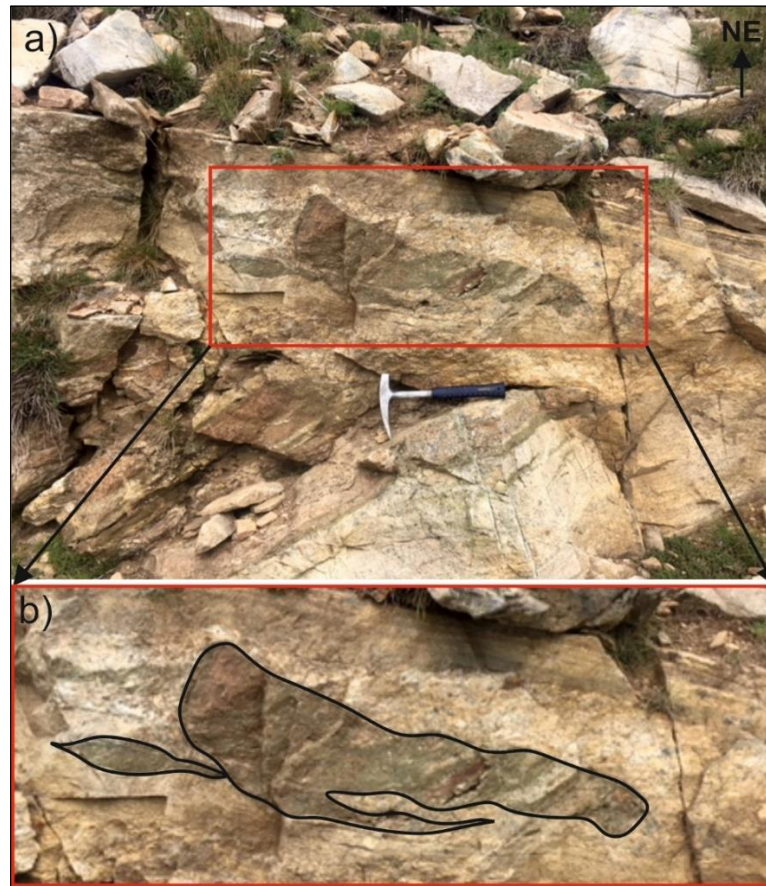


Figure 3.4. Amphibole bands in the gneiss.

The complex history of amphibole-bearing migmatite is evidenced by its composite nature (Zhang et al. 1996, Cruciani et al. 2014; Cruciani et al. 2018). A complex history of fluid interactions, tectonic activity, high-temperature metamorphism, partial melting, amphiboles, leucosomes, and melanosomes, as well as structural elements like as folds and veins, is revealed by these features (Zhang et al. 1996; Cruciani et al. 2014, Cruciani et al. 2018) (Figure 3.5).



Figure 3.5. Amphibole-gneiss migmatization from the northern side of the study area.

The Zirve marble is located at the summit of the Mount Uludağ. Figure 3.6 and Figure 3.7 shows a massive amphibolite intrusions into the marble layers.

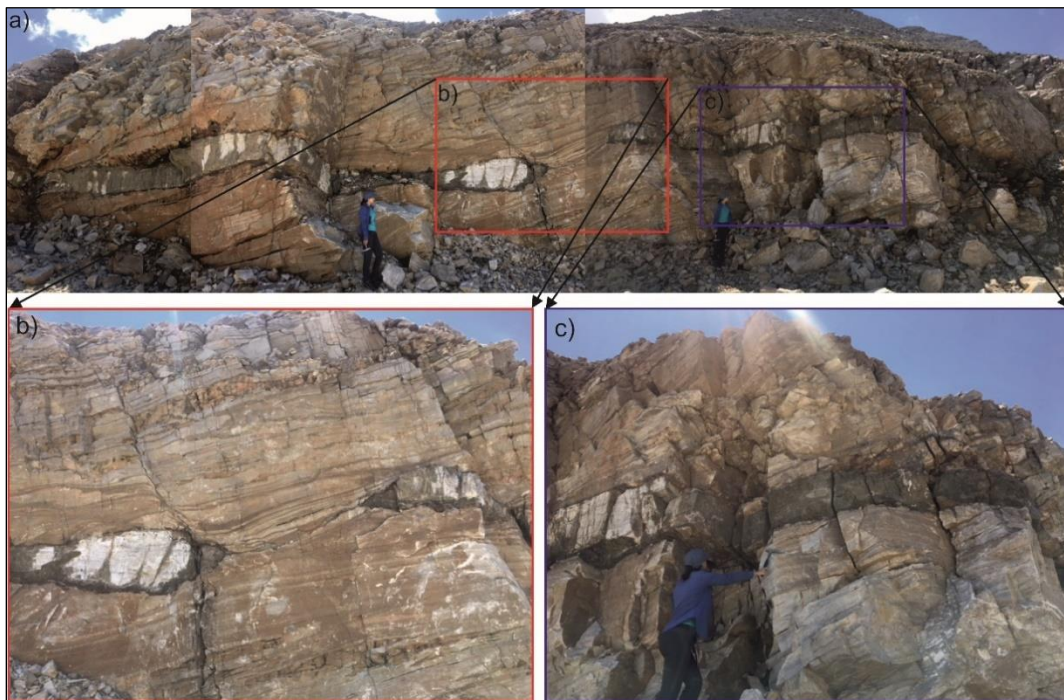


Figure 3.6. Marble layers of the Zirve marble unit from Uludağ Massif, southern peak of the Mount Uludağ. Amphibolite intrusions are seen as a result of right lateral shear sense.

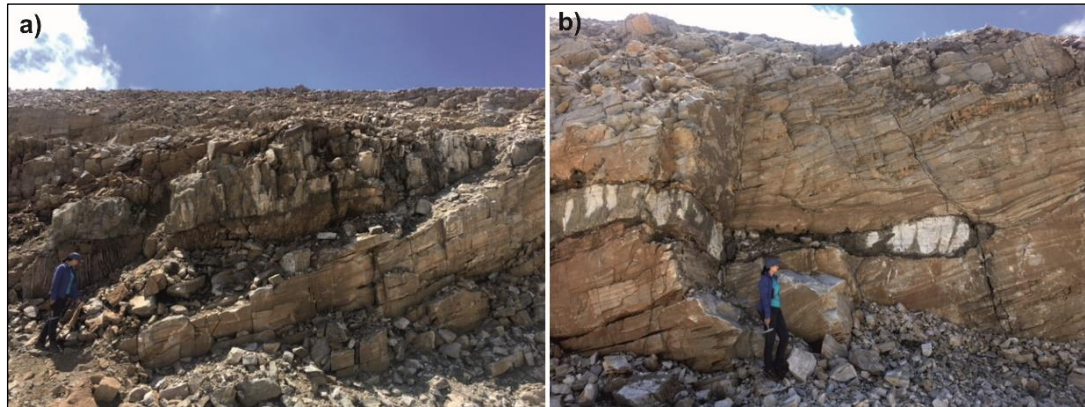


Figure 3.7. Marble layers of the Zirve marble in the Kar Çukuru area, marble bedding measured as N7W-23NE and amphibole boudinaged between layers measured as N5W-23 NE.

3.3 South Uludağ Metagranite and Timing of the Shear Zone

A mylonitic texture, an extended axis parallel to the Soğukpınar fault, and foliation aligned with the widespread fault ($\sim 120^\circ$) are all signs of deformation in the South Uludağ Metagranite (SUM). According to Hutton (1982) and Aczkiewicz et al. (2007), there are further examples of deformed granite intrusions in the shear zone of Donegal, northwest Ireland, and Red River, southwest China. A similar process deformed this granite sample in the Uludağ shear zone since both samples are similar in shape and are associated with the shear zone. Okay et al. (2008) described the granitic intrusion syn-kinematic based on several observations. Among these features are the absence of contact metamorphism, parallel foliation to the Soğukpınar Fault strike, an elongated shape, a microstructure with solid-state and crystal-plastic stress, and a long crystallisation age of 30–39 Ma.

Contact metamorphism between the SUM and the marble that defines its northern limit was not found during this examination either. This suggests that the surrounding environment had consistently high ambient temperatures throughout the granite's formation. No evidence of magmatic microstructure pointing to crystal rotation during the melt phase was found in the samples examined in this investigation. Based on the absence of evidence, the magma was not sufficiently viscous to sustain alignment.

- 1) For example, the crystals of feldspar/hornblende in the samples are arranged in a subparallel manner and do not show any internal deformation.
- 2) The merging of elongated, well-formed crystals without any internal distortion.
- 3) Inadequate deformation of the solid-state material to enable rotation of phenocrystals.
- 4) Igneous flow foliation exhibiting deformation around xenoliths or
- 5) Crystal sorting in convective or magmatic flow, or xenolith shearing, causes schlieren layering (Vernon, 2000).

Alternatively, thin sections from the SUM demonstrated that solid-state flow is happening in a shear zone. To provide an example,

- 1) Internal crystal deformation and recrystallisation
- 2) Extension of recrystallised quartz and mica clusters
- 3) Decrease in grain size (e.g. many of the metagranite and gneiss thin section photos),
- 4) The foliation forms a network around more resistant minerals (e.g. Figure 3.3 to Figure 3.21).
- 5) Microcline twinning occurs in feldspar,
- 6) Myrmekite,

Quartz and feldspar microstructures showed signs of high temperatures, indicates that the heavily foliated zone next to the SUM may hide any contact metamorphism. This particular shear zone suggests that meta-granite makes a vulnerable area mechanically in an area where stress might be focused, which causes temperatures to drop significantly before shear zone activity begins. But even when deformed, the microstructure of hot granite shows that it maintains a temperature advantage over its environment. This proves that the shear zone is active even after the granite has cooled to room temperature.

3.4 Tectonostratigraphic units

The field study led to the identification of four major lithological units in the Uludağ Massif, which is situated between the two main faults shown in

Figure 2.1. and Figure 2.7. Okay et al. (2008) states that units from the Sakarya Zone to the north and the Anatolide-Taurides to the south form the massif's boundaries. As indicated before, the lithological units are described based on the the geographic locations.

3.4.1 North of the Bursa Fault

The region north of the Bursa Fault is part of the Sakarya Zone, as shown in Chapter 2.2.1 (Okay et al. 2008). Schists and other basic units make up most of the outcrops located on the field's northern side. These outcrops also display a lack of significant internal structure. Because of their high weathering resistance, both rock types were found to be challenging to evaluate in thin sections and hand specimens for mineralogy and structure. The schists on the northern side of the study area are very rich in mica, which make them very foliated or schistose. Figure 3.8 shows that the mica-schist is mostly quartz with feldspar, with muscovite and biotite that highlight the foliation.



Figure 3.8. Mica-schist from the north of the study field.

The gneisses of the Gökdere formation are generally grey in colour. As can be seen in Figure 3.9, the locations where the Uludağ Granite intruded into the Gökdere formation were determined and these data were also utilized during the drawing of the geological map. Although, in the north-western and central parts of the area, as far as the terrain conditions allow, the granite was observed to be intruded into the gneisses of the Gökdere formation.

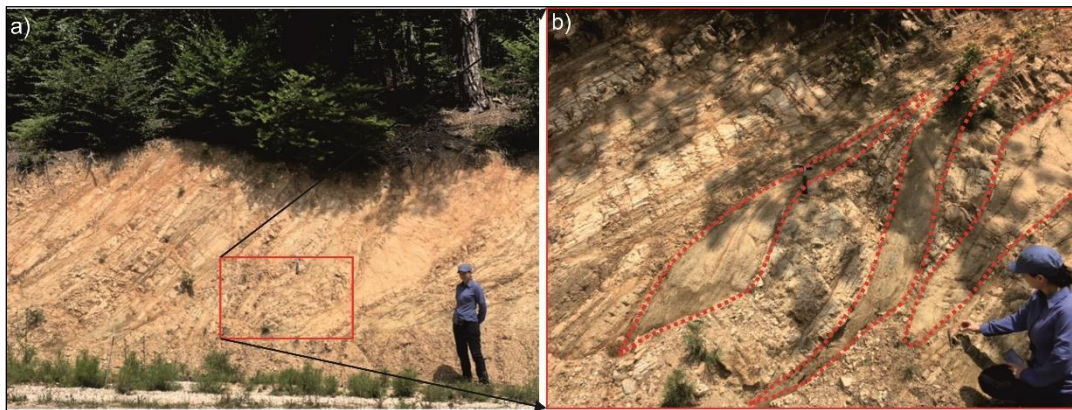


Figure 3.9. The contact zone between the gneisses of the Gökdere formation and Uludağ granites.

It is clearly seen in Figure 3.10 that the gneisses were folded due to tectonism rather than the effect of granite intrusion.



Figure 3.10. Figure shows the folding in gneisses of the Gökdere formation due to tectonic forces.

The northern side similarly presented grey-coloured fine-grained limestone outcrops lacking interior structure. The weathering pattern exhibited the characteristic features of limestone, as seen in Figure 3.11, including the top layers, including dissolution karsts. The predominant geological formation is marble, located near the Bursa Fault on the northern side. The exposed rock formations frequently exhibit a weathering process resulting in an orange hue, and certain regions also display signs of stratification.



Figure 3.11. Outcrops of the Bursa marble on the road from Saitabat to Alaçam.

3.4.2 The Uludağ Massif

Geographically the Uludağ Massif is located between the Bursa Fault and the Eskişehir Fault. There is a formation of pure white calcite marble that may be found just next to the Bursa Fault. As it is gone farther south towards the Eskişehir Fault, the types of rocks shift. They are made up of various minerals, and these rocks have broad pattern of foliation which is related with their mineral's direction. The gneiss samples collected from the northern area are mostly composed of biotite-quartz-plagioclase gneisses. There are also trace amounts of amphibole and muscovite; some samples include garnet, as seen in Figure 4.5 in “Petrographic

Studies and Micro-scale Observations” chapter. This unit has many outcrops composed of mafic gneiss that contains about equal amounts of amphibole and plagioclase. According to the classification system, this rock is an amphibolite with a broad foliation. Near the Eskişehir Fault, the marble reappears to the south and forms the southern limit of the massif. This is located close to the limestone.

It should be noted that the marble is mostly made of calcite, with just trace amounts of quartz. The marble may be differentiated from other types of marble by its varying degrees of hardness. It can be observed in Figure 3.7 that the marble is positioned at an angle of about 120 degrees, and it is located at the highest point of the mountain range (Figure 3.12, Figure 3.13).

The rock formation in this region is enormous, and when seen through the hand specimen, it displays a broad foliation and a specific mineral alignment. It can be observed in Figure 2.7 that a significant igneous intrusion may be found in the northern part of the massif. The spherical shape of the outcrops situated in the middle portion of this intrusion is characterised by the absence of any internal arrangement that can be identified. A typical granitic composition is achieved due to the mineral composition, mostly composed of quartz, plagioclase, K-feldspar, biotite, and muscovite, with only trace amounts of muscovite. The granite has a varied strike that ranges from 8° to 143° , and it is discovered that there is foliation along the outside border of the granite.

3.4.2.1 Kilimligöl Formation

The Kilimligöl Formation was named for the first time by Pehlivan et al. (2014) and analysed as gneiss-bearing amphibolite lenses in previous studies. Ronner (1954) stated that this unit is a lithology overlying marble and gneisses. The Kilimligöl Formation is located at the lowest level of the Uludağ metamorphics. It comes to the surface at a thin level of about 40-50 meters thick and 13-15 km long, extending NW-SE between the Zirve Marbles and metagranites around the Kilimli

Lake and the Kara Lake in the Lakes Region at the summit of Uludağ (Figure 3.12, Figure 3.13).

According to the MTA, H-22 (2013) report, the researchers could not obtain any age data within this formation. In the MTA Bursa H-22 report, it is stated that the Kilimligöl Formation can be compared with the Basic Series (Bingöl, 1969) and the Tozlu Formation in the Kazdağı Massif (Bingöl et al. 1973; Duru et al. 2007), which have similar lithologic characteristics and are composed of metaophiolites.

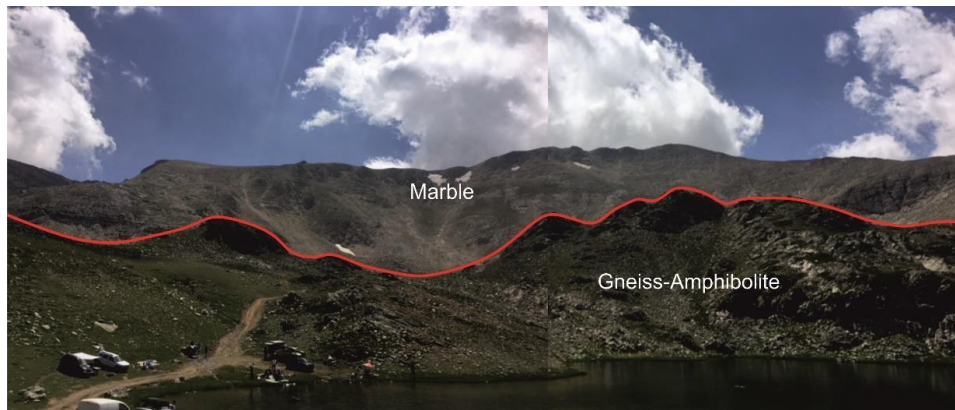


Figure 3.12. The red line shows the contact between the Zirve marble and the Kilimligöl formation.



Figure 3.13. Contact between the Zirve marble and gneiss-amphibolite alternation of the Kilimligöl formation around the Aynalı Lake.

3.4.2.2 Gökdere Formation

The Gökdere formation was named for the first time in the report of Pehlivan et al. (2014) and named after the Gökdere Stream passing through Bursa. Its outcrops occur along Süleymaniye Village in the south of Bursa, west of Bursa, Cumalıkızık, Saitabat and Kıran Villages at the east of Bursa. The unit mainly comprises quartzo-feldspathic gneisses with well-foliated and banded structures. Amphibolite lenses and occasional migmatite levels are observed in the gneisses, which form the main lithology of the formation. The formation is cut by aplite and granitic rocks. It tectonically overlies the Zirve marble. The Bursa marble is conformably overlying this unit. In the central and western parts of the Uludağ Massif, the gneisses are cut by Oligo-Miocene-aged Central Uludağ Granit.



Figure 3.14. Quartzo-feldspathic gneisses of the Gökdere formation showing well-foliation, banded structures with red dashed lines (UTM coordinate: 0698279E – 4438364N).

The MTA H-22 report (2013) states that the age of the Gökdere formation is thought to be pre-Carboniferous, but no age data study has been carried out.

3.4.2.3 The Central Uludağ Granite and The South Uludağ Metagranite

The Oligocene granites and metagranites cutting the Uludağ Metamorphics were defined as the Central Uludağ Granite and the South Uludağ Metagranite by Okay et al. (2008) (Figure 3.15). In this study, the unit was analysed using the same name. While the Central Uludağ Granite is located within the borders of Uludağ National Park from the Süleymaniye Village in the west of the study area to the east, the part extending from the south of the ski centre in the NW-SE direction constitutes the South Uludağ Metagranite.

The reason for the metamorphism of the South Uludağ Metagranite is that this granite is located within the right lateral shear zone formed by the Eskişehir (Soğukpınar) Fault, which extends to the northwest in the latest Eocene-Oligocene (38-27 Ma) interval. It was subjected to ductile deformation in the NW-SE direction (Okay et al. 2008).

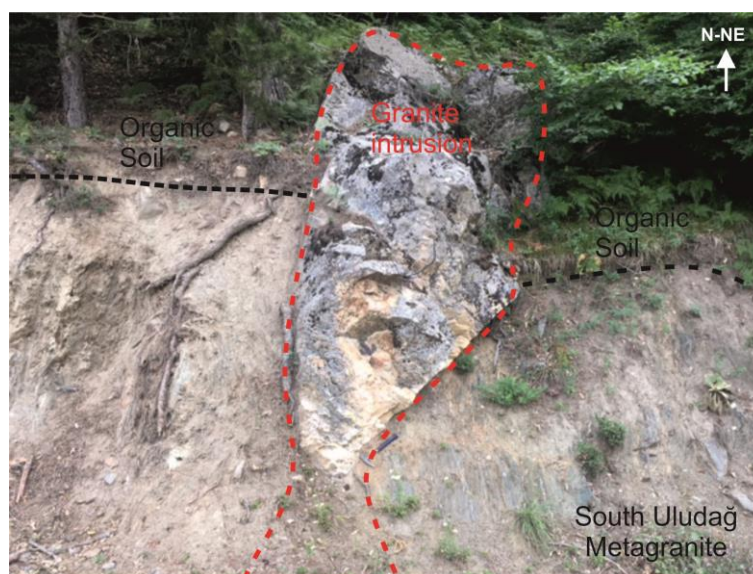


Figure 3.15. Local granite intrusions cut the South Uludağ Metagranite in the NE of Soğukpınar Village (UTM coordinate: 0680628E - 4437989N).

The Central Uludağ Granite mainly comprises quartz, K-feldspar, plagioclase, biotite and muscovite. Okay (2008) determined that the Central Uludağ Granite is approximately 25 My by isotopic age determination methods. In addition, marbles

belonging to the Uludağ Metamorphics were cut along the eastern edge of the Central Uludağ Granite and wolfram mineralisation was formed along this cutting edge.

3.4.3 South of Eskişehir Fault

As can be observed in Figure 2.4 of Chapter 2.2.1, the area that is situated to the south of the Eskişehir Fault is a component of the Anatolide-Taurides block (Okay et al. 2008). The outcrops that were found on the southern side of the massif, which is situated to the south of the Eskişehir Fault, are composed of granite (Figure 3.16), gneiss, and marble that have been subjected to mylonitization and metamorphism. Based on the description provided by Okay et al. (2008), the southern basin comprises schists and ophiolitic melange. Quartz, feldspar, biotite, muscovite, and a trace quantity of chlorite are the elements that make up granite, a common kind of rock. The composition of the granite is similar to that of the Uludağ Massif, as seen in Figure 4.21 to Figure 4.25. Ophiolitic melange contains, sheared serpentinite and ultramafic units like peridotite, which has blocky weathering and an orange hue. The ophiolite outcrops exhibited extensive fracturing and faulting.

3.4.3.1 Kapıdağ Granodiorite

The unit, which is typically observed in the Kapıdağ Peninsula in the northwestern Anatolia, was first named Kapıdağ Granite by Ketin (1946). Since the unit is located in the granodiorite area in the Streickesen (1976) triangle diagram, it was named Kapıdağ granodiorite (Ercan and Türkecan, 1984). Eocene-aged plutons cut the units of the Tavşanlı zone. These plutons, some also found in the study area, are exposed in the south and southeast of Uludağ. This unit, known as Topuk granodiorite in the literature (Okay et al. 1998), was analysed as Kapıdağ Granite in this study (Figure 3.16).

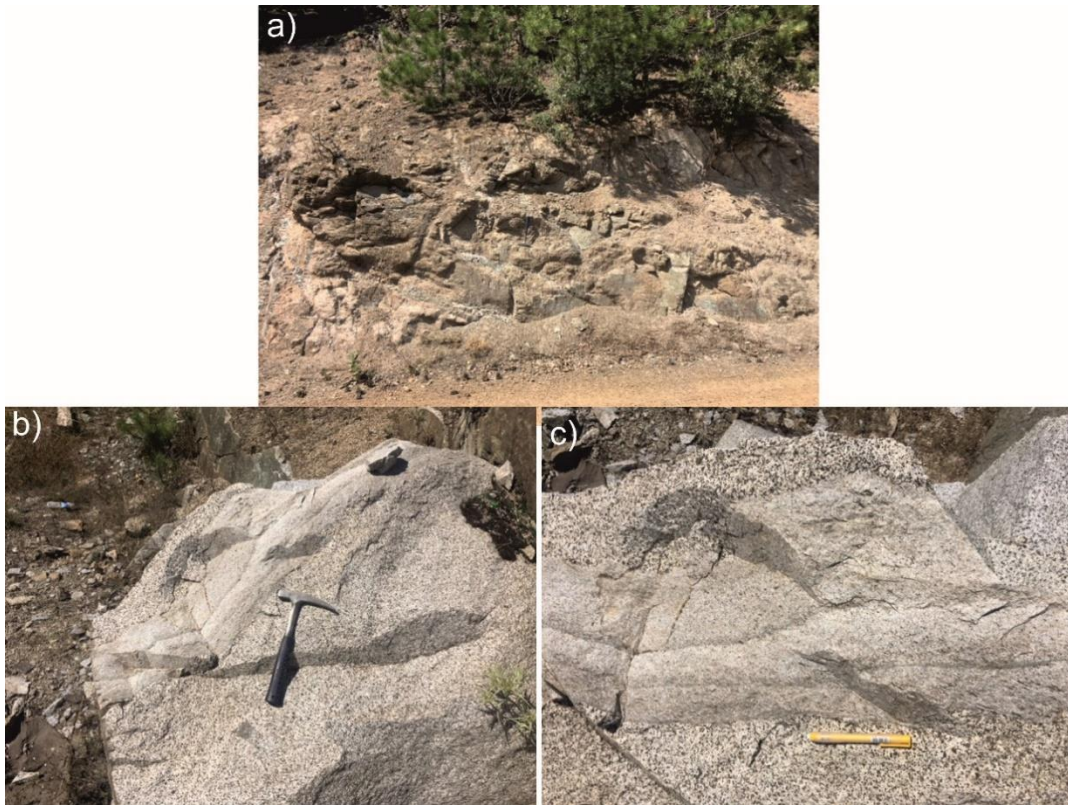


Figure 3.16. Outcrop views of the Kapıdağ Granite in the south of the study area.

The minerals of the unit are quartz, plagioclase, K-feldspar, hornblende, biotite and opaque minerals. Magma intrusions belonging to relatively different phases are frequently observed within the unit. This pluton, a granodioritic and granitic type of intrusion, is highly weathered at the outer surfaces and quite fresh and intact at the inner parts.

Regarding the age of Kapıdağ granodiorite, Delaloye and Bingöl (2000) determined ages between 38-42 Ma according to biotite dating, while Okay et al. (1998) determined the age of the pluton as 48 Ma by the Ar-Ar method. In other words, the age of the unit was determined as Eocene in previous studies.

3.5 Structural Elements of the Massif

This part provides the structural data from the study area, divided into the tectonostratigraphic units and key structures mentioned before.

Their arrangement is based on their geological location relative to the principal structures. All lithologies mentioned in this section have been identified and discussed in the corresponding titles in Section 3.4.

3.5.1 North of the Bursa Fault

North of the schist outcrop, there was extensive foliation with a varied strike of 60° to 120°. A significant amount of mica in the rock was the primary factor that ultimately defined this foliation. The outcrop seemed mostly solid and lacked any internal structure, contributing to the limestone showing very little signs of deformation. There was no evidence of the bedding in the outcrops that were seen.

3.5.2 The Bursa Fault

A representation of the Bursa Fault, which serves as the northern limit of the exposed Uludağ Massif, can be seen in Figure 2.7. A significant number of the outcrops located along the route of the Bursa Fault are composed mostly of marble. Recent portions of the Bursa Fault, which have grown increasingly vulnerable, may be seen in cliff sections along its route, notably from Bakacak Tepesi. These cliff sections are located along the edge of the massif and Bursa Fault observed as a normal fault as previous researchers mentioned (Okay et al, 2008, Selim and Tüysüz, 2013).

Through its connection with the marble deposits located on the northern side of the Uludağ Massif, the Bursa fault creates a network of related faults. These faults display slight changes in their direction. Comparatively speaking to the Eskişehir Fault, this fault is classified as a brittle fault with a broader deformation zone.

During this process, the most common types of deformation are the creation of joints, fractures, fault breccia, and cataclasite.

3.5.3 The Uludağ Massif

Extensive foliation can be seen on the gneiss and marble found on the southern side of the massif. This foliation is generally parallel to the Eskişehir Fault and has an average orientation of 116° . It is possible to divide the foliation of the marble into two distinct categories: the first is one that runs parallel to the fault, and the second strikes at an angle of around 30° and approximately 75° to the fault. The second foliation orientation was mostly seen in the marble unit along the southern boundary of the Uludağ Massif. This orientation was furthermore observed in conjunction with the prevalent fault parallel foliation. There is a possibility that this second foliation indicates a Reidel shear that is taking place inside the shear zone at around 110° .

3.5.4 The Eskişehir Fault

Activation in the field area has been detected along the southern Eskişehir Fault. However, it is less active than the Bursa Fault (Ocakoglu, 2007; Ocakoglu and Açikalın, 2010). The earthquake that caused the most significant damage occurred on the same fault system, although it was located further to the southeast, close to Eskişehir. According to McKenzie (1972), an earthquake, which had a magnitude of 6.4, was found to have occurred in February of 1956. The fault in issue does not have a prominent geomorphic expression, in contrast to the Bursa Fault, which has.

As indicated before, the fault may be found close to the marble that makes up the massif. Because it is getting closer to the fault, the marble is becoming more distorted and exhibiting evidence of shear in the form of folding. Around ten metres in thickness, the fault zone is made up of marbles and phyllites that have been severely distorted and are piled on top of one another.

A shear-deformed granite formation may be seen on the southern side of the fault, which is next to the fault. Quartz, feldspar, biotite, muscovite, and chlorite remnants are all components that form granite. The outcrop is quite apparent and almost completely continuous, with the phyllites displaying more weathering than the marbles sheared. The marble is mostly calcite, with some quartz mixed in. It has bands between a few centimetres and a few millimetres wide. Shear sense markers are found in all lithologies and may be detected in specimens that are handled by hand. Consistently, the shear displacement takes place in a right-lateral direction, stretching from the top to about 120°. The fault strike as a linear feature made up of a single strand that stretches consistently and is present throughout its whole length. Within a region roughly 30 metres in length, it displays a relatively limited zone of severe ductile deformation. A mylonitic fabric can be seen near the fault in the rocks belonging to the South Uludağ Granite and the marble located to the north.

3.5.5 South of Eskişehir Fault

The Kapıdağ (Topuk) granite is situated on the southern side of the Eskişehir Fault, where it forms a long and narrow intrusion that runs parallel to the fault (Figure 2.7). This unit has fault scarps exhibiting slickensides that indicate motion along the Eskişehir Fault.

CHAPTER 4

PETROGRAPHIC STUDIES AND MICRO-SCALE OBSERVATIONS

4.1 Introduction

Thin sections of the rock samples taken from the field were prepared for mineralogical, petrographic, and microtectonic investigations. These studies were done to clarify the rock units' multiple metamorphism and deformation evolutions. Direction of shear movement is determined from the porphyroblasts formed in the mylonitic rocks and the microtectonic structures developing in the deformed rocks. For this purpose, many directional samples of these sections were examined.

Twenty-eight thin sections were prepared at the Thin Section Laboratory in the Department of Geological Engineering, METU, and crossed polarized light (XPL) and plane polarized light (PPL) images of all thin sections were taken by the Leica Application Suite Version 4.0.0 program via Leica DM2500 P polarising microscope at the Thin Section Laboratory in the Geological Engineering Department, Batman University. A detailed interpretation of chosen samples is given in section Implications by Petrographic Interpretation. Petrographic interpretations of thin section samples are given according to the different members of the Uludağ Massif components such as Kilimligöl and Gökdere Formations, and Central Uludağ Granite and South Uludağ Metagranite members. Thin section samples of the Kapıdağ Granite are also interpreted in this chapter to show differences in petrographic features between the Uludağ Granite and the Kapıdağ Granite.

Figure 4.1 presents sample locations on the simplified geological map of the Uludağ Massif and the surrounding area. Table 4.1 shows the samples taken from the field where the samples thin-sectioned and examined are marked with blue. Detailed interpretations of the thin sections are given in Chapter 4.2.

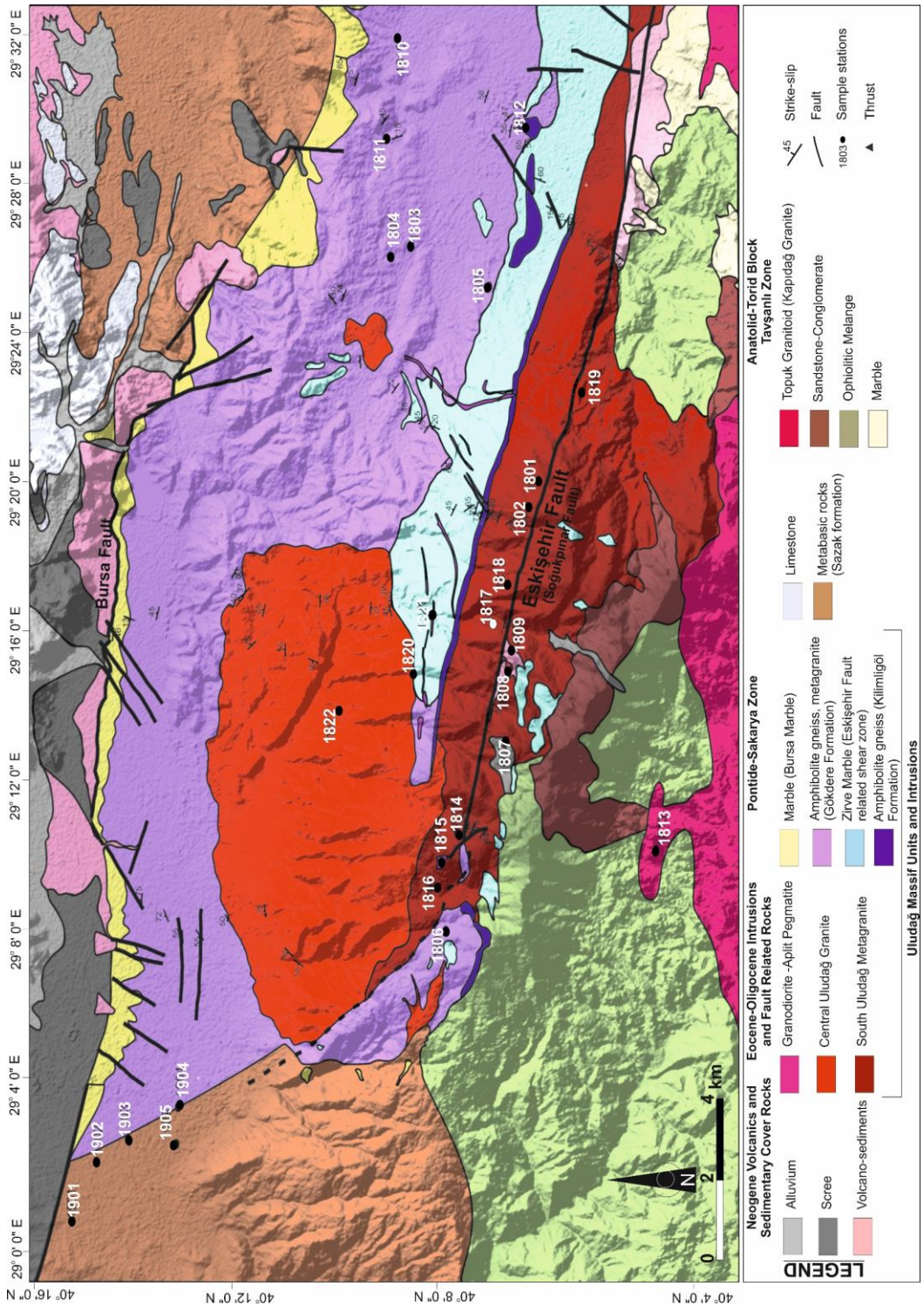


Figure 4.1. Sample locations from the study field.

Table 4.1. Coordinates, lithologies and sampling purposes of the taken samples.

NO	SAMPLE NAME	COORDINATE	LITHOLOGY	SAMPLING PURPOSE
1	1801-J	0687463E-4436254N	SOUTH ULUDAĞ METAGRANITE - METAGRANITE	GEOCHRONOLOGY - GEOCHEMISTRY
2	1801-P	0687463E-4436254N	SOUTH ULUDAĞ METAGRANITE - METAGRANITE	DIRECTIONAL SAMPLE - PETROGRAPHY
3	1802-J	0687272E-4436363N	SOUTH ULUDAĞ METAGRANITE - METAGRANITE	GEOCHRONOLOGY - GEOCHEMISTRY
4	1802-P	0687272E-4436363N	SOUTH ULUDAĞ METAGRANITE - METAGRANITE	DIRECTIONAL SAMPLE - PETROGRAPHY
5	1803-J	0694433E-4440616N	GÖKDERE FORMATION - GNEISS	GEOCHRONOLOGY - GEOCHEMISTRY
6	1804-P	0694213E-4440737N	GÖKDERE FORMATION - GNEISS	DIRECTIONAL SAMPLE - PETROGRAPHY
7	1804-J	0694213E-4440737N	GÖKDERE FORMATION - GNEISS	GEOCHRONOLOGY - GEOCHEMISTRY
8	1805-P	0693505E-4438853N	KİLİMLİGÖL FORMATION-GNEISS	DIRECTIONAL SAMPLE - PETROGRAPHY
9	1806-P	0678020E-4438787N	GÖKDERE FORMATION - GNEISS	DIRECTIONAL SAMPLE - PETROGRAPHY
10	1807-P	0683679E-4436048N	MESUDIYE FORMATION - ARKOSIC CONGLOMERATE	DIRECTIONAL SAMPLE - PETROGRAPHY
11	1808-P	0684064E-4436186N	CENTRAL ULUDAĞ GRANITE - GRANITE	DIRECTIONAL SAMPLE - PETROGRAPHY
12	1809-J	0684316E-4436073N	CENTRAL ULUDAĞ GRANITE - GRANITE	GEOCHRONOLOGY - GEOCHEMISTRY
13	1809-P	0684316E-4436073N	CENTRAL ULUDAĞ GRANITE - GRANITE	DIRECTIONAL SAMPLE - PETROGRAPHY
14	1810-J	0700110E-4438700N	GÖKDERE FORMATION - GNEISS	GEOCHRONOLOGY - GEOCHEMISTRY
15	1810-P	0700110E-4438700N	GÖKDERE FORMATION - GNEISS	DIRECTIONAL SAMPLE - PETROGRAPHY
16	1811-J	0698275E-4438367N	GÖKDERE FORMATION - GNEISS	GEOCHRONOLOGY - GEOCHEMISTRY
17	1811-P	0698275E-4438367N	GÖKDERE FORMATION - GNEISS	DIRECTIONAL SAMPLE - PETROGRAPHY
18	1812-J	0698238E-4436431N	KİLİMLİGÖL FORMATION-GNEISS	GEOCHRONOLOGY - GEOCHEMISTRY
19	1812-P	0698238E-4436431N	KİLİMLİGÖL FORMATION-GNEISS	DIRECTIONAL SAMPLE - PETROGRAPHY
20	1813-J1	0675579E-4430759N	KAPIDAĞ GRANITE - GRANITE	GEOCHRONOLOGY - GEOCHEMISTRY
21	1813-J2	0675579E-4430759N	KAPIDAĞ GRANITE - GRANITE	GEOCHRONOLOGY - GEOCHEMISTRY
22	1813-P1	0675579E-4430759N	KAPIDAĞ GRANITE - GRANITE	DIRECTIONAL SAMPLE - PETROGRAPHY
23	1813-P2	0675579E-4430759N	KAPIDAĞ GRANITE - GRANITE	DIRECTIONAL SAMPLE - PETROGRAPHY
24	1814-J	0681067E-4438279N	SOUTH ULUDAĞ METAGRANITE - METAGRANITE	GEOCHRONOLOGY - GEOCHEMISTRY
25	1814-P	0681067E-4438279N	SOUTH ULUDAĞ METAGRANITE - METAGRANITE	DIRECTIONAL SAMPLE - PETROGRAPHY
26	1815-J	0681007E-4438254N	SOUTH ULUDAĞ METAGRANITE - GRANITE	GEOCHRONOLOGY - GEOCHEMISTRY
27	1816-J	0679386E4438917N	SOUTH ULUDAĞ METAGRANITE - GRANITE	GEOCHRONOLOGY - GEOCHEMISTRY
28	1817-J	0685974E-4436792N	SOUTH ULUDAĞ METAGRANITE - METAGRANITE	GEOCHRONOLOGY - GEOCHEMISTRY
29	1817-P	0685974E-4436792N	SOUTH ULUDAĞ METAGRANITE - METAGRANITE	DIRECTIONAL SAMPLE - PETROGRAPHY
30	1818-P	0687125E-4436327N	SOUTH ULUDAĞ METAGRANITE - METAGRANITE	DIRECTIONAL SAMPLE - PETROGRAPHY
31	1819-J	0690511E-4434829N	SOUTH ULUDAĞ METAGRANITE - METAGRANITE	GEOCHRONOLOGY - GEOCHEMISTRY
32	1819-P	0690511E-4434829N	SOUTH ULUDAĞ METAGRANITE - METAGRANITE	DIRECTIONAL SAMPLE - PETROGRAPHY
33	1820-J	0684777E-4440425N	GÖKDERE FORMATION - GNEISS	GEOCHRONOLOGY - GEOCHEMISTRY
34	1821-J	0686598E-4440640N	CENTRAL ULUDAĞ GRANITE - GRANITE	GEOCHRONOLOGY - GEOCHEMISTRY
35	1822-J	0684134E-4442776N	CENTRAL ULUDAĞ GRANITE - GRANITE	GEOCHRONOLOGY - GEOCHEMISTRY
36	1901-J	0671924E-4443771N	SAZAK FORMATION - METABASITE	GEOCHRONOLOGY - GEOCHEMISTRY
37	1902-P(A)	0674700E-4445731N	GÖKDERE FORMATION - METAGRANITE	GEOCHRONOLOGY - GEOCHEMISTRY
38	1902-P(B)	0674700E-4445731N	GÖKDERE FORMATION - GNEISS	GEOCHRONOLOGY - GEOCHEMISTRY
39	1903-P	0674701E-4445539N	GÖKDERE FORMATION - GNEISS	GEOCHRONOLOGY - GEOCHEMISTRY
40	1904-P	0673928E-4446845N	GÖKDERE FORMATION - METAGRANITE	GEOCHRONOLOGY - GEOCHEMISTRY
41	1905-P	0675307E-4442650N	SAZAK FORMATION - METABASITE	GEOCHRONOLOGY - GEOCHEMISTRY

4.2 Petrographic Interpretation

The minerals in the thin sections are analysed in terms of their textures and structures at first glance (from Figure 4.2 to Figure 4.28). Accordingly, they are classified metagranites, gneisses, granites, and metabasalts.

Detailed interpretation and examination of the thin sections are given in from Figure 4.29 to Figure 4.42 in this part. This chapter divides interpretation processes into four according to the rock types. Firstly, metagranites samples were given and interpreted in Section 4.2.1.

4.2.1 The South Uludağ Metagranites

The South Uludağ Metagranites are located in the central-southern part of the massif in an NW-SE direction. The sample localities of the South Uludağ Metagranites taken from the field in red in Figure 4.1. Information about the minerals in the rocks, texture and internal structures of the rocks are given in this section. In addition, the tectonic forces to which the rock is exposed, and their causes will be analysed from the directional sample specimens.

Observations on the metagranite thin sections reveal various mineralogical and textural changes resulting from the metamorphic process. The minerals of the rock are biotite, muscovite, chlorite, quartz, plagioclase, K-feldspar, sericite. The mineral constituents exhibit recrystallisation and/or deformation features in quartz, alteration in feldspars, and changes in mica minerals like muscovite or biotite. The texture of the rock is typically granoblastic, characterised by equidimensional minerals without the original grain boundaries of the protolith (Figure 4.2). In addition, depending on the intensity of metamorphism, foliation is observed, ranging from weak mineral alignment to well-developed schistosity or gneissic banding (Figure 4.3, Figure 4.4, Figure 4.5). Additionally, new minerals formed during metamorphism, such as epidote and zircon are present as accessory amounts. Alteration features, such as chloritization of biotite and recrystallisation processes, are also observed (Figure 4.3 and Figure 4.5). It is important to note that the specific features observed vary based on the degree of metamorphism and the specific conditions of metamorphic formation.

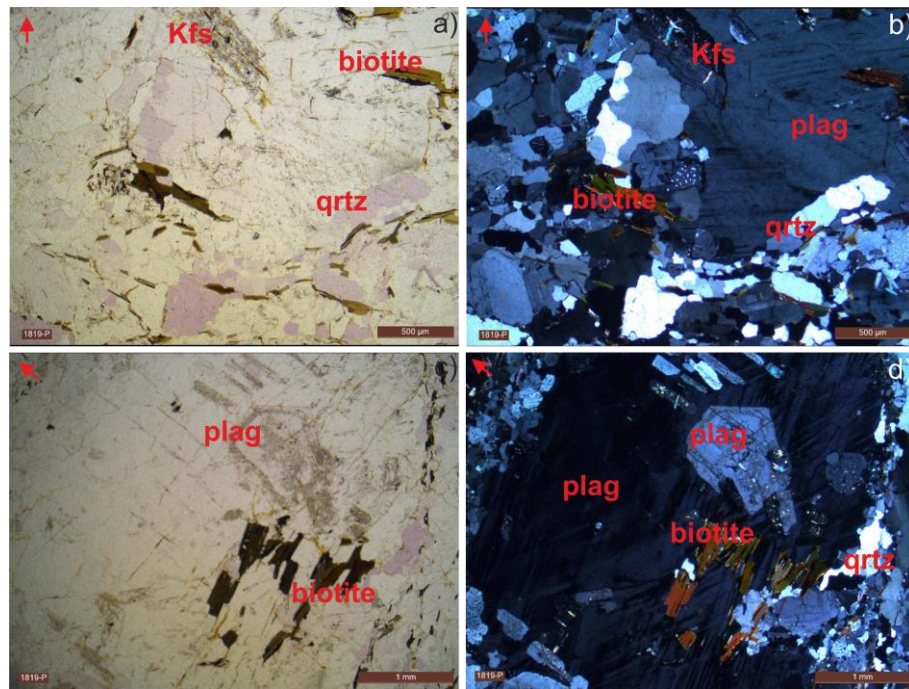


Figure 4.2. The South Uludağ Metagranite (sample 1819). a) and c) PPL images, b) and d) XPL images. (Kfs: alkali feldspar, plag: plagioclase, qrtz: quartz).

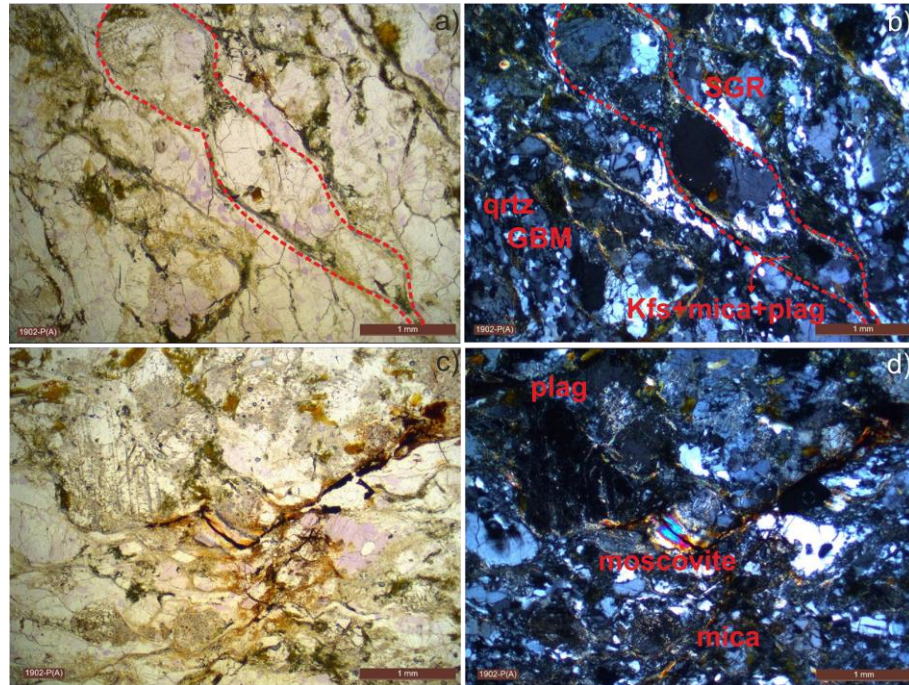


Figure 4.3. The South Uludağ Metagranite (sample 1902-P(A)). a) and c) PPL images, b) and d) XPL images. (GBM: grain boundary migration, Kfs: alkali feldspar, mica: mica, plag: plagioclase, SGR: sub-grain rotation, qrtz: quartz.).

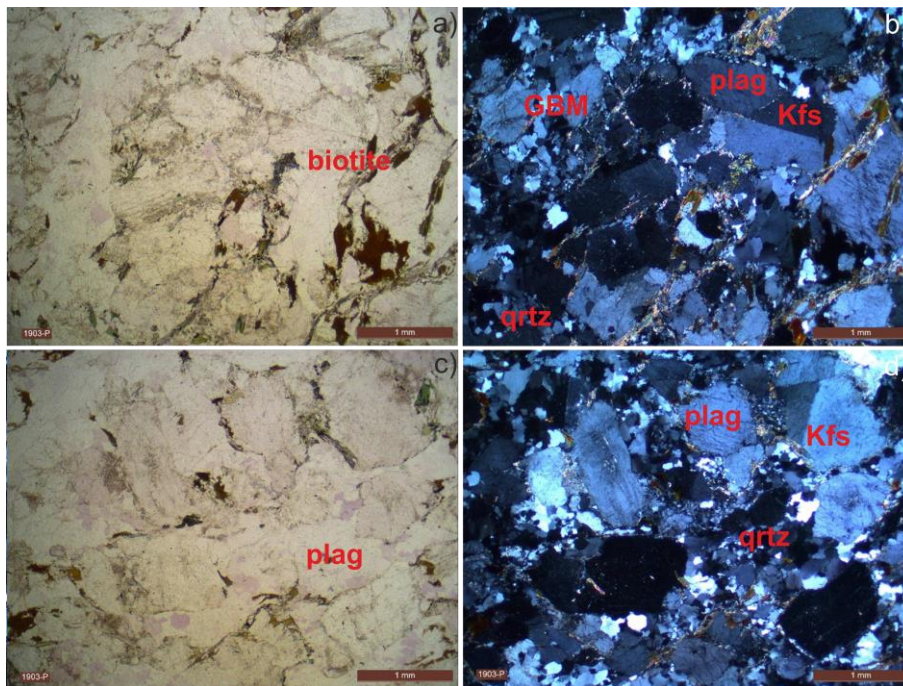


Figure 4.4. The South Uludağ metagranite (sample 1903). a) and c) PPL images, b) and d) XPL images. (GBM: grain boundary migration, Kfs: alkali feldspar, mica: mica, plag: plagioclase, qrtz: quartz.).

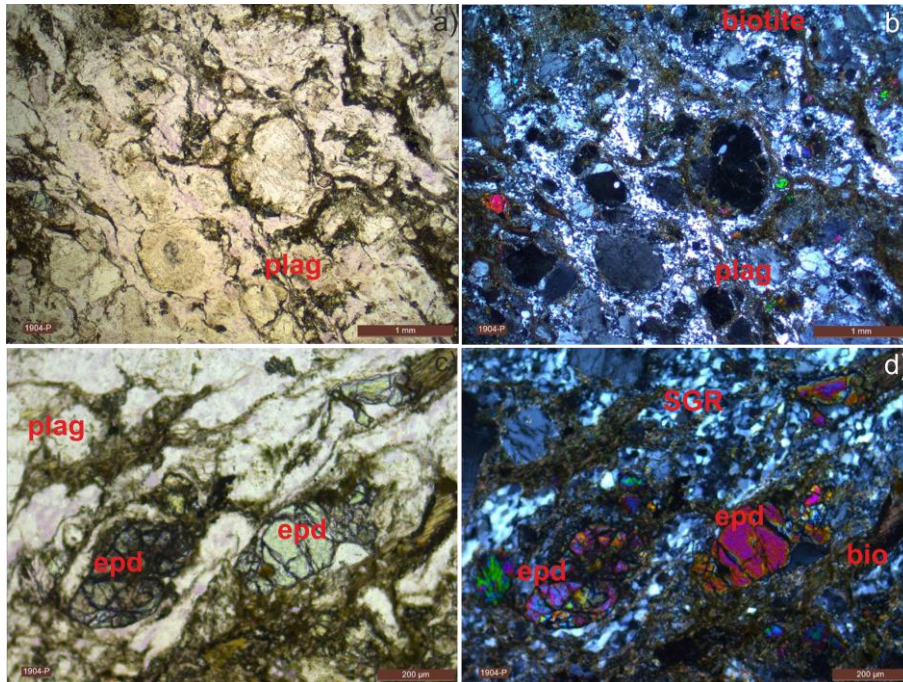


Figure 4.5. The South Uludağ Metagranite (sample 1904). a) and c) PPL images, b) and d) XPL images. (K-fs: alkali feldspar, bio: biotite, plag: plagioclase, qrtz: quartz, epd: epidote)

In the sample 1801 of a metagranite, myrmekite is observed as a fine-grained intergrowth of quartz and feldspar, often oriented parallel to each other (Figure 4.6c and d). Its colour and transparency are distinct under cross-polarised light of a petrographic microscope. Myrmekite is typically associated with other minerals, such as plagioclase, orthoclase, and possibly biotite (Figure 4.6a, b, c, d). Myrmekite is commonly found in granites and can persist through metamorphism, providing crucial information about the rock's history. Myrmekite suggests conditions during granite formation or metamorphism, often indicating sub-solid processes involving feldspar exsolution and magmatic or hydrothermal alteration. This texture is more noticeable in some granitic rocks and can be seen in Figure 4.6d, an example of a metagranite.

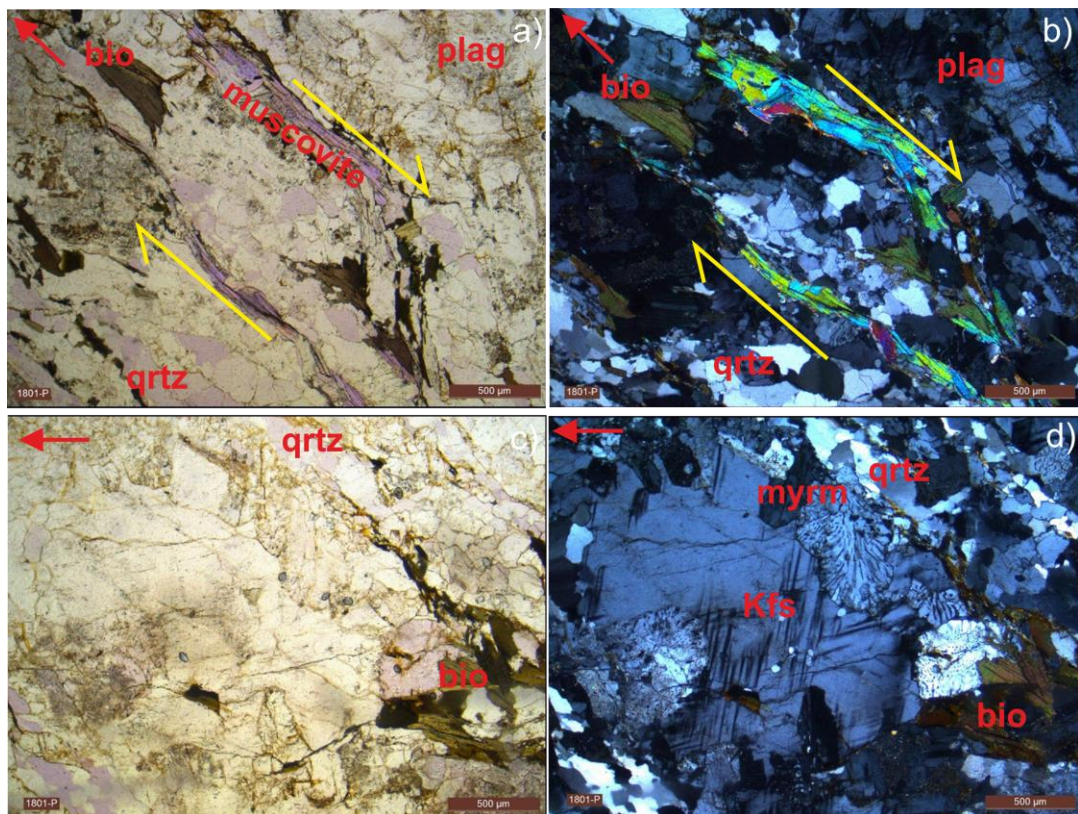


Figure 4.6. The South Uludağ Metagranite (sample 1801). a) and c) PPL images, b) and d) XPL images (red arrow: north direction, yellow arrow: shear direction, bio:biotite, K-fs: alkali feldspar, plag: plagioclase, qtz: quartz, myrm: myrmekite).

The thin section views in Figure 4.6, Figure 4.7 are from directional samples, red arrows show the North, and yellow arrows show the lineament for the minerals related to the tectonic stresses. Mica minerals, such as biotite or muscovite, exhibit directional lineation in metagranites, suggesting a structural fabric within the rock. This lineation is often associated with the alignment of minerals or the orientation of mineral grains in response to deformation during tectonic events or metamorphism (Figure 4.6 and Figure 4.7).

The directional lineation in mica minerals indicates that the rock has undergone deformation, possibly due to tectonic forces or regional metamorphism. The alignment of mica minerals along a particular direction suggests a preferred orientation of mineral grains, reflecting the rock's strain and deformation history (Figure 4.6 a-b and Figure 4.7c-d).

The lineation in mica minerals serves as a tectonic strain marker, providing information about the direction and magnitude of the forces that have affected the rock. It contributes to developing a foliated texture in the rock, a planar fabric resulting from the parallel arrangement of minerals. Lineated mica minerals indicate shear zones within the metagranite, zones of intense deformation characterised by rock movement along a specific plane.

The direction of the lineation offers insights into the direction of applied stress during deformation, which is valuable for reconstructing the region's geological history. The Uludağ metagranite samples mostly show E-W to NE-SW dominated mineral lineations (Figure 4.7, Figure 4.8), but some samples also show N-S directional mineral orientations (Figure 4.6).

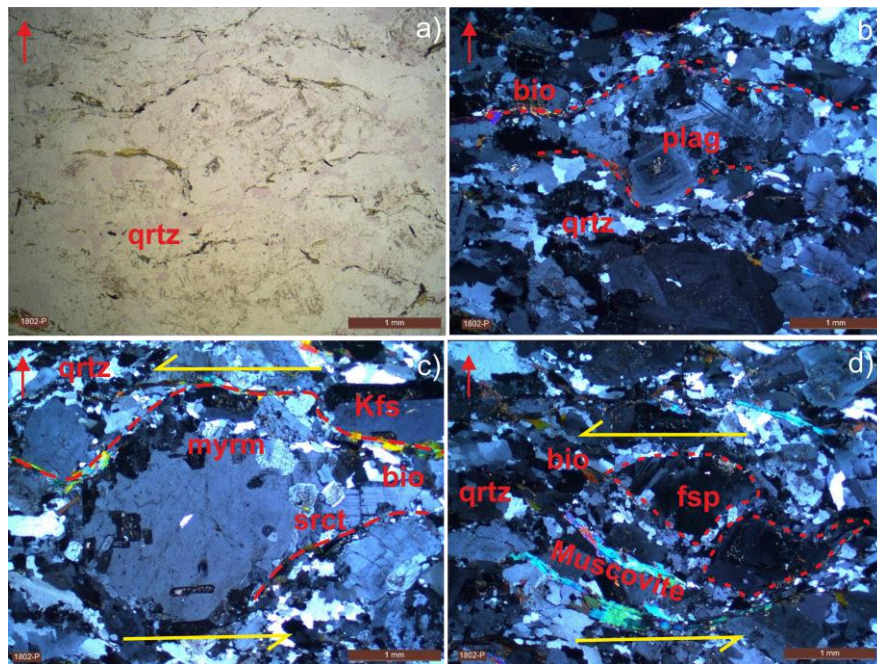


Figure 4.7. The South Uludağ Metagranite (sample 1802) a) and c) PPL images, b) and d) XPL images (red arrow: north direction, yellow arrow: shear direction, bio:bitite, K-fs: alkali feldspar, mica: mica, plag: plagioclase, fsp: feldspar, qrtz: quartz, myrm: myrmekite).

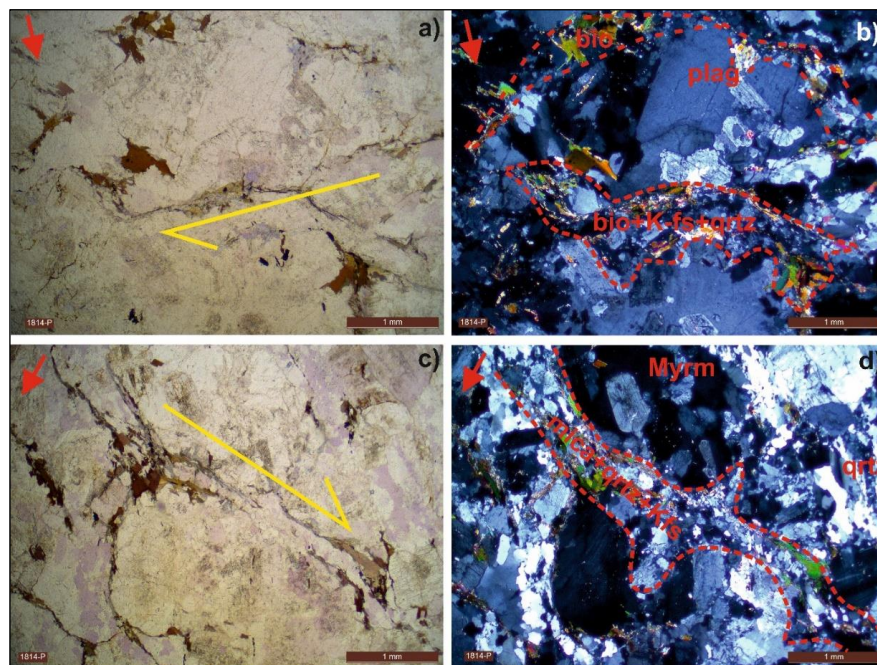


Figure 4.8. The South Uludağ Metagranite (sample 1814) a) and c) PPL images, b) and d) XPL images (red arrow: north direction, yellow arrow: shear direction, bio:bitite, K-fs: alkali feldspar, mica: mica, plag: plagioclase, qrtz: quartz, myrm: myrmekite).

Analysing thin sections of metagranite samples shows sericitisation (Figure 4.9), mineral change can be seen where plagioclase-feldspar minerals in Figure 4.9 a, b, c and d. When examining thin sections, replacement of primary minerals as plagioclase feldspar and/or orthoclase feldspar to sericite are noticed. The sericite grains in thin section slices of metagranite samples have a colour ranging from white to a pale grey because of their birefringence (Figure 4.9 b and d). When seen under cross-polarised light, sericite often displays a birefringence that ranges from low to moderate.

Sericitisation is a typical metagranite alteration process when plagioclase is transformed into sericite, typically with the development of albite and saussurite (Piaz and Lombardo, 1986). In addition, the metagranite might undergo sericite-chlorite alteration zones due to late magmatic-hydrothermal modifications (Luisier et al. 2021). The coexistence of Mg-rich sericite-chlorite schists close to metagranite provides further evidence for hydrothermal activity after the intrusion event (Vaughan-Hammon et al. 2021).

The metagranite samples with sericitisation include additional secondary minerals as quartz and muscovite (mica minerals) (Figure 4.9). The sericitisation is a process by which parent minerals, usually feldspars, are converted into a fine-grained white mica mineral known as sericite and numerous secondary minerals.

Studying the spatial connections between sericitisation minerals and other minerals in thin sections leads information on time and circumstances of sericitisation with other metamorphic or alteration processes in the rock's past. The occurrence of sericite in the thin sections of the metagranite suggests that there is hydrothermal alteration at relatively high temperatures and moderate pressures.

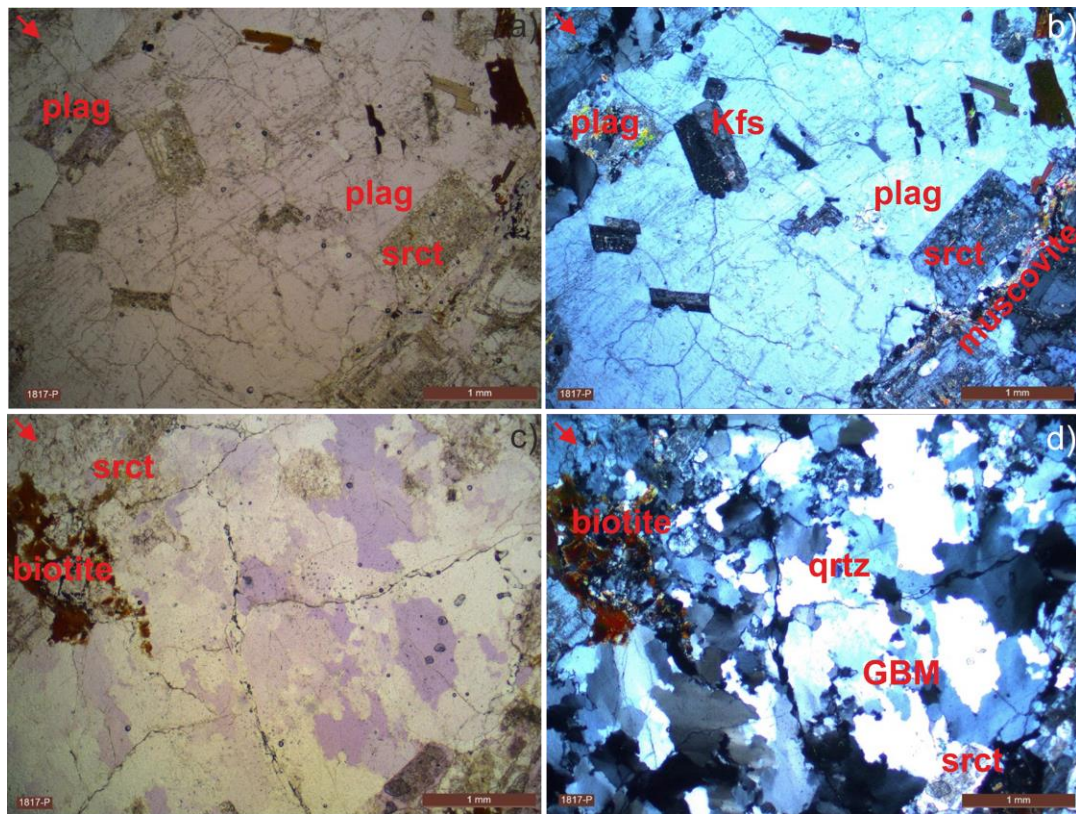


Figure 4.9. The South Uludağ Metagranite (sample 1817) a) and c) PPL images, b) and d) XPL images. (GBM: grain boundary migration, Kfs: alkali feldspar, mica: mica, plag: plagioclase, qtz: quartz, srct: sericitisation).

Presence of features as grain boundary migration (GBM) (Figure 4.9 c and d), sub-grain rotation (SGR) (Figure 4.10 b) and bulging dynamic recrystallisation (BLG) in thin sections reveals dynamic recrystallisation processes during deformation or metamorphism. These processes, which are triggered by stress, can lead to grain reorientation, recrystallisation, and the development of a new crystal lattice. Sub-grain rotation, a common mechanism during dynamic recrystallisation, involves rotating small crystallographically defined regions within a larger grain to achieve a lower energy state. Bulging dynamic recrystallisation occurs when grains undergo significant shape changes, often resulting in bulging or lobate grain boundaries. This process is part of dynamic recrystallisation to achieve a more stable state of minerals, where grains are continuously replaced by new grains with lower stored energy, indicating active deformation or metamorphism.

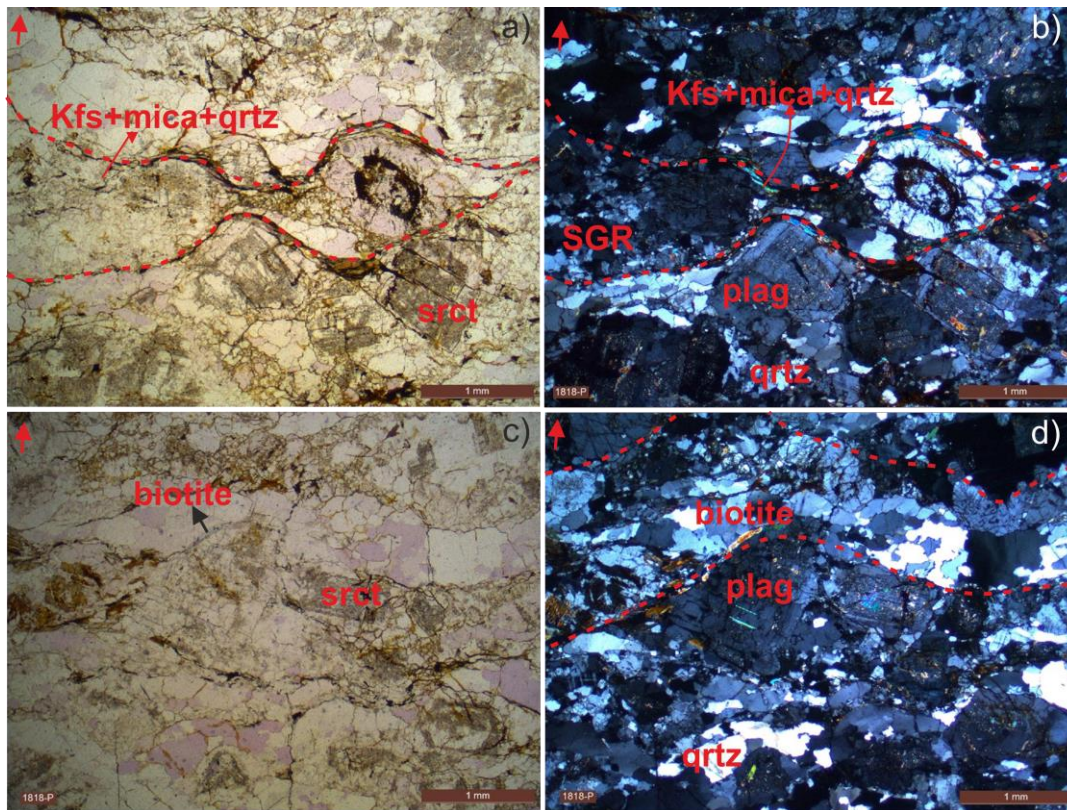


Figure 4.10. The South Uludağ Metagranite (sample 1818) a) and c) PPL images, b) and d) XPL images. (Kfs: alkali feldspar, mica: mica, plag: plagioclase, SGR: sub-grain rotation, qrtz: quartz.).

4.2.2 Uludağ Massif Gneisses

In the studied area, gneisses are the type of rock with distinct mineralogy, foliation, and texture. Their distinctive foliation is a well-developed parallel alignment of minerals into bands or layers, often prominent and visually striking. Gneiss typically exhibits alternating light and dark bands, reflecting variations in mineral composition. It is commonly found in quartz, feldspar, and mica, which contribute to the light and dark colouration in the bands. These bandings are quite visible in the thin sections. Amphibole or pyroxene may also be present in darker bands. Band intensity and thickness vary, with some gneisses having a pronounced colour difference while others may exhibit more subtle variations. Schistosity, a more pronounced planar fabric within the foliation, is often observed in higher

metamorphic grades. Mineral alignment is typically parallel to the foliation, seen in elongated minerals like quartz and platy minerals like mica (Figure 4.11 and Figure 4.12). Gneiss often shows signs of recrystallisation, indicating metamorphic changes, such as the development of new minerals and grain size and shape (Figure 4.11, Figure 4.12 d GBM and SGR).

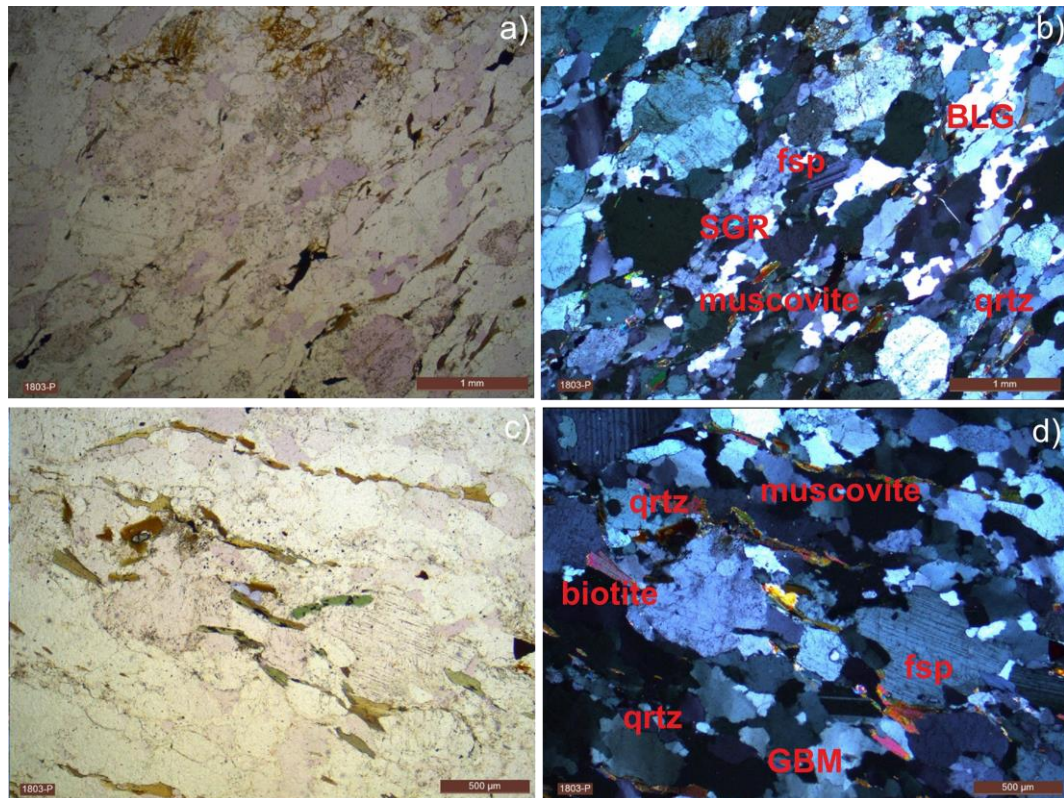


Figure 4.11. The Uludağ Massif Gneiss (sample 1803) a) and c) PPL images, b) and d) XPL images. (Kfs: alkali feldspar, mica: mica, qtz: quartz).

Porphyroblasts (Figure 4.11b, Figure 4.13, Figure 4.15, Figure 4.16, Figure 4.17 Figure 4.18, Figure 4.19, Figure 4.20) large crystals surrounded by a finer-grained matrix, may also be present in some gneisses. Migmatitic gneisses may show evidence of partial melting and veins, with light-coloured veins or patches within the darker matrix (Figure 4.11, Figure 4.14). All these features mentioned above provide a comprehensive understanding of the rock's mineralogical composition, texture, and the processes it has undergone during metamorphism.

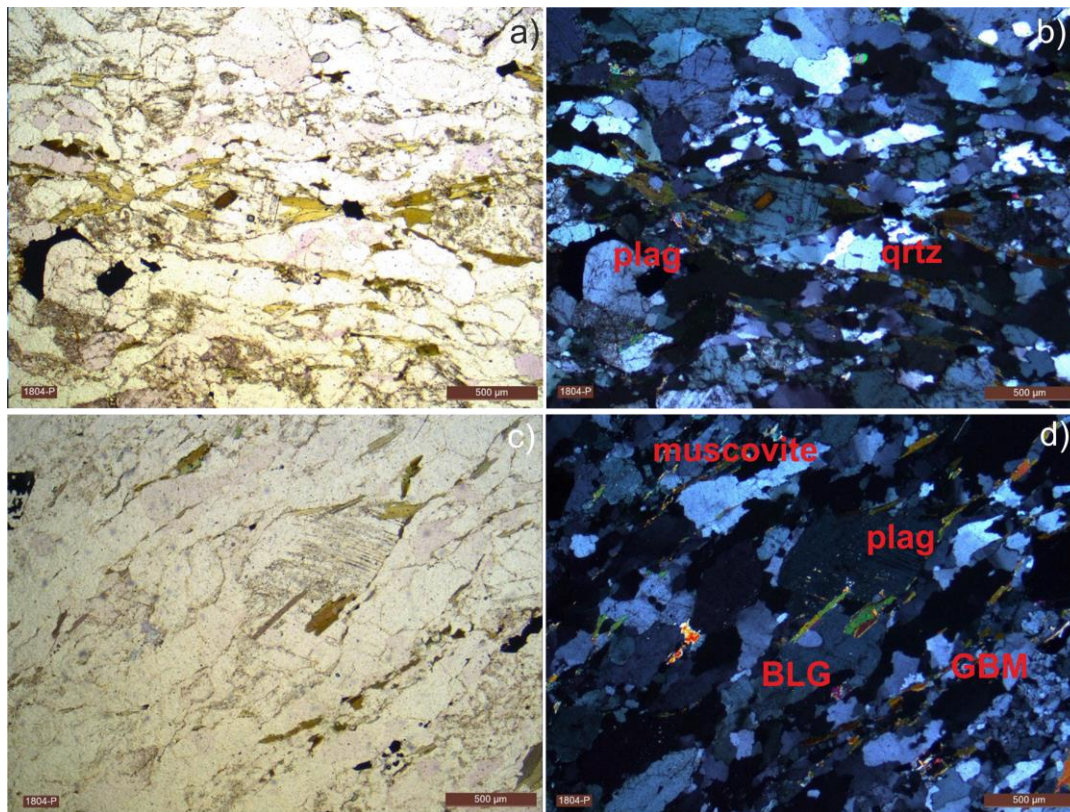


Figure 4.12. The Uludağ Massif Gneiss (sample 1804) a) and c) PPL images, b) and d) XPL images. (BLG: dynamic recrystallisation by bulging, GBM: grain boundary migration, mica: mica, plag: plagioclase, qtz: quartz).

Several mineral assemblages are layered or segregated during metamorphism, gneisses often have a banded or foliated structure. Banded and foliated structures are easily seen in the thin sections of the Uludağ gneisses. These banded and foliated structures are generally shown in red- or yellow-coloured dashed lines in the thin sections' photographs. Differential pressure and temperature conditions during metamorphism are common causes of this banding, which may range from thin to quite thick and intense. It is possible to see the foliation of gneisses in thin sections as the preferred orientation of tabular or elongated minerals, such as amphiboles or micas (from Figure 4.13 to Figure 4.19).

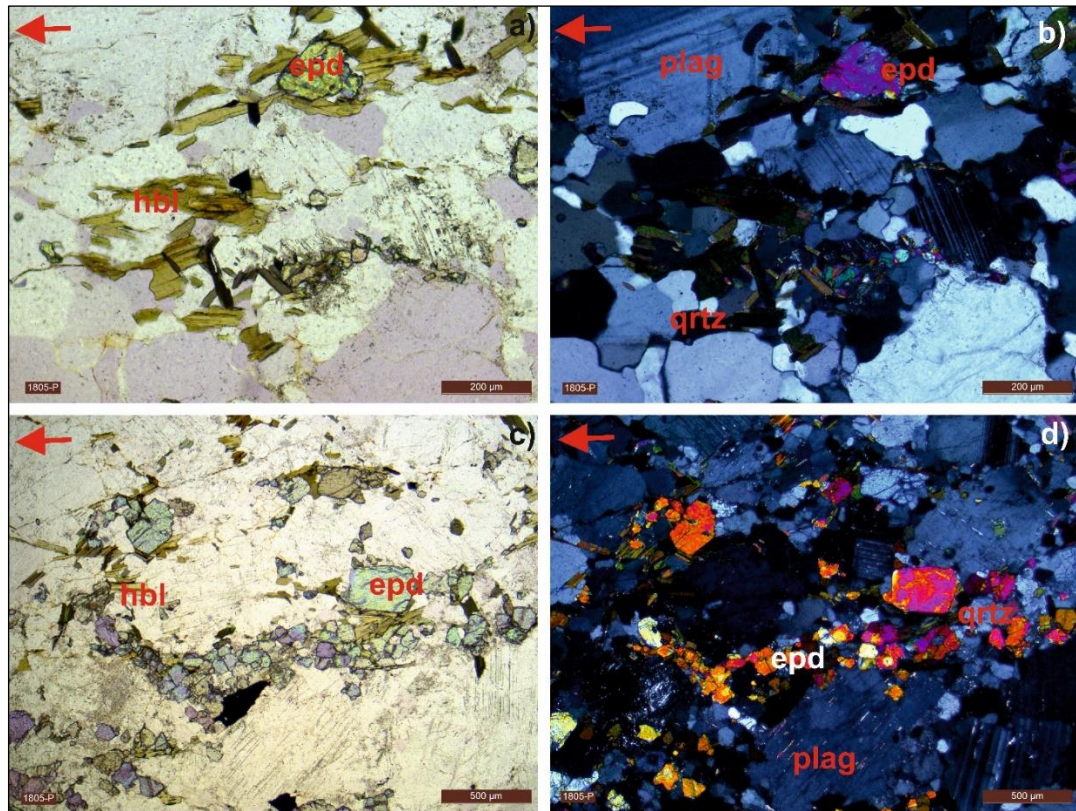


Figure 4.13. The Uludağ Massif Gneiss (sample 1805) a) and c) PPL images, b) and d) XPL images. (epd: epidote, hbl: hornblende, mica: mica, plag: plagioclase, qrtz: quartz).

The alignment of minerals in gneisses gives them their characteristic organised look and may provide valuable information about the direction and intensity of the metamorphic forces that affect the rock. In Figure 4.13, the direction of the metamorphic force is seen in the N-S direction. Also, all other oriented samples give us the N-S dominant metamorphic stress direction for the gneisses.

During the banded and foliated stress orientations layered in thin sections, minerals show grain rotations, shape changes and recrystallisation processes. These changes happened as a result of the metamorphic processes. One is SGR (sub-grain rotation) ((Figure 4.14).

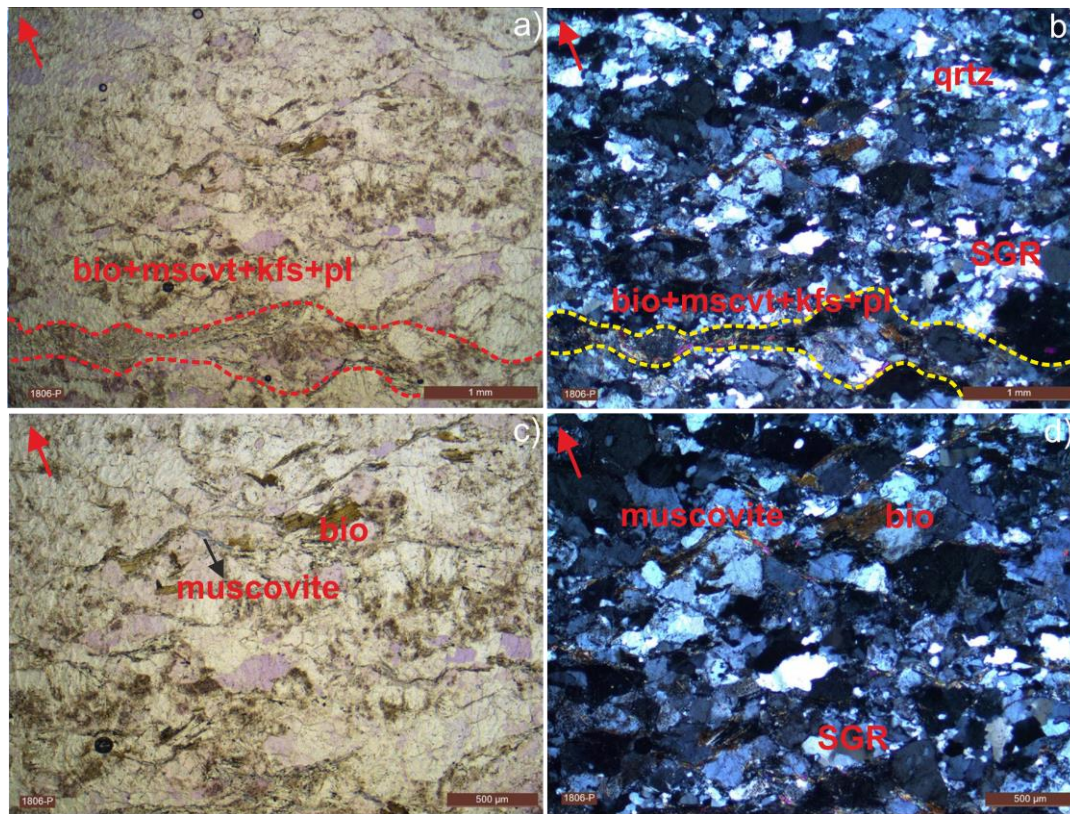


Figure 4.14. The Uludağ Massif Gneiss (sample 1806) a) and c) PPL images, b) and d) XPL images. (red arrow: north direction, bio: biotite, Kfs: alkali feldspar, msct: muscovite, qrtz: quartz, SGR: sub-grain rotation).

The phenomenon of grain boundary migration was associated with the occurrence of dynamic recrystallisation in the context of creep movements, as shown by Guillopé and Poirier (1979). Under certain "stress and temperature" circumstances, grain boundary migration (GBM) assist dynamic recrystallisation (BLG), resulting in fast movement of grain boundaries. The microstructural and metamorphic development of high-pressure granitic gneisses was linked to several deformation modes, such as diffusion creep dominated by grain boundary sliding or rotation (SGR) (Chopin et al. 2012).

The microstructural development of gneisses and metagranites in thin sections is influenced by grain rotation, especially sub-grain rotation (SGR) (Figure 4.15). Processes such as continuous dynamic recrystallisation nucleation may be activated when the sub-grain rotation goes beyond a misorientation angle of 10-15° (Wang et

al. 2014). Within a narrow temperature range, microstructures of granitic rocks display characteristics like sub-grain rotation, making this process essential for their deformation (Gibbons, 1983).

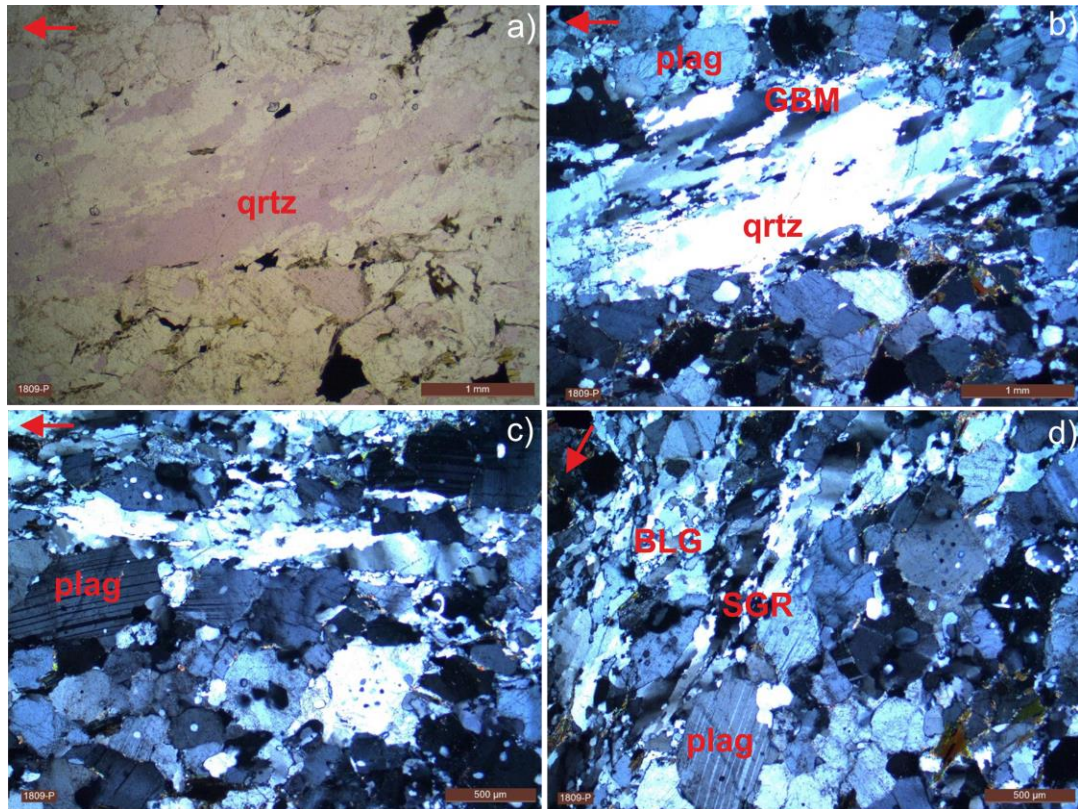


Figure 4.15. The Uludağ Massif Gneiss (sample 1809) a) PPL images, b), c) and d) XPL images. (red arrow: north direction, BLG: dynamic recrystallisation by bulging, GBM: grain boundary migration, plag: plagioclase, qtz: quartz, SGR: sub-grain rotation.).

As a well-known phenomenon in thin sections, grain rotation controlled by grain boundary dislocations has been discovered in high-temperature deformation and recrystallisation (Garlick & Gromet, 2004). Fernández et al. (2016) state that gneisses undergo grain rotation and deformation when thin sections reveal sub-grain development, deformation lamellae, and undulose extinction. Based on Robertson et al. (2019), mylonitic gneisses have microstructural characteristics that point to dynamic recrystallisation due to grain boundary migration. This process

produces equivalent to sub-equant grains with little internal strain and a weak shape preferred orientation (Figure 4.15).

Dynamic recrystallisation in the thin sections of gneiss causes new grains to form by expanding the original grain boundaries (Figure 4.12, Figure 4.15). These are called dynamic recrystallisation by bulging (BLG). Several deforming materials have shown this process, suggesting that it plays a significant role in developing microstructure and refining grains (Grujić et al. 2011; Kim et al. 2020). The fact that quartz mylonites exhibit bulging recrystallisation, sub-grain rotation recrystallisation, and grain boundary migration recrystallisation (Fügenschuh et al. 2004; Grujić et al. 2011) further highlights the significance of bulging in dynamic recrystallisation processes.

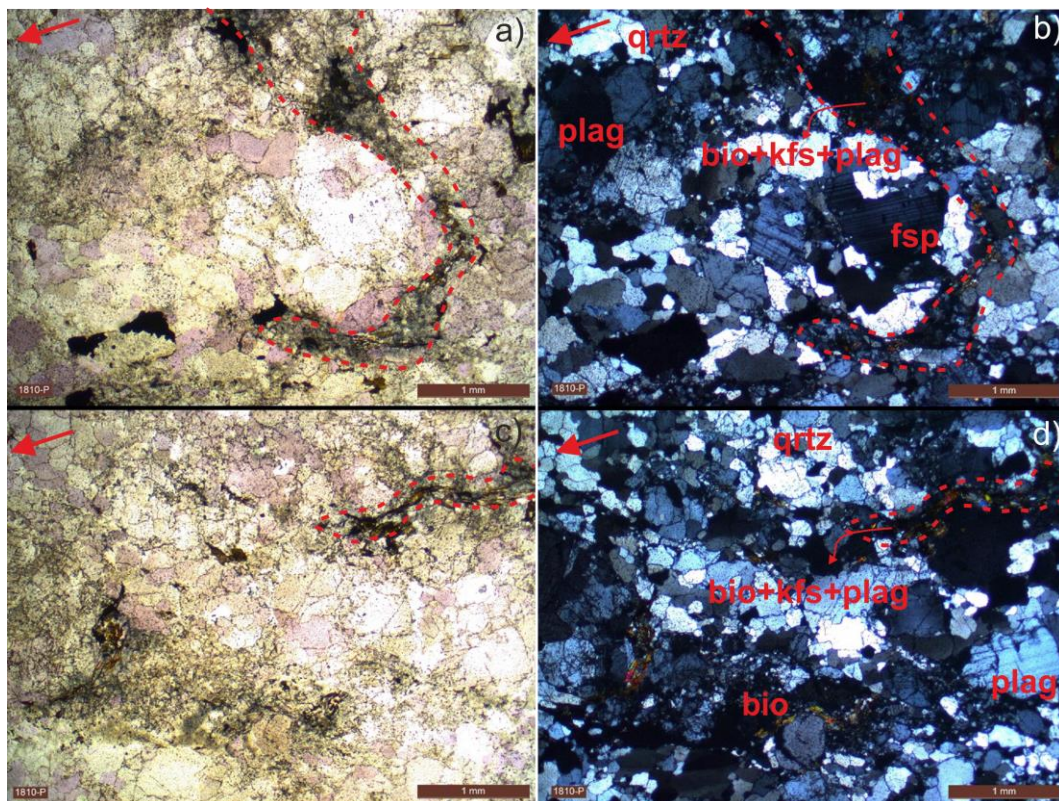


Figure 4.16. The Uludağ Massif Gneiss (sample 1810) a) and c) PPL images, b) and d) XPL images. (red arrow: north direction, bio: biotite, fsp: feldspar, kfs: alkali feldspar, plag: plagioclase, qtz: quartz).

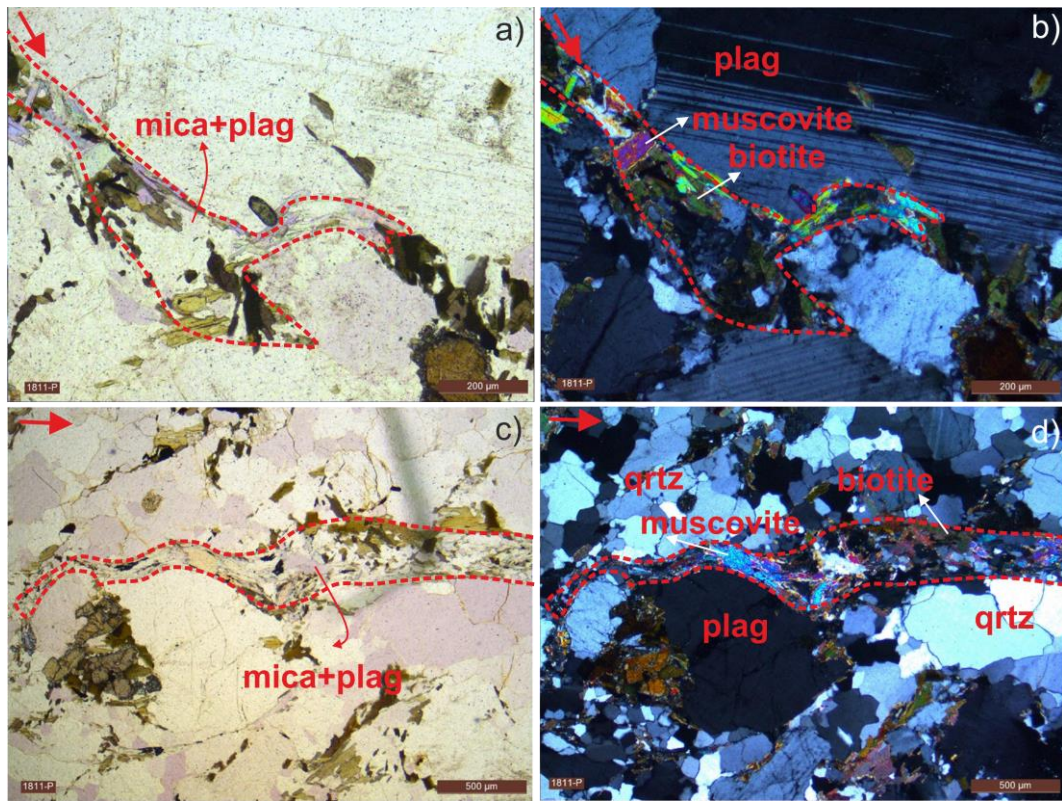


Figure 4.17. The Uludağ Massif Gneiss (sample 1811) a) and c) PPL images, b) and d) XPL images (red arrow: north direction, mica: mica, plag: plagioclase, qrtz: quartz).

Corona texture, a microstructural feature with concentrically arranged mineral zones surrounding a core mineral (Figure 4.18c, d), often associated with metamorphic or metasomatic events is present in the studied gneiss samples. It suggests metasomatism or metamorphism, which could involve the introduction of new minerals or changes in mineral composition through fluid interaction. The corona structure also indicates sequential mineral replacement, with the innermost minerals representing the original composition and the outer zones representing successive mineral reactions. The structure records the rock's reaction history, with different minerals forming at different stages, reflecting temperature, pressure, or fluid composition changes. The specific minerals forming the corona and their sequence can offer insights into the pressure and temperature conditions under which the alteration occurred. A corona structure suggests the infiltration of fluids carrying elements necessary for mineral alteration, possibly related to hydrothermal activity or metasomatic events (Figure 4.18c and d). The core mineral, often called

the "core mineral" or "relic", represents the original mineral subject to alteration. The minerals forming the corona can vary and may include minerals like chlorite, epidote, amphibole, or other alteration products. In migmatitic gneisses, the corona texture may be associated with partial melting events, with the outer zones representing minerals that crystallised during the migmatization process.

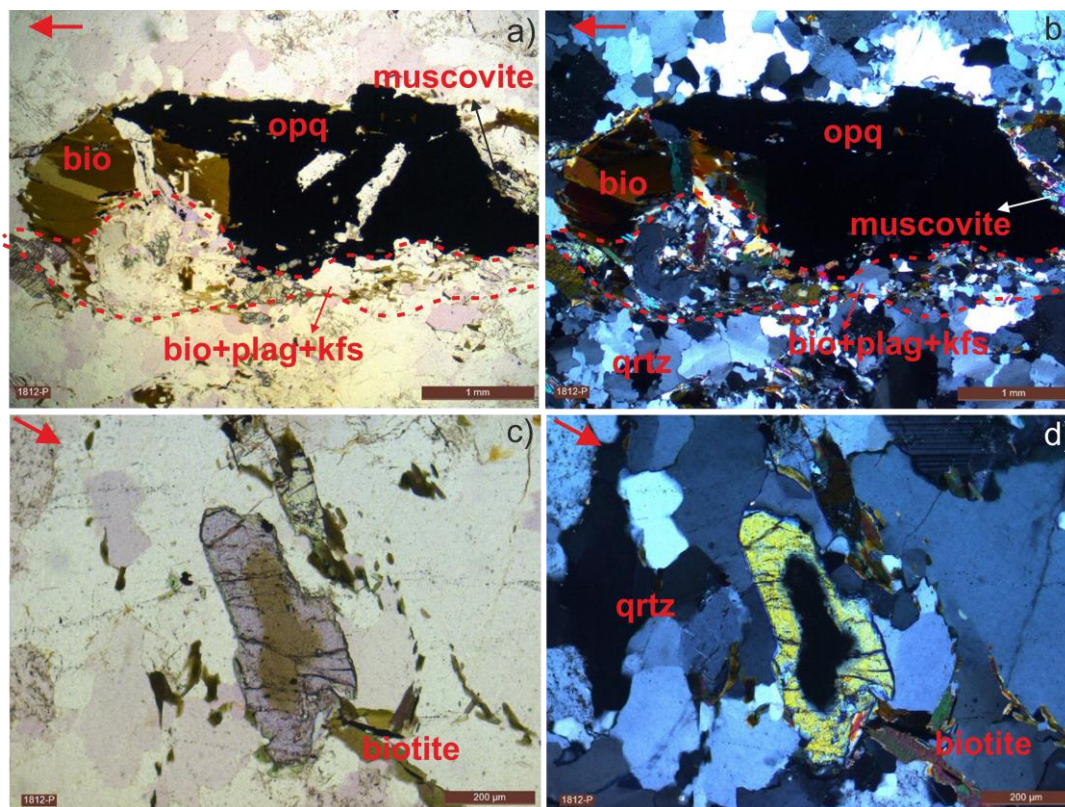


Figure 4.18. The Uludağ Massif Gneiss sample (1812) a) and c) PPL images, b) and d) XPL images. (bio: biotite, hbl: hornblende, kfs: alkali feldspar, plag: plagioclase, qrtz: quartz, opq: opaque).

Orientation of mica minerals with a typical example of kink bands is present in gneiss samples (Figure 4.19). Kink bands of mica mineral in gneisses are the significant characteristics that show deformation and strain inside the rock. According to Bozkurt and Park (1997), kink bands are often seen in biotite and other minerals in the intermediate to upper greenschist facies. These kink bands developed from earlier, single kink bands due to mica reorientation and pressure

solution of quartz (Kirker & McClelland, 1997). During high-stress deformation, kink bands in mica-rich gneisses help with grain nucleation and change the crystallographic preferred orientations (Fan et al. 2021).

Additionally, kink bands in mica crystals are linked to plastic deformation and dynamic recrystallisation. Along with characteristics such as undulose extinction, dynamic recrystallisation, and crystallographic preferred orientations, kink bands were seen in thin sections of gneisses (Harigane et al. 2011). Kink bands in mica minerals show how the minerals have been deformed and how the gneissic rocks have responded to stress.

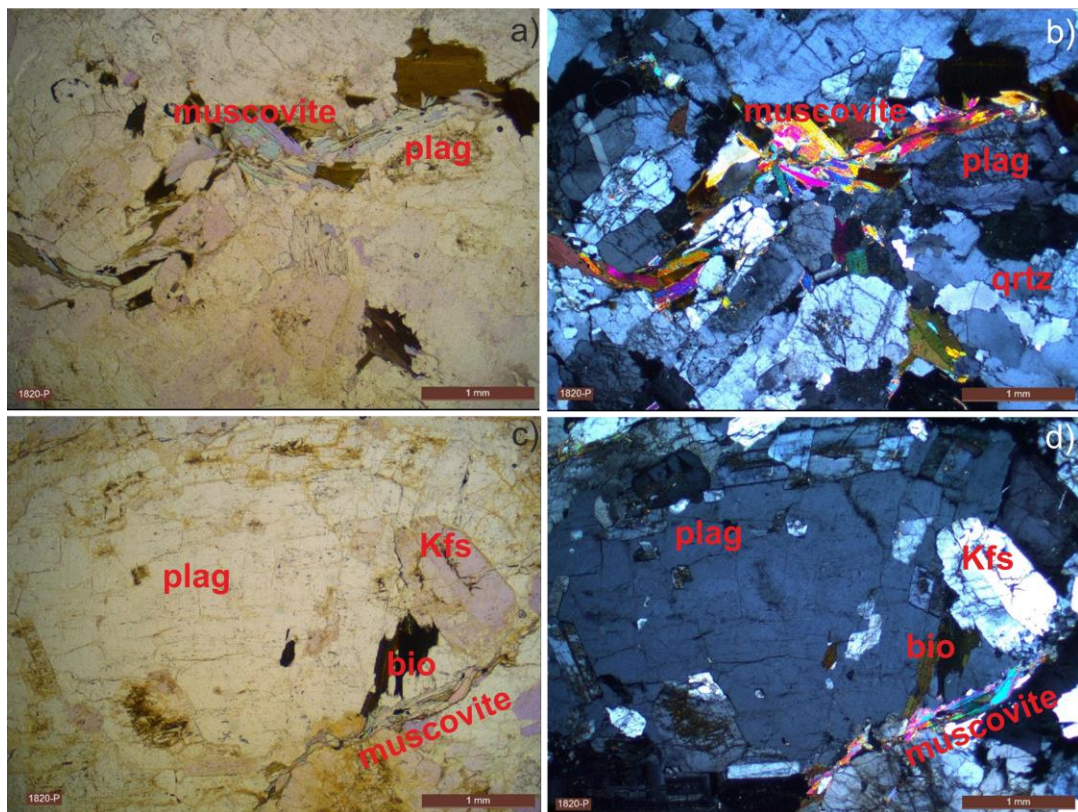


Figure 4.19. The Uludağ Massif Gneiss (sample 1820) a) and c) PPL images, b) and d) XPL images. (Kfs: alkali feldspar, plag: plagioclase, qztz: quartz).

The presence of mineral segregation in gneiss thin sections has a significant role in determining the overall texture of the rock. Separating minerals such as feldspar, quartz, and mica form unique patterns and structures within the gneiss,

emphasising the diverse composition of minerals and the rock's history of metamorphism (Luc Leroy, 2017). The size and location of these mineral segregations vary, affecting the gneiss's overall look and appearance.

As seen in Figure 4.20, a significant occurrence of plagioclase is present in the gneiss that reflect a temperature-related metamorphism, and heat from the environmental/host rock is most likely around 400 °C. The assemblage of these minerals exhibits significant changes in mineralogical composition at temperatures ranging from 300-400°C, although the alterations seen at temperatures over 400°C are comparatively less noticeable (Luc Leroy, 2017).

General features of plagioclase minerals in Figure 4.20 show that gneiss 1902P(B) had.

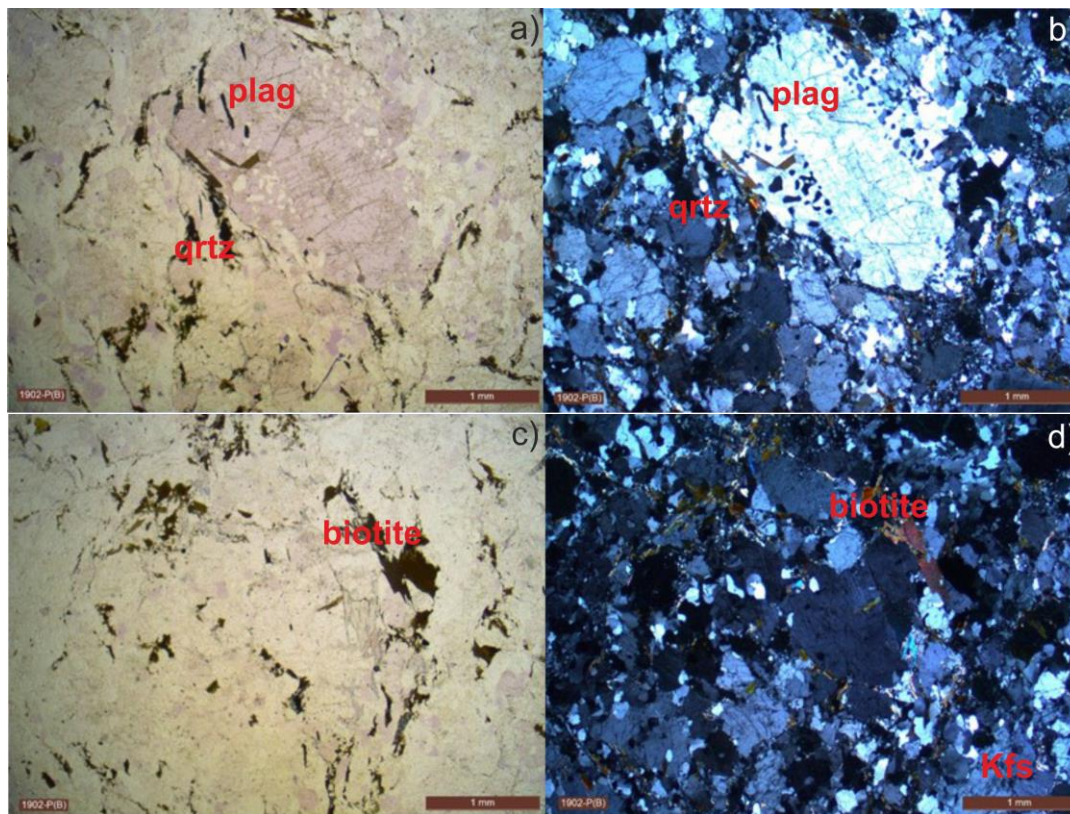


Figure 4.20. The Uludağ Massif Gneiss (sample 1902 P(B)). a) and c) PPL images, b) and d) XPL images. (Kfs: alkali feldspar, mica: mica, plag: plagioclase, qtz: quartz).

4.2.3 Uludağ Granites

4.2.3.1 Central Uludağ Granites

The Central Uludağ Granites mostly comprise distinctive minerals as quartz, feldspar (specifically plagioclase and orthoclase), and mica (biotite or muscovite). Additional minerals, such as amphibole, pyroxene, or oxides, may also exist. It is coarse-grained with interlocking arrangement of sizable crystals. Intergrown quartz and feldspar grains are responsible for the granular texture.

The granite often exhibits heterogeneous distribution in its mineral content and crystal size (Figure 4.21 to Figure 4.27). Pegmatitic zones are characterised by the presence of coarse to too coarse crystals, particularly of feldspar and quartz (Figure 4.21). Small, fine-grained regions, particularly along the edges, are also seen.

Alkali feldspar characterised by the presence of exsolved lamellae of sodium-rich and potassium-rich feldspar, can be seen (Figure 4.22).

Muscovite and biotite are two micas most often seen in thin layers of the granite (Figure 4.23). Biotite crystals appear black or dark brown due to high iron content. Thin elastic sheets of biotite's signature brown colour and intense pleochroism under crossed polarising light are produced by the mineral's flawless basal cleavage (Raslan et al. 2010). Muscovite with transparent, colourless, or light flakes appears (Figure 4.24). Its normal cleavage orientation is just one way, making it easy to separate the thin, flexible sheets produced. Mica in granite thin sections may show a lot of character under the microscope, including inclusions, zoning, and modification (Figure 4.25). These characteristics shed light on the processes and events that have shaped the granite rock's mica mineral composition and development across geological time.

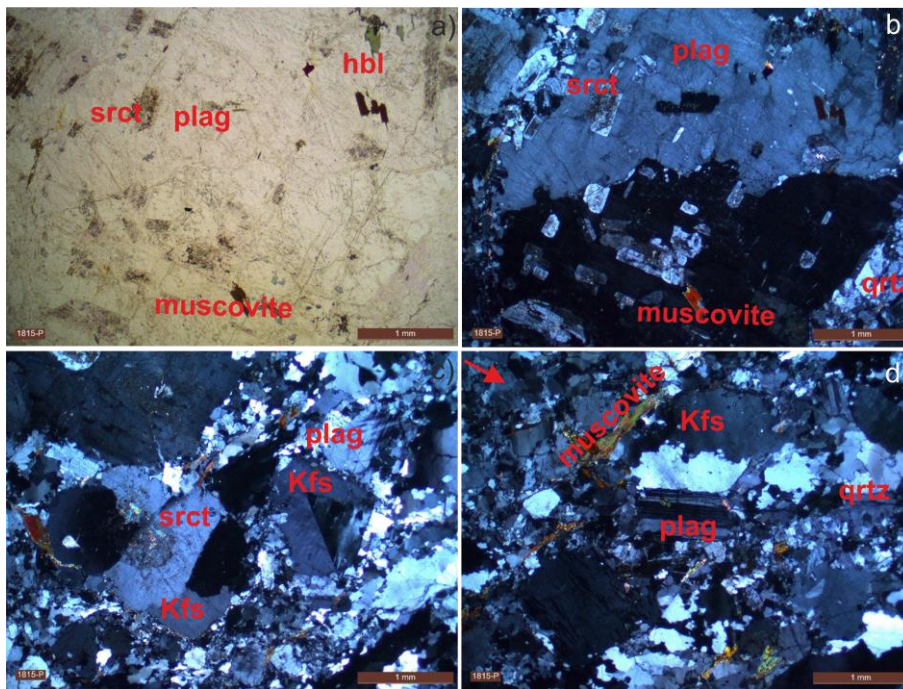


Figure 4.21. The Central Uludağ Granite (sample 1815). a) PPL images, b), c) and d) XPL images. (Kfs: alkali feldspar, srct: sericitisation, plag: plagioclase, qrtz: quartz).

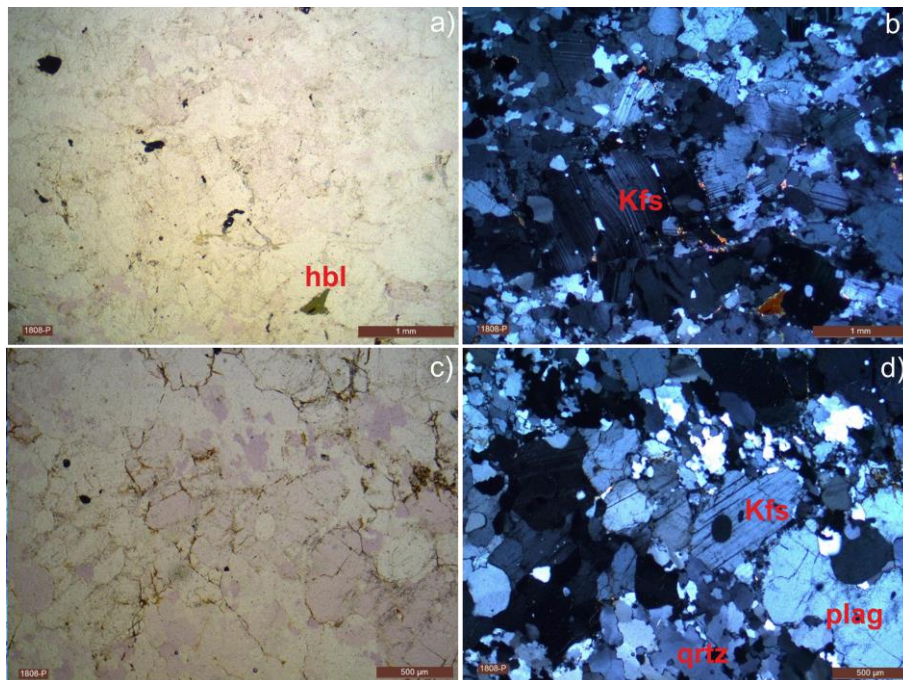


Figure 4.22. The Central Uludağ Granite (sample 1808) a) and c) PPL images, b) and d) XPL images (hbl: hornblende, Kfs: alkali feldspar, plag: plagioclase, qrtz: quartz).

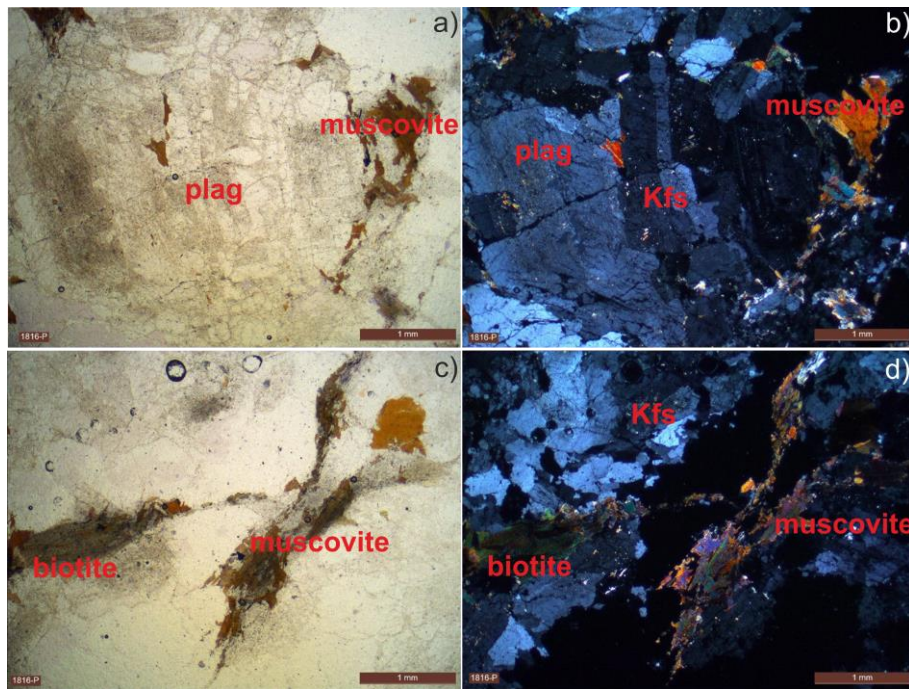


Figure 4.23. The Central Uludağ Granite (sample 1816)a) and c) PPL images, b) and d) XPL images (Kfs: alkali feldspar, plag: plagioclase).

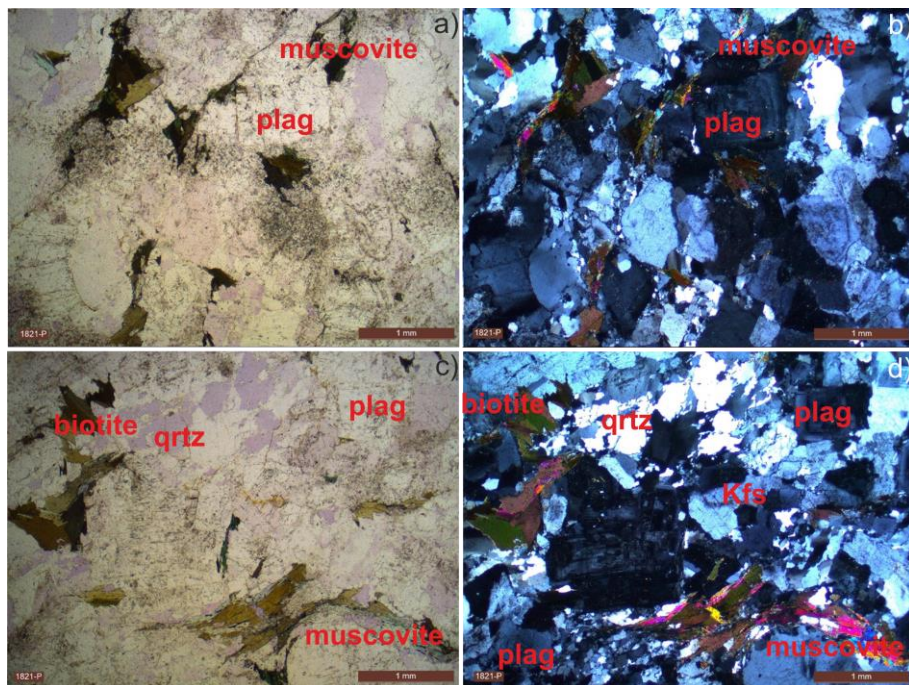


Figure 4.24. The Central Uludağ Granite (sample 1821)a) and c) PPL images, b) and d) XPL images. (Kfs: alkali feldspar, mica: mica, plag: plagioclase, qtz: quartz).

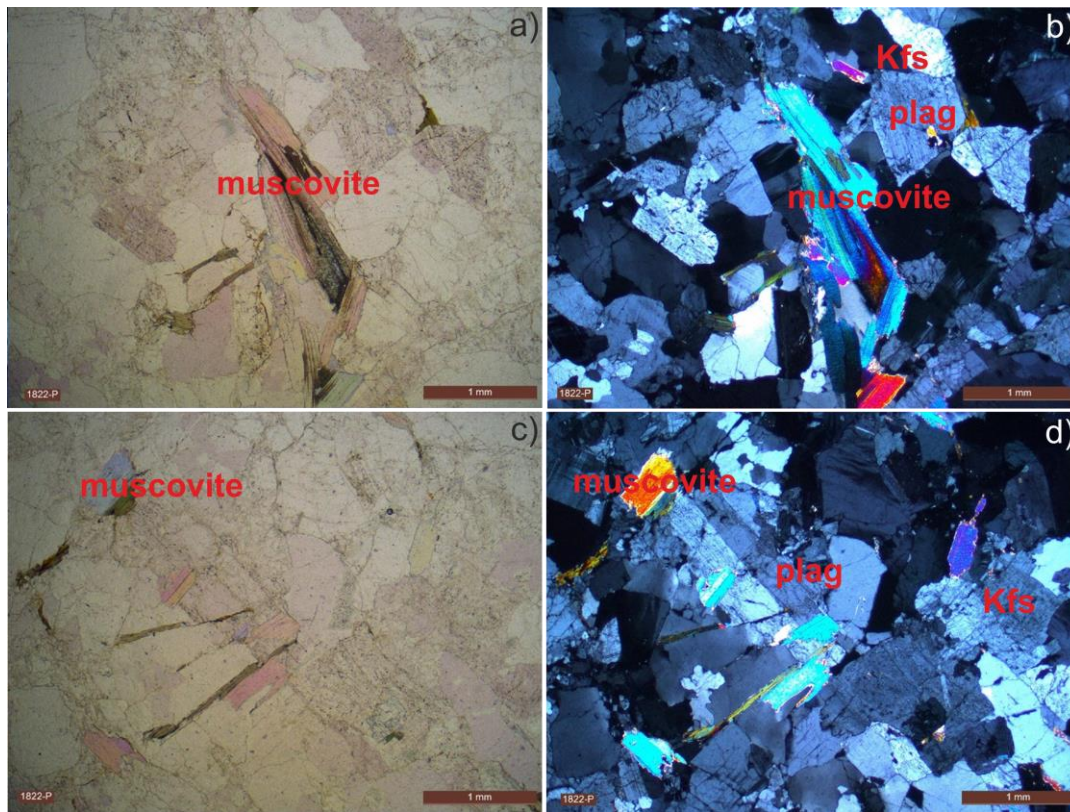


Figure 4.25. The Central Uludağ Granite (sample 1822) a) and c) PPL images, b) and d) XPL images. (Kfs: alkali feldspar, mica: mica, plag: plagioclase).

4.2.3.2 Kapıdağ Granites

The Kapıdağ Granite composing of biotite, hornblende, quartz, alkali feldspar, and plagioclase is coarse grained (Figure 4.26).

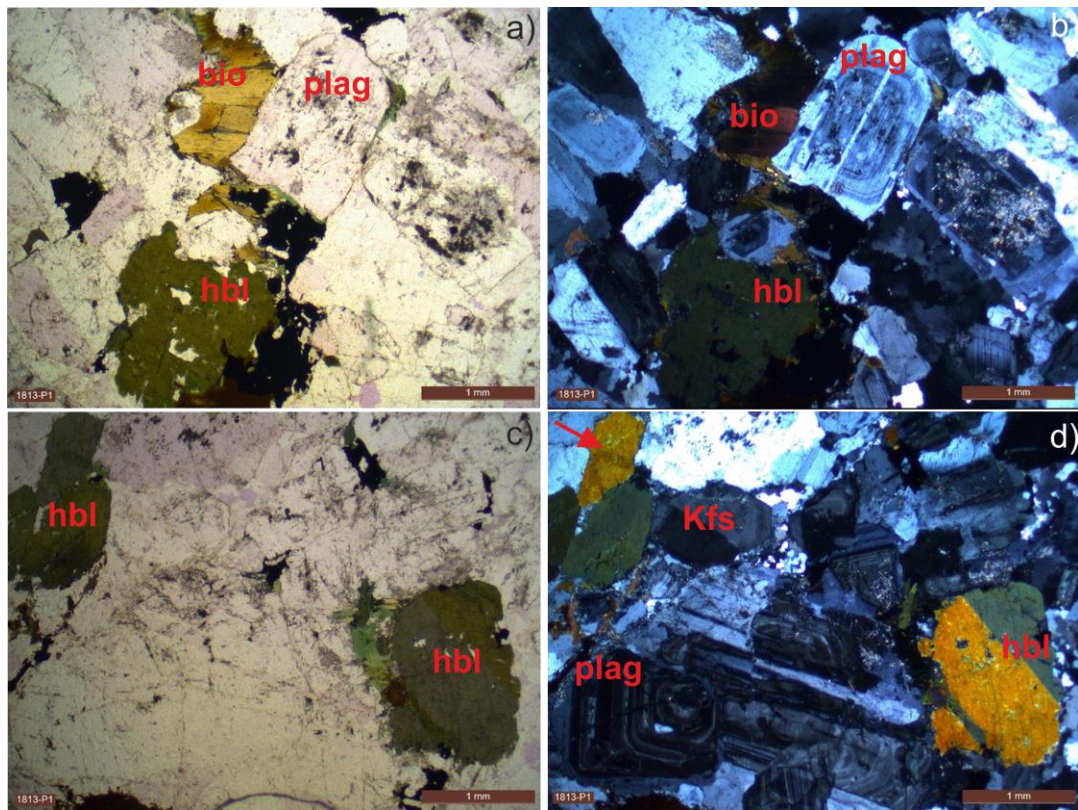


Figure 4.26. The Kapıdağ Granite (sample 1813-(P1)) a) and c) PPL images, b) and d) XPL images (hbl: hornblende, Kfs: alkali feldspar, bio: biotite, plag: plagioclase, qrtz: quartz).

Sericitisation of plagioclase is a common alteration process affecting the Kapıdağ Granite (Figure 4.27). The process is driven by the interaction of the rock with hydrothermal fluids, particularly those rich in water and certain chemical constituents.

The formation environment is commonly associated with epizonal (shallow-depth) and mesozonal (moderate-depth) hydrothermal environments, where fluid circulation and alteration are prevalent. The tectonic setting, including active faults or shear zones, can influence the occurrence of sericitisation.

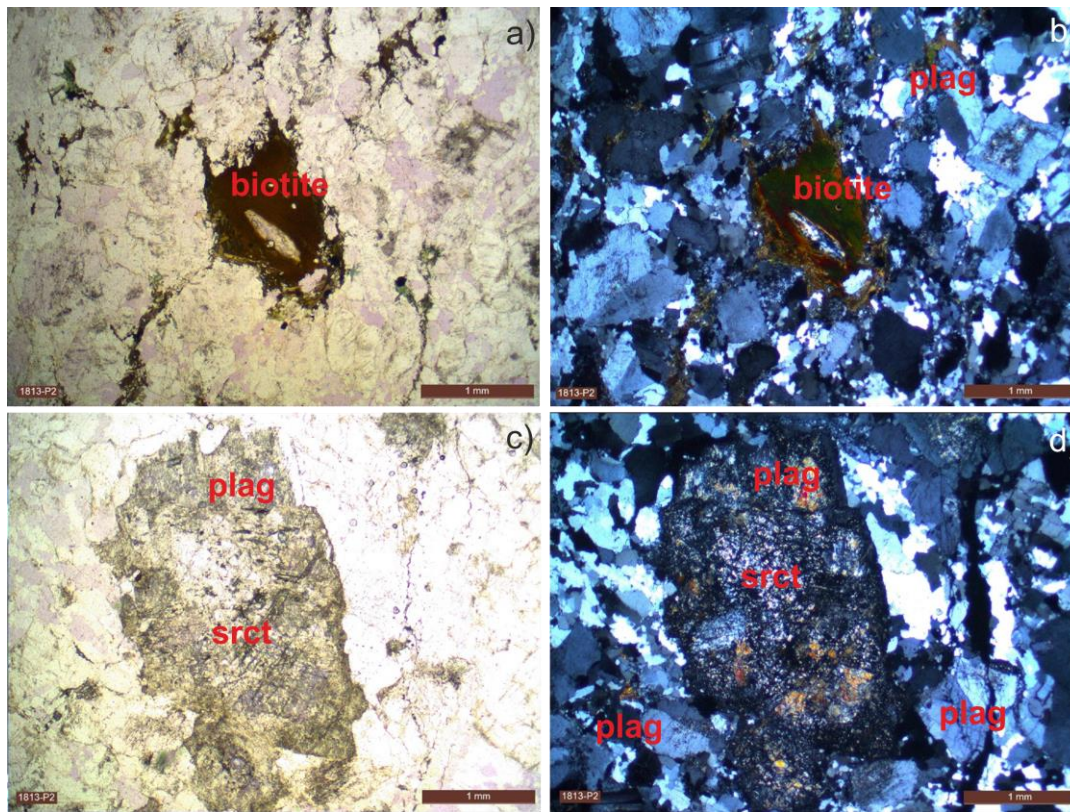


Figure 4.27. The Kapıdağ Granite (sample 1813-(P2)) a) and c) PPL images, b) and d) XPL images. (hbl: hornblende, kfs: alkali feldspar, mica: mica, plag: plagioclase, qrzt: quartz).

4.2.4 The Sazak Formation Metabasalt

Metabasalts have plagioclase, pyroxene (clinopyroxene), as primary minerals. Metamorphic minerals are chlorite, epidote, and actinolite or hornblende. The overall greenish colour of metabasalts is dominated by green minerals like chlorite, epidote, pyroxene, and amphibole (Figure 4.28). Their original texture is porphyritic, with large crystals embedded in a finer-grained matrix (Figure 4.28). Metabasalts exhibit varying grain sizes and foliation, with higher-grade metabasites showing foliated textures indicating directional pressure during metamorphism.

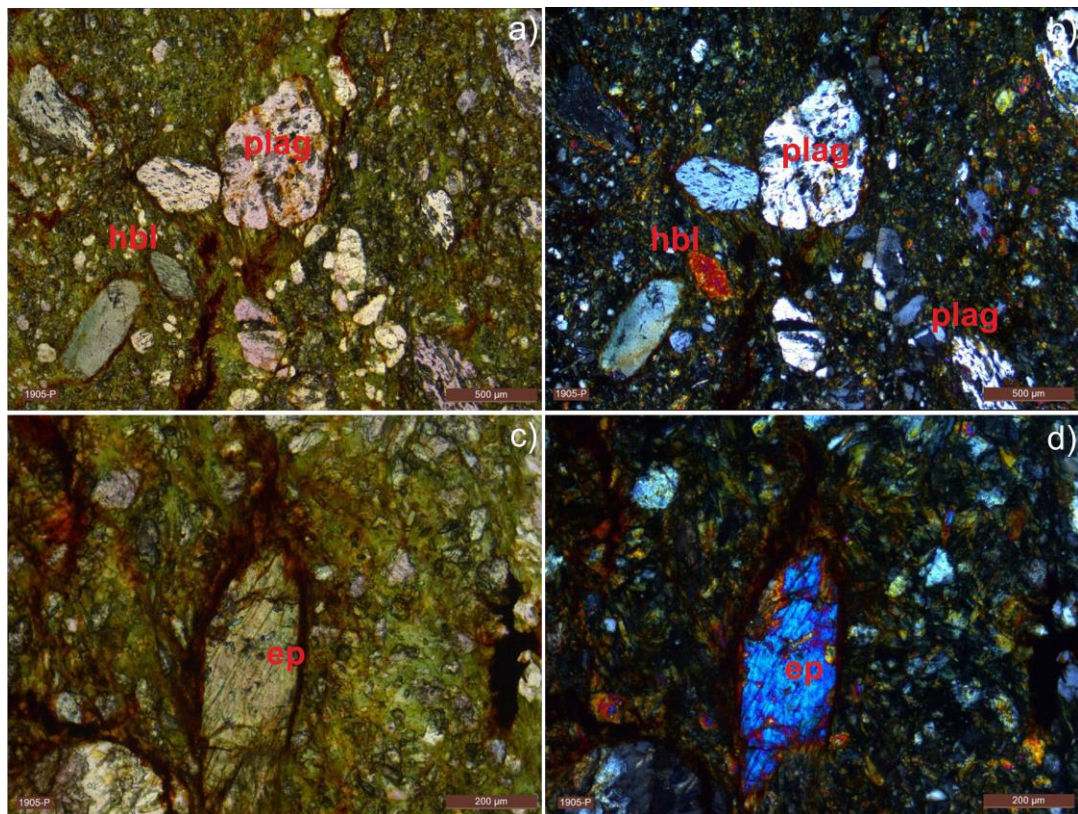


Figure 4.28. The Sazak Formation Metabasalt (sample 1905) a) and c) PPL images, b) and d) XPL images (plag: plagioclase, hbl: hornblende, ep: epidote).

4.3 Implications by Petrographic Interpretation

Detailed interpretation of some of the thin section samples can be seen in this section. Examining thin sections can be seen from Figure 4.29 to Figure 4.42.

Mica minerals, such as biotite or muscovite, exhibit directional lineation in metagranites, suggesting a structural fabric within the rock. This lineation is often associated with the alignment of minerals or the orientation of mineral grains in response to deformation during tectonic events or metamorphism. The directional lineation in mica minerals indicates that the rock has undergone deformation, possibly due to tectonic forces or regional metamorphism. The alignment of mica minerals along a particular direction suggests a preferred orientation of mineral grains, reflecting the rock's strain and deformation history. Figure 4.29 shows

lepidoblastic muscovite (mica) and granoblastic quartz layers in sample 1801 from the Uludağ Metagranites reflecting N/NE-S/SW deformation stress.

Figure 4.29 shows also sericitisation. The main reasons for sericitisation include hydrothermal alteration, where water-rich fluids infiltrate the rock, containing dissolved ions and elements that facilitate mineral alteration. Sericitisation typically occurs under lower to moderate temperature conditions and moderate pressures. Aluminous solutions in hydrothermal fluids favour sericitisation, as they can be enriched in aluminium ions that participate in alteration reactions. The reaction mechanism often involves potassium (K) and aluminium (Al) exchange, leading to the formation of sericite. Sericitisation is often part of a broader alteration assemblage that may include chlorite, epidote, and carbonate minerals.

Large hornblende and plagioclase minerals in granite can have significant geological implications, indicating specific processes or conditions during rock formation. These minerals may exhibit a pegmatitic texture, characteristic of coarse-grained igneous rocks formed from the slow cooling of water-rich magma. The large size of these crystals may suggest that they crystallised during a late stage of the granite's formation under specific conditions. Hydrothermal processes can also influence the size of crystals, as introducing fluids rich in specific elements can lead to the growth of large crystals. Enriching specific elements in the magma can influence the size of crystals, such as iron and magnesium. Large crystals may also be associated with migmatic features, indicating partial melting and subsequent crystallisation. The outer margins of a granite intrusion may cool more rapidly than the interior, forming finer-grained zones. The size of minerals can also be influenced by the dynamics of the intrusion itself, as slow cooling and crystallisation in certain parts of the granite may lead to the growth of larger crystals

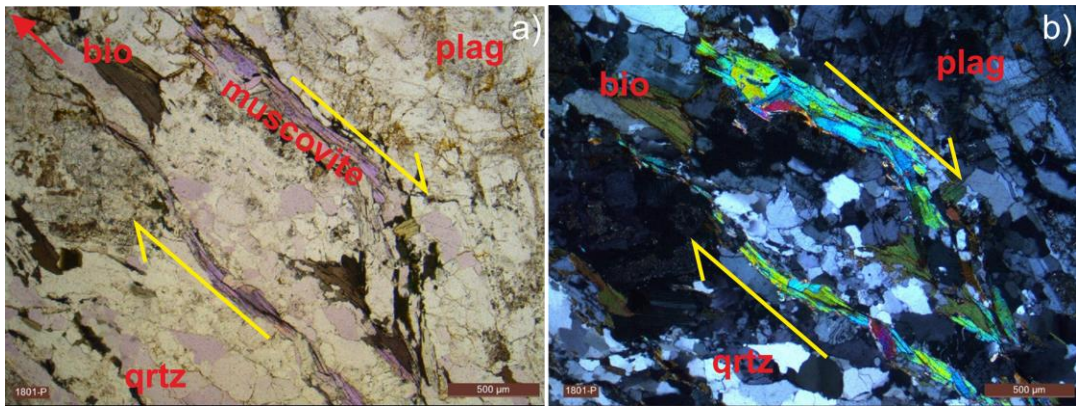


Figure 4.29. Thin section images of the South Uludağ Metagranite (sample 1801-P) (a): PPL, b): XPL; red arrow: north direction; qrtz: quartz, plag: plagioclase, bio: biotite).

Upon examining the South Uludağ Metagranite sample 1801, it is evident that myrmekite structures are significantly present. These structures are created by hydrothermal deformation (Figure 4.30). Myrmekite may also be generated by replacing plagioclase during metasomatism or hydrothermal alteration after the rock fully crystallises. Quartz intergrowths may sometimes destroy plagioclase. While the exact origin may not always be evident, it is undoubtedly a recent occurrence in the rock.

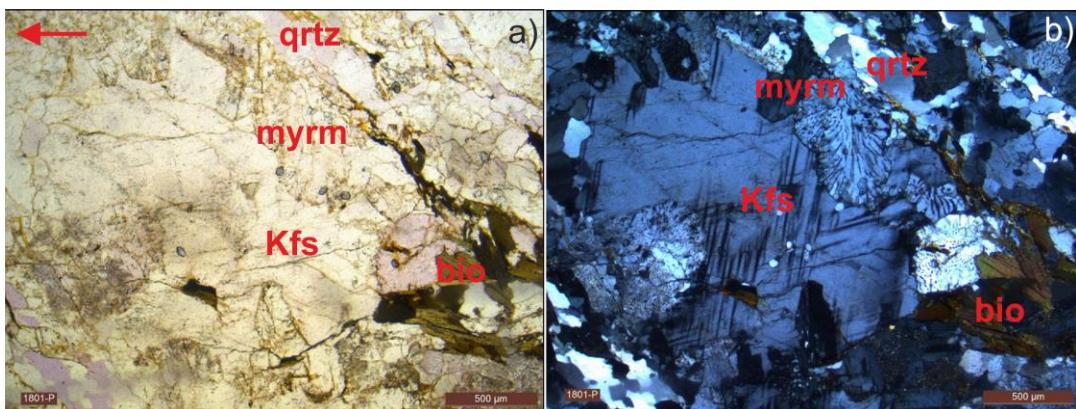


Figure 4.30. Thin section images of the South Uludağ Metagranite (sample 1801-P) (a): PPL, b): XPL; red arrow: north direction; qrtz: quartz, bio: biotite, Kfs: alkali feldspar, myrm: myrmekite).

Orientation shown by mica minerals serves as a tectonic strain marker, providing information about direction and magnitude of the forces that have affected the rock.

It contributes to developing a foliated texture in the rock, a planar fabric resulting from the parallel arrangement of minerals. The presence of lineated mica minerals may indicate shear zones within the metagranite, zones of intense deformation characterised by the movement of rock along a specific plane (Figure 4.31, Figure 4.32). In the case Figure 4.31 and Figure 4.32, Metagranite has N/NE-S/SW mineral alignment in mica.

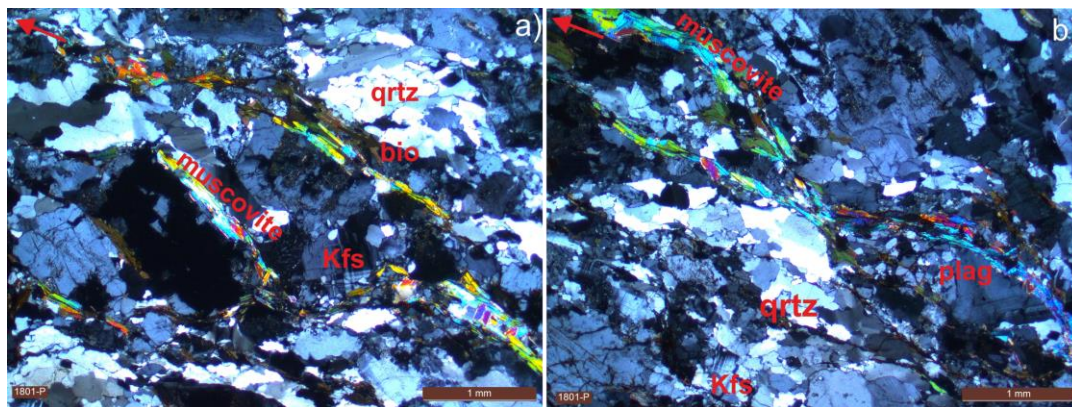


Figure 4.31. Thin section images of the South Uludağ Metagranite (sample 1801-P) (a): XPL, b): XPL; red arrow: north direction; qzt: quartz, plag: plagioclase, Kfs: alkali feldspar).

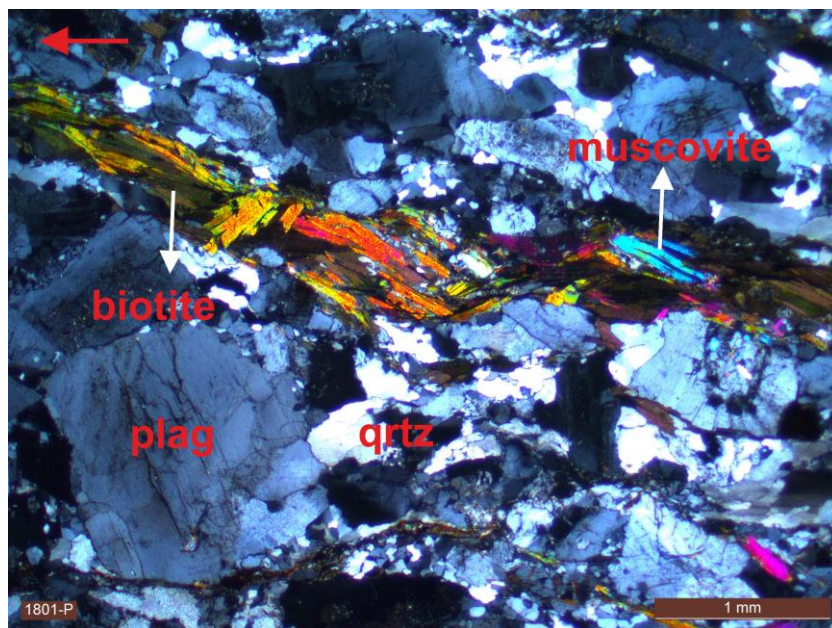


Figure 4.32. Thin section images of the South Uludağ Metagranite (sample 1801-P) (XPL image; red arrow: north direction; qzt: quartz, plag: plagioclase).

Epidote is a common mineral in the Uludağ Massif Gneiss. They often associated with medium- to high-grade metamorphic rocks, suggesting that the rock has undergone metamorphism beyond typical granite conditions. The specific mineral assemblage, including the presence of epidote, can infer the metamorphic grade of the rock, as different minerals are stable under varying pressure and temperature conditions (Figure 4.33, Figure 4.34).

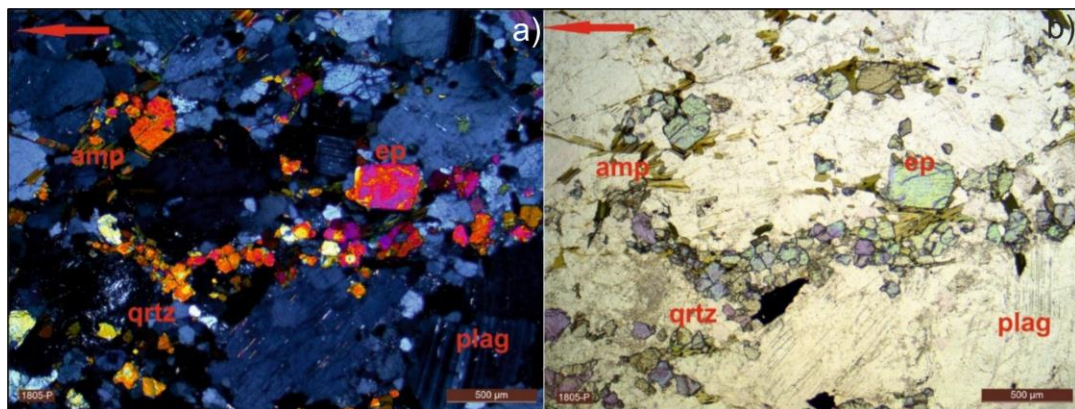


Figure 4.33. Thin section images of the Kilimligöl Formation Gneiss (sample 1805-P) (a): XPL, b): PPL; red arrow: north direction; ep: epidote, qtz: quartz, amp: amphibole, plag: plagioclase).

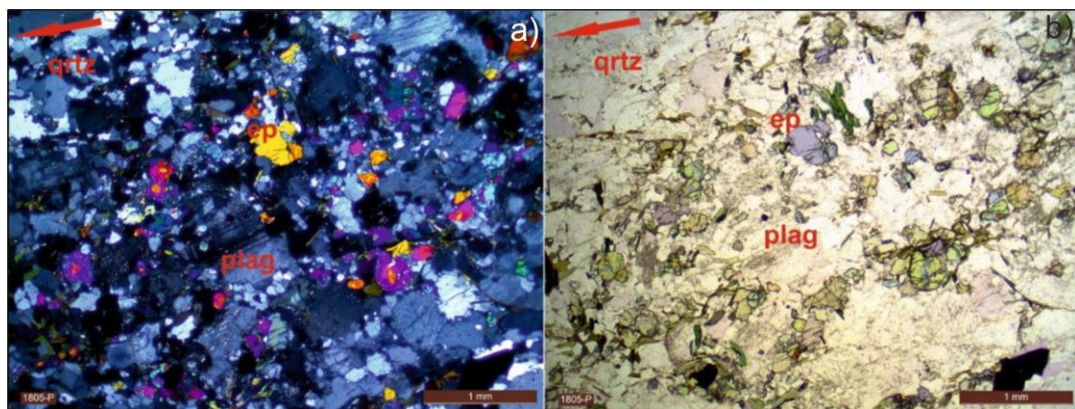


Figure 4.34. Thin section images of the Kilimligöl Formation Gneiss (sample 1805-P) (a): XPL, b): PPL; red arrow: north direction; ep: epidote, qtz: quartz, amp: amphibole, plag: plagioclase).

The presence of epidote adds to the mineralogical diversity of the rock, suggesting that the original mineral assemblage of the granite has been modified and new

minerals have formed as a response to changing geological conditions. Understanding the significance of epidote in a thin section involves considering its mineralogical context, associated minerals, and the broader geological setting (Figure 4.35).

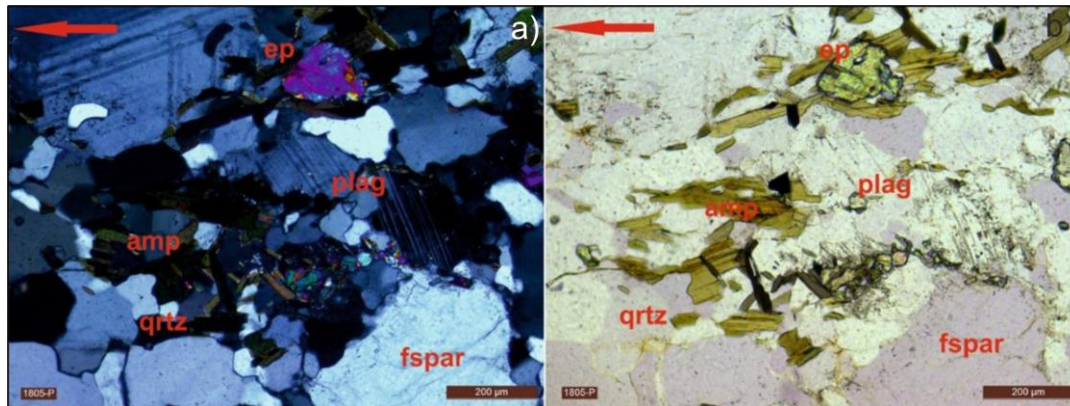


Figure 4.35. Thin section images of the Kilimligöl Formation Gneiss (sample 1805-P) (a): XPL, b): PPL; red arrow: north direction; ep: epidote, qrtz: quartz, amp: amphibole, fspar: feldspar, plag: plagioclase).

The quartz microstructures as observed in Figure 4.36 which depicts the sub-grain rotation (SGR) recrystallisation process in quartz. SGR recrystallisation occurs in quartz, together with the presence of BLG. This recrystallisation is achieved by dynamic recrystallisation, specifically via bulging recrystallisation. Furthermore, the phenomenon of grain boundary migration (GBM) recrystallisation may be observed in the thin sections of the metagranites and the gneisses from the Uludağ Massif (especially shown in Figure 4.13). Typically, recrystallisation occurs in quartz through the processes of GBM and SGR.

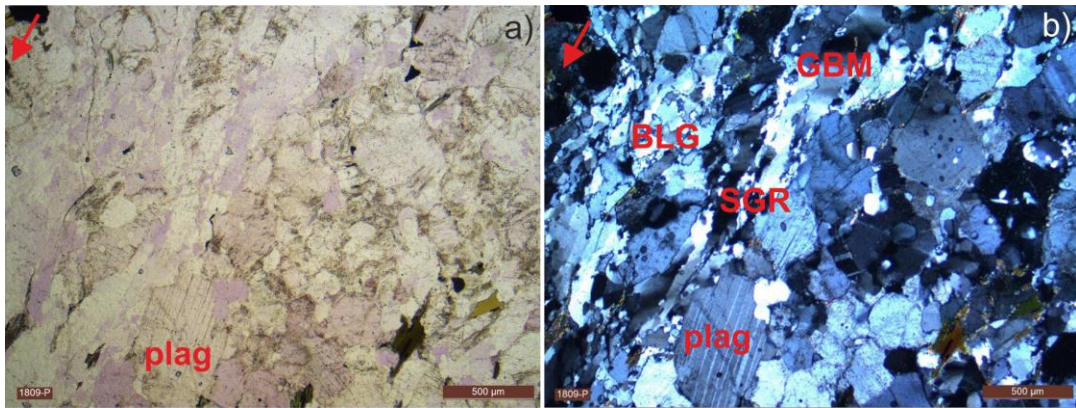


Figure 4.36. Thin section images of the Central Uludağ Granite (sample 1809-P) (left: PPL, right: XPL; red arrow: north direction; qrtz: quartz, plag: plagioclase, bio: biotite).

Zircon is an important mineral present in the studied gneisses, granites and metagranites (Figure 4.37, Figure 4.38). Zircon is an early crystallising mineral resistant to later changes (Tichomirowa et al. 2019). Hermann et al. (2001) have shown that zircon formation in gneisses may happen as the rocks are cooling and being brought to the surface. One important way zircon forms is by creating zircon crystals from partially melted rocks with a high concentration of the element Zirconium (Zr) (Hermann et al. 2001).

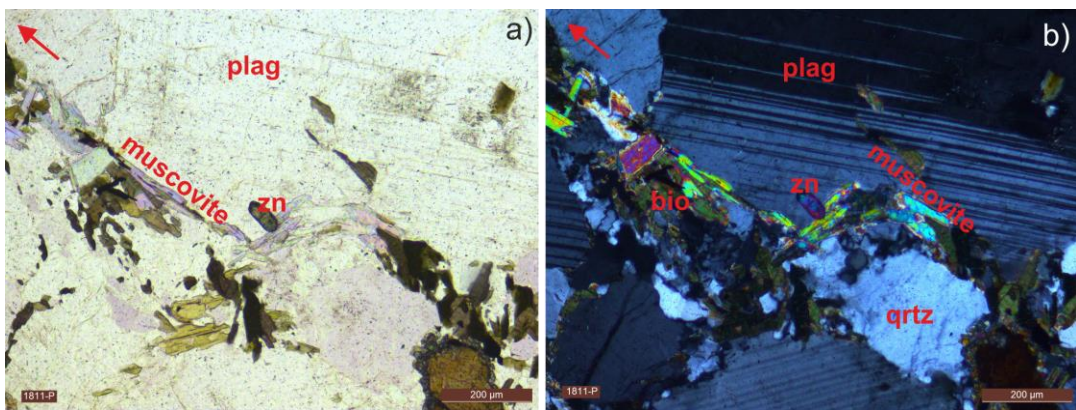


Figure 4.37. Thin section images of the Gökdere Formation Gneiss (sample 1811-P) (a): PPL, b): XPL; red arrow: north direction; qrtz: quartz, plag: plagioclase, bio: biotite, zn: zircon).

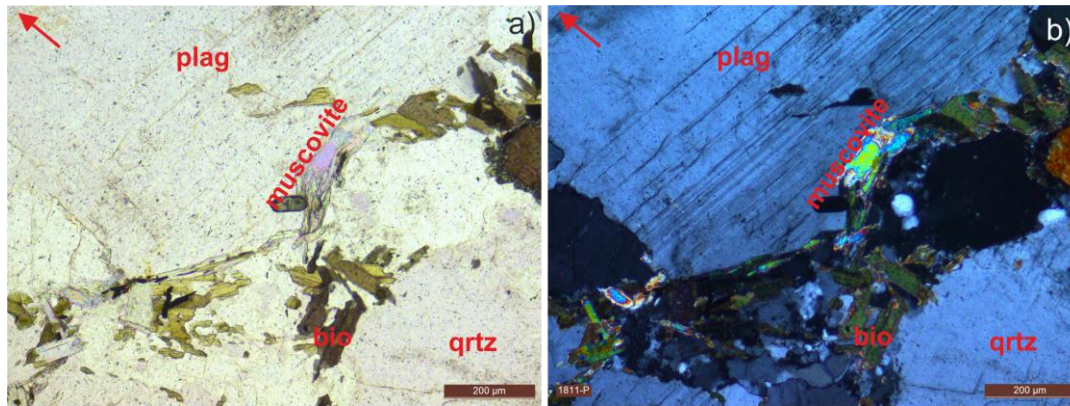


Figure 4.38. Thin section images of the Gökdere Formation Gneiss (sample 1811-P) (a): PPL, b): XPL; red arrow: north direction; plag: plagioclase, bio:biotite).

The Kapıdağ Granite has distinctive characteristics in its thin section and mineral compositions. Thin sections have a granitic structure distinguished by tightly interlocking quartz, feldspar, and biotite or hornblende crystals (Figure 4.39).

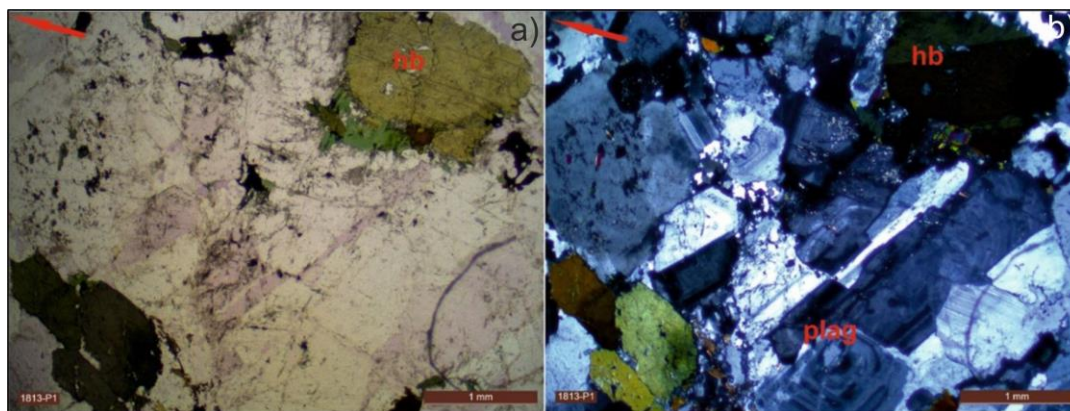


Figure 4.39. Thin section images of the Kapıdağ Granite (sample 1813-P1) (a): PPL, b): XPL; red arrow: north direction; plag: plagioclase, hb: hornblende).

Quartz often takes the form of transparent, uneven particles, but feldspar crystals display various hues ranging from white to pink or salmon (Figure 4.40). Biotite or hornblende minerals in the granite may be visually detected as black, flaky particles scattered throughout the rock matrix (Figure 4.40).

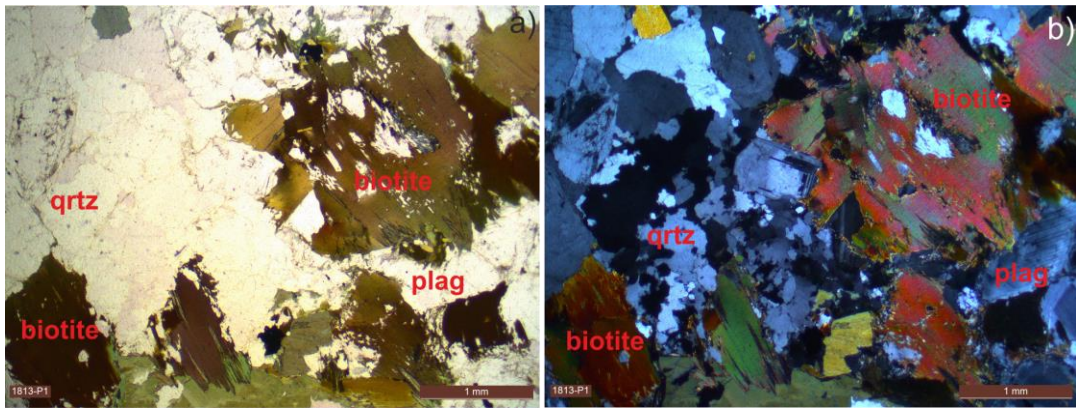


Figure 4.40. Thin section images of the Kapıdağ Granite (sample 1813-P1) (a): PPL, b): XPL; red arrow: north direction; plag: plagioclase, mica: mica).

The mineral compositions of the Kapıdağ Granite have a characteristic granitic makeup, consisting mostly of quartz, feldspar, and mica minerals. Quartz, a prevalent mineral found in granites, enhances the durability and ability of the rocks to withstand weathering. The presence of feldspar minerals, namely orthoclase and plagioclase, significantly impacts the granite's colour and texture. Mica minerals, such as biotite or muscovite, and hornblende as amphibole, provide a dark hue (Figure 4.41, Figure 4.42).

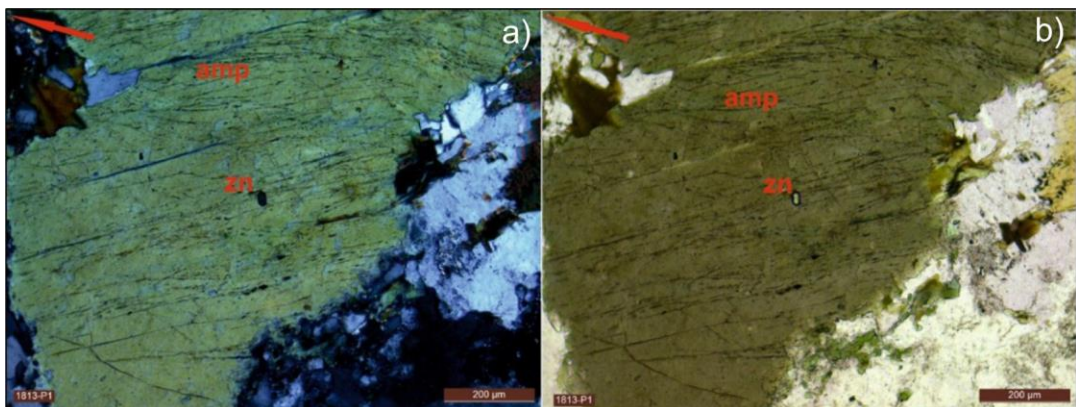


Figure 4.41. Thin section images of the Kapıdağ Granite (sample 1813-P1) (a): XPL, b): PPL; red arrow: north direction; hb: hornblende, zn: zircon).

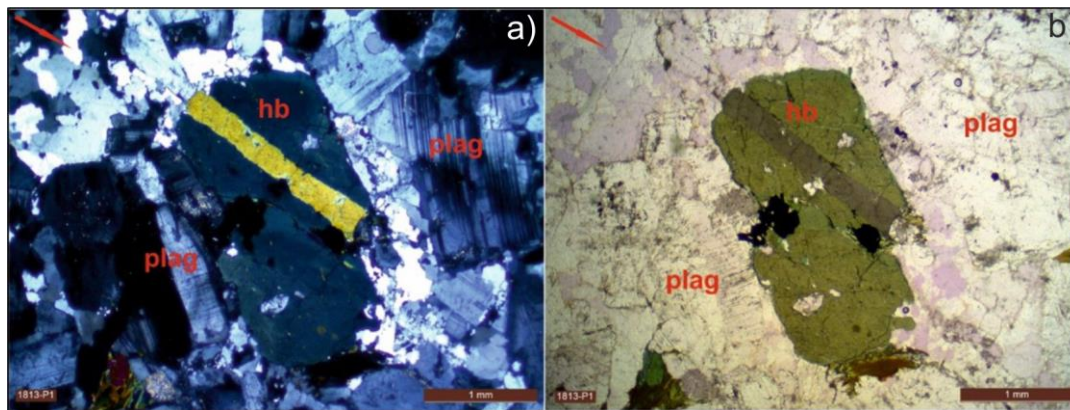


Figure 4.42. Thin section images of the Kapıdağ Granite (sample 1813-P1 , zn: zircon (a): XPL, b): PPL; red arrow: north direction; plag: plagioclase, hb: hornblende).

Intending to get temperature estimates that were unaffected by the mineral assemblages in the adjacent bedrock, Stipp et al. (2002) used data from the Italian Alps (Tonale Fault Zone). The researchers observed a transition from the frictional to the viscous phases occurring at around 280°C. The main process occurring between 280° and 400°C is the recrystallisation of BLG (Figure 4.43). The recrystallisation of SGR occurs around 400° to 500°C, and the change to grain boundary migration (GBM) recrystallisation is noticeable before 500°C (Figure 3.43).

Feldspar has little sericite alteration but displays microcline twinning, as seen in Figure 4.9. No evidence of recrystallisation was seen in the thin sections of amphibolites. Indicators of asymmetric shear stress, mica-fish microstructures, quartz clasts, and recrystallised mica strain shadows are further microstructures linked to the structural changes.

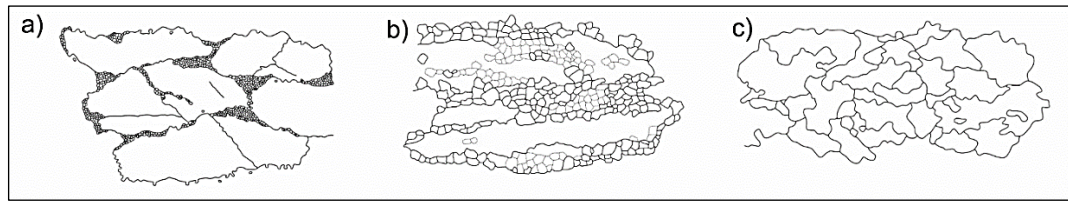


Figure 4.43. Microstructures of all three recrystallisation methods of Stipp et al. (2002). a) Dynamic recrystallisation by bulging (BLG) occurring at grain boundaries and microcracks. b) Sub-grain rotation (SGR) refers to forming core-mantle systems where recrystallised grains replace ribbon grains. c) Grain boundary migration (GBM) leads to inconsistent grain shapes and sizes, as well as the formation of interfingering sutures.

According to the thin section interpretations of the Uludağ Massif rocks, metagranites and gneisses have grain boundary migrations (GBM), sub-grain rotation (SGR) and dynamic recrystallisation by bulging (BLG). All these features are related by the 300°C to 500°C temperature bedrock related.

Dominant mineral lineations are consistent for each rock. For example, metagranite samples have dominantly E-W directioned mineral lineation. On the other hand, gneiss samples show N-S mineral lineation.

All samples of quartz and feldspar exhibited sub-grain rotation (SGR) recrystallisation for gneisses and metagranites of Uludağ. SGR indicating temperatures ranging from 400°C-500°C (Lloyd and Freeman, 1994; Stipp et al. 2002) (Figure 4.44). The samples from the Uludağ Metagranites exhibit microstructures that indicate deformation at higher temperatures. These include grain boundary migration (GBM) recrystallisation (500-700°C) and myrmekite formation (600°C). These observations are supported by Figure 4.6, Figure 4.9, Figure 4.10, Figure 4.13, Figure 4.15, Figure 4.16, Figure 4.20, as well as Figure 4.44. (Stipp et al. 2002; Simpson and Wintsch, 1989).

The quartzo-feldspathic lithologies in the sample suite document the massif's deformation at higher temperatures, as seen in Figure 4.44. During the process of exhumation, there is a noticeable fall in temperature, which is shown by the occurrence of brittle deformation seen in the overall structure of the Bursa Fault. In

Figure 4.44, the depth related pressure-temperature -time route of the Uludağ Massif was created as a result of previous studies (from Okay et al. 2008) and this study considering estimations derived from mineralogy.

The ages of muscovite and biotite indicate that the gneisses underwent cooling from 350°C to 250°C, which are the temperatures at which the minerals became closed systems. This cooling process occurred approximately 50 to 33 million years ago, as reported by Okay et al. (2008). Assuming a geothermal gradient of around 30°C/km, a particular viewpoint may calculate a constant exhumation rate from the data shown in Figure 4.44. According to Okay et al. (2008), the variation in the ages at which the South Uludağ Metagranite crystallised (30-39 Ma) may be attributed to the extended process of crystallisation occurring in a region of intense deformation.

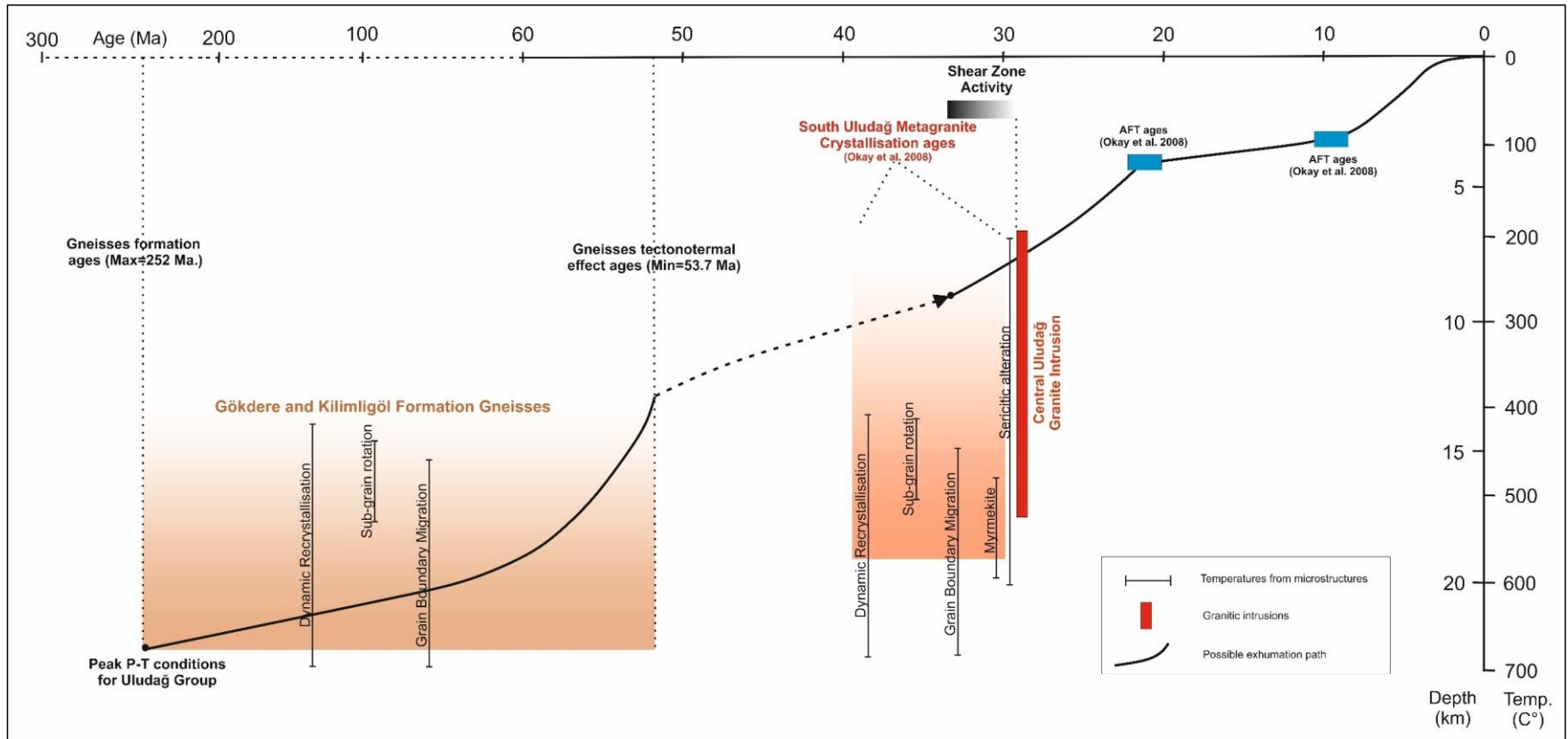


Figure 4.44. Depth-temperature-time path for the exhumation of the Uludag massif, which was created by combining the data obtained in this study with previous studies.

According to the model suggested in Figure 4.44, the granite was intruded before any shear activity occurred, but it had not fully cooled to the surrounding temperature before the shear zone activity developed. Therefore, it can be inferred that the shear zone must have started towards the end of the crystallisation period, around 35 million years ago. The Eskişehir Fault underwent further growth and localisation during the exhumation process because of the significant difference in rheological properties between the granite and the massif. This has significant consequences for the timing of the Uludağ shear zone.

The Central Uludağ Granite has an intrusion age of 27 million years ago, as Okay et al. (2008) determined. This age marks the conclusion of deformation in a strike-slip shear zone with precision. Thus, our research suggests that the period of shear activity occurred approximately 35 to 29 million years ago, placing it in the early Oligocene. The shear zone exhibited right lateral strike-slip shear, as shown by the widespread fault parallel foliation that included right lateral shear indications (Chapter 3). The deformation conditions were ductile, occurring at temperatures ranging from 300°C to 500°C, as determined by analysing quartz-feldspath-related microstructures. Quartz is undergoing deformation via brittle mechanisms around the Bursa Fault. The Apatite fission track ages obtained by Okay et al. (2008) indicate that the exhumation process ended and grouped about 20-22 million years ago and 10-9 million years ago, suggesting two distinct periods of increased uplift. The process of exhumation caused the replacement of formerly flexible materials with more fragile structures, as seen in the northern region of the Uludağ Massif near the Bursa Fault.

CHAPTER 5

GEOCHEMISTRY

5.1 Introduction of Geochemistry

Geochemical data, presented here, are generally divided into four main groups: major elements, trace elements, radiogenic isotopes, and stable isotopes. This study includes a special section focusing specifically on these different categories of geochemical data. The study focuses primarily on major and trace and then radiogenic isotopes. In addition to field observations and petrographic studies, geochemical data are used to understand the geological processes affecting the rocks in scope of the study.

Each rock survey is characterized by major constituents known as key elements. Si, Ti, Al, Fe, Mn, Mg, Ca, Na, K, and P are typical elements of silicate rock. Based on the information shown in Table 5.1, the amounts of these elements are typically expressed as weight percent (wt%) of oxide. Often, major element assessments concentrate only on cations if enough oxygen accompany them. Therefore, the total value of the oxides, the principal constituents, will be approximately one hundred percent, and the entire analysis are used as a general indicator of the substance's reliability.

Trace elements are presented in concentrations below 0.1 wt%, and their levels are usually expressed in parts per million (ppm) or sometimes in parts per billion (10^{-9}) = ppb) (Table 5.1). The key element groups for geochemical interpretations in this study are lanthanides, rare earth elements (REE), highly siderophile elements (HSE) and transition metals (Fe and Mn). Lanthanides have atomic numbers 57-71 (La to Lu) (Figure 5.1), and REE and Y behave similarly. Rare earth elements (REE) are important trace elements in evaluating various processes in igneous, sedimentary, and metamorphic petrology. Lanthanide REE, composed of metals

with atomic numbers 57-71, is a valuable contribution to geochemistry. Elements with low atomic numbers are called light rare earth elements (LREE), while those with higher atomic numbers are called heavy rare earth elements (HREE). Medium rare earth elements (MREE) are used less frequently and focus on the middle members of the group. Transition metals (Sc-Zn) are typically restricted to the first transition series and include Fe and Mn. Although elements in these groups have similar chemical properties, geological processes can exploit these differences and fractionated elements. Trace element geochemistry aims to explore these processes and quantify their extent.

Due to their comparable chemical properties, elements within each group should exhibit comparable geochemical behaviour. However, this may not always be the case, as geological processes can separate elements based on small chemical changes within a group of elements. It is, therefore, based on trace element geochemistry to determine which geological processes may have this effect and how many specific processes are present.

Main oxide elements, trace elements and radiogenic isotopes are used for the geochemistry studies are given in Table 5.1

Table 5.1. Major, trace, and radiogenic isotope elements used in geochemical studies.

Main Oxide Elements(wt.%)	Trace Elements(ppm)				Radiogenic Isotopes
SiO ₂	Li	Cu	Ba	Ho	Rb-Sr
TiO ₂	P	Zn	La	Er	Sm-Nd
Al ₂ O ₃	Be	Ga	Ce	Tm	Lu-Hf
Fe ₂ O ₃	Sc	Rb	Pr	Yb	Re-Os
MnO	Ti	Sr	Nd	Lu	K-Ar
MgO	V	Y	Sm	Hf	K-Ca
CaO	Cr	Zr	Eu	Ta	La-Ce
Na ₂ O	Mn	Nb	Gd	Pb	La-Ba
K ₂ O	Co	Mo	Tb	Th	
P ₂ O ₅	Ni	Cs	Dy	W	

Two different categories of isotopes are distinguished: Radiogenic isotopes and stable isotopes. Isotopes that undergo spontaneous decay due to their fundamental radioactivity are included in the category of radiogenic isotopes. These isotopes also include isotopes that are end products of a decay process. The element pairs K-Ar, Rb-Sr, Sm-Nd, Lu-Hf, U-Pb and Re-Os are listed in Table 5.1. These elements are "parent-daughter" isotope combinations. For example, the ratios are shown proportionately to a non-radiogenic isotope; $^{87}\text{Sr}/^{86}\text{Sr}$, ^{87}Sr is a radiogenic isotope.

The ICP-MS method was used in this project to analyse the major and trace elements listed in Table 5.1. The comprehensive list of trace elements provided here shows the wide range of trace elements that can be reliably identified using this method. If a particular element is not measured, it is labelled "nd" (not determined). If the element cannot be detected because the analytical method is below the detection limits, it may be recorded as "nd".

Thermal ionization mass spectrometry (TIMS) measures the radiogenic isotopes of Sr and Nd. Within this study's scope, the TIMS method performed Sr-Nd radiogenic isotope analyses for the rocks' origin analysis.

The geochemical analyses performed in the scope of this study mainly enable trace and major element chemistry and radiogenic isotopes to identify and understand geochemical processes and determine the tectonic origin of some igneous and metamorphic rocks.

5.2 Trace Element Modelling

One of the main applications of trace elements in modern igneous petrology is testing hypotheses through geochemical modelling. This involves building a model representing geochemical processes and comparing the results of the model with actual measurements. Successful geochemical modelling depends on precisely determining trace element concentration, accurate partition coefficients and knowledge of initial composition. It is important to note that geochemical modelling does not always produce a unique solution due to uncertainties in initial compositions, partition coefficients and the physical processes involved. Therefore, additional constraints, often derived from field observations, major element data, isotopic chemistry, and experimental petrology, are needed to develop the models.

Geochemical modelling results are typically presented in bivariate or multivariate plots and compared to trends observed in measured rock compositions. Several software packages are widely used for these modelling calculations, such as t-IgPet (Carr and Gazel, 2017), Petrograph (Petrelli et al. 2005) and WinRock (Kanen, 2004). Another program was written in R language by Janousek et al. (2016).

Ultimately, trace element modelling is a hypothesis-testing tool and complements a broader approach to understanding complex geological problems by integrating diverse data sources and constraints. It helps reveal geochemical processes operating at different scales, from individual magma chambers to entire volcanic regions and even large-scale reservoirs such as continental crust or depleted upper

mantle. In this study, the program written in R language by Janousek (2016) was used to process geochemical data.

5.3 Radiogenic Isotope Data

Radiogenic isotopes are crucial in geochemistry, determining the age of rocks and minerals and identifying geological processes and resources. They are used in geochronology, a field that focuses on dating rocks and minerals, and isotope geology, which uses radiogenic isotopes to study the Earth's deep interior. This field has led to geochemical constraints on the nature of continental crust and the Earth's mantle that can be combined with physical knowledge to provide a model of the chemical-physical changes occurring deep underground.

5.3.1 Petrogenetic Utilization of Radiogenic Isotopes

Isotope geochemistry is a field that studies the isotopic properties of radiogenic isotopes found in the crust and mantle. The isotope pair cannot be fractionated by crystal-liquid processes, which allows the isotopic character of the source region to be preserved during partial melting. Table 5.2 and Table 5.3 (Rollinson and Pease, 2021) show the current composition of the radiogenic isotope pairs used in this study in the mantle and crust.

Table 5.2. Current isotopic composition of mantle and crustal reservoirs.

	$^{87}\text{Rb}-^{86}\text{Sr}$	$^{147}\text{Sm}-^{143}\text{Nd}$
Oceanic basaltic sources		
DMM^b	Low Rb/Sr Low $^{87}\text{Sr}/^{86}\text{Sr}$	High Sm/Nd High $^{143}\text{Nd}/^{144}\text{Nd}$ (positive ϵNd)
HIMU	Low Rb/Sr Low $^{87}\text{Sr}/^{86}\text{Sr} = 0.7029$	Moderate Sm/Nd $^{143}\text{Nd}/^{144}\text{Nd} = <0.51282$
EM-1	Low Rb/Sr $^{87}\text{Sr}/^{86}\text{Sr}$ (~0.705)	Low Sm/Nd $^{143}\text{Nd}/^{144}\text{Nd} = <0.5112$
EM-2	High Rb/Sr $^{87}\text{Sr}/^{86}\text{Sr} > 0.722$	Low Sm/Nd $^{143}\text{Nd}/^{144}\text{Nd} = 0.511- 0.5121$
Bulk Earth	$^{87}\text{Sr}/^{86}\text{Sr} = 0.7045$	$^{143}\text{Nd}/^{144}\text{Nd} = 0.512634$
Continental crustal sources		
Upper crust (sialic)	High Rb/Sr high $^{87}\text{Sr}/^{86}\text{Sr}$	Low Sm/Nd low $^{143}\text{Nd}/^{144}\text{Nd}$ (negative ϵNd)
Mid crust	Semi-high Rb/Sr =0.2–0.4 $^{87}\text{Sr}/^{86}\text{Sr} = 0.72– 0.74$	Crust shows retarded Nd evolution relative to the chondritic source
Lower crust (mafic)	Rb-depleted Rb/Sr <~0.4 Low $^{87}\text{Sr}/^{86}\text{Sr} = 0.702– 0.705$	Very U-depleted Very low $^{206}\text{Pb}/^{204}\text{Pb}$ (~14.0)

This observation has led to two important developments in isotope geochemistry: identifying unique isotopic properties in source regions and studying mixing

between isotopically distinct sources (Rollinson and Pease, 2021). Isotope geochemistry aims to identify and map different isotope reservoirs in the crust and mantle, characterize these reservoirs for different isotopic systems, and assess the extent to which partial melting, recycling, and mixing processes contribute to their formation.

The isotopic evolution of mantle sources can be attributed to two processes: the mixing process, where various components contribute to the source, and the isotopic growth process, where the composition of the source evolves over geologic time.

5.3.2 Characterization of Isotope Reservoirs

To explain isotopic variance in basalts from oceanic islands and mid-ocean ridges, Zindler and Hart (1986) explored four mantle end-member domains. The continental crust's upper, middle, and lower parts have different geochemical and isotopic properties. The heterogeneous lower crust is less chemically developed than the upper and middle crusts.

Today, the mantle and continental crust contain a variety of isotopically unique reservoirs identified about the composition of Earth's primitive, undifferentiated mantle. Here, you can see the table showing how these various reservoirs' current Sr and Nd isotope chemistry can be used to identify them (Table 5.2 and Table 5.3).

Table 5.3 Sr, Nd and Pb isotope ratios for some common rock types.

Rock Type	$^{87}\text{Sr}/^{86}\text{Sr}$	$^{143}\text{Nd}/^{144}\text{Nd}$
Depleted mantle MORB (DMM)		
Atlantic	0.702300–0.702920	0.512992– 0.513175
Pacific	0.702150– 0.702713	0.513098– 0.513296
Indian	0.702690– 0.704870	0.512437– 0.513189
Ocean Island Basalts (OIB)		
Pitcairn Isl. (EM1)	0.703603– 0.705296	0.512333– 0.512692
Samoa (EM2)	0.705193– 0.705853	0.512705– 0.512900
Continental flood basalts		
Parana/Etendeka	0.70397– 0.71420	0.511860– 0.512799
Columbia River	0.702985– 0.703964	0.512834– 0.513031
Mantle xenoliths		
Continental lithosphere		
Siberia	0.70253– 0.702235	0.512590– 0.513144
Modern pelagic sediment		
Pacific	0.70690– 0.72253	0.512343– 0.512392
Atlantic	0.709288– 0.723619	0.511942– 0.512553

5.3.3 Formation of the Continental Crust

In contrast to BE (Bulk Earth), oceanic basalts are rich in Nd isotopes and low in Sr isotopes, whereas continental crustal rocks exhibit the opposite relationship according to the Sr-Nd isotope correlation figure shown in Figure 5.1. This negative correlation suggests that oceanic basalts and continental crust originate

from similar Nd and Sr isotopes deposited in the mantle. The link between the Earth's crust, mantle and the initial bulk composition of the Earth is modelled using mass balance based on this idea.

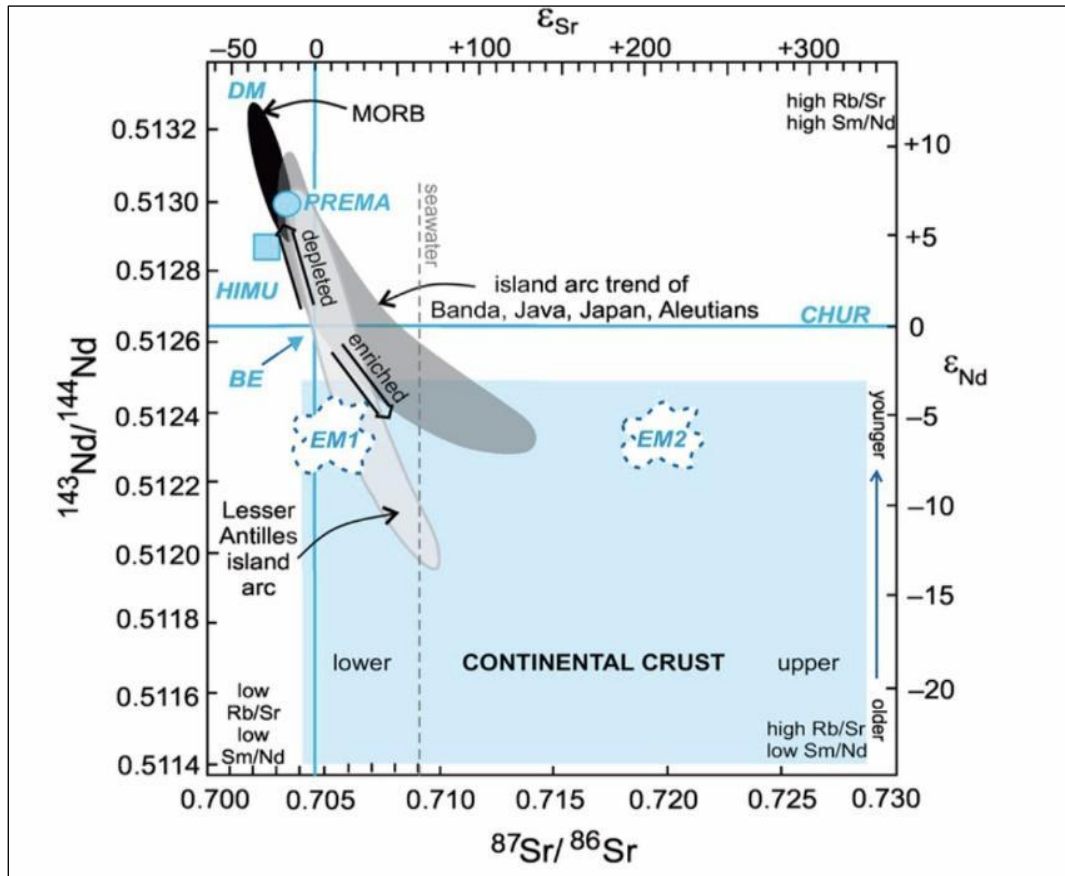


Figure 5.1. Origins of the mantle. Mantle sources are illustrated in $^{87}\text{Sr}/^{86}\text{Sr}(\text{T})$ vs. $^{143}\text{Nd}/^{144}\text{Nd}(\text{T})$ (Zindler and Hart, 1986).

Figure 5.1 shows compositions include the 'common mantle' (PREMA), high μ (U/Pb) (HIMU), enriched mantle (EM1, EM2), depletion mantle (DM) and bulk silicate earth (BE). The "depleted" mantle source of the upper left quadrant represents the "depleted" residual mantle from which discordant elements were removed. Most crustal rocks are found in the lower right 'enriched' quadrant, encompassing young and old upper and lower crusts. Island arc behaviour reflects mixing processes between enriched and depleted mantle sources (Zindler and Hart, 1986; Jackson et al. 2007, and White, 2015).

When U-Pb zircon age data are combined with Sr-Nd radiogenic isotope ratios, the geochemical processes and their interrelationships between magmatic activity and the formation of the new crust will be more easily understood.

5.4 Geochemistry of the Uludağ Massif

Within the scope of this study, Kilimligöl Formation, Gökdere Formation, Central Uludağ Granite, and South Uludağ Metagranite units were sampled to investigate the metamorphic and magmatic evolution of the Uludağ Massif. Moreover, samples were taken from the Kapıdağ Granite in the south of the Uludağ Massif to reveal similarities/differences in their magmatic origins. This chapter discusses the igneous and metamorphic evolution of these units.

5.4.1 Major and Trace Element Geochemistry of the Uludağ Massif

In this section, the major and trace element data of the metamorphic rocks (Kilimligöl, Gökdere formations) and Uludağ Plutonics (Central Uludağ Granite and Kapıdağ Granodiorite cutting the Uludağ Massif towards the south) and South Uludağ Metagranites within the Uludağ Massif is discussed. Possible relationships of all these igneous and metamorphic rocks are evaluated by considering geochemical properties of all rock types.

After petrographic examinations were performed on the samples collected from the study area, the freshest samples were selected and grouped for geochemical analysis (Table 4.1). A total of 23 samples, including 4 samples from the South Uludağ Metagranite, 4 samples from the Central Uludağ Granite, 9 samples from the Gökdere Formation, 2 samples from the Kilimligöl Formation, 2 samples from the Kapıdağ Granite and 2 samples from the Sazak Formation on Uludağ Massif, were geochemically analysed at Acme Laboratories (Ankara, Turkey). The data obtained from these analyses are presented in Table 5.4, Table 5.5, and Table 5.6.

Table 5.4. The table shows oxide, main and trace elements for gneisses and metabasalts.

Sample Name	1802 (metagranite)	1814 (metagranite)	1817 (metagranite)	1819 (metagranite)	1902-PA (metagranite)	1903 (metagranite)	Mean (metagranite)	1813-P1 (granite)	1813-P2 (granite)	1821 (granite)	1822 (granite)	Mean (granite)
TiO2 (wt%)	0.17	0.18	0.20	0.16	0.49	0.15	0.22	0.43	0.10	0.23	0.07	0.21
Al2O3	10.24	9.20	12.28	11.89	11.40	12.06	11.18	16.86	10.68	10.89	11.21	12.41
Fe2O3	1.33	1.19	1.14	1.12	4.10	1.72	1.77	5.23	0.99	1.70	0.57	2.12
MnO	0.02	0.03	0.02	0.02	0.03	0.02	0.02	0.12	0.03	0.03	0.01	0.05
MgO	0.22	0.23	0.27	0.12	1.62	0.45	0.48	1.71	0.22	0.63	0.10	0.66
CaO	1.61	0.99	1.19	0.98	0.92	2.11	1.30	5.83	1.06	2.10	0.59	2.40
Na2O	3.50	3.64	3.59	3.83	2.02	4.29	3.48	3.03	2.42	3.60	2.91	2.99
K2O	2.92	2.16	1.69	2.06	2.53	0.99	2.06	1.64	3.82	2.01	4.29	2.94
P2O5	0.05	0.07	0.07	0.04	0.08	0.06	0.06	0.13	0.02	0.10	0.05	0.08
Cr2O3	0.00	0.00	0.00	0.00	0.00	0.00	0.00	0.00	0.00	0.00	0.00	0.00
Rb (ppm)	90.00	86.60	61.90	69.90	75.80	35.60	69.97	40.30	99.00	86.00	190.10	103.85
Sr	407.00	471.00	515.00	380.00	181.00	456.00	401.67	334.00	101.00	471.00	53.00	239.75
Nb	5.96	6.15	6.55	4.68	8.53	3.22	5.85	8.43	9.62	3.32	7.53	7.23
Co	1.70	1.20	1.80	2.20	5.50	2.20	2.43	8.70	1.70	3.10	0.70	3.55
Cs	3.30	11.90	4.20	4.20	8.00	2.20	5.63	1.20	1.00	6.60	5.50	3.58
Ta	0.30	0.50	0.30	0.30	0.20	0.20	0.30	0.60	1.00	0.20	0.80	0.65
Sc	1.40	1.20	1.50	1.40	11.80	2.30	3.27	12.40	2.00	2.70	2.60	4.93
Pb	21.79	43.30	29.18	26.98	29.47	59.52	35.04	9.17	20.54	36.77	45.22	27.93
U	2.60	3.10	1.90	3.90	1.50	0.40	2.23	2.40	6.50	5.10	3.70	4.43
Th	7.50	16.80	10.60	11.20	12.50	3.50	10.35	7.90	19.80	15.00	2.60	11.33

Table 5.4. (Continued).

Sample Name	1802 (metagranite)	1814 (metagranite)	1817 (metagranite)	1819 (metagranite)	1902-PA (metagranite)	1903 (metagranite)	Mean (metagranite)	1813-P1 (granite)	1813-P2 (granite)	1821 (granite)	1822 (granite)	Mean (granite)
Cu	4.90	3.70	7.00	3.30	6.10	6.30	5.22	4.10	7.50	4.60	2.50	4.68
Ga	19.31	23.42	23.52	21.95	25.19	15.97	21.56	18.23	11.96	22.25	18.91	17.84
Mo	0.31	0.71	0.57	0.69	0.16	0.32	0.46	0.78	0.24	0.74	0.19	0.49
Ba	657.00	1064.00	1055.00	675.00	1672.00	254.00	896.17	492.00	477.00	695.00	93.00	439.25
Zr	5.80	7.50	4.00	4.60	1.70	1.60	4.20	6.40	19.80	6.50	10.60	10.83
Zn	36.70	59.30	25.00	37.40	143.00	37.10	56.42	54.00	14.30	37.70	14.60	30.15
Hf	2.50	0.32	0.18	0.22	0.06	0.07	0.56	0.54	0.96	0.25	0.61	0.59
V	8.00	8.00	10.00	7.00	57.00	18.00	18.00	88.00	8.00	16.00	3.00	28.75
Y	3.20	4.50	3.70	2.30	17.40	8.10	6.53	25.30	9.40	5.90	2.60	10.80
La	20.00	38.40	28.00	23.30	62.10	21.90	32.28	14.60	15.80	27.80	3.60	15.45
Ce	35.19	56.70	44.73	41.49	100.80	20.70	49.94	32.85	34.11	53.28	7.63	31.97
Pr	3.00	5.00	4.00	3.40	11.20	3.20	4.97	3.40	3.20	4.50	0.70	2.95
Nd	10.30	16.30	13.20	11.30	41.80	11.80	17.45	14.00	11.10	15.40	2.50	10.75
Sm	1.90	2.90	2.20	2.00	7.50	2.20	3.12	3.60	2.20	2.80	0.70	2.33
Eu	0.40	0.40	0.30	0.30	1.10	0.80	0.55	0.90	0.30	0.50	0.10	0.45
Gd	1.40	1.90	1.40	1.40	5.80	2.00	2.32	3.70	1.80	2.10	0.60	2.05
Tb	0.20	0.20	0.20	0.20	0.70	0.30	0.30	0.60	0.30	0.30	0.10	0.33
Dy	0.80	1.00	0.80	0.60	3.50	1.30	1.33	4.20	1.50	1.40	0.50	1.90
Ho	0.10	0.20	0.10	0.05	0.60	0.20	0.24	0.90	0.30	0.20	0.05	0.47
Er	0.20	0.40	0.30	0.20	1.50	0.70	0.55	2.90	1.00	0.50	0.20	1.15
Tm	0.05	0.05	0.05	0.05	0.20	0.05	0.20	0.40	0.20	0.05	0.05	0.30

Tablo 5.4. (Continued).

Sample Name	1802 (metagranite)	1814 (metagranite)	1817 (metagranite)	1819 (metagranite)	1902-PA (metagranite)	1903 (metagranite)	Mean (metagranite)	1813-P1 (granite)	1813-P2 (granite)	1821 (granite)	1822 (granite)	Mean (granite)
Yb	0.10	0.20	0.20	0.10	1.00	0.50	0.35	2.90	1.30	0.40	0.20	1.20
Lu	0.05	0.05	0.05	0.05	0.10	0.05	0.10	0.40	0.20	0.05	0.05	0.30
ΣREE	73.59	123.60	95.43	84.29	237.90	65.60	113.40	85.35	73.31	109.18	16.83	71.17
K	2.42	1.79	1.40	1.71	2.10	0.82	1.71	1.36	3.17	1.67	3.56	2.44
P	0.02	0.03	0.03	0.02	0.03	0.03	0.03	0.06	0.01	0.04	0.02	0.03
Ti	0.10	0.11	0.12	0.10	0.29	0.09	0.13	0.26	0.06	0.14	0.04	0.12
Nb/Th	0.79	0.37	0.62	0.42	0.68	0.92	0.63	1.07	0.49	0.22	2.90	1.17
Nb/Y	1.86	1.37	1.77	2.03	0.49	0.40	1.32	0.33	1.02	0.56	2.90	1.20
Zr/Y	1.81	1.67	1.08	2.00	0.10	0.20	1.14	0.25	2.11	1.10	4.08	1.88
Zr/Ti	57.43	71.43	34.19	46.94	5.80	18.39	39.03	24.62	319.35	47.45	271.79	165.80
La/Yb	200.00	192.00	140.00	233.00	62.10	43.80	145.15	5.03	12.15	69.50	18.00	26.17
(La/Yb)N	143.40	137.66	100.38	167.06	44.53	31.40	104.07	3.61	8.71	49.83	12.91	18.77
(La/Sm)N	6.80	8.55	8.22	7.53	5.35	6.43	7.15	2.62	4.64	6.41	3.32	4.25
(Gd/Yb)N	11.58	7.86	5.79	11.58	4.80	3.31	7.48	1.06	1.15	4.34	2.48	2.26
(Eu/Eu*)N	0.72	0.49	0.49	0.52	0.49	1.14	0.64	0.75	0.45	0.60	0.46	0.56

Table 5.5. The table shows oxide, main and trace elements for metagranites and granites.

Sample Name	1803 (gneiss)	1804 (gneiss)	1805 (gneiss)	1806 (gneiss)	1809 (gneiss)	1810 (gneiss)	1811 (gneiss)	1812 (gneiss)	1820 (gneiss)	1902-PB (gneiss)	1904 (gneiss)	Mean (gneiss)	1901 (metabasalt)	1905 (metabasalt)	Mean (metabasalt)
TiO₂ (wt%)	0.20	0.20	0.27	0.22	0.19	0.09	0.10	0.19	0.21	0.15	0.39	0.20	2.06	2.73	2.40
Al₂O₃	14.08	11.76	11.17	15.52	10.38	8.07	9.39	10.45	14.17	10.07	11.30	11.49	16.31	19.77	18.04
Fe₂O₃	2.77	2.62	2.39	1.36	2.63	1.54	1.73	2.54	1.56	1.19	4.37	2.25	11.84	15.76	13.80
MnO	0.04	0.04	0.04	0.01	0.02	0.03	0.02	0.03	0.03	0.01	0.06	0.03	0.14	0.19	0.16
MgO	0.27	0.40	0.46	0.25	0.20	0.07	0.08	0.43	0.53	0.28	1.18	0.38	5.70	6.90	6.30
CaO	1.06	1.29	3.04	0.85	1.15	0.71	0.78	2.84	1.68	1.79	3.44	1.69	7.74	10.00	8.87
Na₂O	3.41	3.69	3.15	4.30	4.30	3.51	3.56	3.32	3.18	3.79	2.80	3.55	2.43	2.05	2.24
K₂O	3.07	1.39	0.58	1.84	0.72	1.72	2.17	0.84	3.63	1.23	1.29	1.68	0.12	0.43	0.28
P₂O₅	0.01	0.02	0.04	0.03	0.03	0.01	0.00	0.10	0.10	0.02	0.05	0.04	0.22	0.26	0.24
Cr₂O₃	0.00	0.00	0.00	0.00	0.00	0.00	0.00	0.00	0.00	0.00	0.00	0.00	0.03	0.02	0.03
Rb (ppm)	60.20	33.10	19.00	61.10	20.20	35.00	43.90	30.10	126.40	31.90	40.20	45.55	2.80	10.90	6.85
Sr	91.00	112.00	184.00	238.00	65.00	20.00	39.00	226.00	420.00	718.00	93.00	200.55	154.00	427.00	290.50
Nb	14.95	17.72	4.12	8.43	4.14	4.98	3.35	2.04	4.07	1.49	3.66	6.27	16.24	20.10	18.17
Co	0.90	1.10	3.70	1.50	1.10	1.00	1.00	2.90	2.20	1.60	8.40	2.31	28.30	54.90	41.60
Cs	1.60	1.10	1.50	5.30	1.50	0.50	0.90	1.80	7.60	2.00	6.50	2.75	0.30	3.00	1.65
Ta	0.30	0.70	0.20	0.30	0.10	0.20	0.05	0.05	0.40	0.05	0.20	0.30	1.20	1.10	1.15
Sc	3.20	2.10	7.70	3.70	9.50	3.70	6.40	4.00	2.20	1.30	18.80	5.69	41.00	54.40	47.70
Pb	48.00	12.38	4.21	8.75	5.09	3.74	8.35	13.06	50.98	12.29	4.72	15.60	2.23	4.20	3.22
U	0.70	0.70	0.70	0.80	0.40	0.90	0.60	0.80	6.60	0.70	0.50	1.22	0.60	0.50	0.55
Th	17.20	16.70	3.50	12.60	2.30	7.60	9.60	32.50	14.70	4.10	2.70	11.23	1.80	2.20	2.00

Table 5.5. (Continued).

Sample Name	1803 (gneiss)	1804 (gneiss)	1805 (gneiss)	1806 (gneiss)	1809 (gneiss)	1810 (gneiss)	1811 (gneiss)	1812 (gneiss)	1820 (gneiss)	1902-PB (gneiss)	1904 (gneiss)	Mean (gneiss)	1901 (metabasalt)	1905 (metabasalt)	Mean (metabasalt)
Cu	11.90	10.10	4.80	10.40	3.60	4.10	8.00	0.80	3.80	3.80	24.70	7.82	57.60	139.20	98.40
Ga	27.44	26.07	15.19	21.46	16.66	16.66	16.76	19.89	21.17	15.70	14.50	19.23	19.50	27.05	23.28
Mo	1.05	0.34	0.76	0.62	1.51	0.52	0.95	0.26	0.23	0.16	0.44	0.62	0.62	0.28	0.45
Ba	1311.00	979.00	156.00	843.00	133.00	432.00	700.00	257.00	988.00	645.00	186.00	602.73	51.00	107.00	79.00
Zr	2.30	2.00	2.30	1.90	1.40	1.50	1.80	2.20	5.80	2.30	2.40	2.35	14.20	5.40	9.80
Zn	52.30	63.60	23.80	7.70	15.20	25.00	27.70	35.70	35.10	37.90	44.40	33.49	86.00	120.00	103.00
Hf	0.58	0.30	0.17	0.12	0.10	0.06	0.06	0.09	0.25	0.06	0.16	0.18	0.55	0.46	0.51
V	4.00	1.00	15.00	17.00	2.00	1.00	1.00	20.00	12.00	9.00	66.00	13.45	335.00	358.00	346.50
Y	21.70	22.60	34.90	4.30	16.00	33.30	10.30	21.40	5.70	4.30	28.50	18.45	32.20	37.90	35.05
La	69.30	54.60	13.50	36.90	7.80	22.80	21.70	87.80	30.90	12.90	8.60	33.35	17.50	19.40	18.45
Ce	135.00	95.40	32.04	62.82	16.11	57.60	63.99	153.90	53.91	21.80	17.28	64.53	42.48	48.15	45.32
Pr	13.70	9.60	3.60	5.50	2.20	5.40	5.50	15.40	4.90	2.40	2.30	6.41	4.80	5.50	5.15
Nd	52.90	37.30	15.80	18.50	9.90	22.20	22.70	57.20	16.70	8.70	10.10	24.73	21.20	25.40	23.30
Sm	11.60	8.30	4.40	3.20	2.70	5.40	5.80	11.30	3.10	1.70	3.00	5.50	5.60	7.10	6.35
Eu	1.50	1.40	1.00	0.50	0.80	0.60	0.50	1.90	0.40	0.40	0.70	0.88	2.00	2.80	2.40
Gd	9.60	7.50	5.20	2.20	2.70	5.50	5.00	8.50	2.20	1.30	3.70	4.85	6.10	7.80	6.95
Tb	1.30	1.10	0.90	0.30	0.50	1.00	0.70	1.10	0.30	0.20	0.70	0.74	1.00	1.30	1.15
Dy	6.30	5.60	6.10	1.10	3.00	6.20	3.20	5.10	1.30	1.00	4.70	3.96	6.40	7.60	7.00
Ho	1.00	1.00	1.30	0.20	0.70	1.30	0.50	0.90	0.20	0.20	1.10	0.76	1.20	1.50	1.35
Er	2.30	2.40	3.90	0.40	2.10	4.00	1.10	2.10	0.50	0.40	3.40	2.05	3.50	4.00	3.75
Tm	0.30	0.30	0.60	0.05	0.30	0.60	0.10	0.30	0.05	0.05	0.50	0.38	0.50	0.50	0.50

Table 5.5. (Continued).

Sample Name	1803 (gneiss)	1804 (gneiss)	1805 (gneiss)	1806 (gneiss)	1809 (gneiss)	1810 (gneiss)	1811 (gneiss)	1812 (gneiss)	1820 (gneiss)	1902-PB (gneiss)	1904 (gneiss)	Mean (gneiss)	1901 (metabasalt)	1905 (metabasalt)	Mean (metabasalt)
Yb	1.50	1.80	3.70	0.30	2.30	3.80	0.80	1.50	0.30	0.30	3.20	1.77	2.40	3.00	2.70
Lu	0.20	0.20	0.60	0.05	0.40	0.50	0.10	0.20	0.05	0.05	0.50	0.34	0.30	0.40	0.35
ΣREE	306.50	226.50	92.64	131.92	51.51	136.90	131.69	347.20	114.71	51.30	59.78	150.06	114.98	134.45	124.72
K	2.55	1.15	0.48	1.53	0.60	1.43	1.80	0.70	3.01	1.02	1.07	1.39	0.10	0.36	0.23
P	0.01	0.01	0.02	0.01	0.01	0.00	0.00	0.04	0.04	0.01	0.02	0.02	0.10	0.11	0.10
Ti	0.12	0.12	0.16	0.13	0.11	0.05	0.06	0.11	0.13	0.09	0.23	0.12	1.24	1.64	1.44
Nb/Th	0.87	1.06	1.18	0.67	1.80	0.66	0.35	0.06	0.28	0.36	1.36	0.79	9.02	9.14	9.08
Nb/Y	0.69	0.78	0.12	1.96	0.26	0.15	0.33	0.10	0.71	0.35	0.13	0.51	0.50	0.53	0.52
Zr/Y	0.11	0.09	0.07	0.44	0.09	0.05	0.17	0.10	1.02	0.53	0.08	0.25	0.44	0.14	0.29
Zr/Ti	18.85	16.81	14.38	14.62	12.28	27.78	29.03	19.47	46.40	26.44	10.39	21.49	11.50	3.30	7.40
La/Yb	46.20	30.33	3.65	123.00	3.39	6.00	27.13	58.53	103.00	43.00	2.69	40.63	7.29	6.47	6.88
(La/Yb)N	33.13	21.75	2.62	88.19	2.43	4.30	19.45	41.97	73.85	30.83	1.93	29.13	5.23	4.64	4.93
(La/Sm)N	3.86	4.25	1.98	7.45	1.87	2.73	2.42	5.02	6.44	4.90	1.85	3.89	2.02	1.77	1.89
(Gd/Yb)N	5.29	3.45	1.16	6.06	0.97	1.20	5.17	4.69	6.06	3.58	0.96	3.51	2.10	2.15	2.13
(Eu/Eu*)N	0.42	0.53	0.64	0.55	0.90	0.33	0.28	0.57	0.45	0.79	0.64	0.55	1.04	1.14	1.09

In this section, alteration control, behavior against a given element, multi-element behavior and tectonomagmatic discrimination diagrams will be examined in general, and then the source discrimination of rocks will be discussed by considering all diagrams.

For this purpose first of all you can see Figure 5.2 according to the samples K_2O and Na_2O loss related alteration control.

Loss of K_2O and Na_2O in rocks is indicative of various alteration processes, including chemical weathering, hydrothermal alteration, and metamorphism. Figure 5.2. give us the Na and K loss. First Diagram shows the K_2O+Na_2O vs. $100(K_2O/(K_2O+Na_2O))$ according to the Hughes (1973) and second diagram shows the Al_2O_3/Na_2O vs. Na_2O from Spitz and Darling (1978).

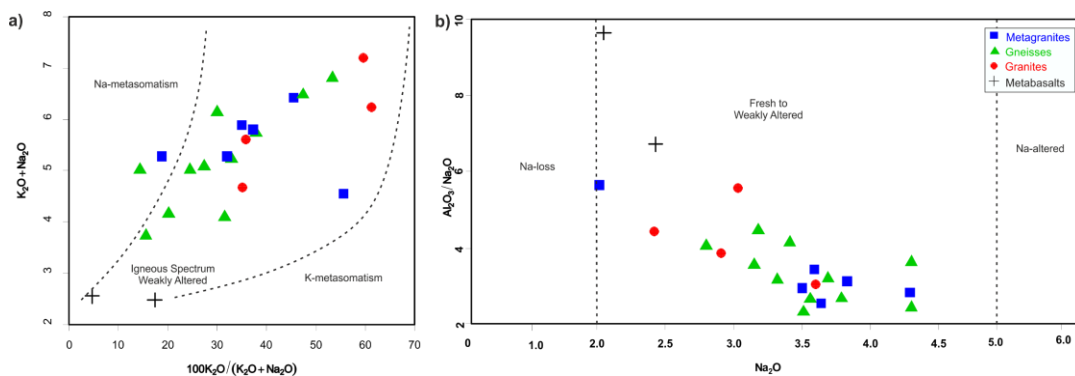


Figure 5.2. Alteration in the samples according to the K_2O and Na_2O loss.

According to the Figure 5.2, two geochemical plots (a and b) that illustrate the chemical composition and alteration patterns of different rock types: metagranites, gneisses, granites, and metabasalts. Plot a) shows the relationship between K_2O+Na_2O and $100K_2O/(K_2O+Na_2O)$. Figure 5.2 points for metagranites, gneisses, and granites mostly fall within the "Igneous Spectrum Weakly Altered" field, suggesting these rocks have not undergone significant alteration. However, some samples trend towards the Na-metasomatism field, indicating sodium enrichment in

some samples. The metabasalts plot separately, showing lower alkali content overall.

Figure 5.2b) displays $\text{Al}_2\text{O}_3/\text{Na}_2\text{O}$ vs Na_2O , which is effective for assessing sodium alteration in rocks. Most of the felsic rocks (metagranites, gneisses, granites) cluster in the "Fresh to Weakly Altered" field, confirming the interpretation from Figure 5.2a). The metabasalts again plot separately, with higher $\text{Al}_2\text{O}_3/\text{Na}_2\text{O}$ ratios and variable Na_2O content.

Figure 5.2 shows that, the felsic rocks (metagranites, gneisses, granites) show similar geochemical characteristics, suggesting a related origin or similar alteration history. Most samples appear relatively unaltered, but there is evidence of some sodium metasomatism in a subset of the felsic rocks. The metabasalts are geochemically distinct from the felsic rocks, which is expected given their different origins (mafic vs. felsic). There is variability within each rock type, indicating some heterogeneity in composition or alteration intensity.

TiO_2 against MgO , $\text{Fe}_2\text{O}_3/\text{Al}_2\text{O}_3$, Fe_2O_3 and P_2O_5 diagrams show general trends observed for all the samples. Zr and Nb against TiO_2 diagrams also can be seen from Figure 5.3

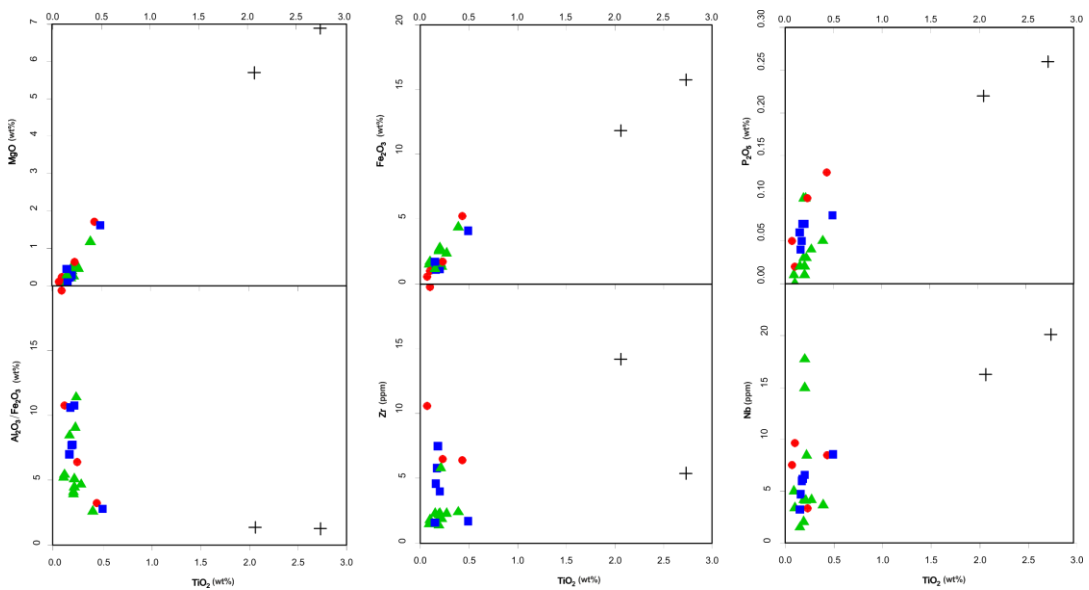


Figure 5.3. Bivariate plots against TiO_2 .

When we look at separately of the each plot of the Figure 5.3, the felsic rocks (metagranites, gneisses, granites) cluster at low TiO_2 (<0.5 wt%) and low MgO (<2 wt%) contents. Metabasalts show significantly higher TiO_2 (>1.5 wt%) and MgO (>5 wt%) contents, reflecting their mafic composition.

Similar to the MgO plot, felsic rocks have low TiO_2 and Fe_2O_3 (<5 wt%) contents. Metabasalts show higher TiO_2 and Fe_2O_3 (>10 wt%) contents, consistent with their mafic nature. Felsic rocks show a slight positive correlation between TiO_2 and P_2O_5 , but with overall low values. Metabasalts have significantly higher P_2O_5 contents, possibly indicating apatite enrichment. Felsic rocks show a wide range of $\text{Al}_2\text{O}_3/\text{Fe}_2\text{O}_3$ ratios at low TiO_2 contents, suggesting variability in plagioclase/mafic mineral ratios. Metabasalts have low $\text{Al}_2\text{O}_3/\text{Fe}_2\text{O}_3$ ratios, consistent with their higher Fe content. Felsic rocks show some variability in Zr content (mostly <10 ppm) at low TiO_2 . Metabasalts have higher Zr contents, possibly reflecting differences in magma fractionation or source composition. Felsic rocks generally have low Nb contents (<10 ppm) with some outliers. Metabasalts show significantly higher Nb contents, which is typical for more evolved mafic rocks.

The clear separation between felsic rocks and metabasalts in all plots of Figure 5.3 indicates distinct petrogenetic origins and compositions. The tight clustering of felsic rocks suggests they are genetically related or derived from similar source materials. The variability within the felsic rock group (especially in $\text{Al}_2\text{O}_3/\text{Fe}_2\text{O}_3$ and trace elements) may indicate some degree of fractional crystallisation or slight differences in source composition.

The metabasalts show characteristics typical of evolved mafic rocks, with enrichments in Ti, Fe, Mg, and certain trace elements (Zr, Nb). The relationships between major and trace elements can provide insights into magmatic processes, metamorphic conditions, and tectonic settings of these rock formations.

Figure 5.4 presents a series of geochemical plots comparing various trace element ratios and concentrations against the Zr/Ti ratio for different rock types. The rock types are represented by different symbols: blue squares (metagranites), green triangles (gneisses), red circles (granites), and black crosses (metabasalts).

Most samples cluster at low Zr/Ti ratios (<0.01), with Th concentrations generally below 20 ppm. Granites (red circles) show the highest Zr/Ti ratios and variable Th content, suggesting more evolved compositions. Metabasalts (black crosses) have the lowest Th and Zr/Ti ratios, consistent with their less evolved, mafic nature.

A positive correlation is observed between Zr/Ti and Nb for most samples. Granites show the highest Nb concentrations and Zr/Ti ratios, indicating enrichment in incompatible elements during fractionation. Metabasalts have low Nb and Zr/Ti ratios, typical of less evolved mafic rocks.

Nb/Th ratios plot shows more scatter, but generally higher Nb/Th ratios for mafic rocks (metabasalts) compared to felsic rocks. The spread in Nb/Th ratios for felsic rocks might indicate varying degrees of crustal contamination or different source characteristics.

Nb/Y ratios are generally low (<2) for most samples, typical of subalkaline rocks. Some granites show higher Nb/Y ratios, potentially indicating a more alkaline affinity for these samples. Granites show the highest Zr/Y ratios, consistent with their more evolved nature and enrichment in incompatible elements.

Higher La/Yb ratios in some samples might indicate greater degrees of fractional crystallisation or derivation from a more enriched source. Metabasalts show low La/Yb ratios, typical of less fractionated mafic rocks.

The clear separation between felsic rocks (metagranites, gneisses, granites) and metabasalts in most plots indicates distinct petrogenetic origins and compositions. The granites consistently show the highest incompatible element concentrations and ratios, suggesting they are the most evolved rocks in the suite.

The variability within the felsic rock groups, particularly in trace element ratios, may indicate different degrees of fractional crystallisation, varying extents of crustal contamination, heterogeneity in source composition. The metabasalts show characteristics typical of less evolved mafic rocks, with low incompatible element concentrations and ratios (Figure 5.4).

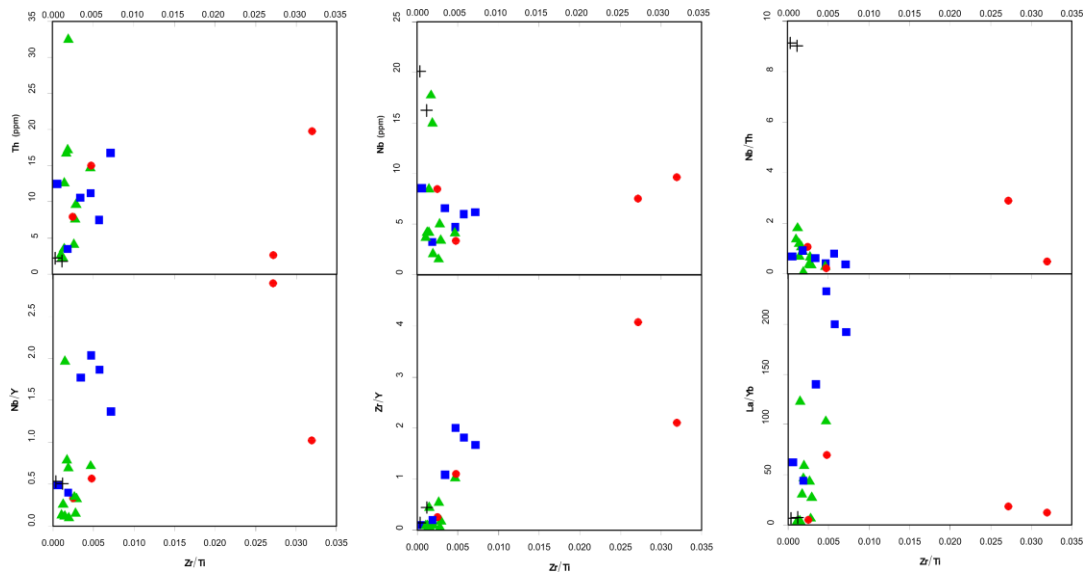


Figure 5.4. Bivariate plots against Zr/Ti.

5.4.2 Tectono-magmatic differentiation of the study area

Tectonic discrimination diagrams are used for revealing the rocks collisional to post-collisional character. In Figure 5.5 you can see 4 different environment which can be explain as; Field 1: typically represents syn-collisional granites. Several green triangles (gneisses) plot in this area, suggesting some of these rocks may have formed during a continental collision event. Field 2: This field often corresponds to within-plate granites. A few gneisses (green triangles) plot here, indicating some of the gneisses may have formed in an extensional or rifting environment. Field 3: This field is generally associated with volcanic arc granites. Some blue squares (metagranites) and green triangles plot in this region, suggesting a subduction-related origin for these samples. Field 4: This field typically represents post-collisional and late-orogenic granites. Most of the red circles (granites) and some blue squares (metagranites) plot here, indicating these rocks likely formed in the later stages of an orogenic event.

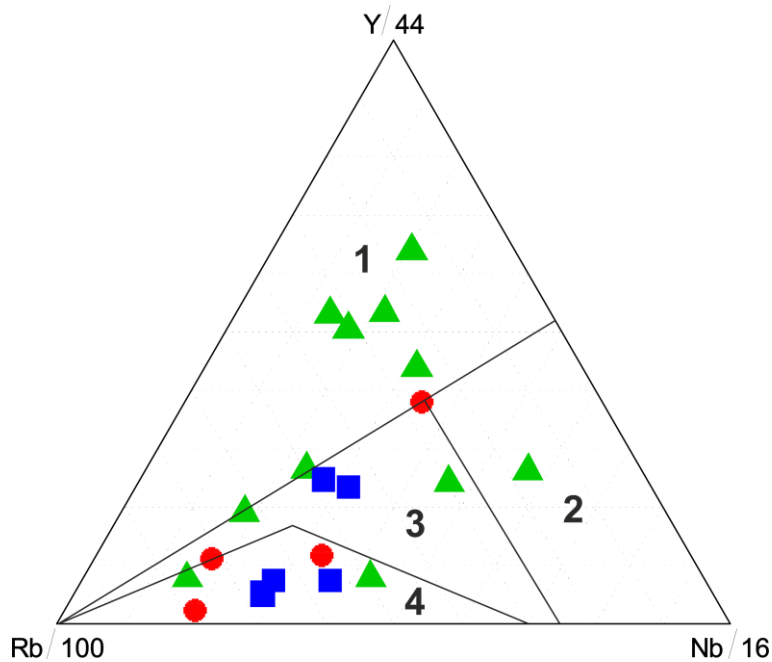


Figure 5.5. Rb/100-Y/44-Nb/16 diagram (Thieblemont and Cabanis, 1990).

The distribution of samples across multiple fields in Figure 5.5 suggests a complex tectonic history for the area, possibly involving multiple phases of magmatism in different tectonic settings. The gneisses (green triangles) show the widest distribution, spanning fields 1, 2, and 3. This could indicate multiple sources or protoliths for these metamorphic rocks, or it might reflect element mobility during metamorphism. The metagranites (blue squares) cluster mainly in fields 3 and 4, suggesting they may have formed in a volcanic arc setting and/or during the later stages of an orogenic event. The granites (red circles) plot predominantly in field 4, indicating they are likely post-collisional or late-orogenic intrusions. The overall trend from field 3 to field 4 for the granitic rocks (blue squares and red circles) could represent an evolution from a subduction-related setting to a post-collisional environment.

The analysis of very incompatible elements (VICE) and moderately incompatible elements (MICE) provides crucial insights into the genetic links, source characteristics, and tectonic settings of the rocks in the Uludağ Massif. The plots of Nb/Y against Zr/Ti, Ti/Y, Nb/Th, La/Yb, and $^{143}\text{Nd}/^{144}\text{Nd}$ (Figure 5.6) reveal significant variations among the different rock units in the Uludağ Massif. These

variations suggest a heterogeneous source region, likely reflecting different degrees of mantle metasomatism and crustal contamination.

Nb/Y vs. Zr/Ti plot shows a clear separation between the metabasalts and the other rock types. The metabasalts have lower Nb/Y and Zr/Ti ratios, suggesting a more depleted mantle source. In contrast, the gneisses, metagranites, and granites show higher and more variable ratios. The spread in Nb/Y ratios for felsic rocks might indicate varying degrees of crustal contamination or different source characteristics.

Nb/Y vs. Ti/Y trend observed in this plot (Figure 5.6) further supports the distinction between the metabasalts and other rock types. The higher Ti/Y ratios in the metabasalts are consistent with a less fractionated, more primitive source, while the lower Ti/Y ratios in the other rocks suggest more extensive fractionation or a more evolved source.

Nb/Y vs. Nb/Th plot is particularly useful for identifying mantle metasomatism. The variable Nb/Th ratios observed in the gneisses and granites suggest different degrees of metasomatic enrichment in their source regions. The metabasalts, with their higher Nb/Th ratios, appear to have been less affected by such processes.

Nb/Y vs. La/Yb variation in La/Yb ratios across the samples indicates different degrees of light rare earth element (LREE) enrichment. The generally higher La/Yb ratios in the gneisses and granites compared to the metabasalts suggest a more enriched source for these rocks, possibly due to crustal contamination or metasomatic processes.

Nb/Y vs. $^{143}\text{Nd}/^{144}\text{Nd}$ plot provides insights into the isotopic characteristics of the source regions. The spread in $^{143}\text{Nd}/^{144}\text{Nd}$ ratios, particularly among the gneisses and granites, suggests mixing between different isotopic reservoirs, possibly including both mantle and crustal components.

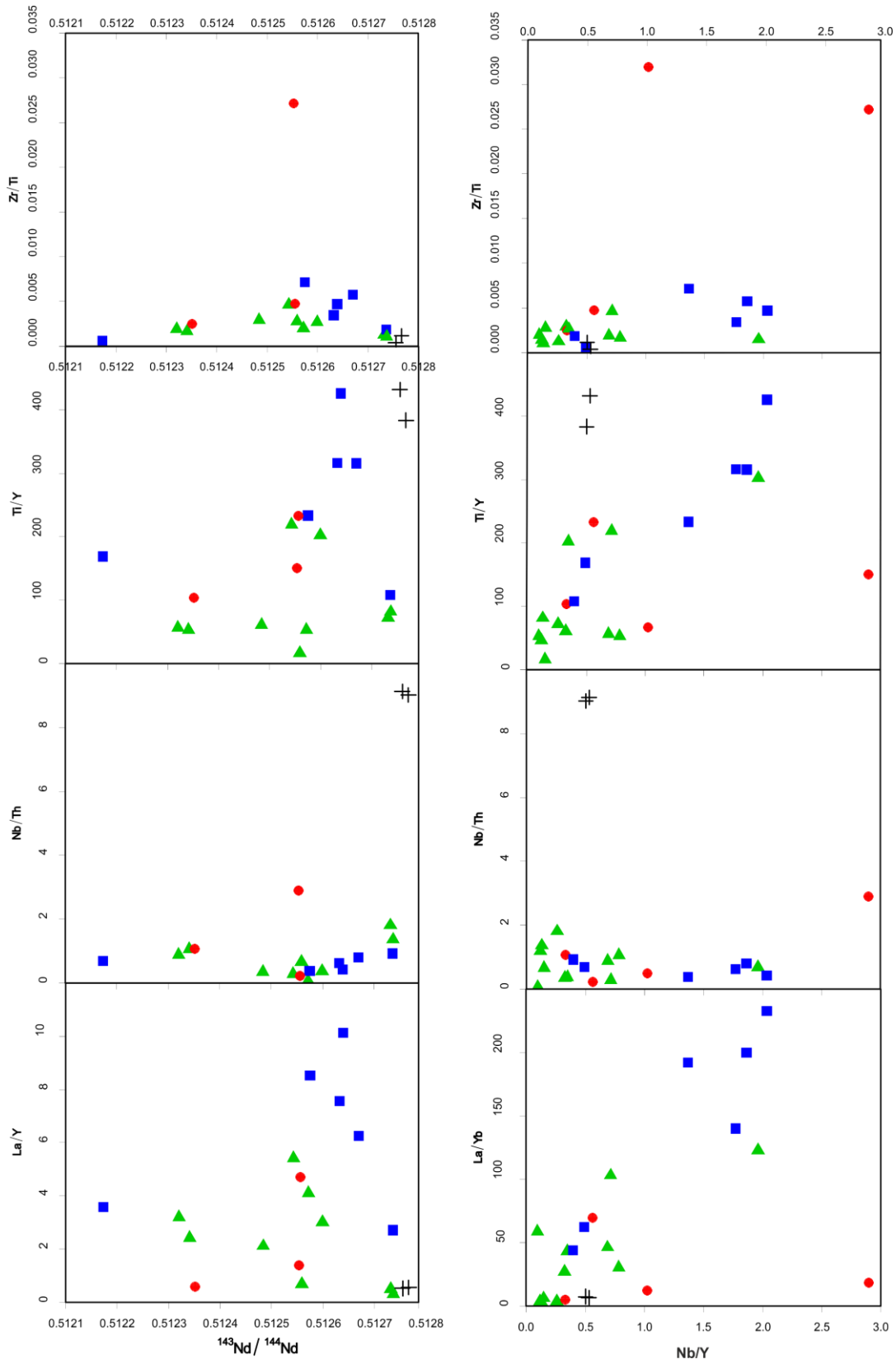


Figure 5.6. Bivariate plots of VICE/MICE ratios against $^{143}\text{Nd}/^{144}\text{Nd}$ and Nb/Y .

In Figure 5.7, all of the samples collected from the study area are plotted on Rb/Y+Nb, Nb/Y, Rb/Ta+Yb and Ta/Yb binary diagrams of Pearce et al. (1984). In the tectonic classification of the samples according to Rb versus Y+Nb, Nb versus Y, Rb versus Ta+Yb and Ta versus Yb, the samples generally show VAG (volcanic arc granite) and synCOLG (collisionally synchronous granite) tectonic separation windows. The Rb/Y+Nb and Nb/Y plots show the occurrence of WPG (intraplate granite).

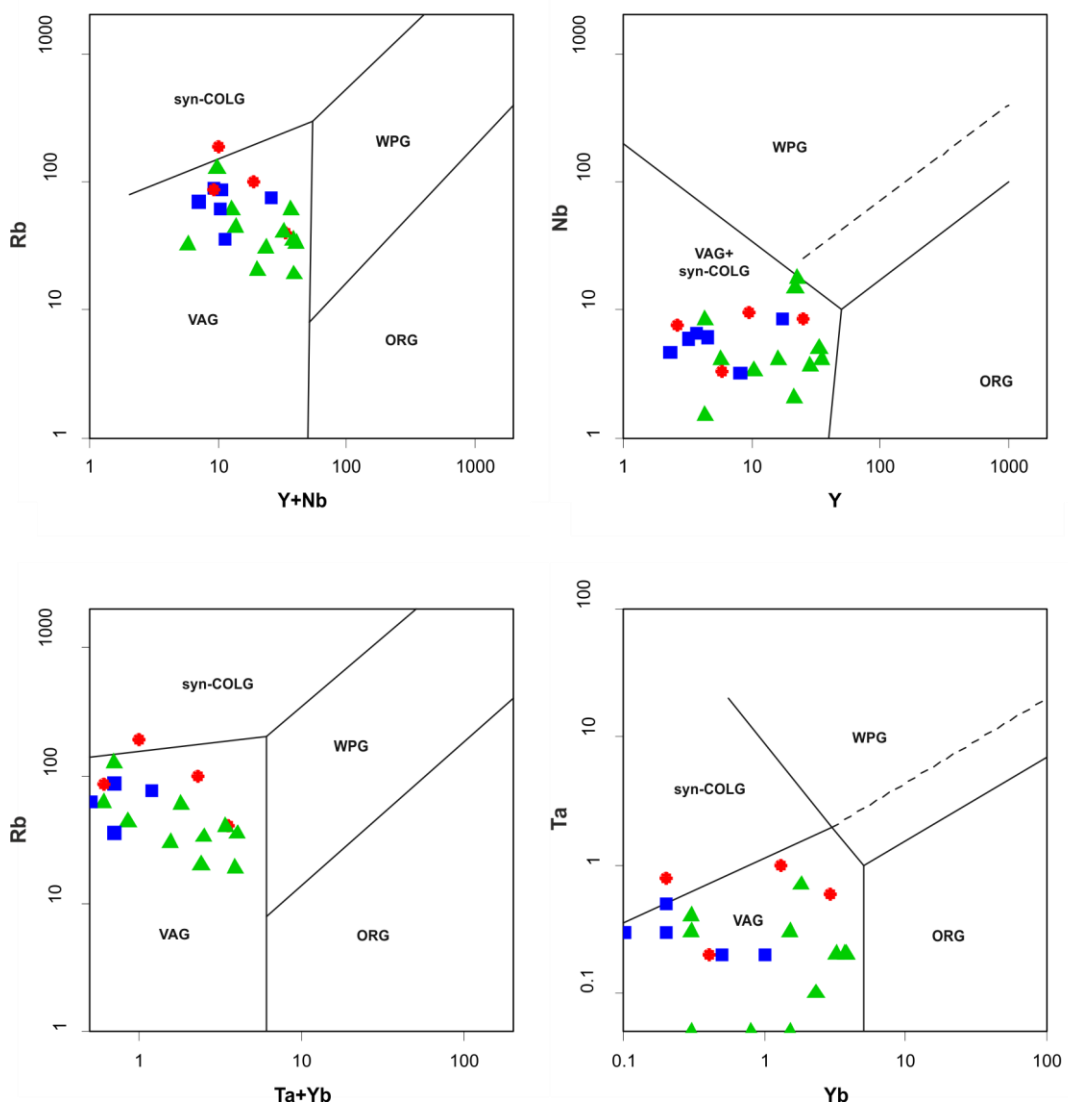


Figure 5.7. Tectonic classification of the samples according to Rb versus Y+Nb, Nb versus Y, Rb versus Ta+Yb and Ta versus Yb (Pearce et al. 1984).

continental margin magmatism. In contrast, some granite and metabasalts are associated with intraplate volcanism. Likewise, the Th/Ta vs. Yb graph in the lower right corner of Figure 5.9 reveals that some gneiss samples have chemical properties indicating that they derived from a region close to the oceanic arc of the active continental margin, while metabasalts have chemical properties indicating that they may have been derived from an environment similar to mid-ocean ridge basalts.

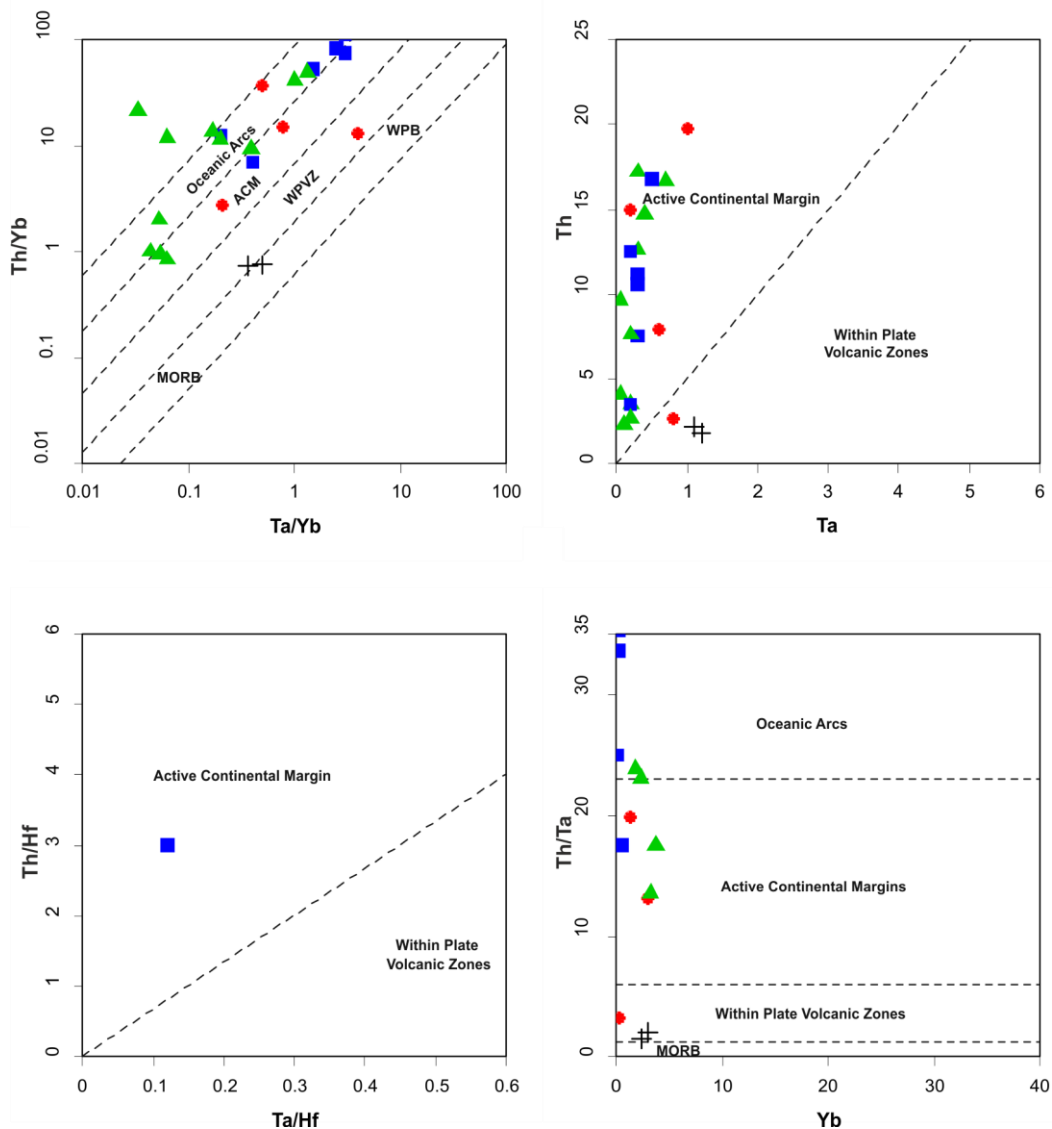


Figure 5.9. The revised Th/Yb - Ta/Yb diagram is divided into three tectonic zones: oceanic arcs, active continental margins (ACM), and intraplate volcanic zones (WPVZ). The intraplate basalts (WPB) and MORB (mid-ocean ridge basalts) represent the zones previously defined by Pearce (1982, 1983), Schandl and Gorton (2002).

When we look at another diagram showing magmatic chemistry relations (Figure 5.10), we see that the rocks forming the Uludağ Massif are generally composed of alkaline or highly alkaline rocks and the granites cutting these rocks are generally formed on the active continental margin or in a volcanic arc related environment. The metabasalts of the Sazak Formation, which tectonically overlies the Uludağ Massif, are likely intraplate basalts may have been formed due to magmatism chemistry showing a transition from alkaline series to tholeiitic series outside this volcanic arc.

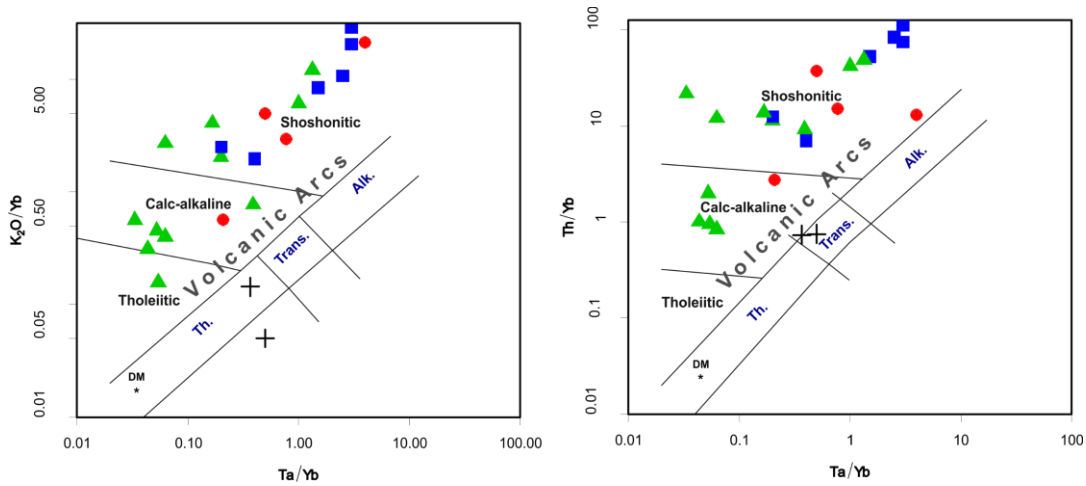


Figure 5.10. The Ta/Yb-Th/Yb diagram (Pearce, 1982) shows that all samples have geochemistry related to volcanic arcs except for the 1901 and 1905 Sazak Formation metabasalts. Metabasalts appear to be in the transition zone.

In Figure 5.11, granite types are classified according to Whalen et al. (1987). Granite samples 1813-P1 and 1813-P2 (Kapıdağ granites) are within the I-S type granite window, while the Central Uludağ granites that cut the Uludağ Massif appear to be A-type granites. A-Type granites have high Nb, Ga, and Y contents and low Al, Mg and Ca contents regarding REEs. In addition to this data, the study of Altunkaynak et al. (2012), which shows that the Topuk Granitoid belongs to the I-Type Granite class, supports this conclusion.

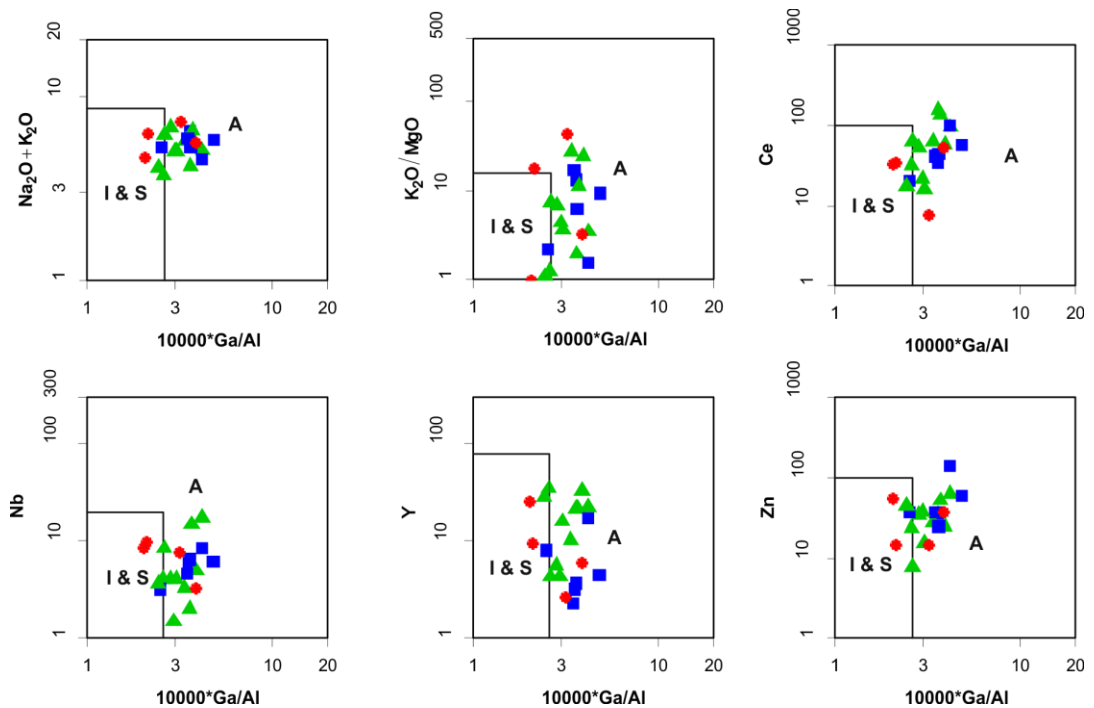


Figure 5.11. Plots of the samples on the granite classification diagrams by Whalen et al. (1987): $10000\text{Ga}/\text{Al}$ versus $\text{K}_2\text{O}/\text{MgO}$, Nb, Ce, Y, Zn binary plots are meaningful for differentiation into A, I and S-type granites.

Rare earth elements (REE) are known to be the least mobile elements during hydrothermal alteration and low-grade metamorphism (Michard, 1989; Peate, 1997). Therefore, rare earth element diagrams normalised to chondrite provide important information about the source of magma and the crystallisation evolution of magma.

When all of the samples are plotted on rare earth element diagram normalised to chondrite and primitive mantle, it is seen that the samples are enriched in light rare earth elements (LREE) compared to heavy rare earth elements (HREE). The graphs in Figure 5.12 and Figure 5.13 give us the primitive mantle normalized spider profile data. All these profiles clearly show that all samples, including granites, gneisses, metagranites and metabasalts, give negative K (Potassium), P (Phosphorus) and Ti (Titanium) anomalies. Negative anomalies in certain elements such as K, P and Ti in spider plots normalised to the primitive mantle are indicative of various geological processes and conditions. The K negative anomaly can reflect

potassium mineral behaviour during igneous processes, such as preferential incorporation into certain minerals or phases. K is commonly found in minerals such as feldspars, micas and some accessory minerals. Fragmentation or preferential crystallisation of these minerals during igneous processes is thought to reduce potassium in the residual melt, causing the negative anomaly. Similar to K, P mineral also shows a negative anomaly in spider plots. This behaviour is probably related to its partitioning during different igneous processes. P is commonly associated with apatite, a mineral in many igneous rocks. Fragmentation or preferential crystallisation of apatite can lead to a reduction of P in the residual melt. The negative Ti anomaly occurs during its association with various minerals and phases during magmatic differentiation. Ti is usually found in minerals such as ilmenite and titanite. The fragmentation of these minerals can cause a decrease in Ti concentrations in the residual melt. Regarding spider plots normalised to the primitive mantle, these negative anomalies (K, P and Ti) are assumed to be extracted in certain mineral phases during the crystallisation of magmas and that fractional crystallisation occurred. In addition, differentiation processes within magmatic systems in which certain minerals or phases contain these elements can lead to the negative anomalies observed in spider graphs.

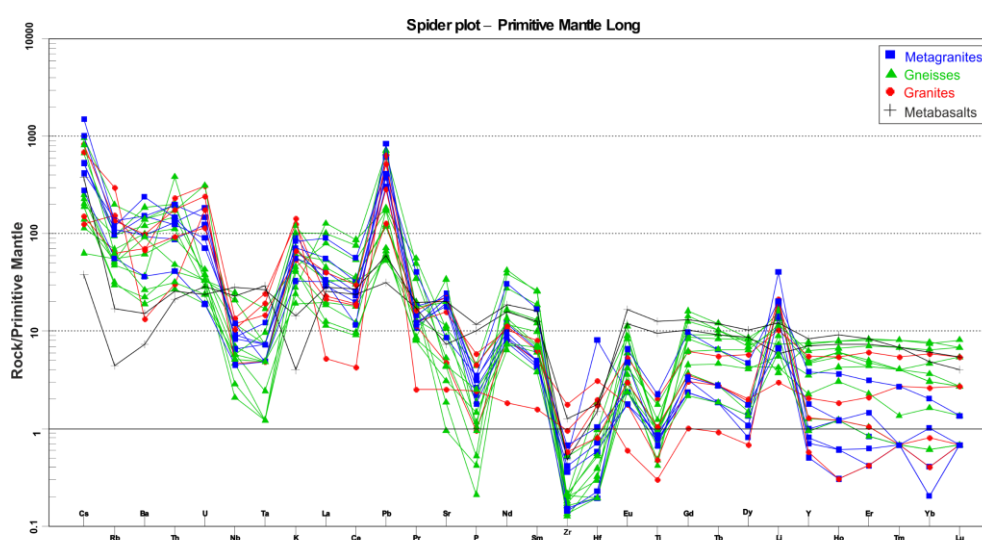


Figure 5.12. Spider diagrams of all samples normalized to primitive mantle (normalizing values are taken from Sun and McDonough, 1989), showing negative K, P and Ti anomalies and relatively negative Zr and Hf anomalies. The figure also shows positive U, Pb and Li anomalies.

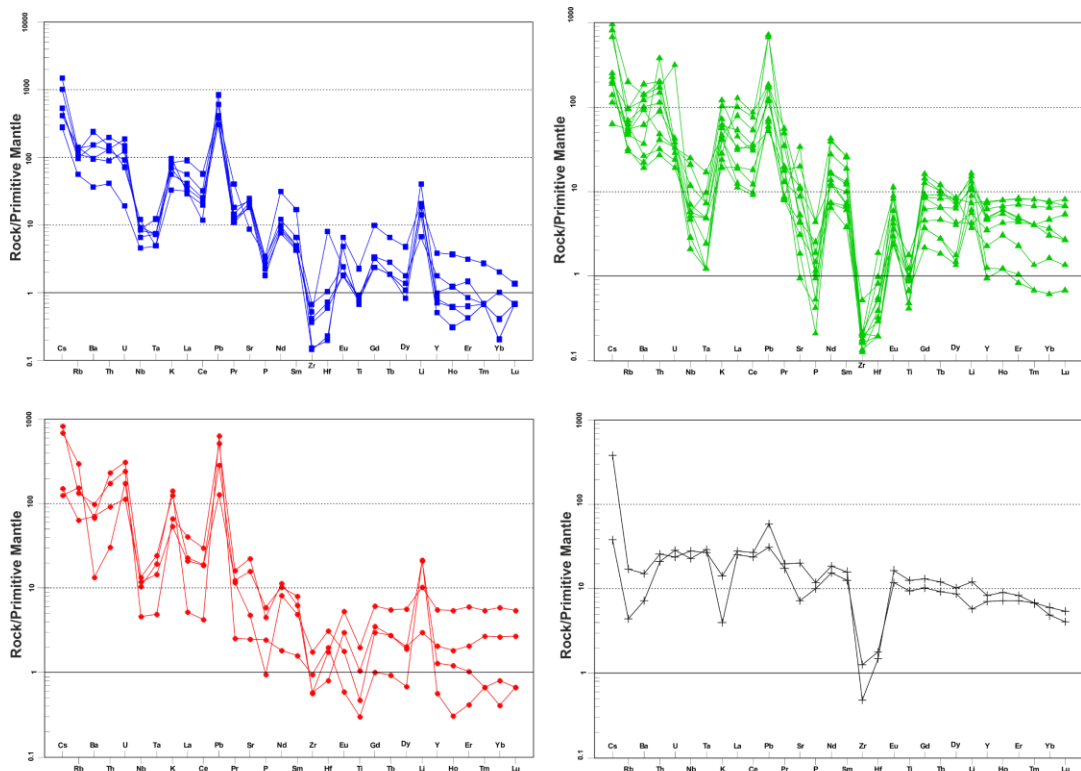


Figure 5.13. Spider plots of the primitive mantle separated by units show negative K, P and Ti anomalies and relatively negative Zr anomalies. U and Pb anomalies are positive.

Figure 5.14 and Figure 5.15 show the REE plots normalised to chondrite values. These figures show LREE enrichment and the presence of an Eu anomaly. Several anomalies or deviations from the standard REE model can occur. These anomalies are usually due to various magmatic processes affecting distribution of rare earth elements. Specific anomalies observed in granitic rocks and their associated minerals can be seen in Figure 5.14 and Figure 5.15. The first is the enrichment of light rare earth elements (LREE). Granitic rocks generally exhibit a marked enrichment in light rare earth elements (La - Sm) compared to heavy rare earth elements (Gd - Lu). This enrichment is primarily attributed to minerals such as feldspars (e.g. plagioclase and alkali feldspar) and micas (e.g. muscovite and biotite), which preferentially contain LREE during their formation. Another anomaly is the Europium (Eu) anomaly. A distinctive feature in some granitic rocks is the Eu anomaly, which shows a significant negative anomaly in REE

patterns normalised to chondrite. Especially in plagioclase-containing rocks that contain more Eu than expected from the overall REE pattern, it is caused by the breakdown of plagioclase or feldspar and its ejection from the melting part of the rock by partial melting (Rollinson, 1993). The Eu anomaly results in a distinct downward slope along the position of Eu on the graph. The development of a negative Eu anomaly characterises the expulsion of plagioclase from the system. The occurrence of a post-magmatism alteration can also cause anomalies in the spider diagram pattern of granitic rocks. Secondary processes, such as hydrothermal alteration or metamorphism, can lead to adding or removing specific REEs, causing deviations in the chemistry indicative of the original igneous texture.

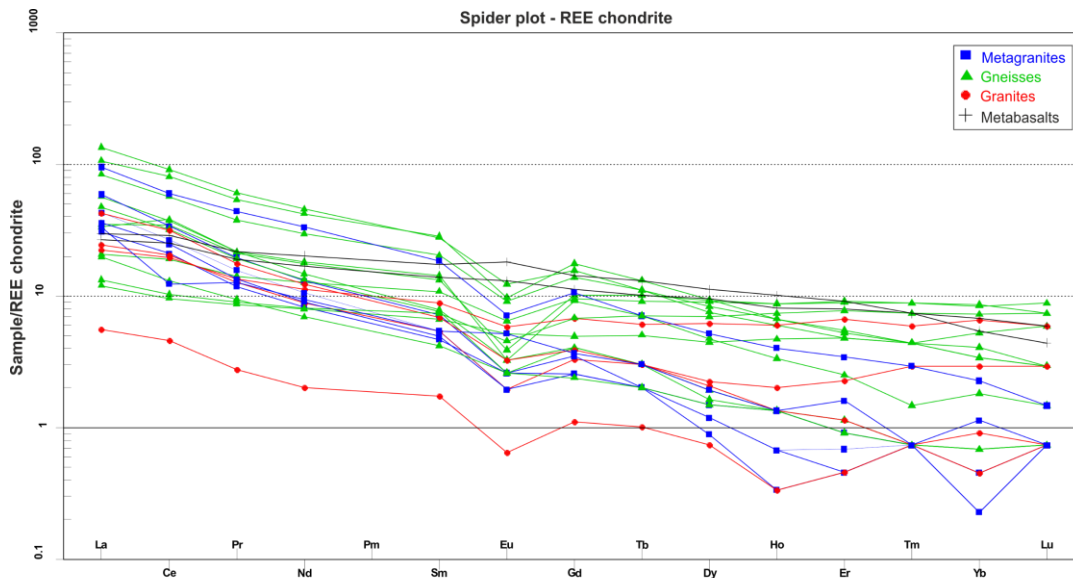


Figure 5.14. Spider diagram of all samples normalized to chondrite (normalizing values are taken from McDonough and Sun, 1995).

Figure 5.14 and Figure 5.15 show negative Eu anomalies for all samples of the Uludağ Massif (except 1901 and 1905 according to the general trends at the graphs). Metabasalts (samples 1901 and 1905) show positive Eu anomalies. All samples except these two samples show negative Eu anomalies. The negative

anomaly in Eu is related to the breakup of feldspar during magma crystallisation or feldspar remaining in the source.

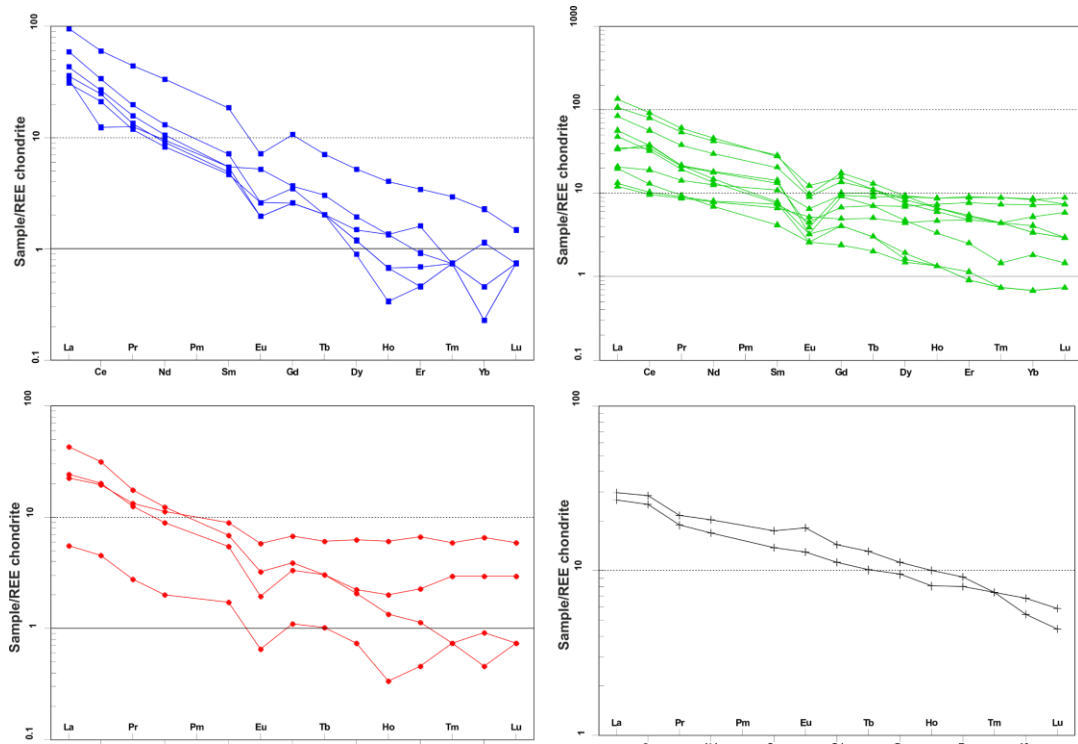


Figure 5.15. Unit-specific REE spider plots normalized to chondrite (normalizing values are taken from McDonough and Sun, 1995).

Figure 5.16 and Figure 5.17 are spider diagrams normalized to the Ocean Ridge Granites (ORG) by Pearce et al. (1984). Sample chemistries show enrichment for elements such as Rb, Ba, Th, Ce and Sm. In contrast, Zr and Hf show depletion.

The enrichment of Rb, Ba, Th, Ce and Sm indicates that it resulted from processes such as fractional crystallisation, assimilation of crustal material or the influence of fluids. Negative anomalies of Zr and Hf in ORG spider plots could mean these elements were less compatible during magmatic processes, forming ocean ridge granites. That could indicate that they were preferentially retained in minerals extracted from the magma source or depleted during the formation of accessory minerals.

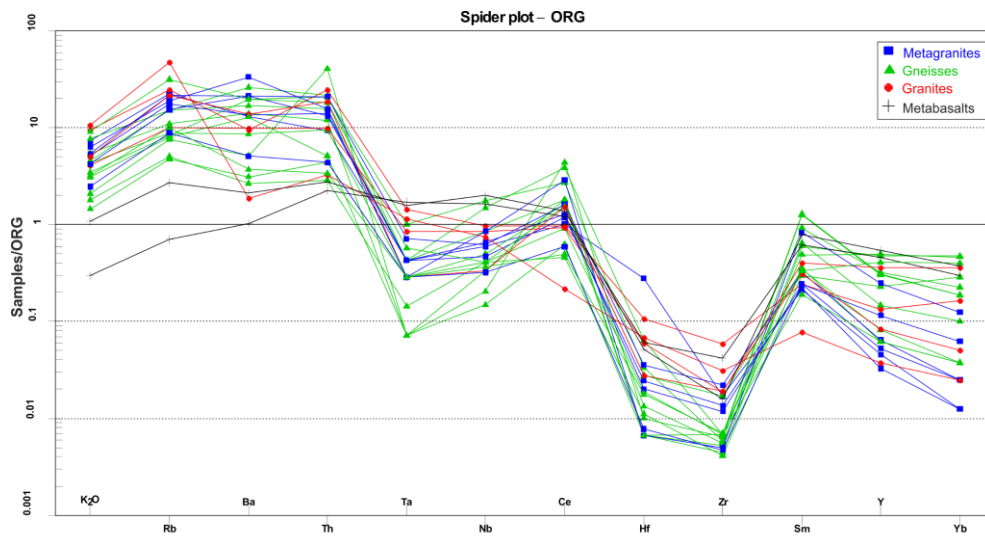


Figure 5.16. Spider diagram of all samples normalized to ORG (Ocean Ridge Granite) shows negative Zr and Hf anomalies (Pearce et al. 1984).

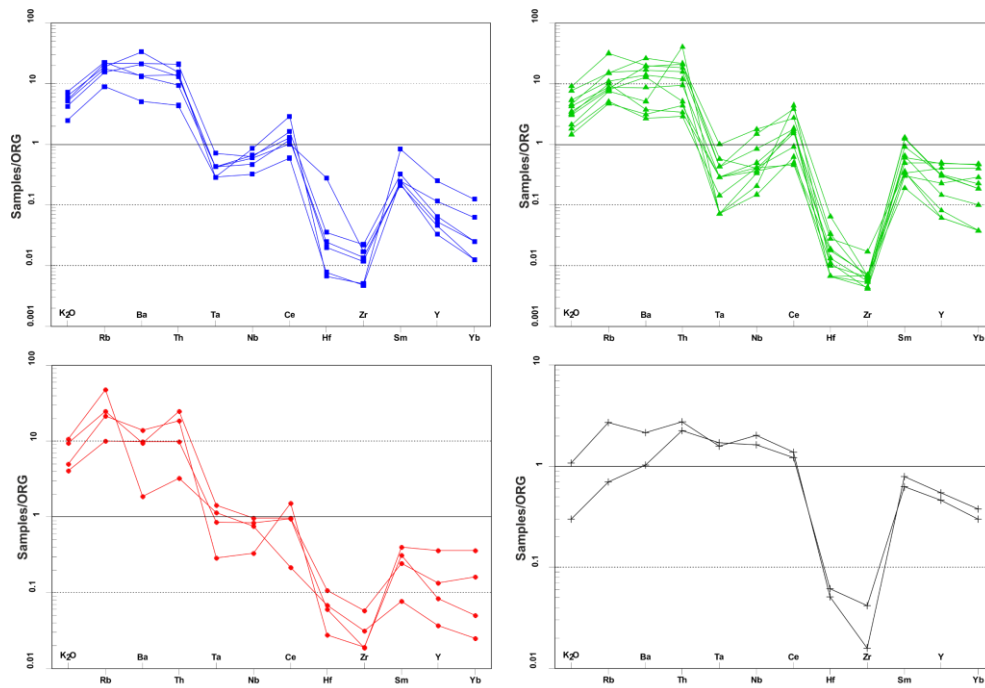


Figure 5.17. Unit-specific spider diagrams of all samples normalized to ORG (Ocean Ridge Granite) show negative Zr and Hf anomalies in each rock unit sample.

According to REE plots normalized to upper crustal chemistry (Figure 5.18 and Figure 5.19), HFSE elements such as Ti, Zr and Hf generally exhibit depletion compared to upper crustal values by Taylor and McLennan (1985). These HFSEs tend to be less abundant in crustal rocks due to their preferential retention in minerals during magmatic processes. LILE) and LREE such as Rb, Ba, Th, Ce and Sm usually show positive anomalies. These elements are more abundant in rocks derived from crustal magma due to their proximity to minerals formed during magmatic differentiation processes. K and P elements show lower concentrations or depletion than chondritic values due to their relative enrichment in the upper crust. These anomalies indicate specific processes such as magmatic differentiation, metamorphism or alteration.

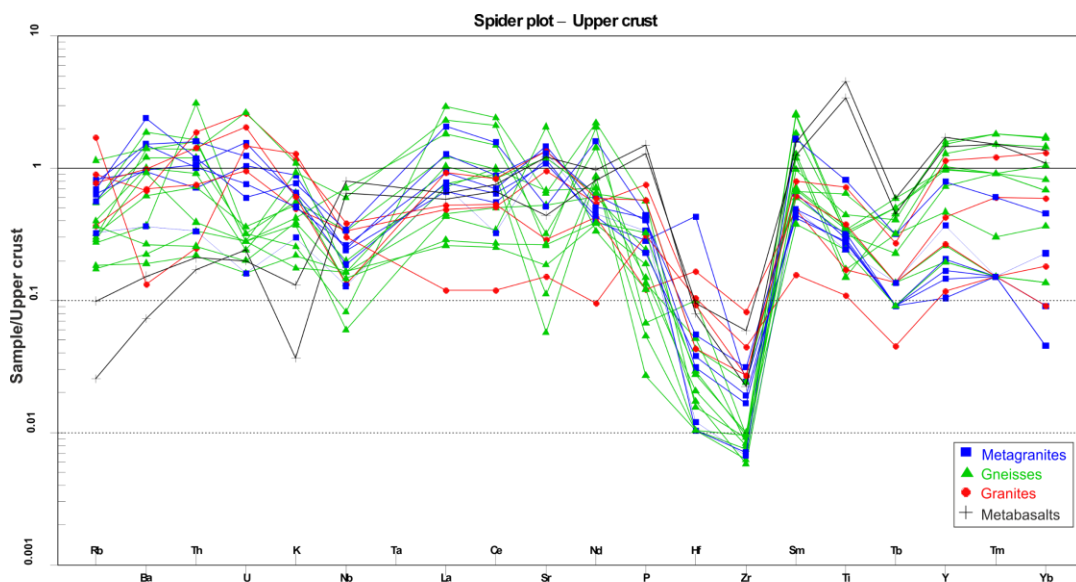


Figure 5.18. REE spider plot for all the samples normalized to the upper crust shows negative K, P and Ti anomalies (normalization values are from Taylor and McLennan, 1985).

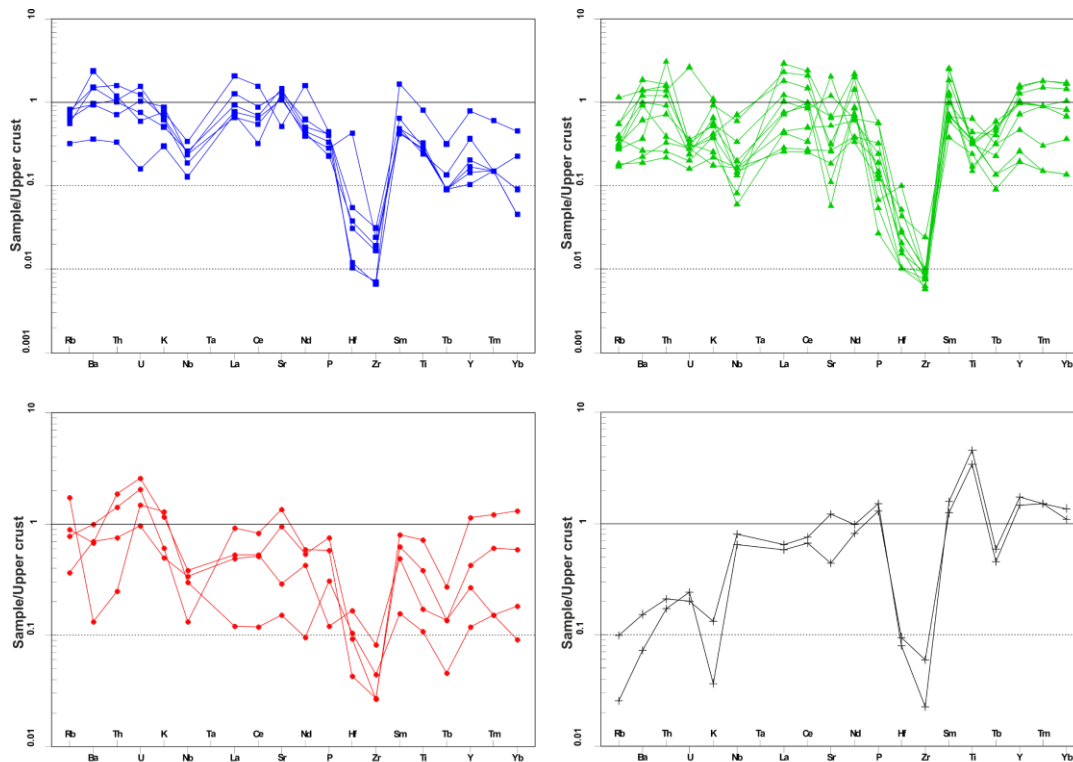


Figure 5.19. Unit-specific REE sider plots for the samples normalized to the upper crust shows negative K, P and Ti anomalies.

5.4.3 Radiogenic Isotopes of the Rocks

Sr and Nd isotope ratios are used in many studies to trace the evolution of metamorphic and igneous rocks. In the scope of this study, $^{87}\text{Sr}/^{86}\text{Sr}$ and $^{144}\text{Nd}/^{143}\text{Nd}$ radiogenic isotope analyses were performed, and the results of the analyses were used to analyze the formation or metamorphism regimes of the samples taken from the field by using radiogenic isotope analysis graphs and to distinguish the magmatic locations of the samples during their formation. The results of the analysis are given in Table 5.6.

Table 5.6. Samples names and radiogenic isotope data results. Table 6.5. Samples names and radiogenic isotope data results.

Sample no.	Rock type	$^{87}\text{Sr}/^{86}\text{Sr}$	Rb (ppm)	Sr (ppm)	$^{87}\text{Sr}/^{86}\text{Sr}(\text{T})$ (*)	$^{143}\text{Nd}/^{144}\text{Nd}$	Nd (ppm)	Sm (ppm)	$^{143}\text{Nd}/^{144}\text{Nd}(\text{T})$ (*)	$\epsilon\text{Nd}(\text{T})$	TDM
1802	metagranite	0.705658 ± 14	90.00	407.00	0.705358	0.512670 ± 2	10.30	1.9	0.512646	0.98	0.683
1803	gneiss	0.713155 ± 13	6.20	91.00	0.707161	0.512320 ± 3	52.90	11.6	0.512129	-4.4	1.463
1804	gneiss	0.711793 ± 15	33.10	112.00	0.709116	0.512341 ± 2	37.30	8.3	0.512147	-4.05	1.459
1809	gneiss	0.707363 ± 23	20.20	65.00	0.704549	0.512732 ± 2	9.90	2.7	0.512495	2.73	1.179
1810	gneiss	0.714110 ± 25	35.00	20.00	0.698252	0.512559 ± 2	22.20	5.4	0.512347	-0.15	1.253
1811	gneiss	0.710916 ± 6	43.90	39.00	0.700719	0.512484 ± 5	22.70	5.8	0.512262	-1.82	1.572
1812	gneiss	0.706357 ± 6	30.10	226.00	0.705151	0.512572 ± 2	57.20	11.3	0.512400	0.88	0.887
1813-P1	granite	0.706324 ± 12	40.30	334.00	0.706091	0.512351 ± 2	14.00	3.6	0.512303	-5.35	1.913
1814	metagranite	0.706200 ± 4	86.60	471.00	0.705951	0.512575 ± 2	16.30	2.9	0.512552	-0.85	0.788
1817	metagranite	0.706035 ± 5	61.90	515.00	0.705872	0.512632 ± 3	13.20	2.2	0.512610	0.29	0.670
1819	metagranite	0.705793 ± 4	69.90	380.00	0.705544	0.512639 ± 1	11.30	2	0.512616	0.4	0.697
1820	gneiss	0.707687 ± 8	126.40	420.00	0.704962	0.512543 ± 6	16.70	3.1	0.512381	0.52	0.868
1821	granite	0.706844 ± 3	86.00	471.00	0.706626	0.512556 ± 2	15.40	2.8	0.512535	-1.28	0.832
1822	granite	0.710399 ± 14	190.10	53.00	0.706122	0.512553 ± 5	2.50	0.7	0.512521	-1.56	1.828
1901	metabasalt	0.705531 ± 25	2.80	154.00	0.705190	0.512767 ± 1	21.20	5.6	0.512291	4.67	0.987
1902-JA	metagranite	0.710154 ± 4	75.80	181.00	0.709586	0.512173 ± 2	41.80	7.5	0.512150	-8.7	1.347
1902-JB	gneiss	0.704660 ± 3	31.90	718.00	0.704258	0.512599 ± 4	8.70	1.7	0.512429	1.45	0.835
1903	metagranite	0.704740 ± 2	35.60	456.00	0.704634	0.512736 ± 2	11.80	2.2	0.512712	2.27	0.596
1904	gneiss	0.708454 ± 14	40.20	93.00	0.707868	0.512737 ± 2	10.10	3	0.512698	2	1.597
1905	metabasalt	0.705331 ± 29	10.90	427.00	0.704852	0.512755 ± 2	25.40	7.1	0.512251	3.9	1.206

*(T) values are different for the lithologies. According to the U-Pb Zircon dating T=33 Ma for metagranites, T=220 Ma for gneisses, T=29.53 Ma for the Central Uludağ Granite, 47.87 Ma for the Kapıdağ Granite (1813-P1) and T=455 Ma for metabasalts.

The graphs obtained from $^{87}\text{Sr}/^{86}\text{Sr}$ and $^{144}\text{Nd}/^{143}\text{Nd}$ radiogenic isotope analyses are analyzed under four headings. These are metagranites, gneisses, granites and basalts, respectively. This study's Geochronology section gives the age data needed for constructing these graphs (Chapter 7). Metamorphism age data of metabasalts were used as a result of the study conducted by Yiğitbaş et al. (2018). Because there is no age data from the geochronology studies from this study. All the age results can be seen from Table 6.2. Some samples from this study has no age data as can be seen from the Table 6.2. Because of that initial age data are taken as mean values of same lithological units if there is no age data. (Metagranites(T)=33Ma, Gneisses(T)=220Ma, Central Uludağ Granites (T)=29,53 Ma and, Kapıdağ Granites(T)=47,87 Ma from this study, metabasalts(T)= 455 Ma (Yiğitbaş et al. 2018)).

The Zindler and Hart (1986) mantle origins plot in Figure 5.28 was used to interpret radiogenic isotope data.

5.4.3.1 The South Uludağ Metagranites

According to the results of radiogenic isotope analyses of the South Uludağ Metagranites, the $^{87}\text{Sr}/^{86}\text{Sr}$ data are between 0.7050 and 0.7095 and ϵNd data ranges from -8.7 to +2.27 when the average age of these rocks is taken as 33 Ma (Figure 5.20).

$^{87}\text{Sr}/^{86}\text{Sr}$ (T) vs. Age graph shows the evolution of $^{87}\text{Sr}/^{86}\text{Sr}$ ratios over time. The blue rectangles at the left represent the current measured $^{87}\text{Sr}/^{86}\text{Sr}$ ratios of the metagranite samples. The dashed blue lines projecting back in time represent the possible evolution paths of these ratios.

The current $^{87}\text{Sr}/^{86}\text{Sr}$ ratios cluster between ~0.704 and 0.710, with one sample having a distinctly higher ratio (~0.709). The evolution lines intersect the Uniform Reservoir (UR) line at various points, indicating different model ages. Most samples show relatively steep slopes, suggesting significant Rb/Sr fractionation during their evolution. ϵNd (T) vs. Age graph shows the evolution of ϵNd values over time. ϵNd is a measure of the deviation of the $^{143}\text{Nd}/^{144}\text{Nd}$ ratio from the

Chondritic Uniform Reservoir (CHUR) value. $\epsilon\text{Nd}(T)$ values of the metagranites range from slightly negative (-8.7) to positive (+2.27) values. The evolution lines project back in time, intersecting the Depleted Mantle (DM) line at various points. The slopes of these lines vary, indicating different Sm/Nd ratios in the source or during evolution.

If we look at the overall the model age graphs, the intersections of the evolution lines with the DM line in the ϵNd plot represent the TDM (Time of Depleted Mantle) model ages. These ages range from approximately 1.0 to 1.8 Ga (billion years), suggesting that the crustal precursors of these metagranites were extracted from the mantle during the Paleoproterozoic to early Mesoproterozoic eras.

The spread in initial ϵNd values (where lines intersect the y-axis) indicates that the metagranites were likely derived from sources with varying degrees of crustal contamination or from heterogeneous crustal sources. The difference between the TDM ages and the presumed crystallisation age of the metagranites ($T \approx 33\text{Ma}$) represents the crustal residence time of their source materials.

The variability in slopes and model ages suggests a complex, multi-stage history for these rocks, possibly involving mixing of materials with different crustal residence times or episodes of crustal reworking. The relatively high $^{87}\text{Sr}/^{86}\text{Sr}$ ratios coupled with the range of ϵNd values suggest that these metagranites likely formed through partial melting of older crustal materials, possibly with some input from more juvenile sources.

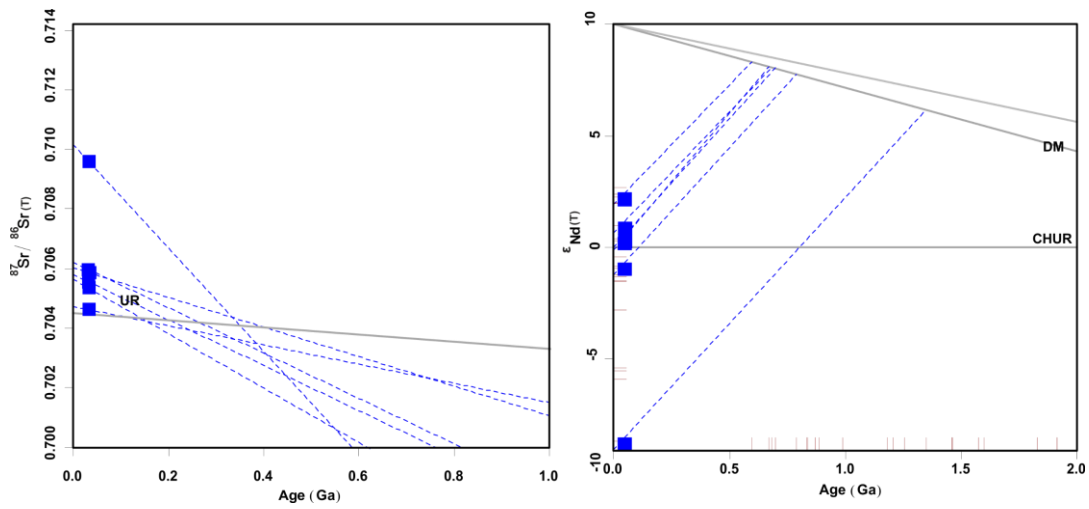


Figure 5.20. $^{87}\text{Sr}/^{86}\text{Sr}$ and ϵNd values when age data is calculated as 33 Ma for metagranites.

Samples from 1802, 1814, 1817, 1819, and 1903 appear to may have been formed by the island-arc volcanism. The crystallisation age of the sample 1902P-A is 33 Ma with ϵNd and $^{87}\text{Sr}/^{86}\text{Sr}$ values, it is probably formed in a region different from other metagranites, probably between island arc volcanism and continental crust. The present and 33 Ma. ago $^{87}\text{Sr}/^{86}\text{Sr}(\text{T})$ and $\epsilon\text{Nd}(\text{T})$ data are given in Figure 5.21.

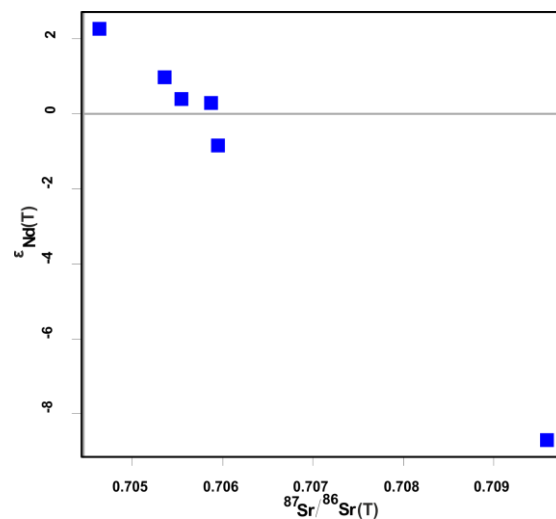


Figure 5.21. $\epsilon\text{Nd}(\text{T})$ - $^{87}\text{Sr}/^{86}\text{Sr}(\text{T})$ Metagranites data.

5.4.3.2 Uludağ Massif Gneisses

According to the results of radiogenic isotope analyses of the gneisses of the Uludağ Massif, the $^{87}\text{Sr}/^{86}\text{Sr}$ (T) data are between 0.7007 and 0.7094 and $\epsilon\text{Nd}(T)$ data varies between -4.6 and +2.8 when the average age of these rocks is taken as 220 Ma (Figure 5.22). The evolution lines project back in time, intersecting the Uniform Reservoir (UR) line at various points. The slopes of these lines vary significantly, indicating different Rb/Sr ratios in the samples. Some lines intersect the UR line at unrealistically old ages (>4.5 Ga), suggesting disturbance in the Rb-Sr system.

With a known crystallization age of (T \approx 220 Ma) gneisses, we can interpret the isotopic compositions at this time point. This corresponds to the Late Triassic period, likely related to a major tectonic or magmatic event.

The TDM ages according to the ϵNd , represented by the intersections of the evolution lines with the DM line, range from approximately 1.0 to 1.5 Ga. This suggests that the protoliths of these gneisses were derived from crustal material that was originally extracted from the mantle during the Mesoproterozoic era. The difference between the TDM ages (1.0-1.5 Ga) and the crystallization age (220 Ma) indicates a significant crustal residence time of 0.8-1.3 Ga for the source materials of these gneisses.

The spread in $\epsilon\text{Nd}(T)$ values at 220 Ma (ranging from about -4.4 to +2.73) suggests that the gneisses were derived from heterogeneous sources or experienced variable degrees of crustal contamination during their formation. The wide range of $^{87}\text{Sr}/^{86}\text{Sr}$ ratios and the unrealistic projections in some samples indicate that the Rb-Sr system has been disturbed, possibly due to metamorphism, fluid interactions, or weathering.

The combination of mostly positive to slightly negative ϵNd values at T (220 Ma) and the Mesoproterozoic TDM ages suggests that these gneisses likely formed through partial melting of relatively juvenile crustal materials, possibly with some mixing of older crustal components.

The Late Triassic age (220 Ma) could be associated with a major orogenic event. The isotopic signatures suggest reworking of Mesoproterozoic crustal materials during this event, possibly in a continental collision or subduction-related setting.

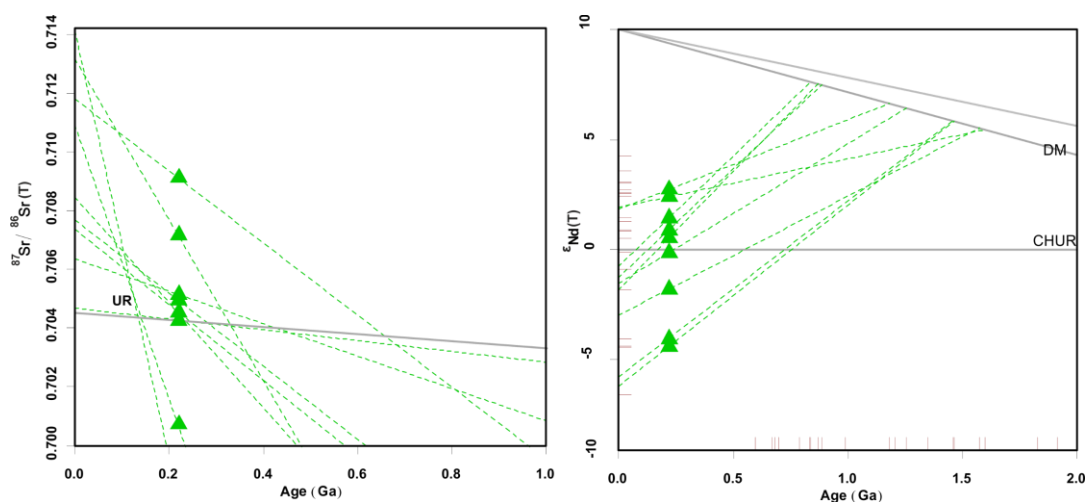


Figure 5.22. $^{87}\text{Sr}/^{86}\text{Sr}$ and ϵ_{Nd} values when age data is calculated as 220 Ma for gneisses.

When the $\epsilon_{\text{Nd}}(\text{T})$ and $^{87}\text{Sr}/^{86}\text{Sr}(\text{T})$ values are analyzed based on 220 Ma age data, it can be concluded that the origin rock of the gneisses is generally related to island arc volcanism. In contrast, the formation mechanism of samples 1810 and 1811 may be related to the subcontinental crust initial. $^{87}\text{Sr}/^{86}\text{Sr}(\text{T})$ and $\epsilon_{\text{Nd}}(\text{T})$ data are given in Figure 5.23.

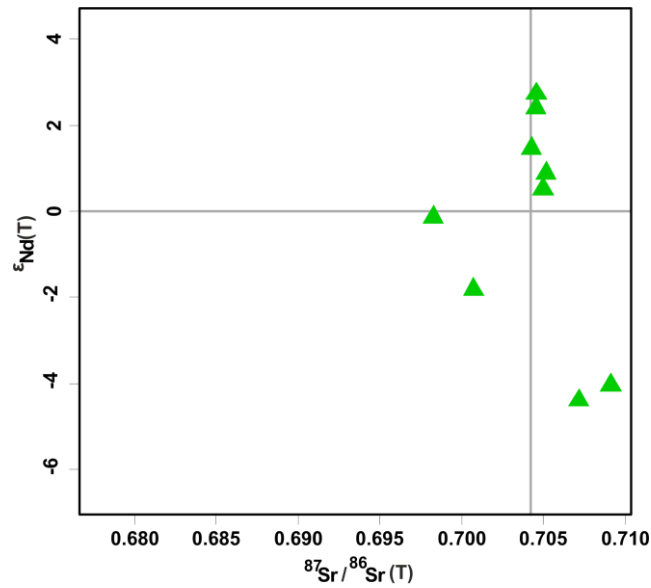


Figure 5.23. $\epsilon_{\text{Nd}}(\text{T})$ - $^{87}\text{Sr}/^{86}\text{Sr}(\text{T})$ gneisses data.

5.4.3.3 Uludağ Granites

According to the results of radiogenic isotope analyses of the Central Uludağ Granite in the Uludağ Massif and the Kapıdağ Granite in the terrain south of the massif, the $^{87}\text{Sr}/^{86}\text{Sr}(\text{T})$ data are between 0.7059 and 0.7068 and $\epsilon_{\text{Nd}}(\text{T})$ data varies between -5.8 and -1.2 when the crystallisation age data of these rocks are taken as 29.53 Ma for the Central Uludağ Granite and 47.87 Ma for the Kapıdağ Granite (1813-P1) (Figure 5.24). The evolution lines project back in time, intersecting the Depleted Mantle (DM) line at various points. The slopes of these lines vary, indicating different Sm/Nd ratios among the samples.

With crystallization ages of 29.53 Ma (Early Oligocene) for Central Uludağ Granites, and 47.87 Ma (Middle Eocene) for the Kapıdağ Granite, we can interpret the isotopic compositions at these time points. These ages correspond to important tectonic events in many parts of the world, possibly related to ongoing continental collision or post-collisional magmatism.

ϵ_{Nd} model ages graph represented by the intersections of the evolution lines with the DM line, range from approximately 0.8 to 1.8 Ga. This possibly suggests that

the source materials of these granites were originally extracted from the mantle during the Neoproterozoic to Paleoproterozoic eras. The significant difference between the TDM ages (0.8-1.8 Ga) and the crystallization ages (29.53-47.87 Ma) indicates a long crustal residence time for the source materials, ranging from about 0.75 to 1.75 Ga.

The negative ϵNd values at the time of crystallization (ranging from about -5.35 to -1.28) suggest that these granites were derived from older crustal materials rather than directly from the mantle. This is consistent with the long crustal residence times calculated.

The tight clustering of $^{87}\text{Sr}/^{86}\text{Sr}$ ratios suggests a relatively homogeneous source in terms of Rb/Sr ratios or efficient mixing of source materials. The combination of negative $\epsilon\text{Nd}(\text{T})$ values and elevated $^{87}\text{Sr}/^{86}\text{Sr}(\text{T})$ ratios at the time of crystallization suggests that these granites likely formed through partial melting of older continental crust, possibly with some minor input from more juvenile sources (Figure 5.24).

The Oligocene-Eocene ages of these granites could be associated with post-collisional magmatism or late-stage orogenic processes. The isotopic signatures suggest reworking of Proterozoic crustal materials during these Cenozoic events.

The slightly older age of the Kapıdağ Granite (47.87 Ma) might represent an earlier phase of magmatism in the region. Its isotopic composition should be compared with the younger granites to assess any temporal evolution in magma sources. The range of $\epsilon\text{Nd}(\text{T})$ values and TDM ages among the samples could indicate some heterogeneity in the source region or variable degrees of crustal assimilation during magma ascent and emplacement.

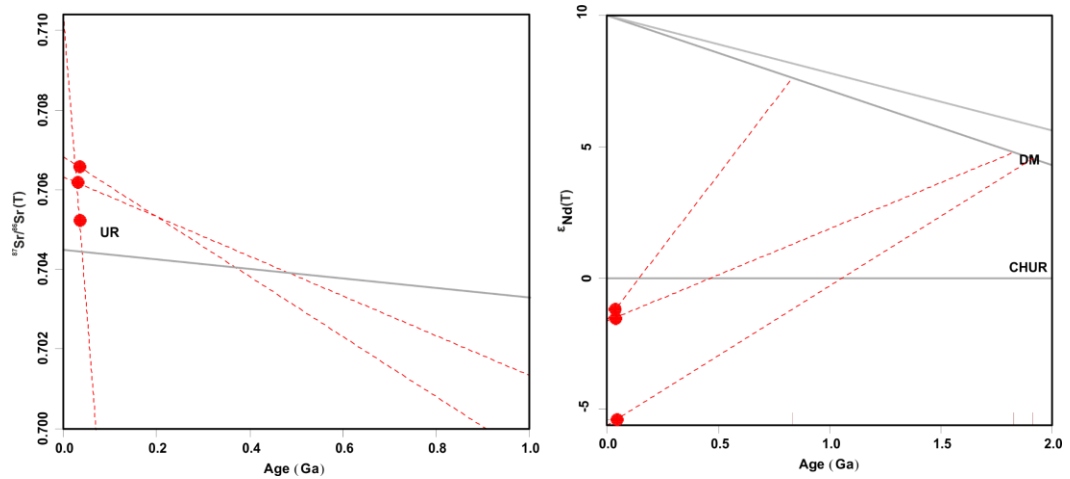


Figure 5.24. $^{87}\text{Sr}/^{86}\text{Sr}$ and ϵ_{Nd} values when age data is calculated as 29.53 Ma for the Central Uludağ Granite and 47.87 Ma for the Kapıdağ Granite (1813-P1) in granites.

When the $\epsilon_{\text{Nd}}(\text{T})$ and $^{87}\text{Sr}/^{86}\text{Sr}(\text{T})$ values are considered the age data of 29.53 Ma for the Central Uludağ Granite and 47.87 Ma for the Kapıdağ Granite (1813-P1), it is concluded that the origin rock of the granites may have been formed likely formed through partial melting of older continental crust, possibly with some minor input from more juvenile sources. 29.53 Ma for the present-day Central Uludağ Granite and 47.87 Ma for the Kapıdağ Granite (1813-P1) are based on the $^{87}\text{Sr}/^{86}\text{Sr}(\text{T})$ and $\epsilon_{\text{Nd}}(\text{T})$ data are given in Figure 5.25.

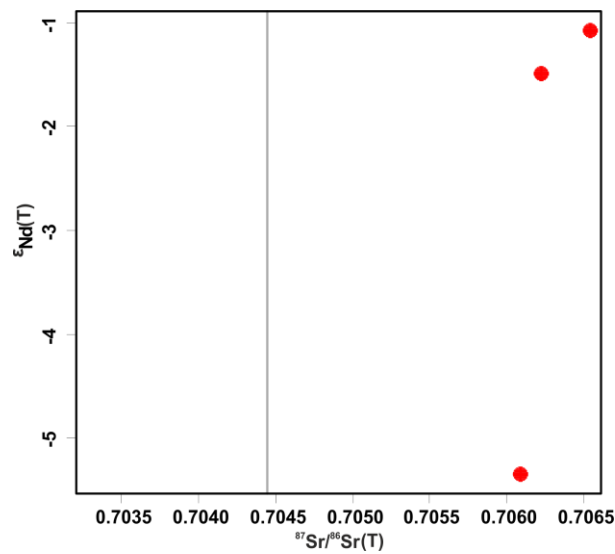


Figure 5.25. $\epsilon\text{Nd} - ^{87}\text{Sr}/^{86}\text{Sr}$ granite data for 29.53 Ma ago for the Central Uludağ Granite and 47.87 Ma ago for the Kapıdağ Granite (1813-P1)

5.4.3.4 Metabasalts

Geochronological age data could not be obtained from the metabasalt samples belonging to the Sazak Formation, which tectonically overlies the Uludağ Massif as a cover. However, the previous study by Yiğitbaş et al. (2018) found the average crystallisation age for this unit as 455 Ma, according to the U-Pb zircon dating. According to this age data, $^{87}\text{Sr}/^{86}\text{Sr}(T)$ data are between 0.70485 and 0.70519 and $\epsilon\text{Nd}(T)$ data vary between +3.9 and +4.67 (Figure 5.26).

First graph shows the evolution of $^{87}\text{Sr}/^{86}\text{Sr}$ ratios over time and relation with UR (undepleted reservoir) in Figure 5.26. The x-axis represents age in Ga (billion years), while the y-axis shows the $^{87}\text{Sr}/^{86}\text{Sr}$ ratio. The solid gray line represents the evolution of the undepleted reservoir (UR), which is essentially the bulk Earth composition. The dashed lines represent possible evolution paths for the metabasalt samples, with the black crosses marking their current positions at $T \approx 455$ Ma.

The samples plot above the UR line, indicating they have higher $^{87}\text{Sr}/^{86}\text{Sr}$ ratios than the bulk Earth at 455 Ma. This suggests the source of these metabasalts were enriched in Rb relative to Sr compared to the bulk Earth, leading to higher $^{87}\text{Sr}/^{86}\text{Sr}$ ratios over time due to radioactive decay of ^{87}Rb to ^{87}Sr .

Figure 5.26, DM (Depleted Mantle) graph shows the evolution of ϵNd values over time. The x-axis is age in Ga, and the y-axis represents $\epsilon\text{Nd}(T)$ values. The solid gray lines represent the evolution of the depleted mantle (DM). The dashed lines and crosses again represent the metabasalt samples.

The samples plot below the DM lines, indicating lower ϵNd values than the depleted mantle at 455 Ma. This suggests the source of these metabasalts was relatively enriched in light rare earth elements (LREEs) compared to the depleted mantle, resulting in lower Sm/Nd ratios and consequently lower ϵNd values over time.

The metabasalt samples show characteristics intermediate between bulk Earth (UR) and depleted mantle (DM) compositions, but closer to UR.

Their source was likely enriched compared to the depleted mantle, possibly indicating involvement of crustal material or an enriched mantle source. The TDM age (where the dashed lines intersect the DM curve) appears to be significantly older than the 455 Ma crystallization age, suggesting a complex petrogenetic history.

This could indicate either:

- a) Derivation from an older, enriched source that separated from the depleted mantle long before 455 Ma.
- b) Mixing between depleted mantle-derived magmas and older crustal material during ascent or emplacement.

These observations point to a complex petrogenetic history for these metabasalts, involving either long-term enriched sources or significant crustal interaction during their formation.

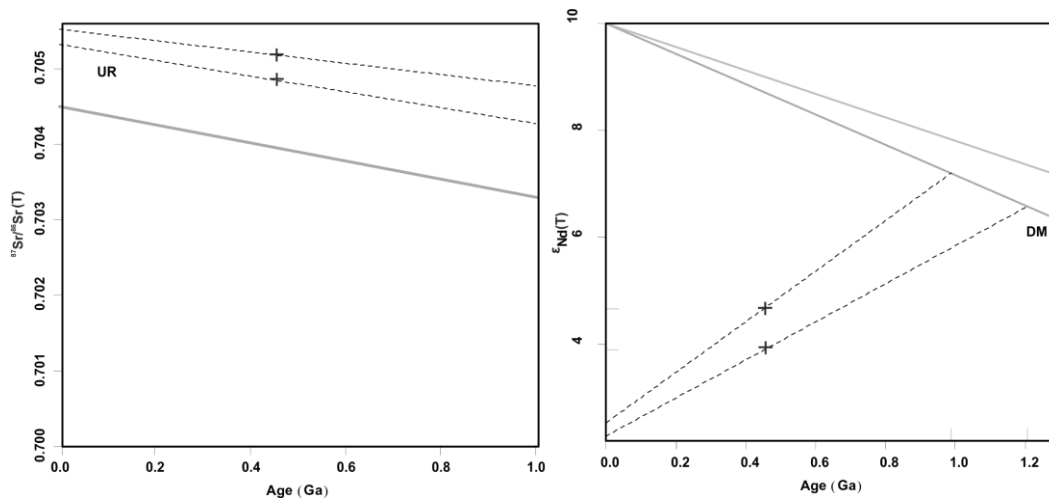


Figure 5.26. $^{87}\text{Sr}/^{86}\text{Sr}$ and ϵNd values when age data is calculated as 455 Ma for metabasalts.

When the $\epsilon\text{Nd}(\text{T})$ and $^{87}\text{Sr}/^{86}\text{Sr}(\text{T})$ values for metabasalts calculated for 455 Ma, it is concluded that the primary rock of the metabasalts was formed as MORB. The $\epsilon\text{Nd}(\text{T})$ data, calculated for 455 Ma, of metabasalts of the Sazak formation are given in Figure 5.27.

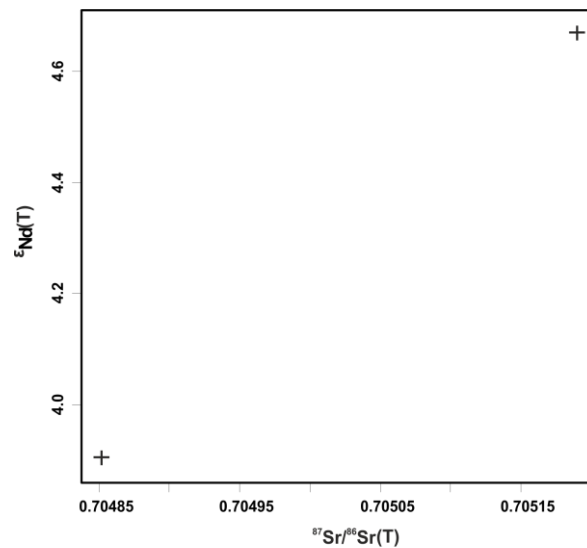


Figure 5.27. $\epsilon\text{Nd}(\text{T})$ - $^{87}\text{Sr}/^{86}\text{Sr}(\text{T})$ data belongs to metabasalts.

Figure 5.28b shows all samples of this study $\epsilon_{\text{Nd}}(\text{T})$ - $^{87}\text{Sr}/^{86}\text{Sr}(\text{T})$ values combined together and their sources can be seen easily from this diagram when compared with Zindler and Hart (1986) diagram (Figure 5.28a).

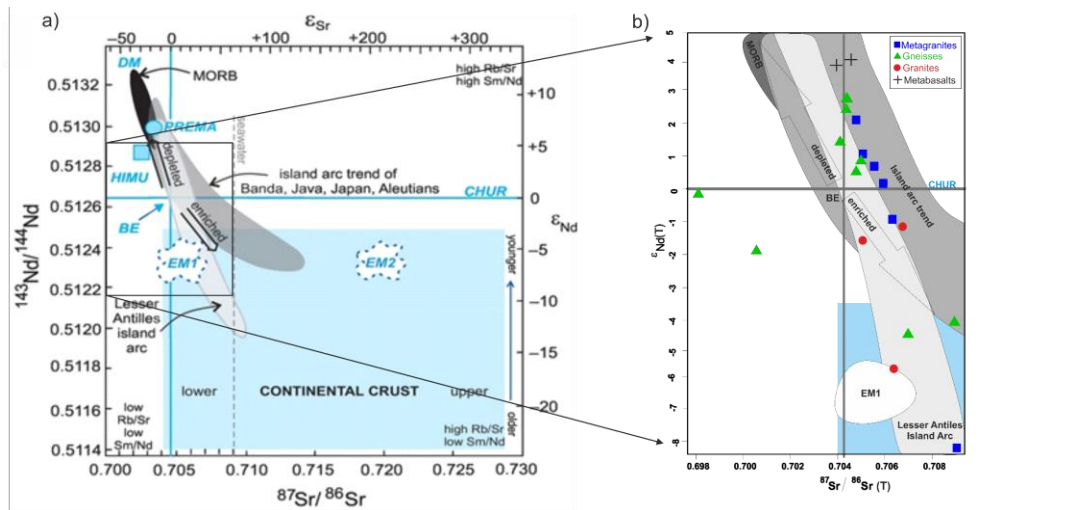


Figure 5.28. a) Zindler and Hart (1986), b) All samples $\epsilon_{\text{Nd}}(\text{T})$ - $^{87}\text{Sr}/^{86}\text{Sr}(\text{T})$ values.

CHAPTER 6

GEOCHRONOLOGY

In the scope of this chapter, geochronological data are presented. Within this study's scope, geochronological studies were carried out in the geochronology laboratory of the central laboratory of Adana Çukurova University using the LA-ICP-MS technique. Geochronological studies are categorised under two headings.

6.1 Sample Preparation

The sample weighing approximately 15-20 kg, depending on the lithology of the rock, was subjected to the following sample preparation stages.

1. Press Crusher: Reducing the size of rock samples collected from the field with a press crusher.
2. Jaw Crusher: The process of reducing the rock, which is crushed into walnut-sized pieces with a press crusher, to the size of a lentil grain.
3. Roller Grinder: The process of reducing the rock, which is approximately the size of a lentil grain, to the size of granulated sugar, commonly to the less than 1 mm size.
4. The sieves are arranged from bottom to top according to the sieve opening size, from small to large, with the pan at the bottom. Between 500 μm and 63 μm are used for U-Pb zircon separations.
5. Shaking Table: The process of separating the minerals of finely ground rock by density on a special shaking table with the help of water.
6. Heavy Liquid: The process of separating the minerals separated by weight on the shaking table again by weight with the help of bromoform (CHBr_3) liquid with a specific gravity of 2,89 g/cm^3 and a special separation funnel.
7. Magnetic Separator: Separation of minerals with a specific gravity greater than 2,89 g/cm^3 with the heavy liquid process by magnetic separation device, this time according to their magnetic properties.

8. Zircon Separation: The process of removing the zircons in the sample with tweezers one by one by examining the sample separated as a result of magnetic separation under a binocular microscope.
9. Mounting: Placing the zircon grains extracted under a binocular microscope on a cylindrical apparatus called "mounts", also under a microscope.
10. Preparation of the mounts for analysis: After the zircon grains are placed on the mounts, the mounts are first coated with epoxy, a special adhesive, to prevent the zircons from falling off the mounts; after the epoxy dries, the mounts are polished and coated with carbon to allow CL (CathodoLuminescence) images to be taken and then analysed by LA-ICP-MS (Laser Ablation-Inductively Coupled Plasma-Mass Spectrometry).
11. Taking CL (Cathodoluminescence) images of the zircons in the mounts with a Scanning Electron Microscope: This is the process of taking CL (cathodoluminescence) images of the zircon grains in the polished and gold- or platinum-coated mounts using an electron microscope to reveal their internal structure to decide their analysing points.

6.2 LA-ICP-MS U-Pb Analysis

For the analysis of each zircon grain of the collected samples, the optimal laser spot diameter was selected between 25-35 μm . The most common Pb correction depends on the ^{204}Pb signal received during analysis and the Pb composition (Stacey and Kramer, 1975). The instrument data were corrected with the program IOLITE (Hellstrom et al. 2008) based on the common Pb signal, elemental discrimination, and instrumental mass discrimination of Pb/Th and Pb/U. Concordance diagrams (2σ error ellipses), concordance ages (95% confidence) and combined frequency and probability density distribution diagrams were generated with Isoplot/ex 4.15 (Ludwig, 2001). The primary standard was 91500 zircon (Wiedenbeck et al. 1995), and the secondary standards were Plešovice zircon (Sláma et al. 2008) and Temora 1 zircon (Black et al. 2003).

6.3 LA-ICP-MS U-Pb Zircon Analysis Results

Seventeen rock samples from different lithologies from the Uludağ Massif were selected for U-Pb zircon analysis. Zircon could not be obtained from 3 of these samples due to laboratory-related problems. The sample numbers, formations and lithologies of the 14 samples analysed by LA-ICP-MS U-Pb analysis are given in Table 6.1

Nine of the 14 samples analyzed gave concordant results. The zircon grains belonging to the analyses that yielded concordant results have an aspect ratio of approximately 2:1 to 3:1, are self-shaped, semi-rounded or semi-euhedral morphology and show igneous zoning. Zircon grains range from approximately 100 μm to 2000 μm (CL images in Figure 6.1 to Figure 6.27). All LA-ICP-MS U-Pb analysis results are presented in tables from Appendices A to N.

Table 6.1 Units analysed for U-Pb zircon, their formations and cathodoluminescence (CL) mount numbers.

MOUNT NO	SAMPLE NO	FORMATION	LITHOLOGY
KF-178	1802	South Uludağ Metagranite	metagranite
KF-177	1814	South Uludağ Metagranite	metagranite
KF-178	1817	South Uludağ Metagranite	metagranite
KF-180	1819	South Uludağ Metagranite	metagranite
KF-181	1903	Gökdere Formation	metagranite
KF-178	1803	Gökdere Formation	gneiss
KF-179	1809	Gökdere Formation	gneiss
KF-179	1810	Gökdere Formation	gneiss
KF-179	1811	Gökdere Formation	gneiss
KF-177	1812	Kilimliğöl Formation	gneiss
KF-180	1820	Gökdere Formation	gneiss
KF-181	1904	Gökdere Formation	gneiss
KF-180	1821	Central Uludağ Granite	granite
KF-177	1813	Kapıdağ Granite	granite

The results of LA-ICP-MS U-Pb analysis are divided and discussed under three main headings according to their lithologies. These are South Uludağ Metagranites, Uludağ Massif Gneisses and Uludağ Granites.

6.3.1 South Uludağ Metagranites

U-Pb analysis was performed on four samples from the South Uludağ Metagranite and 1 sample from the metagranites in the Gökdere formation (Table 6.1). The cathodoluminescence (CL) images and U-Pb analysis result graphs of the samples of Güney Uludağ Metagranite are given from Figure 6.1 to Figure 6.8. According to these results, the metamorphism ages of South Uludağ Metagranite vary between 32.03 Ma and 35.43 Ma. These age data are thought to be related to the ductile

deformation caused by the Eskişehir (Soğukpınar) Fault, which is located in the south of the Uludağ Massif and tectonically affects the South Uludağ Metagranite.

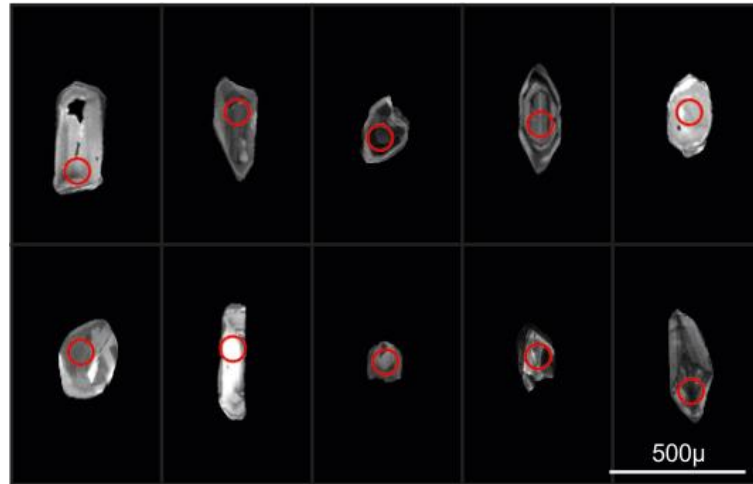


Figure 6.1. Cathodoluminescence (CL) images of typical zircon grains from South Uludağ Metagranite (Sample No. 1802) showing the internal structure and laser analysis location.

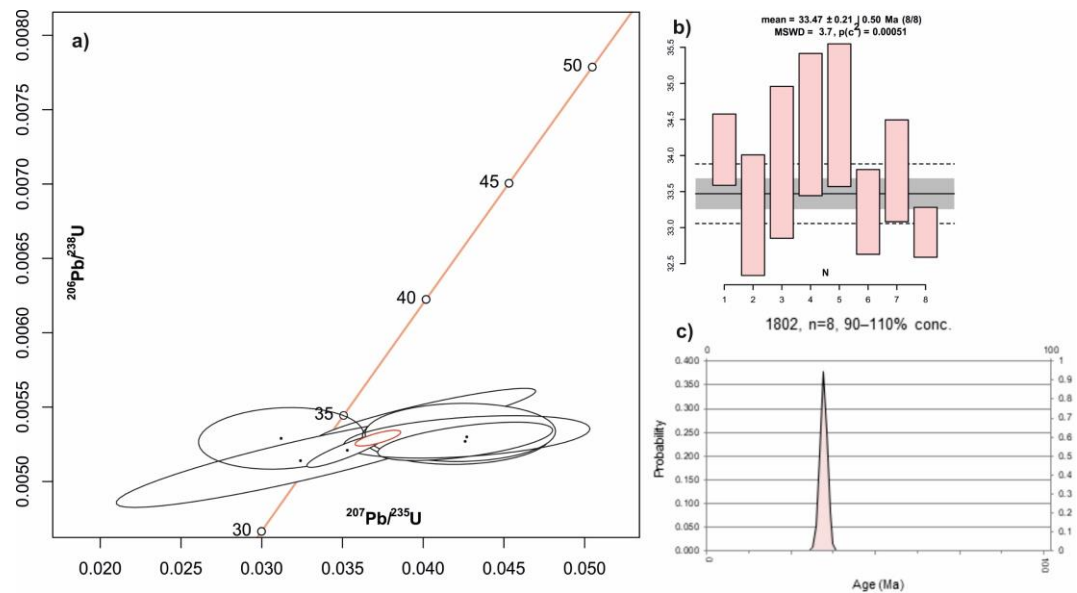


Figure 6.2. U-Pb zircon ages of South Uludağ Metagranite (Sample No. 1802) a) Concordia diagram, b) Mean age diagram and c) Combined binned frequency and probability density distribution plots of zircon grains in the range of 0–100 Ma, show that the metamorphism age of the metagranite sample is 33.47 ± 0.21 Ma.

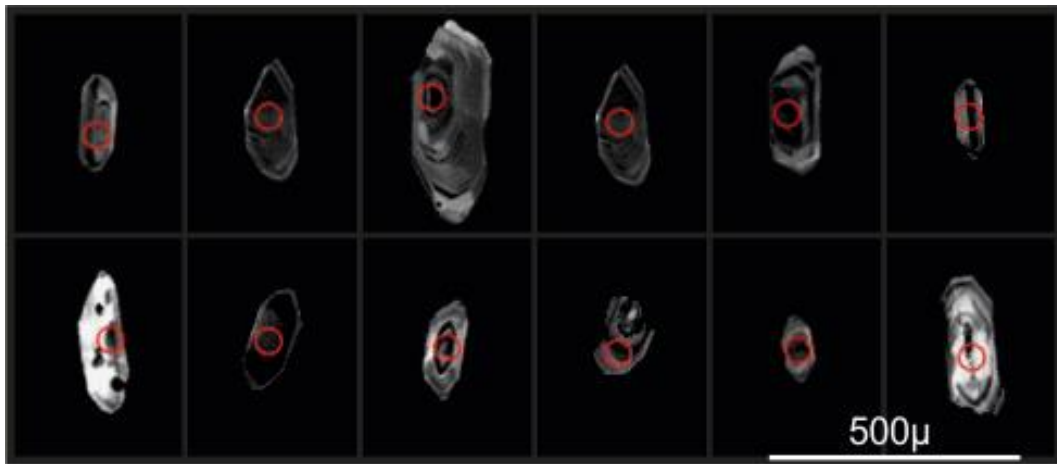


Figure 6.3. Cathodoluminescence (CL) images of typical zircon grains from South Uludağ Metagranite (Sample No. 1814) showing the internal structure and laser analysis location.

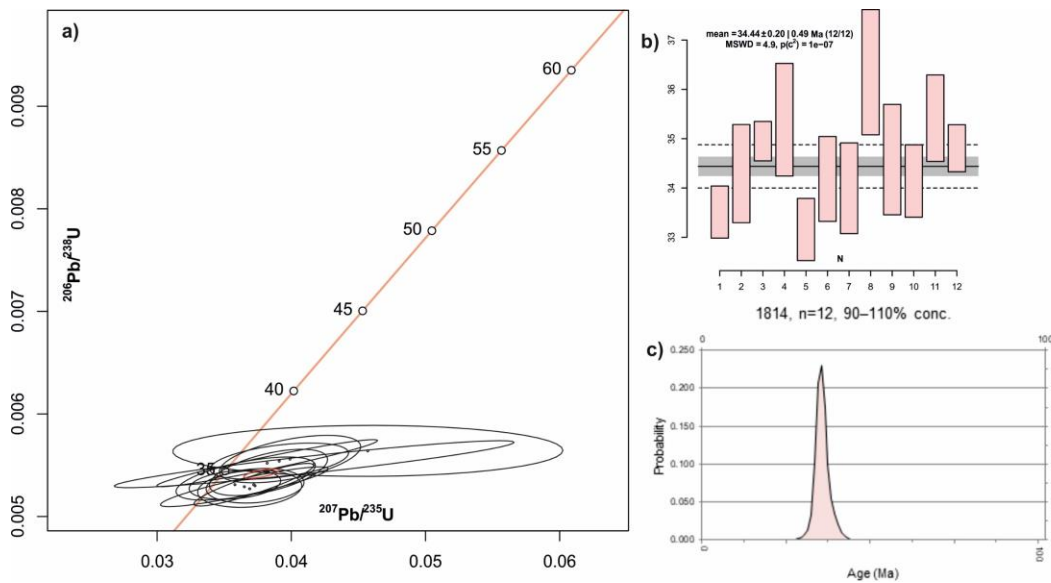


Figure 6.4. U-Pb zircon ages of South Uludağ Metagranite (Sample No. 1814) a) Concordia diagram, b) Mean age diagram and c) Combined binned frequency and probability density distribution plots of zircon grains in the range of 0–100 Ma, show that the metamorphism age of the metagranite for this sample is 34.44 ± 0.20 Ma.

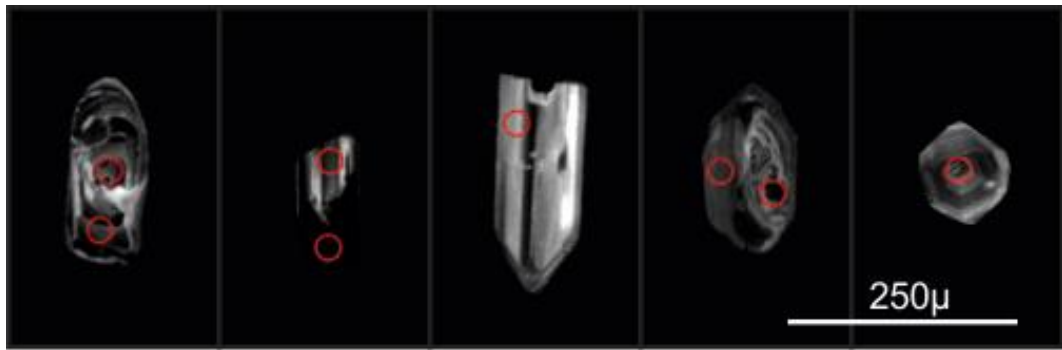


Figure 6.5. Cathodoluminescence (CL) images of typical zircon grains from South Uludağ Metagranite (Sample No. 1817) showing the internal structure and laser analysis location.

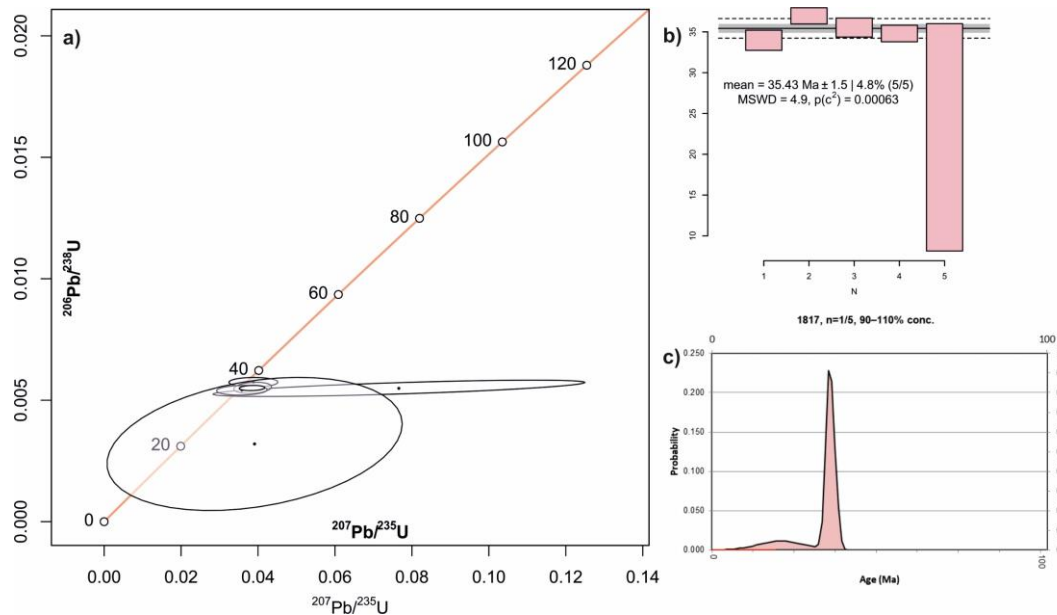


Figure 6.6. U-Pb zircon ages of South Uludağ Metagranite (Sample No. 1817) a) Concordia diagram, b) Mean age diagram and c) Combined binned frequency and probability density distribution plots of zircon grains in the range of 0–100 Ma, show that the metamorphism age of the metagranite sample is 35.43 ± 1.5 Ma.

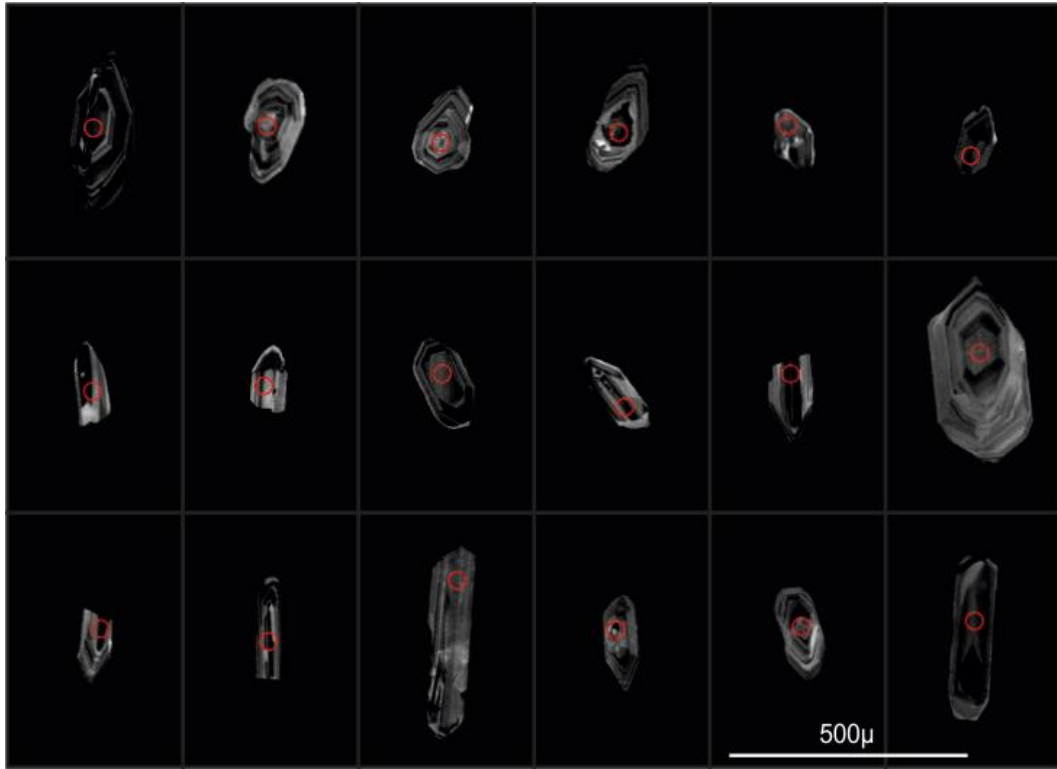


Figure 6.7. Cathodoluminescence (CL) images of typical zircon grains from South Uludağ Metagranite (Sample No. 1819) showing the internal structure and laser analysis location.

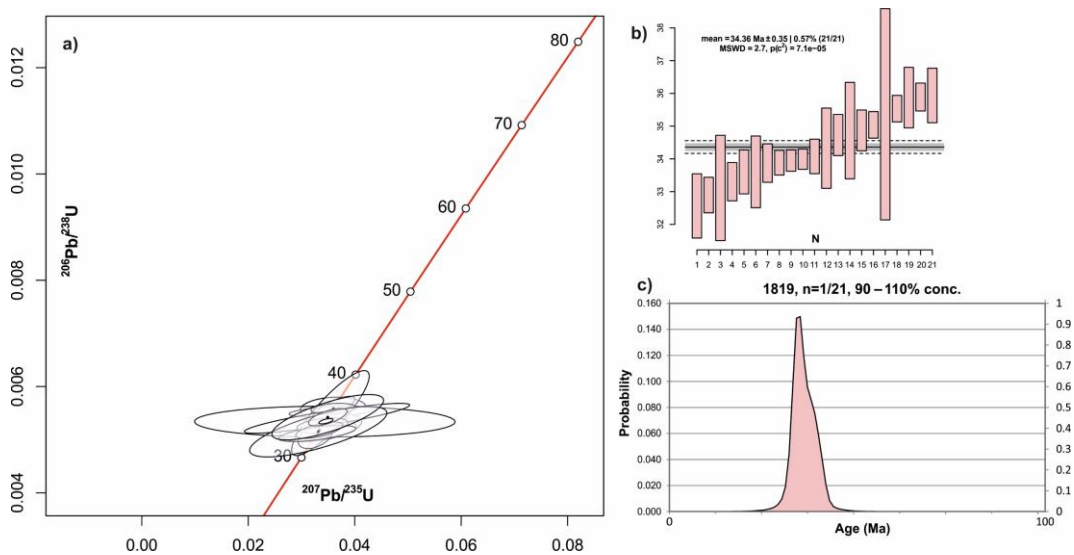


Figure 6.8. U-Pb zircon ages of South Uludağ Metagranite (Sample No. 1819). a) Concordia diagram, b) Mean age diagram and c) Combined binned frequency and probability density distribution plots of zircon grains in the range of 0–100 Ma, show that the age of metamorphism of the metagranite sample is 34.36 ± 0.35 Ma.

CL image (Figure 6.9) and U-Pb analysis result graphs (Figure 6.10) of sample 1903 taken from the metagranite unit of the Gökdere formation located north of the site are given below. According to the results of the analysis, the probable metamorphism age of the metagranite of the Gökdere Formation is 32.03 Ma.

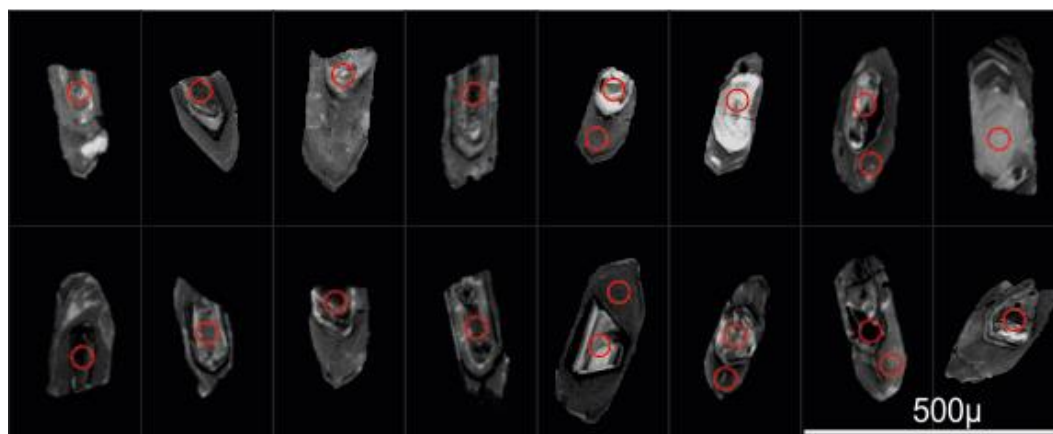


Figure 6.9. Cathodoluminescence (CL) images of typical zircon grains from metagranite sample of the Gökdere formation (Sample No. 1903) showing the internal structure and laser analysis location.

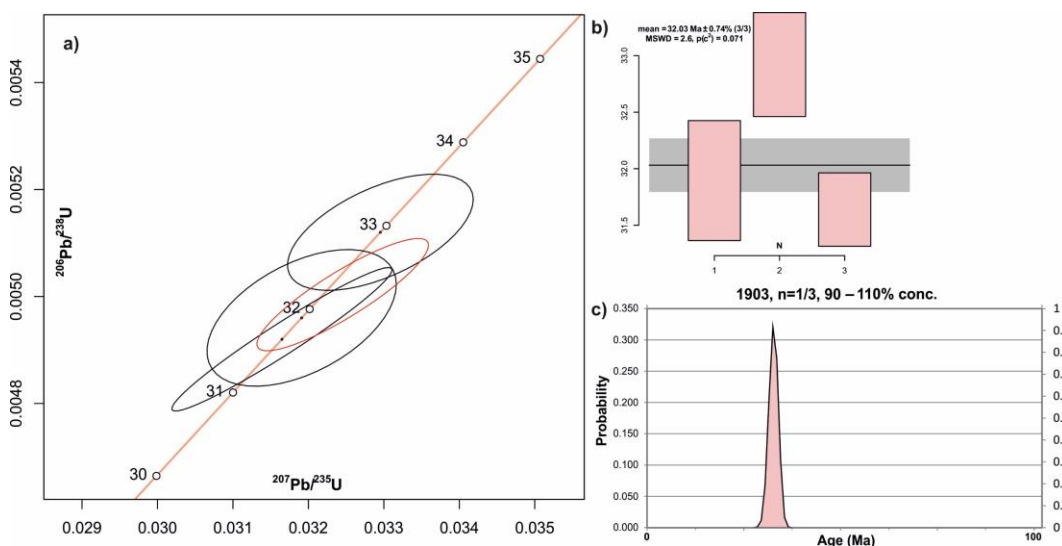


Figure 6.10. U-Pb zircon ages of metagranite of the Gökere formation (Sample No. 1903). a) Concordia diagram, b) Mean age diagram and c) Combined binned frequency and probability density distribution plots of zircon grains in the range of 0–100 Ma, show that the metamorphism age of the metagranite sample is $32.03 \pm 0.74 \text{ Ma}$.

6.3.2 Uludağ Massif Gneisses

CL imaging and U-Pb Analysis were performed for 7 of the gneisses from the Uludağ Massif. 6 of these samples are gneisses belonging to the Gökdere formation, and CL images and U-Pb analysis result graphs are given from Figure 6.11 to Figure 6.22. The protolith crystallisation ages of the gneisses of the Gökdere formation vary between 104 Ma and 252 Ma.

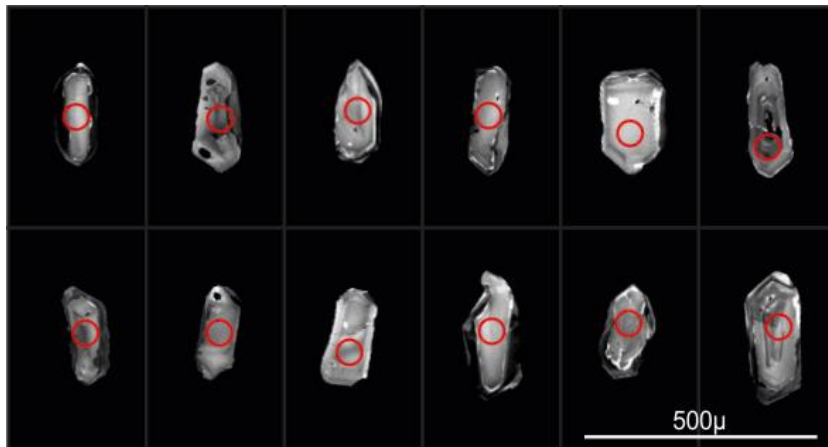


Figure 6.11. Cathodoluminescence (CL) images of typical zircon grains from gneiss sample of the Gökdere formation (Sample No. 1803) showing the internal structure and laser analysis location.

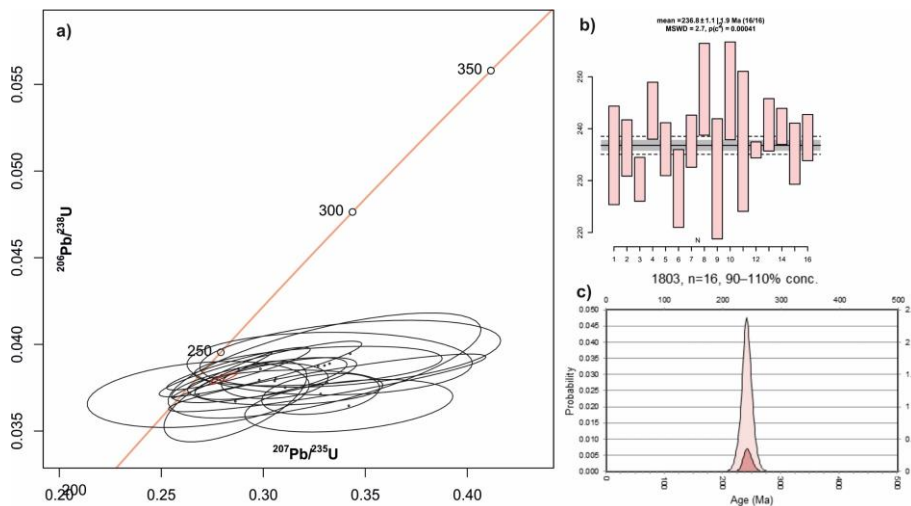


Figure 6.12. U-Pb zircon ages of gneiss sample of the Gökdere formation (Sample No. 1803). a) Concordia diagram, b) Mean age diagram and c) Combined binned frequency and probability density distribution plots of zircon grains in the range of 0–400 Ma, show that the protolith crystallisation age of the gneiss sample is 236.8 ± 1.1 Ma.

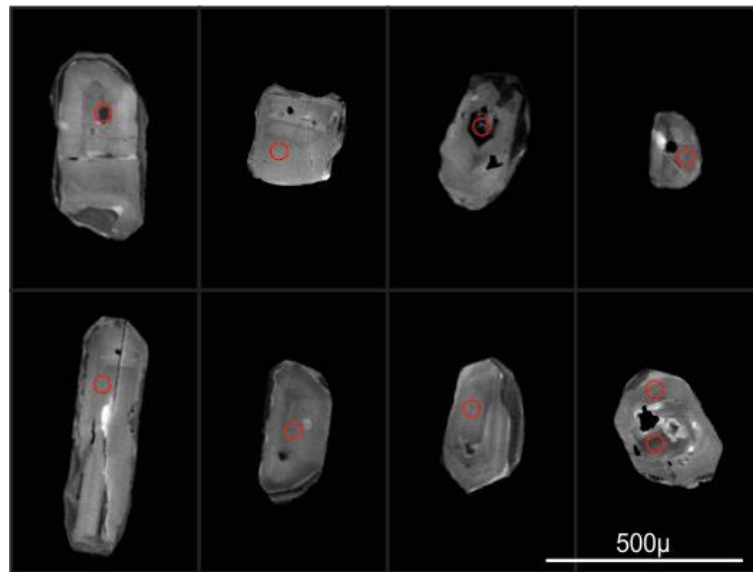


Figure 6.13. Cathodoluminescence (CL) images of typical zircon grains from gneiss sample of the Gökdere formation (Sample No. 1809) showing the internal structure and laser analysis location.

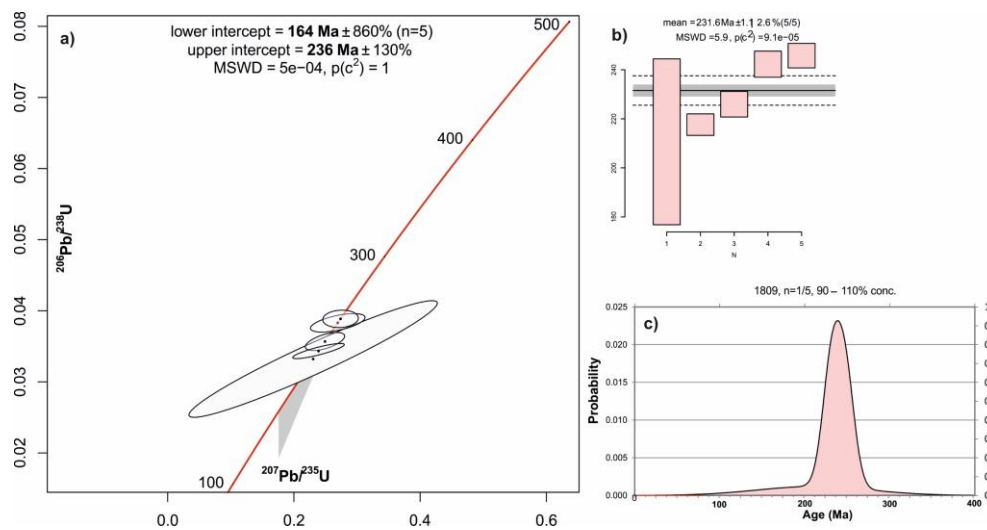


Figure 6.14. U-Pb zircon ages of gneiss sample of the Gökdere formation (Sample No. 1809). a) Concordia diagram, showing the major events. The discordia line intersects the concordia curve at two points. The upper intercept is interpreted as the protolith crystallisation age, whereas the lower intercept defines the final episodic lead loss., b) Mean age diagram and c) Combined binned frequency and probability density distribution plots of zircon grains in the range of 0–400 Ma, show that the protolith crystallisation age is 236 Ma.

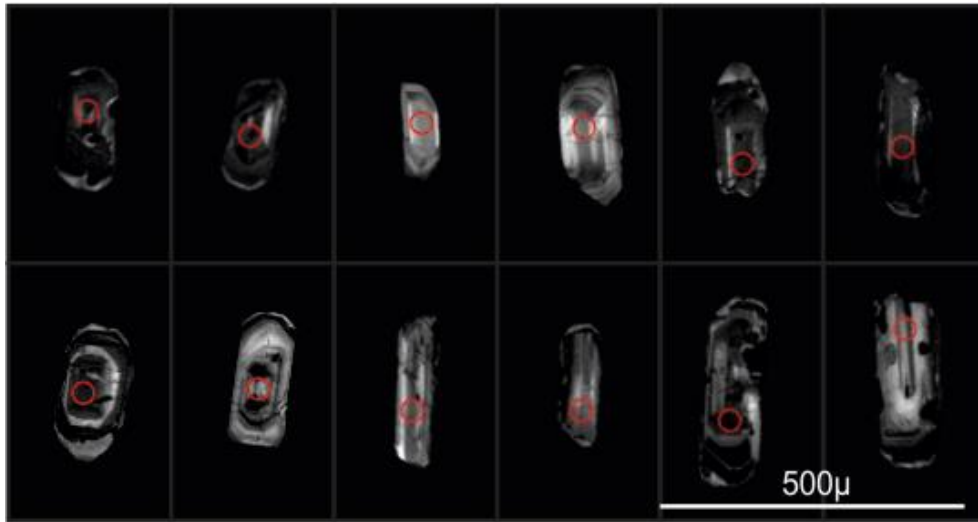


Figure 6.15. Cathodoluminescence (CL) images of typical zircon grains from gneiss sample of the Gökdere formation (Sample No. 1810) showing the internal structure and laser analysis location.

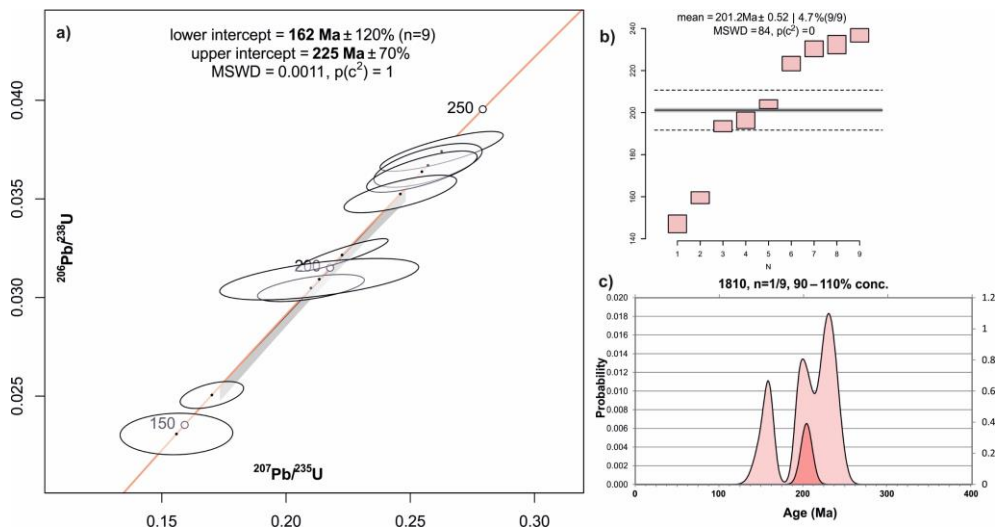


Figure 6.16. U-Pb zircon ages of gneiss sample of the Gökdere formation (Sample No. 1810). a) Concordia diagram, showing the major events. The discordia line intersects the concordia curve at two points. The upper intercept is interpreted as the protolith crystallisation age, whereas the lower intercept defines the final episodic lead loss., b) Mean age diagram and c) Combined binned frequency and probability density distribution plots of zircon grains in the range of 0–400 Ma, show that the protolith crystallisation age is 225 Ma.

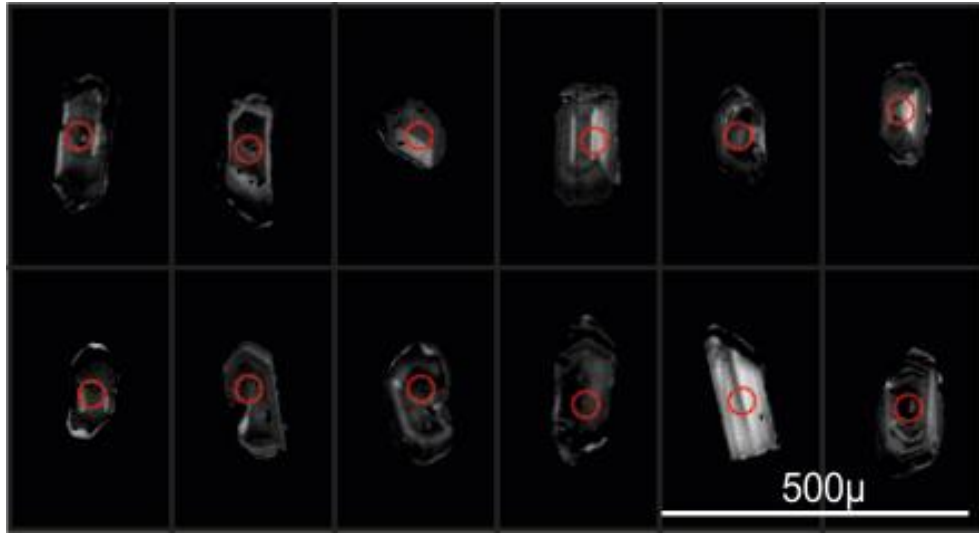


Figure 6.17. Cathodoluminescence (CL) images of typical zircon grains from gneiss sample of the Gökdere formation (Sample No. 1811) showing the internal structure and laser analysis location.

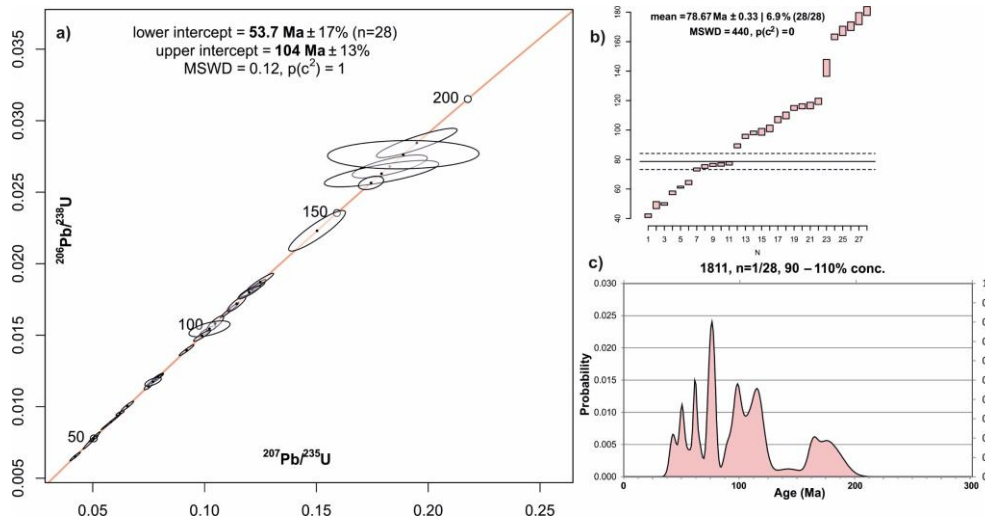


Figure 6.18. U-Pb zircon ages of gneiss sample of the Gökdere formation (Sample No. 1811). a) Concordia diagram, showing the major events. The discordia line intersects the concordia curve at two points. The upper intercept is interpreted as the protolith crystallisation age, whereas the lower intercept defines the final episodic lead loss., b) Mean age diagram and c) Combined binned frequency and probability density distribution plots of zircon grains in the range of 0–300 Ma, show that the protolith crystallisation age is 104 Ma.

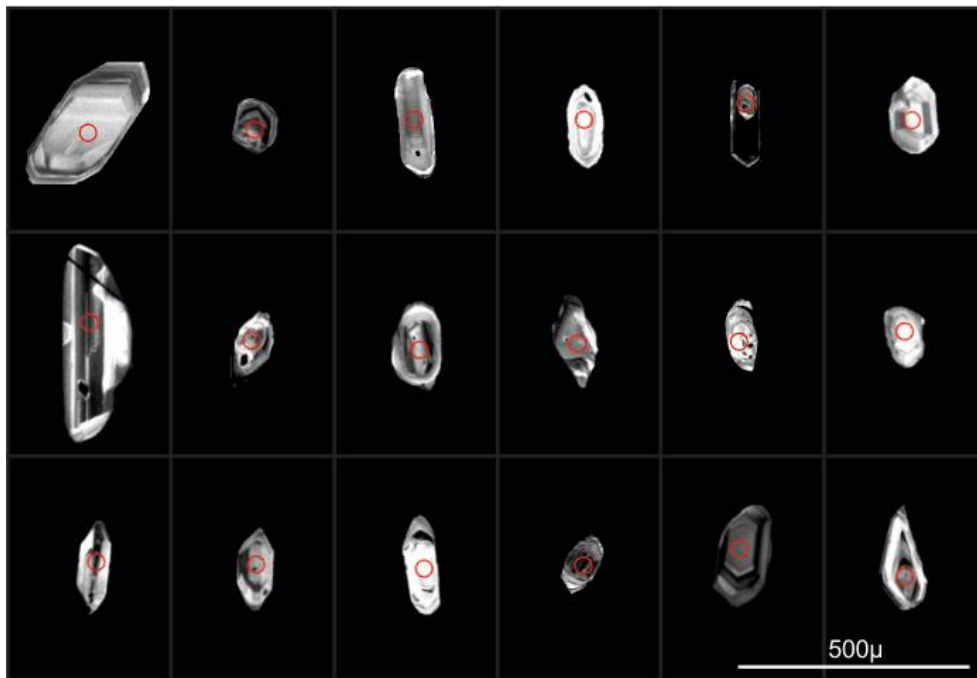


Figure 6.19. Cathodoluminescence (CL) images of typical zircon grains from gneiss sample of the Gökdere formation (Sample No. 1820) showing the internal structure and laser analysis location.

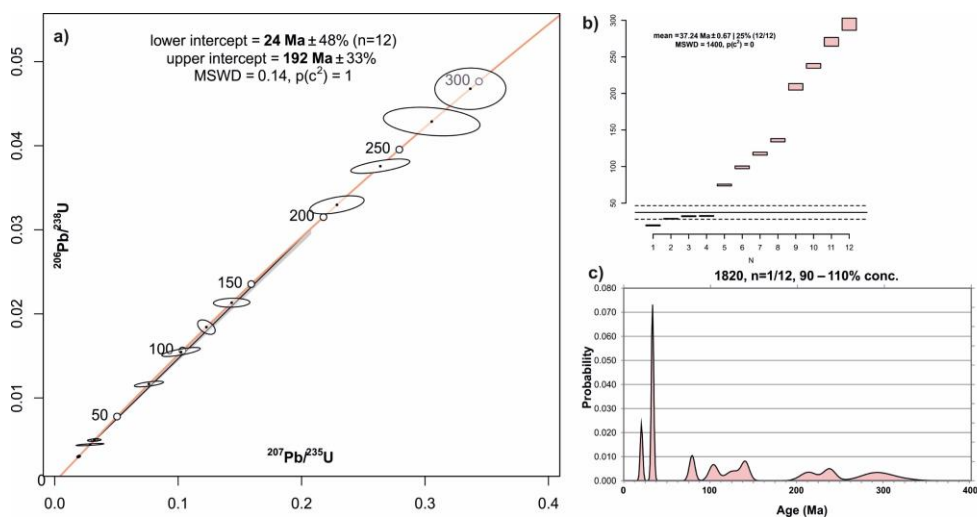


Figure 6.20. U-Pb zircon ages of gneiss sample of the Gökdere formation (Sample No. 1820). a) Concordia diagram, showing the major events. The discordia line intersects the concordia curve at two points. The upper intercept is interpreted as the protolith crystallisation age, whereas the lower intercept defines the final episodic lead loss., b) Mean age diagram and c) Combined binned frequency and probability density distribution plots of zircon grains in the range of 0–400 Ma, show that the protolith crystallisation age is 192 Ma.

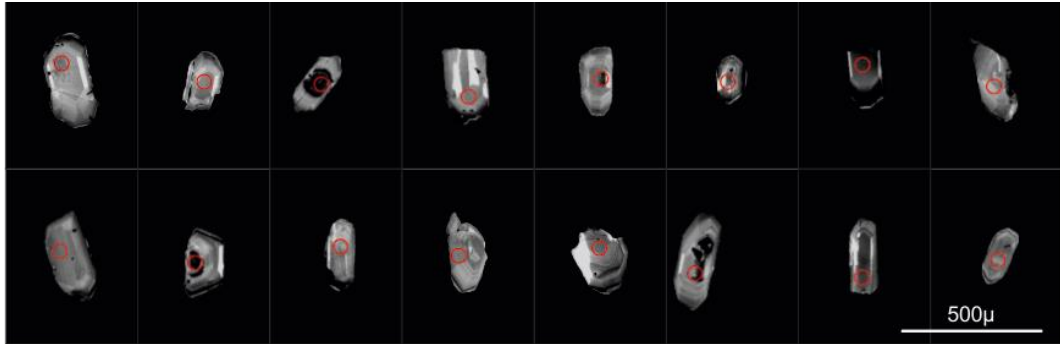


Figure 6.21. Cathodoluminescence (CL) images of typical zircon grains from gneiss sample of the Gökdere formation (Sample No. 1904) showing the internal structure and laser analysis location.

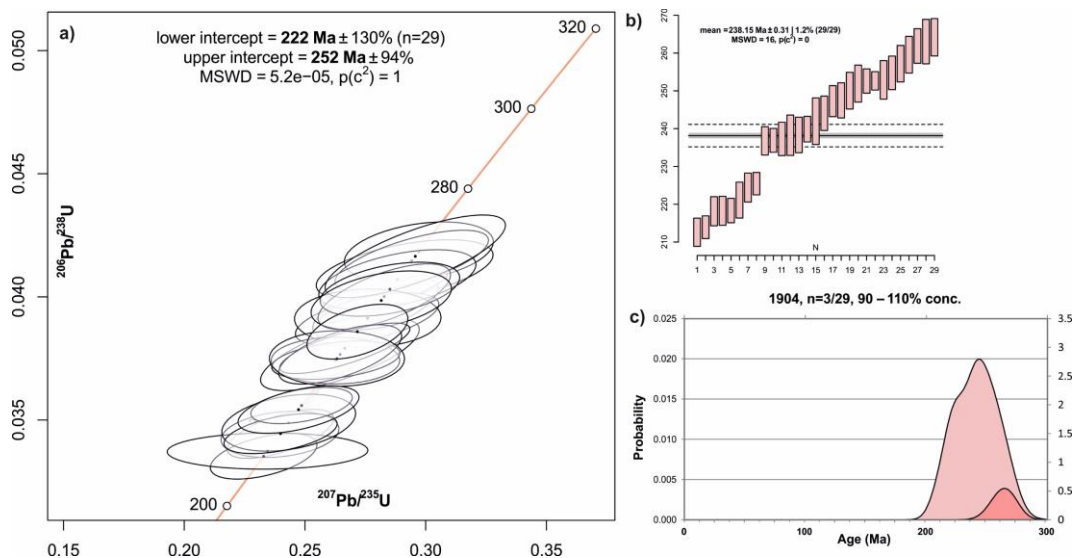


Figure 6.22. U-Pb zircon ages of gneiss sample of the Gökdere formation (Sample No. 1904). a) Concordia diagram, showing the major events. The discordia line intersects the concordia curve at two points. The upper intercept is interpreted as the protolith crystallisation age, whereas the lower intercept defines the final episodic lead loss., b) Mean age diagram and c) Combined binned frequency and probability density distribution plots of zircon grains in the range of 0–400 Ma, show that the protolith crystallisation age is 252 Ma.

One of the seven samples for LA-ICP-MS U-Pb analysis from the Uludağ Massif is a gneiss of the Kilimliğöl formation. The CL images of this sample are given in Figure 6.23, and the U-Pb analysis result is given in Figure 6.24. U-Pb LA-ICP-MS dating of zircons of the gneiss sample from the Kilimliğöl formation yielded as

53.98 ± 0.28 Ma. However, considering the proximity of this sample to the Central Uludağ Granite and the South Uludağ Metagranite in the field, it is concluded that this age can not be the crystallisation age of the protolith. This age is considered as the age of a strong tectono-thermal event.

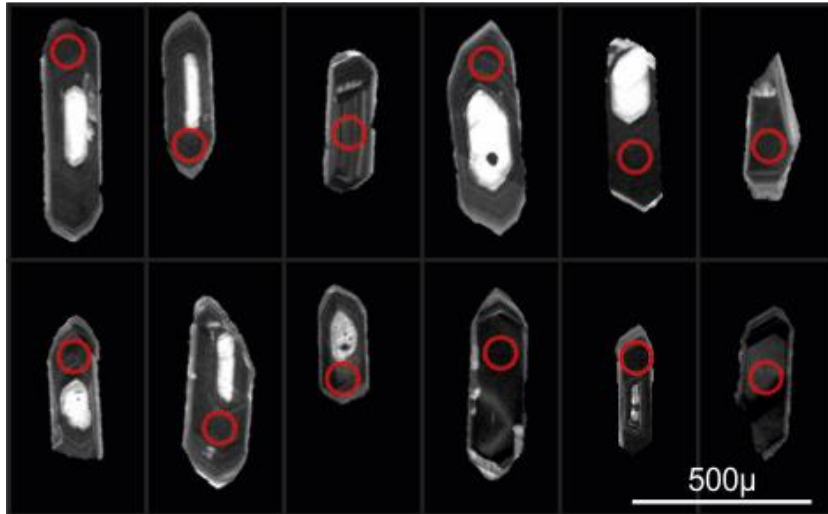


Figure 6.23. Cathodoluminescence (CL) images of typical zircon grains from gneiss sample of the Kilimligöl formation (Sample No. 1812) showing the internal structure and laser analysis location.

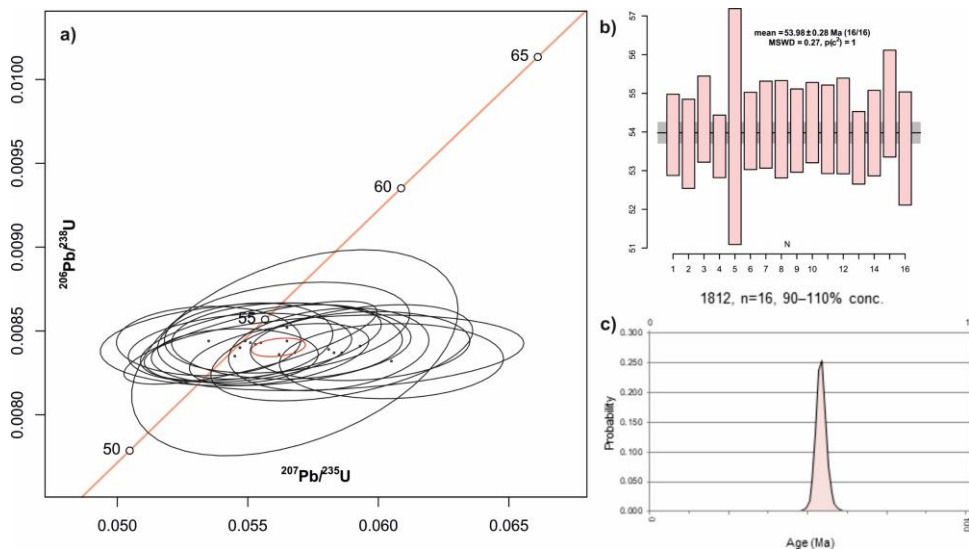


Figure 6.24. U-Pb zircon ages of gneiss sample of the Kilimligöl formation (Sample No. 1812). a) Concordia diagram, b) Mean age diagram and c) Combined binned frequency and probability density distribution plots of zircon grains in the range of 0–100 Ma, show that the age of tectonothermal event for this sample is 53.98±0.28 Ma.

6.3.3 Uludağ Granites

6.3.3.1 Central Uludağ Granite

1 sample is dated by LA-ICP-MS U-Pb analysis of the Central Uludağ Granite. The CL images of this 1 sample are shown in Figure 6.25, and the U-Pb analysis result is shown in Figure 6.26. The age data obtained from the Central Uludağ Granite in this study supports the previous studies (Okay et al. 2018) and the crystallisation age is 29.53 Ma.

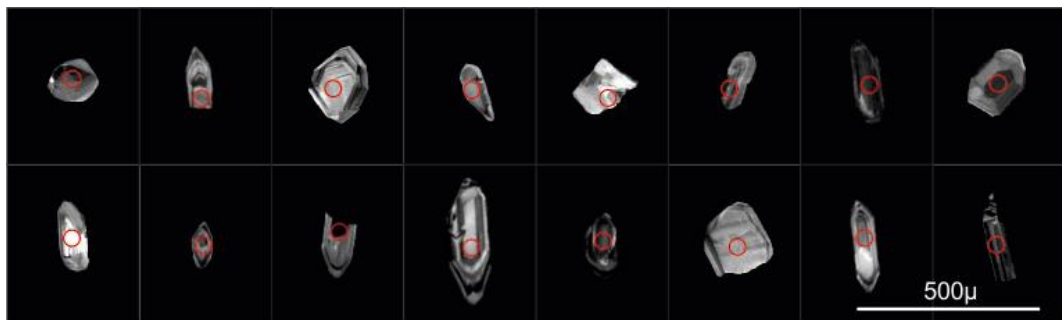


Figure 6.25. Cathodoluminescence (CL) images of typical zircon grains from granite sample of the Central Uludağ Granite (Sample No. 1821) showing the internal structure and laser analysis location.

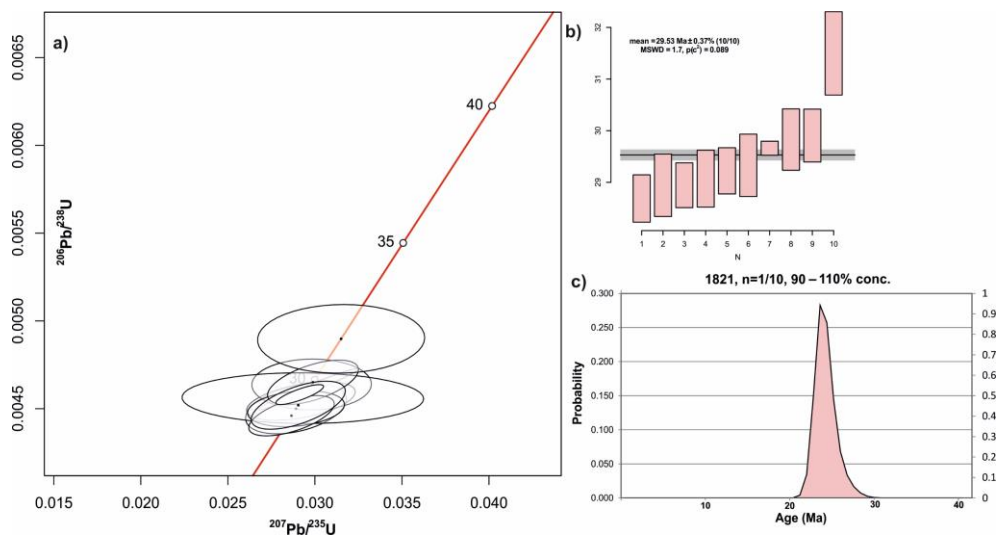


Figure 6.26. U-Pb zircon ages of gneiss sample of the Kilimliğöl formation (Sample No. 1821). a) Concordia diagram, b) Mean age diagram and c) Combined binned frequency and probability density distribution plots of zircon grains in the range of 0–40 Ma, show that the crystallisation age of the granite sample is 29.53 Ma.

6.3.3.2 Kapıdağ Granite

LA-ICP-MS U-Pb analysis was performed on 1 sample from the Kapıdağ granite, which crops out in the south of the Uludağ Massif, to compare the Kapıdağ granite with previous studies. The CL image of this sample is given in Figure 6.27, and the U-Pb analysis results are given in Figure 6.28. When the age data obtained from the analysis results are compared with the previous studies (Altunkaynak et al. 2012), results support each other, and the crystallisation age of the Kapıdağ granite for this study is determined as 47.87 ± 0.27 Ma.

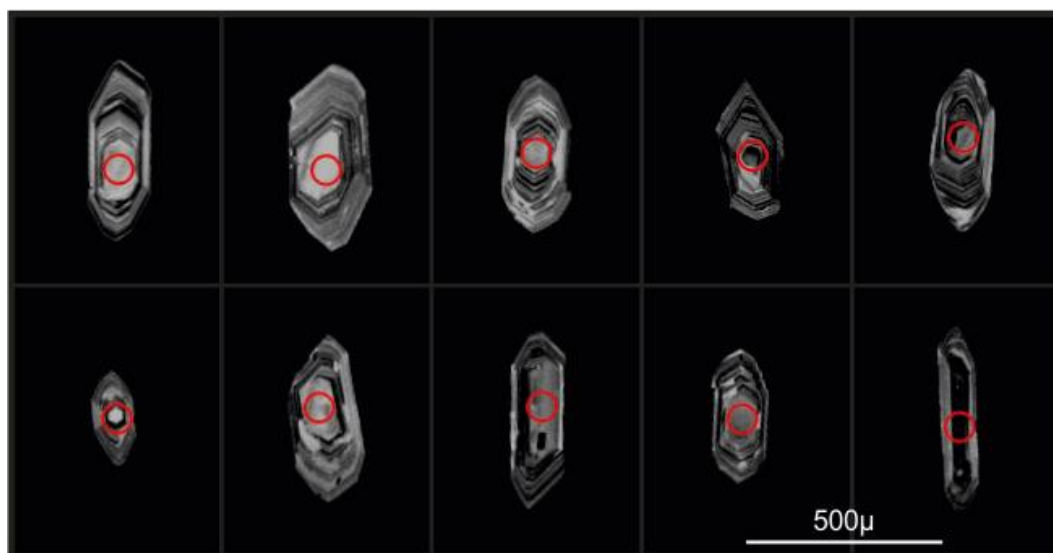


Figure 6.27. Cathodoluminescence (CL) images of typical zircon grains from granite sample of the Kapıdağ granite (Sample No. 1813) showing the internal structure and laser analysis location.

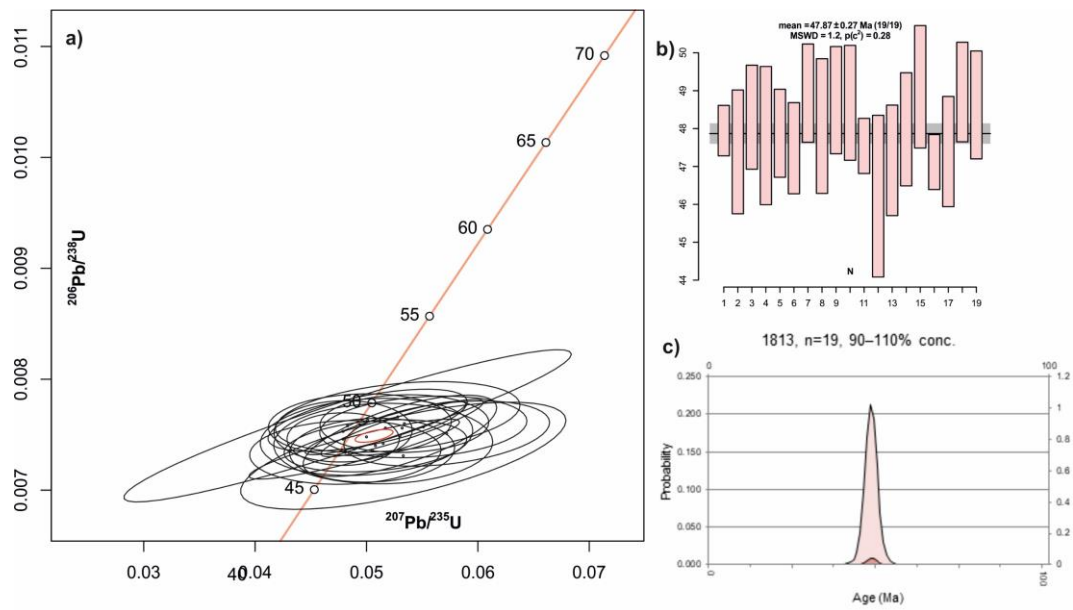


Figure 6.28. U-Pb zircon ages of granite sample of the Kapıdağ granite (Sample No. 1813). a) Concordia diagram, b) Mean age diagram and c) Combined binned frequency and probability density distribution plots of zircon grains in the range of 0–100 Ma, show that the crystallisation age of the granite sample is 47.87 ± 0.27 Ma.

A summary representation of the formations and units that played a role in the formation of the Uludağ Massif from Figure 6.1 to Figure 6.28, together with their coordinates, is shown in Table 6.2. The locations of these units in the field are also given in Figure 7.2 and Figure 7.3a) on the geological map made as the result of the study.

Table 6.2. U-Pb zircon analysis results of samples taken from the field according to coordinates, formation, and lithology.

Sample no	UTM coordinate	Formation	Lithology	Metamorphism Date: MD/ Formation Date: FD/ CD:Crytallization Date/ Tectonothermal Effect:TTE/
1801	0687463E-4436254N	South Uludağ Metagranite	Metagranite	No data
1802	0687272E-4436363N	South Uludağ Metagranite	Metagranite	MD: 33.47 ± 0.21 Ma
1803	0694433E-4440616N	Gökdere Formation	Gneiss	FD: 236.8 ± 1.1 Ma
1804	0694213E-4440737N	Gökdere Formation	Gneiss	No data
1805	0693505E-4438853N	Kilimliğöl Formation	Gneiss	No data
1806	0678020E-4438787N	Gökdere Formation	Gneiss	No data
1807	0683679E-4436048N	Mesudiye Formation	Arkozic conglomerate	No data
1808	0684064E-4436186N	Central Uludağ Granite	Granite	No data
1809	0684316E-4436073N	Contact of Gökdere Formation-Central Uludağ Granite	Gneiss	lower intercept (TTE) = 164 Ma upper intercept (FD) = 236 Ma
1810	0700110E-4438700N	Gökdere Formation	Gneiss	lower intercept (TTE) = 162 Ma upper intercept (FD) = 225Ma
1811	0698275E-4438367N	Gökdere Formation	Gneiss	lower intercept (TTE)= 53.7 Ma upper intercept (FD) = 104 Ma
1812	0698238E-4436431N	Kilimliğöl Formasyonu	Gneiss	TTE: 53.98 ± 0.28 Ma
1813-P1	0675579E-4430759N	Kapıdağ Granite	Granite	CD: 47.87 ± 0.27 Ma
1814	0681067E-4438279N	South Uludağ Metagranite	Metagranit	MD: 34.44 ± 0.20 Ma
1815	0681007E-4438254N	South Uludağ Metagranite	Granite	No data
1816	0679386E4438917N	South Uludağ Metagranite	Granite	No data
1817	0685974E-4436792N	South Uludağ Metagranite	Metagranite	MD: 35.43 ± 1.5 Ma
1818	0687125E-4436327N	South Uludağ Metagranite	Metagranite	No data
1819	0690511E-4434829N	South Uludağ Metagranite	Metagranite	MD: 34.36 Ma
1820	0684777E-4440425N	Contact of Gökdere Formation-Central Uludağ Granite	Gneiss	lower intercept (TTE)= 24 Ma upper intercept (FD) = 192 Ma
1821	0686598E-4440640N	Central Uludağ Granite	Granite	CD: 29.53 Ma
1822	0684134E-4442776N	Central Uludağ Granite	Granite	No data
1901	0671924E-4443771N	Sazak Formation	Metabasite	No data
1902-P(A)	0674700E-4445731N	Gökdere Formation	Metagranite	No data
1902-P(B)	0674700E-4445731N	Gökdere Formation	Gneiss	No data
1903	0674701E-4445539N	Gökdere Formation	Metagranite	MD: 32.03 Ma
1904	0673928E-4446845N	Gökdere Formation	Gneiss	lower intercept (TTE)= 222 Ma upper intercept (FD) = 252 Ma
1905	0675307E-4442650N	Sazak Formation	Metabasite	No data

CHAPTER 7

DISCUSSIONS AND CONCLUSIONS

7.1 Discussions

The metamorphic rocks of the Uludağ Massif from bottom to top are: the Kilimligöl formation, consists mainly of amphibolites, the Zirve marble unconformably overlies these amphibolites, Gökdere formation is tectonically overlying the Zirve marble and mainly consisting gneisses with amphibolite intercalations, and conformably overlain by the Bursa marble. These metamorphic basement rocks cut by the Central Uludağ Granite and the South Uludağ Metagranite

During the fieldwork, samples were collected, geological mapping was carried out throughout the area, and measurements were taken from the formations as given in the previous chapters. Thin sections of the collected samples were made, and examined, and geochemical and geochronological analyses were applied.

The structure and mechanisms activity during the deformation of exhumed ductile shear zones have been the subject of several investigations. Several studies have examined fault zones and their effects on mountain ranges and glaciers. For example, Coward (1976), Sibson (1977), and Imber et al. (1997) focused on the Outer Hebrides Shear Zone. Phillips and Searle (2007) and Wallis et al. (2013) examined the Karakoram Fault Zone. Godin et al. (2006) and Parsons et al. (2016) examined the mid-crustal channel flow in the Annapurna-Dhaulagiri Himalaya. Baldwin and Lister (1998) and West and Hubbard (1997) examined the Norumbega Fault Zone. A combination of microstructural investigation to show the temperature of deformation by calcite twinning (Burkhard, 1993) and recrystallisation in quartz (Stipp et al. 2002) were used to determine the deformation conditions on the exhumed ductile shear zones in this study.

According to Lloyd and Freeman (1994) and Stipp et al. (2002), all of the quartz and feldspar examples exhibited recrystallisation due to sub-grain rotation (SGR), which corresponds to temperatures ranging from around 400 to 500°C. Stipp et al. (2002) and Simpson and Wintsch (1989) found that samples inside the SUM exhibited higher temperature deformation patterns, such as grain boundary migration (GBM) recrystallisation (500-700°C) and myrmekite (600°C) in feldspar. These structures were seen in the microstructure of the compounds.

Several large earthquakes have occurred along the Eskişehir fault system during the instrumental period. The Bursa Fault is an example of a typical fault, and it is still active. Sandison (1855), Sellami et al. (1997), Meade et al. (2002), and Selim and Tüysüz (2013) came up with the idea. A magnitude of $M=6.6$ was recorded for the Bursa earthquake that occurred in 1855, according to Sandison (1855), who chronicled the most recent incident. It is situated at the northernmost edge of the exposed massif and has a vertical difference of around one thousand metres. It descends the Bursa Plain.

An igneous origin is suggested by the fact that the gneiss is distributed uniformly over the whole massif. The absence of metasedimentary strata and mineralogical variations suggest gneisses originated from metamorphic or igneous rocks. Okay et al. (2008) findings were comparable to this one. A piece of the exposed terrane, referred to as The Uludağ Group, comprises the gneiss, which stands beside the marble. The granite intrusion that is situated to the north-northwest of the mountain. Okay et al. (2008) have described a substantial intrusion of granitic rock called the Central Uludağ Granite. A brecciated zone inside the marble is indicative of the development of brittle faulting at a later period. The existence of dykes inside the Central Uludağ Granite offers evidence that lends credence to the idea that the intrusion took place after the termination of strike-slip activity, hence confirming a post-kinematic intrusion. Granite has foliation features often seen in vast igneous intrusions, and these traits may be seen on the borders of the granite. This is a consequence of the tension applied to the rock that served as the host.

Before the uplift during the Miocene, the Eskişehir fault underwent extensive dextral strike-slip deformation. This occurred before the fault transformed into an

oblique normal fault, as Okay et al. (2008) and Özsayın and Dirik (2007) stated. This is made clear in the field by two unique sets of mineral stretching lineations: the sub-horizontal lineations, which are associated with ductile shear, and the sub-vertical lineations, which are formed during exhumation. Both of these ranges of lineations are connected with mineral stretching. Folds that appear inside fault zones, in addition to asymmetrical shards of quartz and feldspar, are unambiguous signs that shear has occurred. Furthermore, they indicate a strike-slip shear that is right-lateral in orientation.

The geological map that Okay et al. (2008) created is mostly based on the map that Ketin created in 1947. Based on this information, it may be deduced that the primary portions of the Eskişehir fault are situated southeast of the deformed granite. Additionally, there may be a development of gneiss. The maps used to produce

Figure 2.1 were obtained from the Mineral Research and Exploration General Directorate, which the MTA represents. The maps provide evidence of the existence of the Eskişehir fault, which runs through the South Uludağ Meagranite.

Following Okay et al. (2008), evidence suggests the formation of the South Uludağ Granite occurred within the same period as the tectonic movements. There is no evidence of contact metamorphism with the rocks directly next to this one. Consequently, this suggests that it was situated at a considerable depth, where the temperature of the surrounding environment was quite high. Furthermore, it oriented itself in a manner parallel to the predominant pattern of foliation and had a flat and sheet-like form. During the middle of the Cretaceous era, the Anatolide-Taurides experienced a process of closure, which led to the ophiolitic melange being positioned in the southern basin near the granite. According to Okay et al. (2008), the chemical is a complex of accretionary compounds undergoing severe shearing.

Tetragonal forces, mostly exhibited as strain inside the massif, cause the occurrences that have been seen. Based on the existence of a broad fault-parallel and mylonitic fabric, it may be inferred that the rocks in the massif, namely the

gneiss and South Uludağ Granites, were subjected to comparable tectonic stresses within a ductile shear zone. These locations, which are situated outside of the shear zone and the massif, often exhibit the most significant changes in strain direction. Various rocks, which display various variances, derive from various tectonic terranes located in the Uludağ massif and shear zone. Similar to the Eskişehir Fault Zone, which symbolises the IAES (Okay et al. 2008), it is probable that these changes are related to accretionary tectonics. This assumption is supported by the fact that it is feasible. A change in the area's tectonics is indicated by the Bursa Fault and the weak formations located on the northern side. This occurred because the massif was raised off the border between the brittle and ductile zones and brought down to the surface of the Earth.

The differentiation between granitic gneisses and metagranites may be complex. While several studies propose that these rocks may have originated from a single magmatic phase that experienced metamorphism and deformation (Shabanian et al. 2020), others emphasise the significance of comprehending the separate ages and evolutionary trajectories of these rocks (Shabanian et al. 2020). The rocks described in this study have undergone metamorphism under specific circumstances, including granulite facies metamorphism and subsequent retrogression to amphibolite facies (Cockell et al. 2002). These processes have had a significant impact on the gneisses and metagranites.

All samples of quartz and feldspar exhibited sub-grain rotation (SGR) recrystallisation for gneisses and metagranites of Uludağ. SGR indicating temperatures ranging from 400-500°C (Lloyd and Freeman, 1994; Stipp et al. 2002) (Figure 4.44). The samples from the Uludağ Metagranites exhibit microstructures that indicate deformation at higher temperatures. These include grain boundary migration (GBM) recrystallisation (500-700°C) and myrmekite formation (600°C). These observations are supported by Figure 4.6, Figure 4.9, Figure 4.10, Figure 4.13, Figure 4.15, Figure 4.16, Figure 4.20, as well as Figure 4.44. (Stipp et al. 2002; Simpson and Wintsch, 1989).

The quartzo-feldspathic lithologies in the sample suite document the massif's deformation at higher temperatures, as seen in Figure 4.44. During the process of

exhumation, there is a noticeable fall in temperature, which is shown by the occurrence of brittle deformation seen in the overall structure of the Bursa Fault. In Figure 4.44, the depth related pressure-temperature-time route of the Uludağ Massif was created as a result of previous studies (from Okay et al. 2008) and this study considering estimations derived from mineralogy.

The ages of muscovite and biotite indicate that the gneisses underwent cooling from 350° to 250°C, which are the temperatures at which the minerals became closed systems. This cooling process occurred approximately 50 to 33 million years ago, as reported by Okay et al. (2008). Assuming a geothermal gradient of around 30°C/km, a particular viewpoint may calculate a constant exhumation rate from the data shown in Figure 4.44. According to Okay et al. (2008), the variation in the ages at which the South Uludağ Metagranite crystallised (30-39 Ma) may be attributed to the extended process of crystallisation occurring in a region of intense deformation.

According to the previous studies, the granite was intruded before any shear activity occurred, but it had not fully cooled to the surrounding temperature before the shear zone activity developed (Okay et al. 2008). Therefore, it can be inferred that the shear zone must have started towards the end of the crystallisation period, around 35 million years ago. The Eskişehir Fault underwent further growth and localization during the exhumation process because of the significant difference in rheological properties between the granite and the massif. This has significant consequences for the timing of the Uludağ shear zone.

The Central Uludağ Granite has an intrusion age of 27 Ma, as Okay et al. (2008) determined. This age marks the conclusion of deformation in a strike-slip shear zone. Thus, our research suggests that the period of shear activity occurred approximately 35 to 29 Ma, placing it in the early Oligocene.

The shear zone exhibited right lateral strike-slip shear, as shown by the widespread fault parallel foliation that included right lateral shear indications (Chapter 3). The deformation conditions were ductile, occurring at temperatures ranging from 300 to

500°C, as determined by analysing quartz-feldspath-related microstructures. Quartz is undergoing deformation via brittle mechanisms around the Bursa Fault.

The Apatite fission track ages obtained by Okay et al. (2008) indicate that the exhumation process ended. The dates are grouped about 20-22 Ma and 10-9 Ma, suggesting two distinct periods of increased uplift. The process of exhumation caused the replacement of formerly flexible materials with more brittle structures, as seen in the northern region of the Uludağ Massif near the Bursa Fault. These include fault breccia on a large scale.

7.2 Tectono-metamorphic Evolution of the Uludağ Massif

When the Bursa Fault in the north, which surrounds the massif, and the Soğukpınar Fault in the south, which forms the northwest end of the Eskişehir Fault, are compared, it is observed that the Bursa Fault is a normal fault formed as a result of brittle deformation. The samples, collected around the Bursa Fault show more brittle macro and microstructure with cataclastic, brecciated zones, fractures, and veining. This fault suggests that the crustal rocks were formed by showing brittle behaviour in the part of the crustal rocks that reacted to the deformation caused by friction during their emergence to the earth's surface. The Bursa Fault, easily seen in the vicinity, slopes towards the Bursa Plain, where elevation dramatically decreases.

There is no evidence that the marbles and gneisses found in the massif as members of the Uludağ Group are paragneiss. Marble and gneiss are the components of the massif rock, which is thought to be a part of the Uludağ Group and has taken its present position by surfacing. The dykes in the marble unit originate from the intrusions of the Central Uludağ Granite.

The Soğukpınar Fault has a right-lateral strike-slip component as a component of the Eskişehir fault system. Right-lateral strike-slip deformation probably occurred on the Eskişehir fault before it was activated as a strike-slip fault during the

Miocene uplift of the Uludağ Massif. These deformations are characterized by shearing, right-lateral strike-slip shearing, asymmetric quartz and feldspar clasts, and mineral stress striations. Our field observations show that the Eskişehir fault passes through the deformed South Uludağ Metagranite (Figure 7.2 and Figure 7.3). Petrographic interpretations of the metagranites show that the South Uludağ Metagranite is syn-kinematic and is located at a depth where the ambient temperature is high.

The massif has been stressed due to tectonic forces, the formation of structures parallel to the fault everywhere within a ductile shear zone, and mylonitic texture indicating the same tectonic effects. The Bursa Fault and fragile structures formed because of the rise of the massif from the brittle/ductile transition zone to the surface are examples of the change in the region's tectonics.

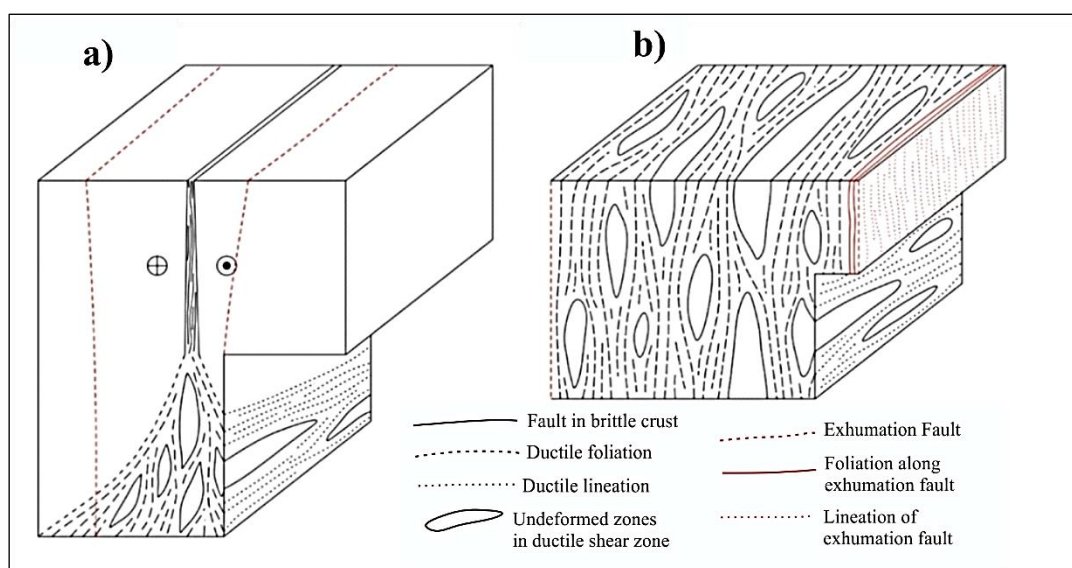


Figure 7.1. A ductile shear zone is overprinted on the figure during the exhumation process. a) In the middle of the crust, a ductile shear zone is actively deforming, with comparatively undisturbed zones surrounding it. The mid-crustal ductile shear zone is exhumed along the faults illustrated in b). The faults engaged in exhumation show a sub-vertical lineation that overprints the initial sub-horizontal ductile lineation.

The main deformation types that affected the evolution of the Uludağ Massif may be listed as follows and can be seen in Figure 7.1.

1) Bursa Fault (fault in the brittle crust), which borders the Uludağ Massif from the north and shows normal fault characteristics,

2) Ductile foliation leading to the formation of foliated units, e.g. South Uludağ Metagranite, Kilimligöl and Gökdere formation gneisses and all foliated metamorphic structures (Ductile Foliation),

3) Ductile lineation consisting of units formed because of tensile deformation,

4) Fault (Soğukpınar Fault) causing the units to surface (Exhumation Fault),

5) Foliation along the exhumation fault,

6) Lineation of the exhumation fault.

7) Emplacement of the Central Uludağ Granite (Magmatism) and,

8) Magmatism related temperature.

The data obtained from the field study conducted in Bursa, Uludağ Massif and its surroundings and the 1/25.000 scale map of the area are given in Figure 7.2 and Figure 7.3a. In addition, the cross-section diagram on the X-X' line on the map is given in Figure 7.3a is made without scale and shown in Figure 7.3b.

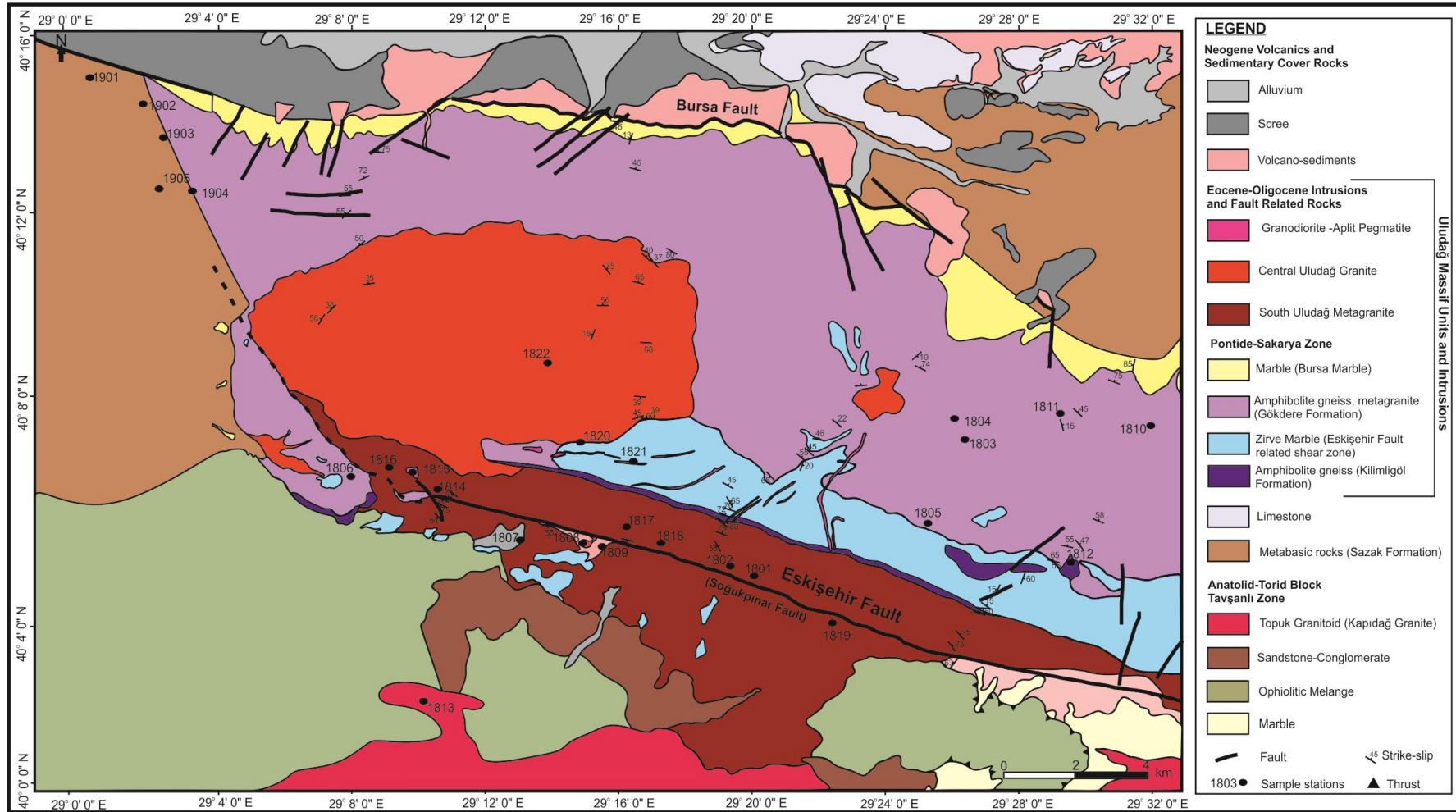


Figure 7.2. Geological map of the study area reconstructed as a result of field observations.

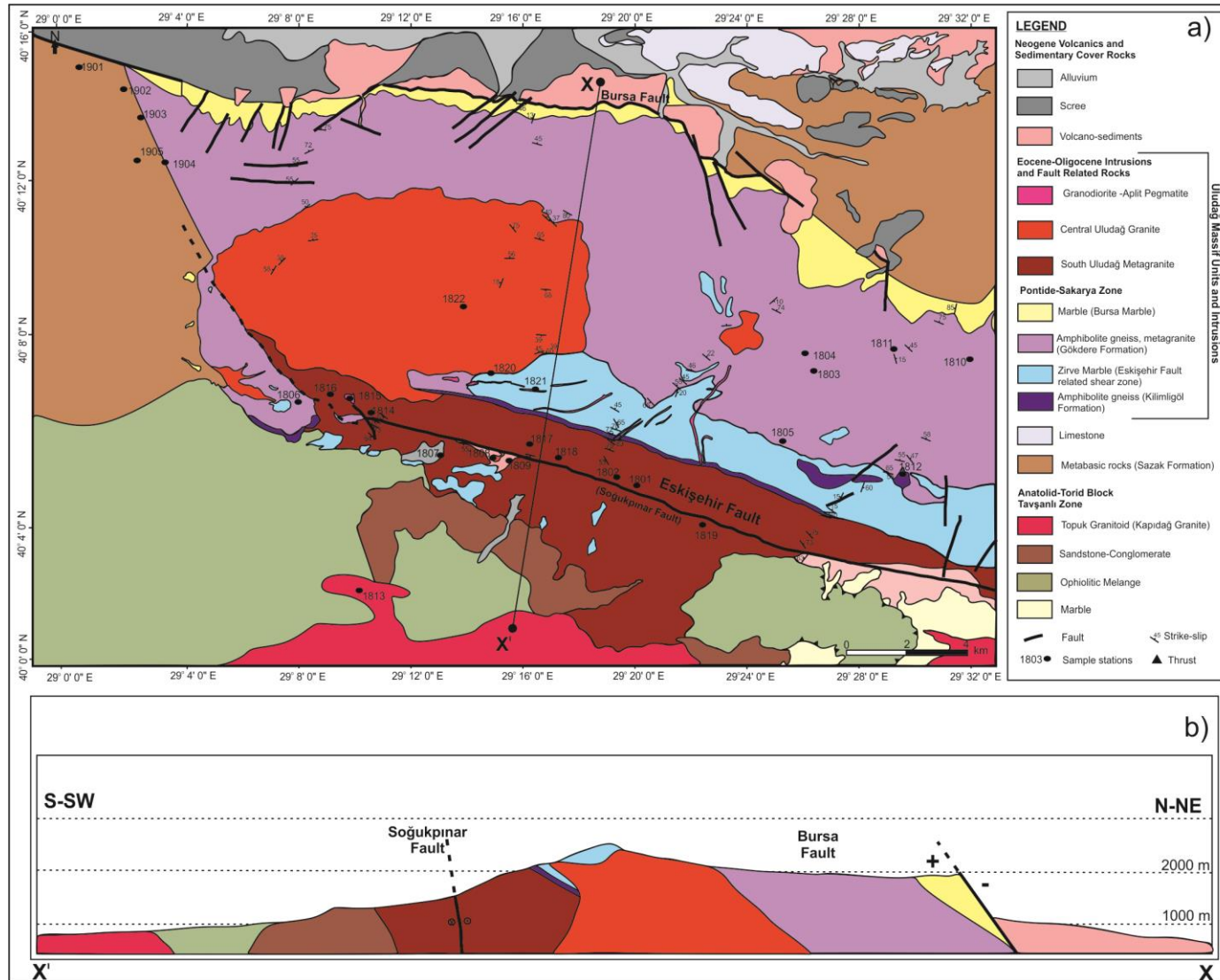


Figure 7.3. a) Geological map of the study area reconstructed from field observations and b) X'-X cross-section taken from this geological map.

7.3 Magmatic and Geochemical Evolution of the Uludağ Massif

According to geochemical data, tectono-magmatic discrimination diagrams show that all granite, metagranite, and gneiss samples originated from volcanic arc volcanism or active continent margin magmatism that occurred during the continent-continent collision. In contrast, metabasalt samples originated from intraplate magmatism. Sample (1822) of the Central Uludağ Granite, differs from other samples with similar lithologic characteristics and appears to be a granite sample related to intraplate volcanism rather than active tectonism. When we look at the geochemical properties of all these samples, granite sample number 1822 shows alkaline properties, while the other samples show more calc-alkaline chemical properties. According to the granite type classification, Central Uludağ Granite shows A-type granite chemistry, while Kapıdağ Granite shows I-S-type granite chemistry.

Regarding REE plots normalized to the primitive mantle, the negative anomalies of K, P and Ti indicate that they were preferentially extracted in certain mineral phases during the crystallisation of magmas and that fractional crystallisation occurred. In addition, the differentiation processes of certain minerals or phases within magmatic systems containing these elements led to the negative anomalies observed in REE plots.

REE plots normalized by chondrite show LREE enrichment and Eu anomalies. These anomalies are usually caused by various mineralogical processes that affect the distribution of rare earth elements. The first is the enrichment of light rare earth elements (LREE). Granitic rocks generally exhibit a marked enrichment of light rare earth elements (La - Sm) compared to heavy rare earth elements (Gd - Lu). This enrichment is primarily attributed to minerals such as feldspars (e.g., plagioclase and alkali feldspar) and micas (e.g., muscovite and biotite), which preferentially contain LREE during their formation. Another anomaly is the Eu anomaly. A distinctive feature in some granitic rocks is the Eu anomaly, which

shows a significant negative deviation in REE patterns normalized to chondrite. This anomaly, especially in plagioclase-containing rocks that contain more Eu than expected from the overall REE pattern, is caused by the breakdown of plagioclase or feldspar and its ejection from the melting part of the rock by partial melting. Post-magmatism alteration can also cause anomalies in the REE pattern of granitic rocks. Secondary processes such as hydrothermal alteration or metamorphism have led to the addition or removal of specific REEs, causing deviations in the chemistry indicative of the original magmatic texture.

Zr and Hf are considered low ion radius and high persistence elements (HFSEs). Depletion or negative anomalies in ORG (mid-ocean ridge) REE plots could mean these elements were less compatible during magmatic processes, forming ocean ridge granites. That situation could indicate that they were preferentially retained in minerals extracted from the magma source or were depleted during the formation of accessory minerals.

Elements such as Rb, Ba, Th, Ce, and Sm, which are large ion radius lithophile elements (LILE) and light rare earth elements (LREE), often show enrichment or positive anomalies in the upper crust REE plot. These elements are more abundant in rocks derived from crustal magma due to their proximity to minerals formed during magmatic differentiation processes.

Together with other high-field elements (HFSEs) such as Ti, Zr, and Hf, the upper crust often shows depletion or negative anomalies in the REE plot. It shows lower concentrations in crustal rocks due to its contact with minerals formed during igneous processes.

7.4 Interpretation of Geochronology and Isotope Geochemistry Together

As a result of LA-ICP-MS U-Pb Zircon analysis, metamorphism ages for metagranites, formation ages for gneisses and tectono-thermal impact ages for

some of them, and crystallisation ages for granites were obtained. Since age data could not be obtained from the Sazak Formation metabasalts, which are observed as the cover unit of the Uludağ Massif in the western, northwestern, and northeastern parts of the area, the protolith age data of the same unit in the study of Yiğitbaş et al. (2018), 455 Ma. was used. The age data obtained in this study are summarized in Table 6.2.

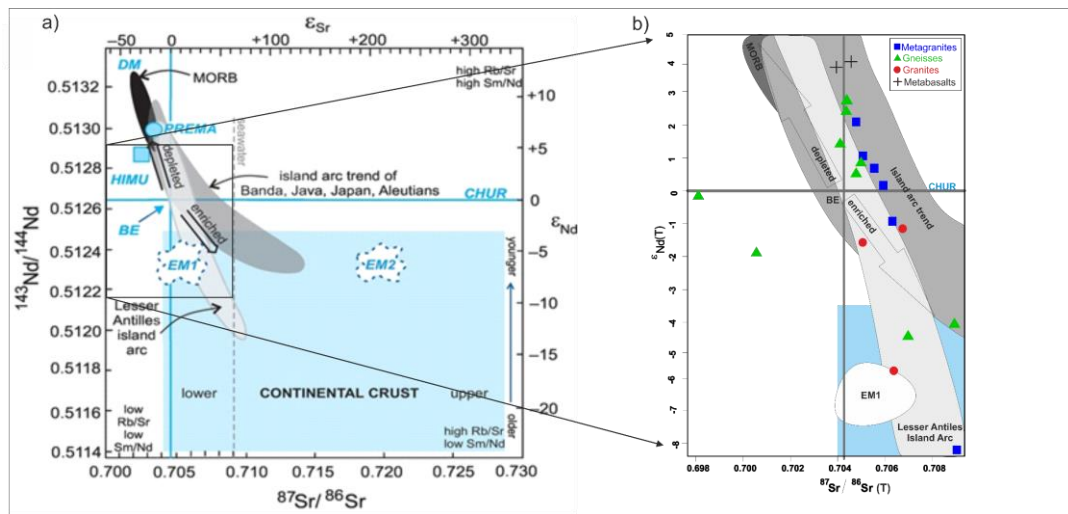


Figure 7.4. a) Mantle sources from Zindler and Hart (1986) and Rollinson and Pease (2021), b) mantle source results of this study.

The data on isotopes include the entire compositional spectrum of the rocks analyzed for this study. The initial isotope ratios are inhomogeneously distributed, with $^{87}\text{Sr}/^{86}\text{Sr}$ ratios ranging from 0.705331 to 0.71410 and $^{143}\text{Nd}/^{144}\text{Nd}$ ratios ranging from 0.512173 to 0.512767.

Samples of the study generally plot within the "island arc trend" identified in the left figure (Figure 7.4), between the BE and CHUR lines. This suggests a volcanic arc or subduction-related origin for these rocks.

Metagranites and gneisses show a trend from lower ϵ_{Nd} and $^{87}\text{Sr}/^{86}\text{Sr}$ ratios towards higher values. This could indicate varying degrees of crustal contamination

or different source regions in the mantle. For gneisses, when the ϵNd and $^{87}\text{Sr}/^{86}\text{Sr}$ values are analyzed based on 220 Ma. age data, it is concluded that, in general, the origin rock of the gneisses is related to island arc volcanism (Figure 7.4). In contrast, the formation mechanism of samples 1810 and 1811 (two gneiss sample) may be related to the subcontinental crust (Figure 7.4) The granite samples (red circles) plot in a tighter cluster with generally lower ϵNd values compared to the metamorphic rocks. This suggests they may have formed from partial melting of continental crust or have incorporated more crustal material during their formation. U-Pb zircon data could not be obtained for the metabasalts in this study, the U-Pb zircon age data from the same unit in Yiğitbaş et al. (2018) were used. For metabasalts, when ϵNd and $^{87}\text{Sr}/^{86}\text{Sr}$ values are calculated based on 455 Ma age data. Metabasalts plot with the highest ϵNd values and lowest $^{87}\text{Sr}/^{86}\text{Sr}$ ratios among our samples, indicating a more primitive, mantle-derived composition (Figure 7.4).

Overall trend, there is a general negative correlation between ϵNd and $^{87}\text{Sr}/^{86}\text{Sr}$ in the samples. This is consistent with mixing between a more depleted mantle source (higher ϵNd , lower $^{87}\text{Sr}/^{86}\text{Sr}$) and a more enriched crustal component (lower ϵNd , higher $^{87}\text{Sr}/^{86}\text{Sr}$). Comparing global trends with this study, samples plot close to the "Lesser Antilles Island Arc" field, suggesting similarities in petrogenesis or source regions to this well-studied arc system.

In conclusion, the study results suggests a complex interplay between mantle-derived magmas and crustal components in the formation of these rocks. The metabasalts likely represent the most primitive, mantle-derived compositions, while the granites and some metamorphic rocks show evidence of increased crustal input or contamination. The spread in isotopic compositions indicates heterogeneity in source regions or varying degrees of crustal assimilation during the formation of these rocks in what appears to be an island arc or subduction-related tectonic setting.

7.5 Geological Evolution

The İzmir-Ankara-Erzincan Suture Zone (IAESZ) is an important tectonic element in northern Türkiye, separating the Sakarya zone from the Anatolid-Torid block in the north and the Tavşanlı Zone in the south. This suture zone is associated with collision and subduction of oceanic crust with the continental margin and led to the formation of a subduction zone, a continental margin volcanic arc, and a back-arc basin with sedimentary infill (Rice et al. 2006). The IAESZ is characterized by ophiolitic clasts representing the remnants of an oceanic basement that developed between the Sakarya and Tavşanlı zones in the early Mesozoic. The collision and subduction processes in the IAESZ are reflected in the geological record. There is evidence of uplift in the region during the Early Paleocene (Okay et al. 2001) and the tectono-thermal impact age of 53.7 Ma obtained from the Gökdere formation gneiss number 1811 in this study (Table 6.2).

Furthermore, the IAESZ was formed following the northward subduction of the Tethys oceanic lithosphere during the Early Tertiary continental collision (Önen, 2003). The geologic evolution of the IAESZ includes complex tectonic processes such as subduction, collision, and orogenesis. Furthermore, the IAESZ played an important role in the tectonic evolution of northern Türkiye by forming a volcanic belt within the Neotethys suture zone (Tüysüz et al. 1995).

The closure of the Neotethys Ocean between the Sakarya Continent and the Tavşanlı Zone occurred during the Late Cretaceous to Early Miocene (Göncüoğlu et al. 2000). The Neotethys Ocean began to subduct northward beneath the southern margin of the Sakarya Zone in the Turonian and a volcanic arc remained active along the Pontides until Campanian (Ocakoglu et al. 2018). The IAESZ marks the closure of the Neotetis seaway that separated the Sakarya continent in the north from the Anatolid-Taurid platform in the south (Altunkaynak, 2007).

In summary, the closure of the Neotethys Ocean between the Sakarya Continent and the Tavşanlı Zone occurred during the Late Cretaceous to Early Miocene, and

significant subduction and collisions led to the final closure of the oceanic region in the Middle Eocene. This geological process involved complex tectonic interactions and volcanic activities that shaped the region's evolution over millions of years. The İzmir-Ankara-Erzincan Suture Zone results from the collision and subduction of the oceanic crust with the continental margin. It has led to a complex tectonic setting with diverse geologic features in and around the Uludağ Massif, located on the southern margin of the Sakarya Zone. This geological evolution can be explained as shown in Figure 7.5. for the last 100 Ma.

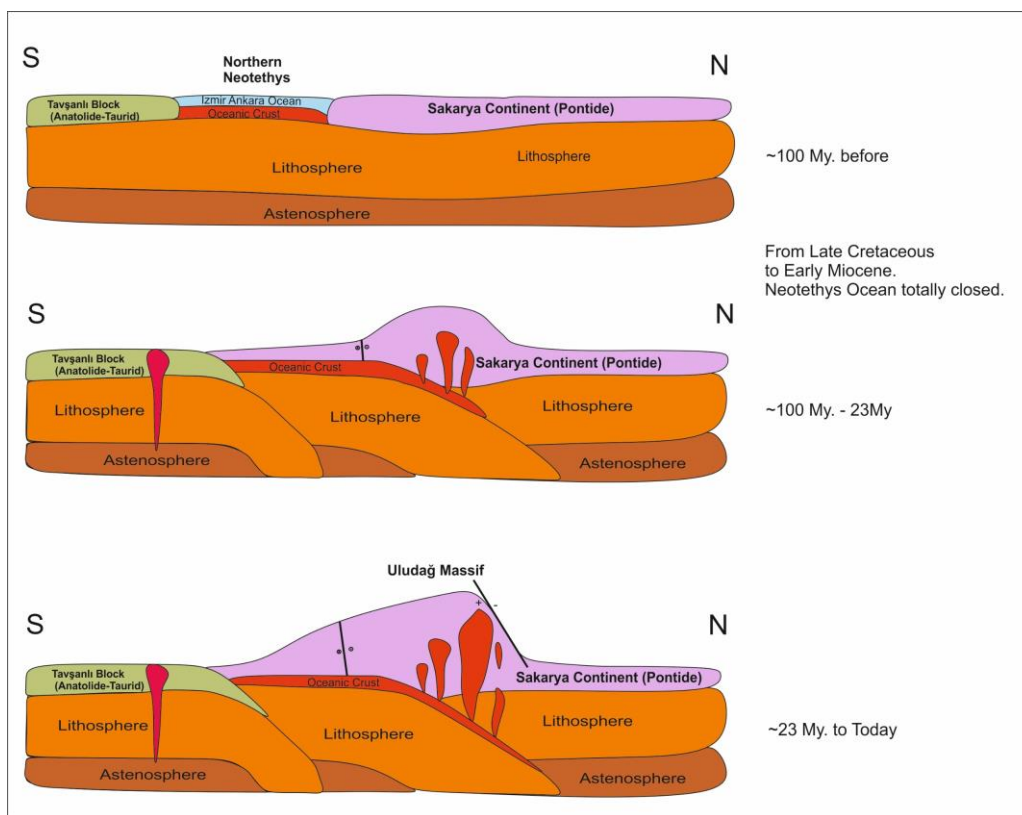


Figure 7.5. Simplified geological evolution model of the Uludağ Massif and its environment.

Finally, the main factors determining the formation of the Uludağ Massif can be explained in Figure 7.6. According to this figure, the primordial rocks at the basement of the Sakarya continent are about 450 Ma are visible. As the Hercynian/Variscan orogenesis affected the region, these rocks underwent metamorphism. I assume that this process may have been lasted from the Devonian

(400 Ma) to the Early Permian (290 Ma). The new rocks may have been formed due to the magmatism that dominated the region in the Permian could have been formed in the Middle-Late Permian (250-220 Ma). These primitive rocks may have been formed later. It can be thought that a very large-scale tectonic force and metamorphism conditions started in the region with the convergence and collision of the Tavşanlı Zone and the Sakarya Continent, which will cause the Neotethys Ocean to begin to close in the region where the fieldwork was carried out.

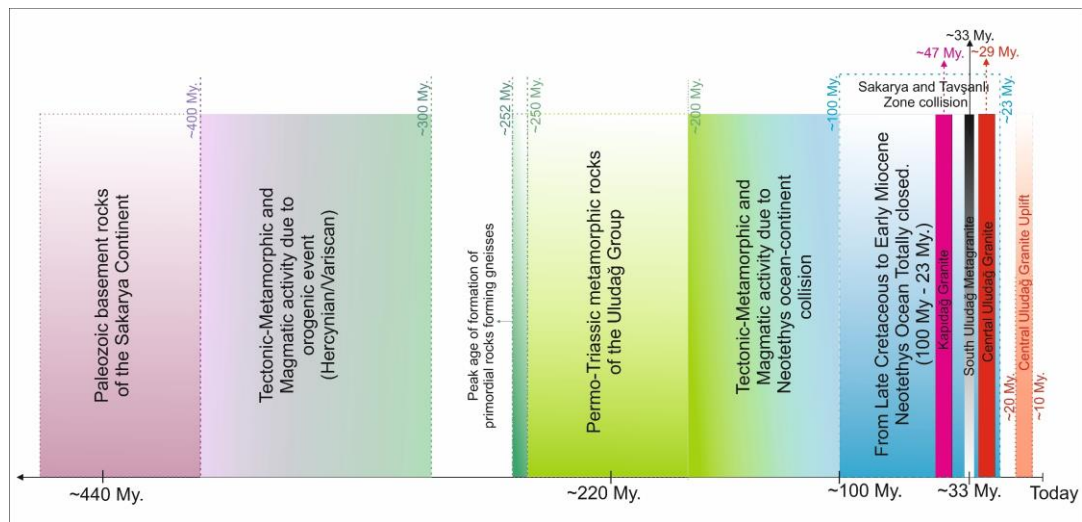


Figure 7.6. The general geological history of the Uludağ Massif and its surroundings.

With all these continental collisions and the closure of the Neotethys Ocean, the Kapıdağ Granites were formed about 47 Ma near the northern edge of the Tavşanlı Zone. The magmatism at the southern edge of the Sakarya Zone occurred about 29 Ma. These granitic rocks may have been formed due to the island arc volcanisms that occurred during the continental collision and the closure of the Neotethys Ocean. Finally, it is concluded that the Uludağ Granites were uplifted between approximately the last 10 and 20 Ma and took their present position.

7.6 Conclusions and Final Thoughts

7.6.1 Relationship between Uludağ and Kazdağ Massifs

This study provides new insights into the similarities and differences between the Uludağ and the Kazdağ massifs, both key components of the Sakarya Zone basement in Northwestern Anatolia.

The Kilimligöl formation in the Uludağ Massif shows similar lithological characteristics to the Fındıklı formation in the Kazdağ Massif, supporting the hypothesis of a common origin. Both formations consist primarily of amphibolites and gneisses, suggesting a shared metamorphic history. However, our U-Pb zircon dating of the Kilimligöl formation gneisses yielded ages ranging from 220-252 Ma, which are significantly older than the Carboniferous ages previously reported for the Kazdağ Massif (Okay and Satır, 2000). This suggests that while the two massifs may share a common tectonic setting, their detailed evolutionary histories may differ.

The Zirve marble in the Uludağ Massif and the Sarıkız marble in the Kazdağ Massif both represent major carbonate units within their respective sequences. Our field observations and petrographic analysis confirm their similar compositions and structural positions, supporting the idea that they may be equivalent units, as suggested by Okay et al. (2008).

The Gökdere formation in the Uludağ Massif, characterized by quartzo-feldspathic gneisses, shows similarities to the Sütüven formation in the Kazdağ Massif. This study's geochemical analysis of the Gökdere formation gneisses reveals a calc-alkaline, volcanic arc signature, consistent with the proposed origin of the Sütüven formation (Duru et al. 2004). This supports the hypothesis of a shared tectonic environment for both massifs during their formation.

7.6.2 Relationship between granitic intrusions

The U-Pb zircon ages obtained for the Central Uludağ Granite (29.53 Ma) and the Kapıdağ Granite (47.87 Ma) confirm their Tertiary age, similar to the Evciler and Eybek granites of the Kazdağ Massif (Altunkaynak et al. 2012). However, our geochemical analysis reveals that while the Kapıdağ Granite shows I-S type characteristics, the Central Uludağ Granite displays A-type signatures. This suggests a more complex magmatic evolution than previously recognized, with a transition from subduction/collision-related to post-collisional extensional magmatism, similar to the model proposed by Dilek and Altunkaynak (2007) for Western Anatolia.

The South Uludağ Metagranite, with U-Pb zircon ages of 32-35 Ma, is significantly younger than the Devonian-aged Çamlık Metagranite of the Kazdağ Massif (Okay, 1996). This indicates that despite their spatial relationships, these metagranites represent distinct magmatic events. Structural and petrographic analysis of the South Uludağ Metagranite suggests it was emplaced syn-kinematically during the development of the Oligocene shear zone, rather than representing an older, Carboniferous migmatitic event as proposed by Okay et al. (2008).

7.6.3 Role of major faults in the evolution of the Uludağ Massif

The Soğukpınar fault, forming the southern boundary of the massif, shows evidence of right-lateral strike-slip movement. Our microstructural analysis of rocks from the shear zone indicates deformation temperatures of 400-500°C, suggesting that this fault played a crucial role in the exhumation of mid-crustal rocks. The alignment of the South Uludağ Metagranite with this fault supports its importance in controlling magma emplacement during the Oligocene, consistent with the model proposed by Okay et al. (2008).

The Bursa fault, forming the northern boundary of the massif, shows clear evidence of normal faulting. Our field observations reveal a significant topographic step and the presence of brittle fault rocks, indicating that this fault was active during the later stages of massif exhumation. This is consistent with the findings of Selim and Tüysüz (2013), who proposed that the Bursa fault has been active since the Late Miocene. The transition from ductile deformation along the Soğukpınar fault to brittle deformation along the Bursa fault is consistent with progressive cooling and uplift of the massif through time, as suggested by Okay et al. (2008).

7.6.4 Tectono-metamorphic and magmatic evolution

Integrating our new geochronological, geochemical, and structural data allows us to propose a refined model for the tectono-metamorphic and magmatic evolution of the Uludağ Massif:

- Permian-Triassic (252-220 Ma): Formation of the protoliths of the gneisses of the Gökdere and Kilimligöl formations in a volcanic arc or active continental margin setting, consistent with the Paleo-Tethyan subduction model proposed by Şengör and Yılmaz (1981).
- Cretaceous-Paleocene: Main phase of amphibolite-facies metamorphism, possibly associated with the collision between the Sakarya Zone and Anatolide-Tauride Block (Okay and Tüysüz, 1999).
- Eocene (47.87 Ma): Emplacement of the Kapıdağ Granite as part of post-collisional I-S type magmatism, consistent with the timing proposed by Altunkaynak et al. (2012).
- Early Oligocene (35-32 Ma): Development of a major dextral strike-slip shear zone along the Soğukpınar fault, with syn-kinematic intrusion of the South Uludağ Metagranite, as suggested by Okay et al. (2008).

- Late Oligocene (29.53 Ma): Transition to an extensional regime, with emplacement of the A-type Central Uludağ Granite, reflecting the onset of post-collisional extension in Western Anatolia (Dilek and Altunkaynak, 2007).
- Miocene-Present: Continued exhumation and cooling of the massif, with development of the Bursa normal fault (Selim and Tüysüz, 2013).

This model reconciles the diverse dataset obtained in our study and provides a coherent framework for understanding the complex geological history of the Uludağ Massif. It highlights the importance of integrating multiple analytical techniques to unravel the evolution of complex orogenic regions.

In conclusion, this study has significantly advanced our understanding of the geological evolution of the Uludağ Massif and its relationship to other tectonic units in Northwestern Anatolia. We have provided new constraints on the timing of major tectonic, metamorphic, and magmatic events, and clarified the roles of major structures in the exhumation history of the massif. These results have important implications for regional tectonic models and our understanding of orogenic processes in general.

7.7 Recommendations

Considering all the results obtained, the Uludağ Massif units, which are located in the northwest of Anatolia and form the basement of the Sakarya Zone, and the Kazdağı Massif units, which are also located in the northwest of Anatolia and west of the Uludağ Massif and also form the basement of the Sakarya Zone, show great similarities in terms of the formation and crystallisation ages of these units according to the previous studies. Although, geochemical and geochronological studies of the Kazdağı Massif units have already been carried out, it is important to conduct a comparison study by taking samples from similar units in both massifs

within the same study. It is important to conduct another lithological unit-based geochemical and geochronological study for both massifs forming the south of the Sakarya Continent to compare them at their basement levels to better understand northwestern Anatolia's geology.

REFERENCES

- Altunkaynak, Ş. (2007). Collision-driven slab breakoff magmatism in northwestern anatolia, turkey. *The Journal of Geology*, 115(1), 63-82. <https://doi.org/10.1086/509268>.
- Altunkaynak, Ş., Sunal, G., Aldanmaz, E., Genç, C. Ş., Dilek, Y., Furnes, H., ... & Yıldız, M. (2012). Eocene granitic magmatism in NW Anatolia (Turkey) revisited: new implications from comparative zircon SHRIMP U–Pb and ⁴⁰Ar–³⁹Ar geochronology and isotope geochemistry on magma genesis and emplacement. *Lithos*, 155, 289-309.
- Ambraseys, N. (2002). The seismic activity of the Marmara Sea region over the last 2000 years. *Bulletin of the Seismological Society of America*, 92(1), 1-18.
- Anczkiewicz, R., Viola, G., Müntener, O., Thirlwall, M., Villa, I. M. & Quong, N. Q. (2007). Structure and shearing conditions in the Day Nui Con Voi massif: Implications for the evolution of the Red River shear zone in northern Vietnam. *Tectonics*, 26.
- Anders, E., Grevesse, N. (1989). Abundances of the elements: Meteoritic and solar. *Geochimica et Cosmochimica Acta*, 53, 197– 214.
- Baldwin, S. L. & Lister, G. S. (1998). Thermochronology of the South Cyclades Shear Zone, Ios, Greece: Effects of ductile shear in the argon partial retention zone. *Journal of Geophysical Research: Solid Earth*, 103, 7315-7336.
- Barka, A. A., Reilinger, R., Şaroğlu, F., Sengör, A. M. C. (1995). The Isparta Angle: Its importance in the Eastern Mediterranean region. *IIESCA-1995*. 1, -17.

- Berberian, F. & Berberian, M. (1981). Tectono-plutonic episodes in Iran. In: Zagros, Hindu Kush, Himalaya Geodynamic Evolution. American Geophysical Union, Washington, DC, 5-32.
- Bingöl, E. (1969). Kazdağ Masifi'nin merkezi ve güneydoğu kısmının jeolojisi. MTA Enst. Dergisi, Sayı 72, s. 110-123, Ankara.
- Bingöl, E., Akyürek, B. ve Korkmazer, B. (1973). Biga Yarımadası'nın jeolojisi ve Karakaya formasyonunun bazı özellikleri. Cumhuriyetin 50. Yılı Yerbilimleri Kongresi Tebliğleri, MTA, s. 70-77, Ankara.
- Bingöl, E., Delaloye, M., & Ataman, G. (1982). Granitic intrusions in Western Anatolia: a contribution to the geodynamic study of this area. *Eclogae Geol. Helv.* Vol. 75/2.,437-446.
- Black, L.P., Kamo, S.L., Allen, C.M., Aleinikoff, J.N., Davis, D.W., Korsch, R.J., Foudoulis, C. (2003). TEMORA 1: a new Zircon standard for phanerozoic U-Pb geochronology. *Chemical Geology* 200, 155-170.
- Bolhar, R., Whitehouse, M.J., Milani, L., Magalhães, N., Golding, S.D., Bybee, G., LeBras, L., Bekker, A. (2020). Atmospheric S and lithospheric Pb in sulphides from the 2.06 Ga Phalaborwa phoscorite-carbonatite complex, South Africa. *Earth and Planetary Science Letters* 530, 115939.
- Bozkurt, E. (2001). Neotectonics of Turkey—a synthesis. *Geodinamica Acta*, 14, 3-30.
- Bozkurt, E. and Park, R. (1997). Microstructures of deformed grains in the augen gneisses of southern menderes massif (western turkey) and their tectonic significance. *Geologische Rundschau*, 86(1), 103-119. <https://doi.org/10.1007/s005310050125>
- Brückner, L. M., Trepmann, C. A., & Kaliwoda, M. (2023). Rheology dependent on the distance to the propagating thrust tip—(ultra-)mylonites and

- pseudotachylytes of the silvretta basal thrust. *Tectonics*, 42(10).
<https://doi.org/10.1029/2023tc008010>
- Burkhard, M. (1993). Calcite twins, their geometry, appearance and significance as stress-strain markers and indicators of tectonic regime: a review. *Journal of Structural Geology*, 15, 351-368.
- Cabanis, B. & Lecolle, M. (1989). Le diagramme La/10-Y/15-Nb/8: un outil pour la discrimination des séries volcaniques et la mise en évidence des processus de mélange et/ou de contamination crustale. *Comptes rendus de l'Académie des sciences. Série 2, Mécanique, Physique, Chimie, Sciences de l'univers, Sciences de la Terre* 309, 2023–2029.
- Carr, M.J., Gazel, E. (2017). Igpets software for modelling igneous processes: Examples of application using the open educational version. *Mineralogy and Petrology* 111, 283– 289.
- Chen, Y., Watanabe, K., Kusuda, H., Kusaka, E., & Mabuchi, M. (2011). Crack growth in westerly granite during a cyclic loading test. *Engineering Geology*, 117(3-4), 189-197. <https://doi.org/10.1016/j.enggeo.2010.10.017>.
- Chopin, F., Schulmann, K., Štípská, P., Martelat, J., Pitra, P., Lexa, O., ... & Petri, B. (2012). Microstructural and metamorphic evolution of a high-pressure granitic orthogneiss during continental subduction (orlica–śniežnik dome, bohemian massif). *Journal of Metamorphic Geology*, 30(4), 347-376. <https://doi.org/10.1111/j.1525-1314.2011.00970.x>.
- Cockell, C. S., Lee, P., Osinski, G. R., Horneck, G., & Broady, P. A. (2002). Impact-induced microbial endolithic habitats. *Meteoritics & Planetary Science*, 37(10), 1287-1298. <https://doi.org/10.1111/j.1945-5100.2002.tb01029.x>.
- Coward, M. (1976). Strain within ductile shear zones. *Tectonophysics*, 34, 181-197.

- Cruciani, G., Franceschelli, M., Groppo, C., Oggiano, G., & Spano, M. (2014). Re-equilibration history and p–t path of eclogites from variscan sardinia, italy: a case study from the medium-grade metamorphic complex. *International Journal of Earth Sciences*, 104(3), 797-814. <https://doi.org/10.1007/s00531-014-1095-5>
- Cruciani, G., Franceschelli, M., Scodina, M., & Puxeddu, M. (2018). Garnet zoning in kyanite-bearing eclogite from golfo aranci: new data on the early prograde p–t evolution in ne sardinia, italy. *Geological Journal*, 54(1), 190-205. <https://doi.org/10.1002/gj.3169>
- Currin, A., Wolff, P., Koepke, J., Almeev, R., Zhang, C., Zihlmann, B., ... & Teagle, D. (2018). Chlorine-rich amphibole in deep layered gabbros as evidence for brine/rock interaction in the lower oceanic crust: a case study from the wadi wariyah, samail ophiolite, sultanate of oman. *Lithos*, 323, 125-136. <https://doi.org/10.1016/j.lithos.2018.09.015>
- Dal Piaz, G. V., & Lombardo, B. (1986). Early Alpine eclogite metamorphism in the Penninic Monte Rosa-Gran Paradiso basement nappes of the northwestern Alps. *Geological Society of America Memoirs*, 164, 249-266.
- Delaloye, M., & Bingöl, E. (2000). Granitoids from western and northwestern Anatolia: geochemistry and modeling of geodynamic evolution. *International Geology Review*, 42(3), 241-268.
- Delaloye, M., and Bingöl E. (2000). Granitoids from Western and Northwestern Anatolia: Geochemistry and modelling of geodynamic evolution, *International Geology Review*, 42, 241-268.
- Demetriades, A. (2014). Basic considerations: Sampling, the key for a successful applied geochemical survey for mineral exploration and environmental purposes. In: Holland, H.D., Turekian, K.K. (eds.), *Treatise on geochemistry*, 2nd ed. Elsevier, Oxford. 15: 1– 31.

- Dilek, Y., & Altunkaynak, Ş. (2007). Cenozoic crustal evolution and mantle dynamics of post-collisional magmatism in western Anatolia. *International Geology Review*, 49(5), 431-453.
- Duru, M., Pehlivan, Ş., Şentürk, Y., Yavaş, F. and Kar, H. (2004) New Results on the Lithostratigraphy of the Kazdağ Massif in Northwest Turkey, *Turkish Journal of Earth Sciences*: Vol. 13: No. 2, Article 4. <https://journals.tubitak.gov.tr/earth/vol13/iss2/4>.
- Duru, M., Pehlivan, S., Dönmez, M., Ilgar, A., & Akcay, A. E. (2007). 1: 100.000 ölçekli Türkiye jeoloji haritaları, Bandırma H 18 paftası No 102, Maden Tetkik ve Arama Genel Müdürlüğü, 50 p.
- Ercan, T., & Türkecan, A. (1984). A general review of the plutons in western Anatolia, Aegean Islands, Greece and Bulgaria. In *Ketin Symposium* (pp. 20-21).
- Fan, S., Prior, D. J., Hager, T. F., Cross, A. W., Goldsby, D. L., & Negrini, M. (2021). Kinking facilitates grain nucleation and modifies crystallographic preferred orientations during high-stress ice deformation. <https://doi.org/10.31223/x5rg9g>.
- Fernandez, F., Llana-Funez, S., Valverde-Vaquero, P., Marcos, A., & Castineiras, P. (2016). Insights on High-Grade Deformation in Quartzo-Feldspathic Gneisses During the Early Variscan Exhumation of the Cabo Ortegal Nappe, NW Iberia. *Solid Earth*, 7(2), 579-598. <https://doi.org/10.5194/se-7-579-2016>.
- Floyd, P. A., Göncüoğlu, M. C., Winchester, J. A. & Yaliniz, M. K. (2000). Geochemical character and tectonic environment of Neotethyan ophiolitic fragments and metabasites in the Central Anatolian Crystalline Complex, Turkey. *Geological Society, London, Special Publications*, 173, 183-202.
- Fügenschuh, B., Gromet, L., Stünitz, H., & Schmid, S. (2004). Contemporaneous plutonism and strike-slip faulting: a case study from the tonale fault zone

- north of the adamello pluton (italian alps). *Tectonics*, 23(3).
<https://doi.org/10.1029/2003tc001515>.
- Genc, S. (1987). Geology of the Region between Uludag and Iznik Lake. IGCP, Project N, 5, 19-25.
- Godin, L., Grujic, D., Law, R. & Searle, M. (2006). Channel flow, ductile extrusion and exhumation in continental collision zones: an introduction. Geological Society, London, Special Publications, 268, 1-23.
- Göncüoğlu, M., Turhan, N., Şentürk, K., Özcan, A., Uysal, Ş., & Yaliniz, M. (2000). A geotraverse across northwestern turkey: tectonic units of the central sakarya region and their tectonic evolution. Geological Society London Special Publications, 173(1), 139-161.
<https://doi.org/10.1144/gsl.sp.2000.173.01.06>.
- Görür, N., Oktay, F., Seymen, I. & Şengör, A. (1984). Palaeotectonic evolution of the Tuzgölü basin complex, Central Turkey: sedimentary record of a Neo-Tethyan closure. Geological Society, London, Special Publications, 17, 467-482.
- Grujic, D., Stipp, M., & Wooden, J. L. (2011). Thermometry of quartz mylonites: Importance of dynamic recrystallisation on Ti-in-quartz reequilibration. *Geochemistry, Geophysics, Geosystems*, 12(6).
- Harigane, Y., Michibayashi, K., & Ohara, Y. (2011). Relicts of deformed lithospheric mantle within serpentinites and weathered peridotites from the godzilla megamullion, parece vela back-arc basin, philippine sea. *Island Arc*, 20(2), 174-187. <https://doi.org/10.1111/j.1440-1738.2011.00759.x>.
- Harris, N. B., Pearce, J. A., & Tindle, A. G. (1986). Geochemical characteristics of collision-zone magmatism. Geological Society, London, Special Publications, 19(1), 67-81.

- Hughes, C. J. (1973). Spilites, keratophyres and igneous spectrum. *Geological Magazine*, 109(6), 513–527.
- Garlick, S. and Gromet, L. (2004). Diffusion creep and partial melting in high temperature mylonitic gneisses, hope valley shear zone, new england appalachians, usa. *Journal of Metamorphic Geology*, 22(1), 45-62. <https://doi.org/10.1111/j.1525-1314.2004.00496.x>.
- Gibbons, W. (1983). The Monian ‘Penmynydd Zone of Metamorphism’ in Llŷn, North Wales. *Geological Journal*, 18(1), 21-41. <https://doi.org/10.1002/gj.3350180103>.
- Guillope, M., & Poirier, J. P. (1979). Dynamic recrystallization during creep of single-crystalline halite: An experimental study. *Journal of Geophysical Research: Solid Earth*, 84(B10), 5557-5567.
- Hellstrom, John & Paton, Chad & Woodhead, Jon & Hergt, Janet. (2008). Iolite: software for spatially resolved LA-(quad and MC) ICPMS analysis. *Mineralogical Association of Canada short course series*. 40. 343–348.
- Hermann, J., Rubatto, D., Korsakov, A., & Shatsky, V. S. (2001). Multiple zircon growth during fast exhumation of diamondiferous, deeply subducted continental crust (Kokchetav massif, Kazakhstan). *Contributions to Mineralogy and Petrology*, 141(1), 66-82. <https://doi.org/10.1007/s004100000218>
- Hutton, D. (1982). A tectonic model for the emplacement of the Main Donegal Granite, NW Ireland. *Journal of the Geological Society*, 139, 615-631.
- Imber, J., Holdsworth, R., Butler, C. & Lloyd, G. (1997). Fault-zone weakening processes along the reactivated Outer Hebrides Fault Zone, Scotland. *Journal of the Geological Society*, 154, 105-109.

- Işık, V. & Tekeli, O. (2001). Late orogenic crustal extension in the northern Menderes massif (western Turkey): evidence for metamorphic core complex formation. *International Journal of Earth Sciences*, 89, 757-765.
- Jackson, M.G., Hart, S.R., Koppers, A.P., Staudigel, H., Konter, J., Blusztajn, J., Kurz, M., Russell, J.A. (2007). The return of subducted continental crust in Samoan lavas. *Nature* 448, 684– 687.
- Janousek, V., Moyen, J.F., Martin, H., Erban, V., Farrow, C. (2016). *Geochemical modelling of igneous processes – Principles and recipes in R language: Bringing the power of R to a geochemical community*. Springer-Verlag, Berlin.
- Jarvis, K.E., Williams, J.G. (1989). The analysis of geological samples by slurry nebulisation inductively coupled plasma-mass spectrometry (ICPMS). *Chemical Geology* 77, 53– 63.
- Kahle, H.-G., Straub, C., Reilinger, R., McClusky, S., King, R., Hurst, K., Veis, G., Kastens, K. & Cross, P. (1998). The strain rate field in the eastern Mediterranean region, estimated by repeated GPS measurements. *Tectonophysics*, 294, 237-252.
- Kamber, B.S. (2015). The evolving nature of terrestrial crust from the Hadean, through the Archaean, into the Proterozoic. *Precambrian Research* 258, 48– 82.
- Kanar, F., Pehlivan, Ş., Kandemir, Ö., Tok, T., Çakır, K. (2013). 1/100.000 Ölçekli Türkiye Jeoloji Haritaları Serisi, Maden Tetkik ve Arama Genel Müdürlüğü, Bursa-H22 Paftası, No:192.
- Kanen, R. (2004). WinRock. www.geologynet.com/manuals/WinRockMan.pdf.
- Ketin, İ. (1946). Geological investigations in the Marmara Island and the Kapıdağ Peninsula (Marmara Adası ve Kapıdağ Yarımadası'nda jeolojik incelemeler). *İÜ Sci Fac Bull Serie B XI (2)*, 69-81.

- Ketin, İ. (1947). Uludağ masifinin tektoniği hakkında. Türkiye Jeoloji Bülteni, 1(1), 60-88.
- Kim, H., Fujii, H., & Lee, S. (2020). Corrosion behavior and microstructure of stir zone in Fe-30Mn-3Al-3Si twinning-induced plasticity steel after friction stir welding. *Metals*, 10(11), 1557. <https://doi.org/10.3390/met10111557>.
- Kirker, A. and McClelland, E. (1997). Deflection of magnetic remanence during progressive cleavage development in the Pembroke Old Red sandstone. *Geophysical Journal International*, 130(1), 240-250. <https://doi.org/10.1111/j.1365-246x.1997.tb01002.x>.
- Koçyiğit, A. (2005). The Denizli graben-horst system and the eastern limit of western Anatolian continental extension: basin fill, structure, deformational mode, throw amount and episodic evolutionary history, SW Turkey. *Geodinamica Acta*, 18, 167-208.
- Kramers, J.D., Tolstikhin, I.N. (1997). Two terrestrial lead isotope paradoxes, forward transport modelling, core formation and the history of the continental crust. *Chemical Geology* 139(1–4), 75–110.
- Lepland, A. and Whitehouse, M. J. (2010). Metamorphic alteration, mineral paragenesis and geochemical re-equilibration of early Archean quartz–amphibole–pyroxene gneiss from Akilia, southwest Greenland. *International Journal of Earth Sciences*, 100(1), 1-22. <https://doi.org/10.1007/s00531-010-0515-4>
- Luc Leroy, N. M., Joseph, N. D. O. P., & Bienvenu, J. M. (2017). Investigations of thermal damage on the physical and mechanical properties of gneiss rock specimen. *J Powder Metall Min*, 6(176), 2. doi:10.4172/2168-9806.1000176.
- Lloyd, G. E. & Freeman, B. (1994). Dynamic recrystallization of quartz under greenschist conditions. *Journal of Structural Geology*, 16, 867-881.
- Ludwig, Kenneth. (2001). Users Manual for Isoplot/Ex Rev. 2.49.

- Luisier, C., Baumgartner, L. P., Putlitz, B., & Vennemann, T. (2021). Whiteschist genesis through metasomatism and metamorphism in the Monte Rosa nappe (Western Alps). *Contributions to Mineralogy and Petrology*, 176, 1-24.<https://doi.org/10.1007/s00410-020-01759-0>
- Malpas, J., Calon, T. & Squires, G. (1993). The development of a late Cretaceous microplate suture zone in SW Cyprus. *Geological Society, London, Special Publications*, 76, 177-195.
- Martin, H. (1986). Effect of steeper Archean geothermal gradient on geochemistry of subduction-zone magmas. *Geology* 14, 753–756.
- McKenzie, D. (1972). Active tectonics of the Mediterranean region. *Geophysical Journal of the Royal Astronomical Society*, 30, 109-185.
- Meade, B. J., Hager, B. H., McClusky, S. C., Reilinger, R. E., Ergintav, S., Lenk, O., Barka, A. & Özener, H. (2002). Estimates of seismic potential in the Marmara Sea region from block models of secular deformation constrained by Global Positioning System measurements. *Bulletin of the Seismological Society of America*, 92, 208-215.
- Michard, A. (1989). Rare earth element systematics in hydrothermal fluids. *Geochimica et Cosmochimica Acta*, 53(3), 745-750.
- Moix, P., Beccaletto, L., Kozur, H. W., Hochard, C., Rosselet, F. & Stampfli, G. M. (2008). A new classification of the Turkish terranes and sutures and its implication for the paleotectonic history of the region. *Tectonophysics*, 451, 7-39.
- Molnar, P. & Tapponnier, P. (1975). Cenozoic tectonics of Asia: Effects of a continental collision. *Science*, 189, 419-426.
- Molnar, P. & Tapponnier, P. (1978). Active tectonics of Tibet. *Journal of Geophysical Research: Solid Earth*, 83, 5361-5375.

- Mongelli, G., Critelli, S., Perri, F., Sonnino, M., Perrone, V. (2006). Sedimentary recycling, provenance and paleoweathering from chemistry and mineralogy of Mesozoic continental red-bed mudrocks, Peloritani mountains, southern Italy. *Geochemical Journal* 40, 197– 209.
- Mongelli, G., Critelli, S., Perri, F., Sonnino, M., Perrone, V. (2006). Sedimentary recycling, provenance and paleoweathering from chemistry and mineralogy of Mesozoic continental red-bed mudrocks, Peloritani mountains, southern Italy. *Geochemical Journal* 40, 197– 209.
- O'Connor, J.T. (1965). A classification for quartz-rich igneous rock based on feldspar ratios. U.S.G.S. Professional Paper 525B, B79– B84.
- Ocakoğlu, F. & Açıklın, S. (2010). Field evidences of secondary surface ruptures occurred during the 20 February 1956 Eskişehir earthquake in the NW Anatolia. *Journal of earth system science*, 119, 841-851.
- Ocakoğlu, F. (2007). A re-evaluation of the Eskişehir Fault Zone as a recent extensional structure in NW Turkey. *Journal of Asian Earth Sciences*, 31, 91-103.
- Ocakoğlu, F., Hakyemez, A., Acikalın, S., Altiner, S., Büyükmeriç, Y., Licht, A., ... & Campbell, C. (2018). Chronology of subduction and collision along the izmir-ankara suture in western anatolia: records from the central sakarya basin. *International Geology Review*, 61(10), 1244-1269. <https://doi.org/10.1080/00206814.2018.1507009>.
- Okay, A. I. (1996). Paleo-and Neo-Tethyan events in northwest Turkey: geological and geochronological constraints. *Tectonics of Asia*, 420-441.
- Okay, A. I. & Tuysuz, O. (1999). Tethyan sutures of northern Turkey. *Geological Society, London, Special Publications*, 156, 475-515.
- Okay, A. I. (2008). *Geology of Turkey: a synopsis*. *Anschnitt*, 21, 19-42.

- Okay, A. I., Harris, N. B., & Kelley, S. P. (1998). Exhumation of blueschists along a Tethyan suture in northwest Turkey. *Tectonophysics*, 285(3-4), 275-299.
- Okay, A. I., Tuysuz, O., Satir, M., Ozkan-Altiner, S., Altiner, D., Sherlock, S. & Eren, R. H. (2006). Cretaceous and Triassic subduction-accretion, high-pressure-low-temperature metamorphism, and continental growth in the Central Pontides, Turkey. *Geological Society of America Bulletin*, 118, 1247-1269.
- Okay, A., Tansel, İ., & Tüysüz, O. (2001). Obduction, subduction and collision as reflected in the upper cretaceous–lower eocene sedimentary record of Western Turkey. *Geological Magazine*, 138(2), 117-142. <https://doi.org/10.1017/s0016756801005088>.
- Okay, A. I., & Satir, M. (2000). Coeval plutonism and metamorphism in a latest Oligocene metamorphic core complex in northwest Turkey. *Geological Magazine*, 137(5), 495-516.
- Okay, A.I. & Satir, M. (2006). Geochronology of Eocene plutonism and metamorphism in northwest. *Geodinamica Acta*, 19, 251-266.
- Okay, A.I., Satir, M., Zattin, M., Cavazza, W., Topuz, G. (2008). An Oligocene ductile strikeslip shear zone: the Uludağ Massif, Northwest Turkey-implications for the westward translation of Anatolia. *Geological Society of America Bulletin* 120, 893–911.
- Önen, A. (2003). Neotethyan ophiolitic rocks of the anatolides of nw turkey and comparison with tauride ophiolites. *Journal of the Geological Society*, 160(6), 947-962. <https://doi.org/10.1144/0016-764902-125>.
- Özsayın, E. & Dirik, K. (2007). Quaternary activity of the Cihanbeyli and Yeniceoba fault zones: İnönü-Eskişehir fault system, Central Anatolia. *Turkish Journal of Earth Sciences*, 16, 471-492.

- Parsons, A., Law, R., Lloyd, G., Phillips, R. & Searle, M. (2016). Thermo-kinematic evolution of the Annapurna-Dhaulagiri Himalaya, central Nepal: The Composite Orogenic System. *Geochemistry, Geophysics, Geosystems*, 17, 1511-1539.
- Pearce, J. A., (1982). Trace element characteristics of lavas from destructive plate boundaries. In: Thorpe R.S. (ed.) *Andesites: Orogenic Andesites and Related Rocks*. John Wiley & Sons, Chichester, pp. 525-548, ISBN 0 471 28034 8.
- Pearce, J. A., (1983). Role of the sub-continental lithosphere in magma genesis at active continental margins. 230-249.
- Pearce, J. A., Harris, N. B., & Tindle, A. G. (1984). Trace element discrimination diagrams for the tectonic interpretation of granitic rocks. *Journal of petrology*, 25(4), 956-983.
- Peate, D. W. (1997). The parana-etendeka province. *Geophysical Monograph-American Geophysical Union*, 100, 217-246.
- Pehlivan, Ş., Kandemir, Ö., Kanar, F. ve Tok, T. (2014). Karakaya Kuşağı'nın jeolojisi ve jeodinamik evrimi-Bursa Bölümü, MTA raporu.
- Petrelli, M., Poli, G., Perugini, D., Peccerillo, A., (2005). PetroGraph: A new software to visualize, model, and present geochemical data in igneous petrology. *Geochemistry, Geophysics, Geosystems* 6, doi:10.1029/2005GC000932.
- Phillips, R. J. & Searle, M. P. (2007). Macrostructural and microstructural architecture of the Karakoram Fault: Relationship between magmatism and strike-slip faulting. *Tectonics*, 26.
- Ramsay, M. H. (1997). Sampling and sample preparation. In: Gill, R. (ed.), *Modern analytical geochemistry: An introduction to quantitative chemical analysis for earth, environmental and material scientists*. Addison Wesley Longman, Harlow. 12– 28.

- Raslan, M. F., Ali, M. A., & El-Feky, M. G. (2010). Mineralogy and radioactivity of pegmatites from south wadi khuda area, eastern desert, egypt. *Chinese Journal of Geochemistry*, 29(4), 343-354. <https://doi.org/10.1007/s11631-010-0466-2>.
- Reilinger, R., McClusky, S., Oral, M., King, R., Toksoz, M., Barka, A., Kinik, I., Lenk, O. & Sanli, I. (1997). Global Positioning System measurements of present-day crustal movements in the Arabia-Africa-Eurasia plate collision zone. *Journal of Geophysical Research: Solid Earth* (1978–2012), 102, 9983-9999.
- Reilinger, R., McClusky, S., Vernant, P., Lawrence, S., Ergintav, S., Cakmak, R., Ozener, H., Kadirov, F., Guliev, I., Stepanyan, R., Nadariya, M., Hahubia, G., Mahmoud, S., Sakr, K., Arrajehi, A., Paradissis, D., Al-Aydrus, A., Prilepin, M., Guseva, T., Evren, E., Dmitrova, A., Filikov, S. V., Gomez, F., Al-Ghazzi, R. & Karam, G. (2006). GPS constraints on continental deformation in the Africa-Arabia-Eurasia continental collision zone and implications for the dynamics of plate interactions. *Journal of Geophysical Research*, 111.
- Rice, S., Robertson, A., & Ustaömer, T. (2006). Late cretaceous-early cenozoic tectonic evolution of the eurasian active margin in the central and eastern pontides, northern turkey. *Geological Society London Special Publications*, 260(1), 413-445. <https://doi.org/10.1144/gsl.sp.2006.260.01.17>.
- Robertson, A., Lee, G., Lee, S., Buntin, P., Drexler, M., Abdelhafiz, A., ... & Alamgir, F. (2019). Atomic structure and dynamics of epitaxial platinum bilayers on graphene. *Acs Nano*, 13(10), 12162-12170. <https://doi.org/10.1021/acsnano.9b06701>.
- Rollinson, H.R. (1993). "Using Geochemical Data: Evaluation, Presentation, Interpretation." Longman Scientific & Technical, Singapore.

- Rollinson, H.R. & Pease, V. (2021). *Using Geochemical Data: To Understand Geological Processes*. 2nd Edition, Cambridge University Press, Cambridge.
- Ronner, F., (1954). Uludağ volfram yatakları ile yakın civarının Jeolojisi ve tektoniği. Rap. 2203, MTA Enst. Arşivi
- Ross, P. S. & Bédard, L. P. (2009). Magmatic affinity of modern and ancient subalkaline volcanic rocks determined from trace-element discriminant diagrams. *Canadian Journal of Earth Sciences* 46, 823–839.
- Sandison, D. (1855). Notice of the Earthquakes at Brussa. *Quarterly Journal of the Geological Society*, 11, 543-544.
- Schandl, E. S. & Gorton, M. P. (2002). Application of high field strength elements to discriminate tectonic settings in VMS environments. *Economic Geology* 97, 629–642.
- Selçuk, A. S. & Gökten, Y. E. (2012). Neotectonic Characteristics of the İnönü-Eskişehir Fault System in the Kaymaz (Eskişehir) Region: Influence on the Development of the Mahmudiye-Çifteler-Emirdağ Basin. *Turkish Journal of Earth Sciences*, 21, 521-545.
- Selim, H. H. & Tüysüz, O. (2013). The Bursa–Gönen Depression, NW Turkey: a complex basin developed on the North Anatolian Fault. *Geological Magazine*, 150, 801-821.
- Sellami, S., Pavoni, N., Mayer-Rosa, D., Mueller, S., Eyidogan, H., Aktar, M., Gürbüz, C., Barıs, S., Polat, O. & Yalcın, N. (1997). Seismicity and seismotectonics of the Bursa region. *The Marmara Poly-Project*, ETH, Zurich, 449-486.
- Şengör, A. M. C. & Yılmaz, Y. (1981). Tethyan evolution of Turkey: a plate tectonic approach. *Tectonophysics*, 75, 181-241.

- Şengör, A. M. C. (1985). Strike-slip faulting and related basin formation in zones of tectonic escape: Turkey as a case study. *Journal of Society of Economic Paleontology and Mineralogists*, 37, 227-264.
- Şengör, A. M. C. (1987). Tectonics of the Tethysides: Orogenic collage development in a collisional setting. *Annual Review of Earth and Planetary Sciences*, 15, 213.
- Shabanian, N., Davoudian, A., Azizi, H., Asahara, Y., Neubauer, F., Genser, J., ... & Lee, J. (2020). Petrogenesis of the carboniferous ghaleh-dezh metagranite, sanandaj–sirjan zone, iran: constraints from new zircon u–pb and $^{40}\text{Ar}/^{39}\text{Ar}$ ages and sr–nd isotopes. *Geological Magazine*, 157(11), 1823-1852. <https://doi.org/10.1017/s0016756820000096>.
- Sibson, R. (1977). Fault rocks and fault mechanisms. *Journal of the Geological Society*, 133, 191-213.
- Simpson, C. & Wintsch, R. (1989). Evidence for deformation-induced K-feldspar replacement by myrmekite. *Journal of metamorphic Geology*, 7, 261-275.
- Sláma, J.; Košler, J.; Condon, D.J.; Crowley, J.L.; Gerdes, A.; Hanchar, J.M.; Horstwood, M.S.; Morris, G.A.; Nasdala, L.; Norberg, N. Plešovice zircon—A new natural reference material for U–Pb and Hf isotopic microanalysis. *Chem. Geol.* (2008). 249, 1–35.
- Spitz, G., & Darling, R. (1978). Major and minor element lithogeochemical anomalies surrounding the Louvem copper deposit, Val d'Or, Quebec. *Canadian Journal of Earth Sciences*, 15, 1161–1169.
- Stacey, J.S., Kramers, J.D. (1975). Approximation of terrestrial lead isotope evolution by a two-stage model. *Earth and Planetary Science Letters* 26, 207–221.
- Stampfli, G. M. & Kozur, H. W. (2006). Europe from the Variscan to the Alpine cycles. *Geological Society, London, Memoirs*, 32, 57-82.

- Stampfli, G. M. (2000). Tethyan oceans. Geological Society, London, Special Publications, 173, 1-23.
- Stampfli, G. M., Mosar, J., Favre, P., Pillevuit, A. & Vannay, J.-C. (2001). Permo-Mesozoic evolution of the western Tethys realm: The Neo-Tethys east Mediterranean basin connection. Mémoires du Muséum national d'histoire naturelle, 186, 51-108.
- Steiger, R.H., Jager, E. (1977). Subcommittee on geochronology: Convention of the use of decay constants in geo- and cosmo-chronology. Earth and Planetary Science Letters 36, 359– 362.
- Stipp, M., Stuènitz, H., Heilbronner, R. & Schmid, S. M. (2002). The eastern Tonale fault zone: a ‘natural laboratory’ for crystal plastic deformation of quartz over a temperature range from 250° to 700°C. Journal of Structural Geology, 24, 1861-1884.
- Streckeisen, A. (1976). To each plutonic rock its proper name. Earth-science reviews, 12(1), 1-33.
- Sun, S.S., McDonough, W.F. (1989). Chemical and isotopic systematics of oceanic basalts: Implications for mantle composition and processes. In: Saunders, A.D., Norry, M.J. (eds.), Magmatism in ocean basins. Geological Society Special Publication 42. Geological Society, London. 313– 345.
- Tapponnier, P., Peltzer, G., Le Dain, A., Armijo, R. & Cobbold, P. (1982). Propagating extrusion tectonics in Asia: New insights from simple experiments with plasticine. Geology, 10, 611-616.
- Tatsumoto, M., Knight, R.J., Allegre, C.J. (1973). Time difference in the formation of meteorites as determined from the ratio of lead-207 to lead- 206. Science 180, 1279– 1283.
- Taylor, S. R., & McLennan, S. M. (1985). The continental crust: its composition and evolution.

- Tichomirowa, M., Gerdes, A., Lapp, M., Leonhardt, D., & Whitehouse, M. (2019). The chemical evolution from older (323–318 ma) towards younger highly evolved tin granites (315–314 ma)—sources and metal enrichment in variscan granites of the western erzgebirge (central european variscides, germany). *Minerals*, 9(12), 769. <https://doi.org/10.3390/min9120769>
- Thiéblemont, D., & Cabanis, B. (1990). Utilisation d'un diagramme (Rb/100)—Tb—Ta pour la discrimination geochemique et l'etude petrogenetique des roches magmatiques acides. *Bulletin De La Societé Géologique De France* (8), VI(1), 23–35.
- Tilton, G.R. (1973). Isotopic lead ages of chondritic meteorites. *Earth and Planetary Science Letters* 19, 321– 329.
- Türkecan, A., & Yurtsever, A. (2022). 1:500.000 ölçekli Türkiye Jeoloji Haritası İstanbul Paftası – 2002. *MTA Yerbilimleri Ve Madencilik Dergisi*, 1(1), 1-8.
- Tüysüz, O., Dellaloğlu, A., & Terzioğlu, N. (1995). A magmatic belt within the neo-tethyan suture zone and its role in the tectonic evolution of northern turkey. *Tectonophysics*, 243(1-2), 173-191. [https://doi.org/10.1016/0040-1951\(94\)00197-h](https://doi.org/10.1016/0040-1951(94)00197-h).
- Vaughan-Hammon, J. D., Luisier, C., Baumgartner, L. P., & Schmalholz, S. M. (2021). Peak Alpine metamorphic conditions from staurolite-bearing metapelites in the Monte Rosa nappe (Central European Alps) and geodynamic implications. *Journal of Metamorphic Geology*, 39(7), 897-917.
- Vernon, R. (2000). Review of microstructural evidence of magmatic and solid-state flow. *Visual Geosciences*, 5, 1-23.
- Wallis, D., Phillips, R. J. & Lloyd, G. E. (2013). Fault weakening across the frictional-viscous transition zone, Karakoram Fault Zone, NW Himalaya. *Tectonics*, 32, 1227-1246.

- Wang, L., Teng, J., Chen, M., Hirata, A., n, E., Zhang, Z., ... & Han, X. (2014). Grain rotation mediated by grain boundary dislocations in nanocrystalline platinum. *Nature Communications*, 5(1). <https://doi.org/10.1038/ncomms5402>.
- West, D. P. & Hubbard, M. S. (1997). Progressive localization of deformation during exhumation of a major strike-slip shear zone: Norumbega fault zone, south-central Maine, USA. *Tectonophysics*, 273, 185-201.
- Whalen J, B., Currie K. L. & Chappell B. W. (1987). A-type granites: geochemical characteristics, discrimination and petrogenesis. *Contributions to Mineralogy and Petrology* 95, 407–419.
- White, W.M. (2015). *Isotope geochemistry*. Wiley, Chichester.
- White, W.M., Klein, E.M. (2014). Composition of the oceanic crust. In: Holland, H., Turekian, K.K. (eds.), *Treatise on geochemistry*, 2nd ed. Elsevier, Oxford. 4: 457– 496.
- Wiedenbeck, M. A. P. C., Alle, P., Corfu, F. Y., Griffin, W. L., Meier, M., Oberli, F. V., ... & Spiegel, W. (1995). Three natural zircon standards for U-Th-Pb, Lu-Hf, trace element and REE analyses. *Geostandards newsletter*, 19(1), 1-23.
- Wong, H., Lüdmann, T., Ulug, A. & Görür, N. (1995). The Sea of Marmara: a plate boundary sea in an escape tectonic regime. *Tectonophysics*, 244, 231-250.
- Workman, R.K., Hart, S. (2005). Major and trace element composition of the depleted MORB mantle (DMM). *Earth and Planetary Science Letters* 231, 53– 72.
- Yıldırım, C., Emre, Ö. & Doğan, A. (2005). The uplift of the Uludağ Massif and the Bursa and Uludağ faults, in *Workshop on the Seismicity of the Eskişehir*

fault zone and Related systems, Abstracts: Eskişehir, Eskişehir Osmangazi University, p. 8.

Yiğitbaş, E., Tunç, İ.O., Özkara, Ö. (2018). Sakarya Zonunun Kuzeybatı Kesimlerinde Alt Karakaya Kompleksi ve Nilüfer Biriminin Yaşı, Stratigrafik ve Yapısal Nitelikleri ve Jeolojik Anlamı. TÜBİTAK ÇAYDAG-115Y214 Nolu Proje Raporu (in Turkish).

Zhang, R., Liou, J., & Tsai, C. (1996). Petrogenesis of a high-temperature metamorphic terrane: a new tectonic interpretation for the north dabieshan, central china. *Journal of Metamorphic Geology*, 14(3), 319-333. <https://doi.org/10.1111/j.1525-1314.1996.00319.x>

Zindler, A., Hart, S.R. (1986). Chemical geodynamics. *Annual Review of Earth and Planetary Sciences* 14, 493– 571.

APPENDICES

A. LA-ICP-MS U-Pb zircon analysis results for sample 1802

Spot No	Concentrations				Ages			
	²⁰⁷ Pb/ ²³⁵ U	1 σ %	²⁰⁶ Pb/ ²³⁸ U	1 σ %	²⁰⁶ Pb/ ²³⁸ U	2 σ (abs)	²⁰⁷ Pb/ ²³⁵ U	2 σ (abs)
a2	0.0401	7.0	0.00544	1.4	35	1	40	5
a3	0.0367	9.2	0.00533	1.9	34	1	36	7
a4	0.0341	15.2	0.00518	1.7	33	1	34	10
a5	0.0421	5.7	0.00531	1.5	34	1	42	5
a6	0.0423	5.7	0.00533	1.5	34	1	42	5
a9	0.0426	5.2	0.00527	1.0	34	1	42	4
a10	0.0511	24.1	0.00541	2.2	34	1	47	18

B. LA-ICP-MS U-Pb zircon analysis results for sample 1803

Spot No	Concentrations				Ages			
	²⁰⁷ Pb/ ²³⁵ U	1 σ %	²⁰⁶ Pb/ ²³⁸ U	1 σ %	²⁰⁶ Pb/ ²³⁸ U	2 σ (abs)	²⁰⁷ Pb/ ²³⁵ U	2 σ (abs)
a1	0.3283	6.7	0.03818	2.5	241	12	285	33
a2	0.3137	5.2	0.03934	1.3	249	6	271	25
a3	0.2939	7.2	0.03898	1.4	246	7	256	33
a7	0.3389	7.9	0.03930	1.5	248	7	284	36
a11	0.3061	5.3	0.03803	1.3	241	6	266	22
a12	0.3266	6.2	0.03646	1.8	231	8	282	30
a13	0.3222	4.2	0.03803	1.1	242	6	283	22
a17	0.3211	6.6	0.03804	1.2	241	6	273	31
a21s	0.2720	6.7	0.03706	1.7	235	8	253	37
a22	0.3494	8.0	0.03933	1.9	249	9	293	39
a24	0.3140	9.6	0.03835	1.4	243	7	265	31
a25	0.3224	4.2	0.03800	1.1	240	5	279	20
a26	0.3056	3.5	0.03789	1.1	240	5	268	17
a27	0.3006	5.4	0.03793	1.2	240	6	262	24
a28	0.3028	4.3	0.03653	1.7	231	8	266	20
a30	0.3002	7.9	0.03942	2.0	249	10	262	35

C. LA-ICP-MS U-Pb zircon analysis results for sample 1809

Spot No	Concentrations				Ages			
	²⁰⁷ Pb/ ²³⁵ U	1 σ %	²⁰⁶ Pb/ ²³⁸ U	1 σ %	²⁰⁶ Pb/ ²³⁸ U	2 σ (abs)	²⁰⁷ Pb/ ²³⁵ U	2 σ (abs)
a1	0.25	53.5	0.03	16.4	211.0	67.4	195.9	175.2
a2	0.33	6.7	0.04	2.4	230.2	10.7	279.7	32.7
a9	0.53	6.5	0.04	2.2	233.1	10.1	416.8	39.6
a5	0.39	8.0	0.04	2.3	248.4	11.1	314.3	42.2
a7	0.33	5.8	0.04	2.1	248.5	10.3	278.9	29.6

D. LA-ICP-MS U-Pb zircon analysis results for sample 1810

Spot No	Concentrations				Ages			
	²⁰⁷ Pb/ ²³⁵	1 σ	²⁰⁶ Pb/ ²³⁸	1 σ	²⁰⁶ Pb/ ²³⁸	2 σ	²⁰⁷ Pb/ ²³⁵	2 σ
	U	%	U	%	U	(abs)	U	(abs)
a9	0.24	6.7	0.02	3.1	151.2	9.4	207.5	26.0
a3	0.17	5.0	0.03	1.8	159.4	5.8	155.8	14.6
a5	0.23	6.2	0.03	1.5	194.8	5.7	208.2	23.4
a2	0.22	5.5	0.03	1.7	204.0	6.8	200.3	20.2
a12	0.47	6.9	0.03	2.4	209.8	10.1	369.2	44.2
a10	0.28	5.5	0.04	1.8	225.2	7.8	251.2	26.7
a6	0.26	5.7	0.04	1.9	230.5	8.4	228.3	23.8
a4	0.26	5.6	0.04	2.0	232.2	9.0	226.7	23.3
a1	0.31	5.6	0.04	1.8	239.0	8.4	264.3	27.2

E. LA-ICP-MS U-Pb zircon analysis results for sample 1811

Spot No	Concentrations				Ages			
	$^{207}\text{Pb}/^{235}\text{U}$		$^{206}\text{Pb}/^{238}\text{U}$		$^{206}\text{Pb}/^{238}\text{U}$		$^{207}\text{Pb}/^{235}\text{U}$	
	U	1 σ %	U	1 σ %	U	2 σ (abs)	U	2 σ (abs)
a45	0.01	6.38	0.01	3.11	41.91	2.60	10.31	1.31
a44	0.01	5.88	0.01	5.33	49.00	5.21	10.66	1.25
a46	0.01	6.25	0.01	1.89	49.87	1.88	11.95	1.48
a3	0.02	7.71	0.01	4.09	57.32	4.66	15.26	2.33
a43	0.01	5.56	0.01	1.14	61.26	1.39	14.78	1.63
a4	0.02	5.44	0.01	2.30	64.37	2.94	15.96	1.73
a2	0.02	4.77	0.01	1.37	73.27	1.99	16.30	1.55
a28	0.04	5.17	0.01	1.73	75.32	2.59	39.58	4.05
a25	0.02	6.53	0.01	2.06	76.32	3.12	17.00	2.21
a1	0.02	4.84	0.01	1.46	76.62	2.22	17.08	1.64
a18	0.03	3.38	0.01	1.48	77.35	2.28	32.10	2.13
a24	0.02	5.51	0.01	1.79	89.27	3.18	17.58	1.93
a41	0.03	5.40	0.01	1.69	95.69	3.21	27.05	2.90
a5	0.03	5.50	0.02	1.41	98.09	2.76	27.19	2.96
a29	0.12	5.15	0.02	2.39	100.00	4.75	118.09	11.52
a22	0.02	6.41	0.02	2.26	101.10	4.53	22.54	2.86
a20	0.03	3.64	0.02	2.07	107.09	4.40	33.88	2.43
a23	0.02	6.68	0.02	2.07	109.93	4.52	21.90	2.89
a40	0.04	5.53	0.02	1.70	114.99	3.88	38.06	4.14
a38	0.04	5.68	0.02	1.90	116.13	4.39	43.42	4.85
a6	0.03	5.50	0.02	2.33	116.62	5.39	34.15	3.72
a39	0.04	5.67	0.02	2.17	119.43	5.14	39.01	4.37
a17	0.07	7.66	0.02	4.21	141.98	11.85	70.54	10.52
a37	0.07	4.77	0.03	1.19	163.23	3.84	69.03	6.43
a8	0.21	5.49	0.03	2.04	171.91	6.92	193.73	20.67
a9	0.29	6.82	0.03	2.37	172.98	8.10	246.03	29.95
a7	0.23	5.58	0.03	2.38	182.42	8.58	203.40	21.03
a10	0.37	6.65	0.03	2.51	185.24	9.19	305.95	36.51

F. LA-ICP-MS U-Pb zircon analysis results for sample 1812

Spot No	Concentrations				Ages			
	²⁰⁷ Pb/ ²³⁵ U	1 σ %	²⁰⁶ Pb/ ²³⁸ U	1 σ %	²⁰⁶ Pb/ ²³⁸ U	2 σ (abs)	²⁰⁷ Pb/ ²³⁵ U	2 σ (abs)
a2	0.0547	3.2	0.00840	1.0	54	1	54	3
a3	0.0583	5.1	0.00837	1.1	54	1	57	6
a5	0.0565	3.2	0.00844	1.1	54	1	56	3
a7	0.0611	7.3	0.00833	2.0	53	2	60	8
a8	0.0568	4.5	0.00837	3.0	54	3	56	5
a9	0.0604	3.3	0.00829	1.4	53	2	59	4
a12	0.0560	2.8	0.00827	1.0	53	1	55	3
a13	0.0597	6.2	0.00841	2.4	54	3	59	7
a14	0.0568	4.3	0.00845	1.9	54	2	56	5
a15	0.0567	3.6	0.00844	1.4	54	1	56	4
a16	0.0593	2.9	0.00833	1.1	53	1	58	3
a17	0.0548	3.0	0.00846	1.1	54	1	54	3
a19	0.0583	2.7	0.00834	1.2	54	1	57	3
a20	0.0580	4.0	0.00850	1.8	55	2	57	4
a21	0.0639	4.5	0.00829	1.4	53	1	63	6
a22	0.0599	2.9	0.00840	1.1	54	1	59	3
a23	0.0614	9.1	0.00859	2.3	55	3	60	11
a25	0.0560	2.4	0.00829	1.0	53	1	55	3
a26	0.0554	4.2	0.00835	1.9	54	2	55	5
a27	0.0607	2.9	0.00828	1.2	53	1	60	3
a28	0.0560	4.8	0.00832	2.0	53	2	55	5
a29	0.0577	3.2	0.00831	1.1	53	1	57	4
a30	0.0606	2.4	0.00834	1.0	54	1	60	3

G. LA-ICP-MS U-Pb zircon analysis results for sample 1813

Spot No	Concentrations				Ages			
	²⁰⁷ Pb/ ²³⁵ U	1 σ %	²⁰⁶ Pb/ ²³⁸ U	1 σ %	²⁰⁶ Pb/ ²³⁸ U	2 σ (abs)	²⁰⁷ Pb/ ²³⁵ U	2 σ (abs)
a1	0.0602	9.2	0.00763	1.7	49	2	58	10
a2S	0.0578	5.2	0.00742	1.5	48	1	57	6
a3S	0.0560	6.7	0.00741	1.7	48	2	55	7
a4S	0.0601	12.8	0.00758	3.9	49	4	59	15
a6	0.0510	10.5	0.00739	1.7	47	2	49	10
a7	0.0555	8.8	0.00768	2.1	49	2	54	9
a8	0.0580	8.0	0.00750	1.9	48	2	57	9
a10	0.0517	5.7	0.00756	1.3	49	1	51	6
a11S	0.0457	5.0	0.00734	1.1	47	1	45	4
a12	0.0578	7.5	0.00773	1.8	50	2	56	8
a13S	0.0390	16.8	0.00750	3.0	48	3	38	13
a14S	0.0497	10.0	0.00762	1.7	49	2	48	9
a17	0.0530	6.7	0.00749	2.0	48	2	52	7
a18S	0.0479	5.3	0.00753	1.5	48	1	47	5
a19	0.0515	7.8	0.00742	2.0	48	2	50	8
a20	0.0479	4.3	0.00746	1.3	48	1	47	4
a21	0.0508	6.6	0.00740	1.3	48	1	50	6
a22	0.0501	7.3	0.00763	1.5	49	1	49	7
a23	0.0500	7.8	0.00748	1.9	48	2	49	8
a24	0.0494	6.8	0.00759	1.5	49	1	48	7
a25	0.0566	10.1	0.00759	2.4	49	2	55	11
a27	0.0534	10.1	0.00744	2.4	48	2	52	10
a29	0.0556	6.5	0.00746	1.5	48	1	55	7
a30	0.0491	8.1	0.00771	1.5	50	1	48	8
a31	0.0458	8.0	0.00745	1.8	48	2	45	7
a32	0.0528	8.5	0.00766	1.7	49	2	51	9
a34S	0.0779	32.9	0.00738	3.5	47	3	71	42
a35	0.0505	6.0	0.00736	1.6	47	1	50	6
a36S	0.0480	10.0	0.00759	3.3	49	3	47	9
a38	0.0541	5.4	0.00746	1.8	48	2	53	6
a39S	0.0534	5.8	0.00760	1.4	49	1	52	6
a40	0.0543	6.7	0.00754	1.5	48	1	54	7

H. A-ICP-MS U-Pb zircon analysis results for sample 1814

Spot No	Concentrations				Ages			
	²⁰⁷ Pb/ ²³⁵ U	1 σ %	²⁰⁶ Pb/ ²³⁸ U	1 σ %	²⁰⁶ Pb/ ²³⁸ U	2 σ (abs)	²⁰⁷ Pb/ ²³⁵ U	2 σ (abs)
a1	0.0602	9.2	0.00763	1.7	49	2	58	10
a2S	0.0578	5.2	0.00742	1.5	48	1	57	6
a3S	0.0560	6.7	0.00741	1.7	48	2	55	7
a4S	0.0601	12.8	0.00758	3.9	49	4	59	15
a6	0.0510	10.5	0.00739	1.7	47	2	49	10
a7	0.0555	8.8	0.00768	2.1	49	2	54	9
a8	0.0580	8.0	0.00750	1.9	48	2	57	9
a10	0.0517	5.7	0.00756	1.3	49	1	51	6
a11S	0.0457	5.0	0.00734	1.1	47	1	45	4
a12	0.0578	7.5	0.00773	1.8	50	2	56	8
a13S	0.0390	16.8	0.00750	3.0	48	3	38	13
a14S	0.0497	10.0	0.00762	1.7	49	2	48	9
a17	0.0530	6.7	0.00749	2.0	48	2	52	7
a18S	0.0479	5.3	0.00753	1.5	48	1	47	5
a19	0.0515	7.8	0.00742	2.0	48	2	50	8
a20	0.0479	4.3	0.00746	1.3	48	1	47	4
a21	0.0508	6.6	0.00740	1.3	48	1	50	6
a22	0.0501	7.3	0.00763	1.5	49	1	49	7
a23	0.0500	7.8	0.00748	1.9	48	2	49	8
a24	0.0494	6.8	0.00759	1.5	49	1	48	7
a25	0.0566	10.1	0.00759	2.4	49	2	55	11
a27	0.0534	10.1	0.00744	2.4	48	2	52	10
a29	0.0556	6.5	0.00746	1.5	48	1	55	7
a30	0.0491	8.1	0.00771	1.5	50	1	48	8
a31	0.0458	8.0	0.00745	1.8	48	2	45	7
a32	0.0528	8.5	0.00766	1.7	49	2	51	9
a34S	0.0779	32.9	0.00738	3.5	47	3	71	42
a35	0.0505	6.0	0.00736	1.6	47	1	50	6
a36S	0.0480	10.0	0.00759	3.3	49	3	47	9
a38	0.0541	5.4	0.00746	1.8	48	2	53	6
a39S	0.0534	5.8	0.00760	1.4	49	1	52	6
a40	0.0543	6.7	0.00754	1.5	48	1	54	7

I. LA-ICP-MS U-Pb zircon analysis results for sample 1817

Spot No	Concentrations				Ages			
	$^{207}\text{Pb}/^{235}\text{U}$	1 σ	$^{206}\text{Pb}/^{238}\text{U}$	1 σ	$^{206}\text{Pb}/^{238}\text{U}$	2 σ	$^{207}\text{Pb}/^{235}\text{U}$	2 σ
		%		%		(abs)		(abs)
a1	0.0766	25.8	0.00549	2.5	35	2	56	13
a2	0.0388	6.7	0.00574	1.4	37	1	38	5
a4	0.0386	5.2	0.00551	1.7	35	1	38	4
a5	0.0358	7.5	0.00541	1.5	35	1	35	5

J. LA-ICP-MS U-Pb zircon analysis results for sample 1819

Spot No	Concentrations				Ages			
	$^{207}\text{Pb}/^{235}\text{U}$	1 σ	$^{206}\text{Pb}/^{238}\text{U}$	1 σ	$^{206}\text{Pb}/^{238}\text{U}$	2 σ	$^{207}\text{Pb}/^{235}\text{U}$	2 σ
	U	%	U	%	U	(abs)	U	(abs)
a31	0.05	5.1	0.01	3.1	33.3	2.1	46.5	4.6
a33	0.05	10.2	0.01	2.0	33.9	1.3	49.3	9.5
a5	0.02	5.0	0.01	1.4	33.9	1.0	23.3	2.3
a34	0.04	7.1	0.01	2.0	33.9	1.3	43.2	6.0
a22	0.03	5.6	0.01	1.7	34.1	1.2	31.4	3.5
a32	0.04	7.4	0.01	1.8	34.5	1.3	43.8	6.3
a38	0.04	6.6	0.01	2.0	35.0	1.4	36.5	4.8
a10	0.03	5.7	0.01	1.5	35.1	1.1	34.1	3.8
a39	0.05	16.0	0.01	5.3	35.6	3.8	46.4	14.3
a26	0.04	12.9	0.01	9.7	35.7	6.9	41.9	10.7
a9	0.03	14.1	0.01	2.6	35.9	1.8	28.3	7.6
a25	0.02	10.6	0.01	2.7	35.9	1.9	22.2	4.7
a21	0.08	8.0	0.01	3.6	36.1	2.6	75.9	11.9
a30	0.06	18.6	0.01	3.6	36.2	2.6	47.9	14.6
a24	0.07	24.4	0.01	3.8	36.3	2.8	65.3	28.1
a20	0.09	5.6	0.01	2.2	36.9	1.6	89.3	9.6
a37	0.10	13.0	0.01	6.8	37.0	5.0	96.3	23.4
a11	0.10	5.5	0.01	1.5	37.5	1.1	93.8	9.8
a29	0.09	3.6	0.01	1.3	38.9	1.0	88.1	6.1
a19	0.14	4.9	0.01	1.9	39.8	1.5	132.8	12.1
a13	0.13	5.2	0.01	1.4	40.7	1.1	121.1	12.0

K. LA-ICP-MS U-Pb zircon analysis results for sample 1820

Spot No	Concentrations				Ages			
	²⁰⁷ Pb/ ²³⁵ U	1 σ %	²⁰⁶ Pb/ ²³⁸ U	1 σ %	²⁰⁶ Pb/ ²³⁸ U	2 σ (abs)	²⁰⁷ Pb/ ²³⁵ U	2 σ (abs)
a6	0.030	4.0	0.003	3.5	20.1	1.4	29.8	2.3
a3	0.034	6.4	0.005	1.7	32.5	1.1	33.6	4.2
a9	0.107	9.3	0.005	2.3	33.0	1.5	99.9	17.6
a10	0.055	7.2	0.005	2.0	33.3	1.3	53.6	7.5
a5	0.149	6.2	0.012	2.0	78.7	3.2	138.1	16.4
a12	0.183	6.7	0.016	2.4	103.3	5.0	166.3	20.8
a8	0.274	1.9	0.020	3.3	125.9	8.3	245.6	8.2
a13	0.223	4.6	0.022	1.7	140.3	4.6	201.7	16.8
a7	0.311	5.1	0.034	2.2	213.3	9.5	268.8	24.9
a1	0.263	6.0	0.038	1.5	237.6	6.9	230.9	25.1
a14	0.659	4.1	0.046	2.8	288.8	15.8	502.3	34.6
a11	0.520	4.0	0.048	3.6	303.6	21.3	417.7	27.3

L. LA-ICP-MS U-Pb zircon analysis results for sample 1821

Spot No	Concentrations				Ages			
	²⁰⁷ Pb/ ²³⁵ U	1 σ %	²⁰⁶ Pb/ ²³⁸ U	1 σ %	²⁰⁶ Pb/ ²³⁸ U	2 σ (abs)	²⁰⁷ Pb/ ²³⁵ U	2 σ (abs)
a5	0.0108	11.9	0.003	3.2	20.0	1.3	10.9	2.5
a7	0.0080	6.2	0.003	1.7	21.8	0.7	8.0	1.0
a4	0.0058	17.0	0.004	11.7	23.7	5.6	5.8	2.0
a8	0.0360	12.6	0.004	2.7	25.1	1.4	35.1	8.7
a9	0.0594	27.2	0.004	15.2	25.6	7.8	57.7	31.2
a23	0.0243	6.5	0.004	1.7	28.7	1.0	24.3	3.1
a10	0.0255	7.4	0.004	2.1	28.9	1.2	25.4	3.7
a21	0.0250	7.3	0.004	1.5	28.9	0.8	25.0	3.6
a24	0.0271	6.5	0.005	2.0	29.1	1.2	27.0	3.5
a3	0.0357	5.5	0.005	1.9	29.2	1.1	35.4	3.9
a13	0.0311	6.7	0.005	1.6	29.4	1.0	31.0	4.1
a12	0.0306	6.3	0.005	1.7	29.7	1.0	30.4	3.8
a22	0.0264	6.4	0.005	1.8	29.9	1.1	26.3	3.3
a16	0.0393	5.9	0.005	2.1	30.3	1.3	38.9	4.5
a17	0.0570	8.5	0.005	2.2	30.8	1.4	56.2	9.3
a20	0.0297	50.0	0.005	9.7	31.2	6.0	28.0	26.9
a11	0.0432	21.2	0.005	3.5	32.0	2.2	42.5	17.7
a25	0.0456	7.2	0.005	2.7	32.3	1.8	45.1	6.4
a14	0.0501	11.4	0.005	2.2	33.7	1.5	49.4	11.1
a26	0.0542	6.8	0.005	1.5	35.1	1.1	53.3	7.0
a27	0.0318	6.1	0.006	1.5	35.4	1.1	31.6	3.8
a28	0.0474	4.9	0.006	1.5	37.6	1.2	47.0	4.5

M. LA-ICP-MS U-Pb zircon analysis results for sample 1903

Spot No	Concentrations				Ages			
	$^{207}\text{Pb}/^{235}\text{U}$	1 σ %	$^{206}\text{Pb}/^{238}\text{U}$	1 σ %	$^{206}\text{Pb}/^{238}\text{U}$	2 σ (abs)	$^{207}\text{Pb}/^{235}\text{U}$	2 σ (abs)
	U		U		U		U	
a15	0.007	6.2	0.004	1.9	28	1	7	1
a18	0.008	6.9	0.005	1.8	32	1	8	1
a13	0.008	8.5	0.005	1.7	32	1	9	1
a17	0.011	6.3	0.005	1.4	33	1	11	1
a19	0.012	5.7	0.006	1.6	39	1	12	1
a21	0.012	6.0	0.007	3.3	44	3	12	1
a23	0.045	4.9	0.007	3.4	45	3	44	4
a24	0.070	5.9	0.009	1.8	57	2	68	8
a25	0.057	5.8	0.009	1.5	59	2	56	6
a14	0.016	7.2	0.010	3.6	61	4	17	2
a2	0.120	6.0	0.010	1.4	66	2	113	13

N. LA-ICP-MS U-Pb zircon analysis results for sample 1904

Spot No	Concentrations				Ages			
	²⁰⁷ Pb/ ²³⁵ U	1 σ %	²⁰⁶ Pb/ ²³⁸ U	1 σ %	²⁰⁶ Pb/ ²³⁸ U	2 σ (abs)	²⁰⁷ Pb/ ²³⁵ U	2 σ (abs)
a3	0.216	6.6	0.033	1.8	210	7	193	24
a1	0.233	6.2	0.034	1.9	218	8	207	23
a2	0.237	6.8	0.034	1.8	218	8	209	26
a8	0.265	7.0	0.035	2.2	222	10	230	29
a4	0.407	7.1	0.035	1.5	223	6	343	40
a29	0.351	4.8	0.035	1.6	224	7	299	25
a35	0.256	6.5	0.036	1.8	225	8	229	28
a30	0.356	4.2	0.037	1.4	231	6	304	23
a12	0.180	10.3	0.037	2.8	235	13	163	31
a31	0.251	6.6	0.037	2.1	237	10	224	28
a32	0.296	6.3	0.038	2.0	239	9	254	29
a21	0.331	5.4	0.038	1.7	240	8	283	27
a25	0.346	5.3	0.038	1.4	241	7	299	29
a14	0.334	7.0	0.038	2.6	242	13	280	35
a28	0.303	6.1	0.038	1.8	242	8	260	29
a10	0.241	4.9	0.038	2.6	242	12	215	20
a34	0.263	5.2	0.038	1.9	243	9	232	22
a20	0.301	6.7	0.039	2.0	249	10	257	31
a15	0.246	6.8	0.040	2.1	250	10	216	27
a7	0.265	5.6	0.040	1.6	251	8	233	24
a26	0.311	6.3	0.040	2.0	253	10	270	31
a23	0.297	6.2	0.040	2.2	253	11	255	29
a24	0.296	6.5	0.040	1.8	255	9	258	31
a19	0.365	6.2	0.041	2.0	261	10	305	34
a9	0.336	7.4	0.041	2.0	262	10	280	37
a11	0.280	7.2	0.042	1.9	262	10	246	32
a18	0.327	6.6	0.042	2.0	263	10	276	33
a22	0.361	7.3	0.042	2.7	266	14	298	37
a13	0.298	6.2	0.043	1.6	271	9	256	29

CURRICULUM VITAE

Surname, Name: Şahin, Gülen

EDUCATION

Degree	Institution	Year of Graduation
M.Sc.	Royal Holloway University of London Earth Sciences	2015
M.Eng.	Çanakkale Onsekiz Mart University Geological Engineering	2013
B.Eng.	Çanakkale Onsekiz Mart University Geological Engineering	2011
High School	Çankırı Süleyman Demirel Science High School, Çankırı	2006

FOREIGN LANGUAGES

Advanced English,

PUBLICATIONS

Yetkin, M., Dedeoğlu, İ. Ö., & Tunç, G. (2024). February 6, 2023, Kahramanmaraş twin earthquakes: Evaluation of ground motions and seismic performance of buildings for Elazığ, southeast of Türkiye. *Soil Dynamics and Earthquake Engineering*, 181, 108678. <https://dx.doi.org/10.1016/j.soildyn.2024.108678>

Tunç, G., Dedeoğlu, İ. Ö., & Alpaslan, N. (2024). Karacadağ Volkanitlerinin Mühendislik Özellikleri Üzerine Bir Araştırma. *76. Türkiye Jeoloji Kurultayı*, 1(1), 460-460. (Özet Bildiri/Poster)

Dedeođlu, İ. Ö., Tunç, G., & Alpaslan, N. (2023). Evaluation of dynamic behavior by linear equivalent analysis of North Batman, Turkey. *Bulletin of Engineering Geology and the Environment*, 82(4), 139. <https://dx.doi.org/10.1007/s10064-023-03169-5>

Tunç, G. & Özden, S. (2021). Stress State Analysis And Active Tectonics Of Çavdarhisar (Kütahya) Province, (NW Anatolia, Turkey) From Pre-Late Cenozoic To Quaternary. *European Geosciences Union (EGU) 2021*, <https://doi.org/10.5194/egusphere-egu21-464> (Özet Bildiri/Sözlü Sunum)

Tunç Gülen (2022). Doğrultu Atımlı Fay Tektoniđi Boyunca Havza Gelişimi: Landsat TM ve SRTM Görüntüleri ile Altyn Tagh Fay Sistemi Havza Örnekleri. *74. Türkiye Jeoloji Kurultayı*, 1(1), 501-501. (Özet Bildiri/Poster)

Şahin Gülen, Özden Süha (2013). Çavdarhisar (Kütahya) ve Yakın Civarının Geçsenozoyik Yaşlı Gerilme Durumları ve Aktif Tektoniđi, Batı Anadolu, Türkiye. *66. Türkiye Jeoloji Kurultayı* (Özet Bildiri/Poster)